https://doi.org/10.61092/iaea.6x1h-6pf8

INDC(NDS)- 0691
Distr. AC/AD/FE/J/PR/RD

IAEA
International Atomic Energy Agency

INDC International Nuclear Data Committee

Primary Radiation Damage Cross Sections

Summary Report of the Second Research Coordination Meeting

IAEA Headquarters, Vienna, Austria

29 June - 2 July 2015

prepared by

R.E. Stoller, Oak Ridge National Laboratory, Oak Ridge, TN, USA

L.R. Greenwood, Pacific Northwest National Laboratory, Richland, WA, USA

S.P. Simakov, Nuclear Data Section of IAEA, Vienna, Austria

December 2015

IAEA Nuclear Data Section
Vienna International Centre, P.O. Box 100, 1400 Vienna, Austria

Selected INDC documents may be downloaded in electronic form from
http://www-nds.iaea.org/publications
or sent as an e-mail attachment.
Requests for hardcopy or e-mail transmittal should be directed to
NDS.Contact-Point@iaea.org
or to:
Nuclear Data Section
International Atomic Energy Agency
Vienna International Centre
PO Box 100
1400 Vienna
Austria

Printed by the IAEA in Austria

December 2015

INDC(NDS)-0691
Distr. AC/AD/FE/G/J/PR/RD

Summary Report

of the Second Research Coordination Meeting of the IAEA CRP no. F44003

Primary Radiation Damage Cross Sections

IAEA Headquarters, Vienna, Austria

29 June - 2 July 2015

prepared by

R.E. Stoller, Oak Ridge National Laboratory, Oak Ridge, TN, USA

L.R. Greenwood, Pacific Northwest National Laboratory, Richland, WA, USA

S.P. Simakov, Nuclear Data Section of IAEA, Vienna, Austria

Abstract

In 2013 the Nuclear Data Section of IAEA has initiated a Coordinated Research Project (CRP) with the main goal of reviewing and recommending primary damage response functions for neutron and ion irradiations of crystalline materials. The output of this CRP has to be a database of recommended damage cross sections for selected materials with corresponding documentation, which will serve the needs of the fission, fusion and accelerator communities. The second Research Coordination Meeting (RCM-2) was held 29 June to 2 July 2015 at the IAEA Headquarters in Vienna. This Summary Report documents the individual contributions, summarises the results and progress achieved since RCM-1, lists the joint decisions and actions adopted for the further research.

December 2015

Table of Contents

I. Introduction

Objectives and outcomes of the Coordinated Research Project

The Nuclear Data Section of the IAEA, in accordance with the recommendation of the International Nuclear Data Committee (INDC) meeting held in May 2012 [1] and the dedicated Technical Meeting "Primary Radiation Damage Cross Sections" held in October 2012 [2], has initiated a Coordinated Research Project F44003 for period from 2013 through 2017 (as currently planned).

The overall and specific technical information is available on the CRP web-page, maintained by NDS of IAEA: https://www-nds.iaea.org/CRPdpa/.

The first Research Coordination Meeting (RCM-1) was held 4 to 8 November 2013. The background, purpose, and objectives of the CRP were intensively discussed there and summarised in the RCM-1 Report INDC(NDS)-0648 [3].

The main CRP outputs are expected to be the damage response functions such as: *NRT*-, *arc*-(athermal recombination-corrected) atom displacement (dpa), atom replacement (*rpa*) and gas production cross sections including their uncertainties as numerical databases. The CRP final document will describe the database and the results of research.

We emphasize that the *arc*-dpa and *rpa* equations are not intended to replace the *NRT*-dpa, which is still valid as a convenient energy deposition unit and is useful for applications such as comparing different kinds of irradiations. Rather, they are an alternative if one wishes to have a somewhat more accurate estimate of the actual damage production or number of replaced (mixed) atoms.

However the *arc*-dpa concept has certain advantages in comparison with *NRT* since it captures additional physical phenomena occurring during the characteristic time 0.1 - 1 ns, when recoils cascades evolve and relax:

- the PKA cascade morphology and hence the damage energy eventually delivered to the lattice atoms are fully and exactly simulated, that means exact accounting for the incident neutron spectrum and correct inter-comparison of the different facilities on the basis of the accumulated dpa-fluence;
- allows empirical validation against frozen defects at cryogenic temperature (whereas *NRT* is an unobservable quantity);
- accounts for the ambient temperature and damage production rate during hot cascade phase;
- becomes more feasible parameter for comparison of damage induced by neutrons and charged particles or ions.

The second Research Coordination Meeting (RCM-2)

The second RCM of the IAEA CRP on "Primary Radiation Damage Cross Sections" was held at IAEA Headquarters, Vienna, Austria from 29 June to 2 July 2015. The following holders of the CRP Research Agreements or their representatives have attended this meeting: M.R. Gilbert, L.R. Greenwood, P. Griffin, P. Helgesson, Y. Iwamoto, A. Kahler, V. Khryachkov, A. Konobeev, A. Koning, J. Kwon, N. Lazarev, L. Luneville, F. Mota, K. Nordlund, D. Simeone, H. Sjöstrand, J.-C. Sublet, R.E. Stoller, D. Terentyev and C. Woo. M. Caturla could not attend. O. Cabellos cancelled his CRP Agreement because of joining the NEA Data Bank of OECD in Paris. J.-P. Crocombette and D. Leichtle took part as observers. The Nuclear Data Section of IAEA was represented by S.P. Simakov (Project Scientific Officer), R. Capote, N. Otuka, V. Semkova and A. Trkov.

The Meeting was opened by R. Capote, Deputy Section Head of the IAEA Nuclear Data Section, who welcomed the participants and underlined the importance of this CRP for establishing well defined nuclear data as a baseline for the analysis of radiation damage in the materials.

A. Oechs, who was responsible for the Meeting preparation issues, made several announcements.

It was followed by the self-introduction of participants.

The participants have elected R.E. Stoller as the Chairman and L.R. Greenwood as the Rapporteur of this Meeting and approved its Agenda (Appendix I).

The list of participants and their affiliations are summarized in Appendix II.

The current administrative and main technical issues of CRP, the objectives and goals of the Meeting were outlined by S.P. Simakov.

During this Meeting participants made more than twenty technical presentations (which are available on the *CRP/RCM-2 web page*) in which they reported the results of researches carried out and the scope of work they plan to do in the context of this CRP.

The overview of the project evolution and results achieved are summarised in Section II. The set of consolidated recommendations for the further actions as a result of held discussions are outlined in Section III.

The individual summaries of the CRP participants' presentations and work foreseen in the frame of CRP are collected in Section IV.

The Nuclear Data Section acknowledged all participants for their cooperation and contributions to the Meeting.

II. Evolution of CRP since RCM-1

This section summarises the progress achieved and trends identified in the frame of this CRP from the RCM-1 (the **bold font** highlights the key physical quantities, *italic font* stresses the main findings or opened issues).

Nuclear data for Radiation Damage

The **energy spectra of the Primary Knocked-out Atoms** (PKA) are the starting point for the consequent damage energy and displacement cross sections calculations. However, as several participants (A. Konobeev and U. Fischer, Y. Iwamoto et al., P. Griffin, J.-Ch. Sublet and M.R. Gilbert, F. Mota et al., see their Summaries in Section IV) have shown, the PKA spectra derived from the main evaluated neutron cross section libraries ENDF/B-VII.1 [4], JENDL-4 [5], JEFF-3.2 [6], TENDL-2014 [7] are different. The notable deviations among them were observed already at neutron energies of a few MeV, and essentially increase at 14 MeV and higher energies, where multiple particle emission reactions such as (n,2n) open.

The recommendation of the most reliable calculation models and selection of representative (to serve as a reference) evaluated files of PKA spectra remain the primary task of this CRP.

The **kinematic energy deposition in materials (KERMA factors)** calculated from the PKA spectra using various evaluations consequently also disagree (up to factor of 2). Moreover the calculated KERMA do not always agree with the existing experimental data. Even for Iron, the calculated KERMA systematically underestimates the known measurements. It is worthwhile to note that no measurements were carried out so far below a neutron energy of 5 MeV, where, for example at thermal energies, KERMA calculated from different libraries can differ by factor of 10.

It was found that the majority of published experimental KERMA data are missed in EXFOR. NDS has performed systematic search of published results and has initiated the compilation of missing data in EXFOR (https://www-nds.iaea.org/CRPdpa/DataMissed.pdf).

It is impossible to measure the initial number of atoms knocked out by incident neutrons as predicted by the *NRT*-dpa cross section. However, the number of Frenkel pairs surviving after cascade relaxation

can be estimated based on electrical resistivity measurements, if the sample is irradiated and maintained at cryogenic temperature to immobilize defects prior to the measurements. **This information can be used to experimentally calibrate the *arc-dpa* cross section.**

In the frame of this CRP, Y. Iwamoto and co-workers carried out the new measurement of the electrical resistivity increase in Cu at 12°K by 125 MeV protons and derived *arc*-dpa [8].

However, the conversion to the arc-dpa cross section requires the knowledge of resistivity change per Frenkel-pair which currently is only known within an uncertainty of 50%. What information could be used to reduce this uncertainty?

Status of **gas production cross sections**. For Iron, the main structural element, the set of representative independent measurements covers the neutron energy range from 5 to 120 MeV. The comparison of evaluated and experimental data has shown reasonable agreement in the case of DXS [9] and ENDF/B-VII.1 libraries, whereas other nuclear data evaluations, e.g. TENDL-2014, essentially underestimates the measurements in whole energy range, and whereas JENDL-4 has issues above 20 MeV. For other elements and isotopes of our interest (Cr, Cu, Zr, W, Ti, Al, V, Si, C …) experimental data are still scarce and the corresponding evaluated cross sections essentially differ.

In the frame of this CRP the new measurements of the (n,α) cross sections for Cr isotopes were performed by IPPE, Obninsk (see V. Khryachkov et al., Section IV).

The systematic evaluation of gas production cross sections for structural elements has been carried out by KIT, Karlsruhe, basing on the modern modelling and available experimental data [10 - 13]. The latest evaluated data for neutron and proton induced gas production reactions on Ti and W up to 3 GeV [12] were included in DXS this year.

The two-step neutron reactions sequence ^{58}Ni(n,γ)^{59}Ni(n,α)^{56}Fe notably contributes to both the He production and the damage energy in Ni-bearing steels exposed to a thermal neutron spectrum. P. Helgesson with co-workers has performed a preliminary evaluation of the ^{59}Ni(n,α)^{56}Fe and ^{59}Ni(n,p)^{58}Co cross sections (see Section IV).

The measurements and evaluations of the cross sections for gas-production reactions including uncertainties for the abovementioned materials remain an actual task of this CRP.

Presently the **evaluated nuclear reaction data relevant to the radiation damage have no uncertainties or energy-energy correlation matrices** whereas many other evaluated quantities do have quantified uncertainties in modern cross section libraries. The first attempts in this direction were done in the frame of this CRP.

P. Griffin et al. (see Section IV) performed inter-comparative analysis of uncertainties for ^{28}Si using (i) the cross section covariances data available for the basic reaction channels in the evaluated libraries (MF 33) and (ii) a Total Monte Carlo (TMC) analysis [14] which allows the non-linear uncertainty propagation from the model-based variation in the TALYS cross sections into the kerma and displacement components. He also addressed to the impact of the "model defects" (the different approaches to generate the Si ions damage partition function) on displacement uncertainties.

P. Helgesson and co-workers [15] have also used the TMC method to assess uncertainty for various n + ^{59}Ni reaction channels including He and H production in the new cross section evaluation. The specific point was that they weighted random nuclear data files with likelihood function computed from comparison with experimental data and covariance matrices generated from EXFOR.

Elaboration and implementation of approaches to propagate the uncertainties of nuclear reaction cross sections and recoil energy delivered to atoms to the damage and gas production cross sections has to be continued.

Processing of evaluated data. Most of CRP participants use the code NJOY-2012 (or previous versions) [16] to compute damage energy and gas production cross sections from the evaluated files recorded in the ENDF-6 format. Actual status of data processing by NJOY was reported by A.C.

Kahler (see Section IV). Several drawbacks were found by CRP participants and reported to him. As examples:

- the number of "particle pairs" used in the LRF = 7 format is limited to 11;
- module GROUPR fails to process the output tape from MIXR (new update patch for NJOY-2012 will resolve this);
- definition of Damage energy in HEATR is inconsistent with the NRT equation for dpa cross section that is well notable for the recoil energies just above the lattice threshold (it was firstly pointed out by P. Griffin, for illustration see*:* *https://www-nds.iaea.org/CRPdpa/NJOY-dpa_vs_ASTM693.pdf*);
- a distinction needs to be made in the treatment of the displacement threshold energy when one computes the non-ionizing kerma and the dpa.

To remove bugs and avoid incorrect use of NJOY, the sample inputs decks for the evaluated nuclear data processing have to be collected and made available to community inspection on the CRP web-page https://www-nds.iaea.org/CRPdpa/. Several sample input files are already there and participants are invited to use them, propose corrections or new input decks when necessary.

It is necessary to note that several participants of CRP have developed their own codes:

- DART - to calculate PKA spectra using ENDF/B-VI or -VII and to simulate dpa cross sections in pure and compound materials (L. Luneville et al. [17], also in Section IV);
- SPECTRA-PKA - to take group-wise recoil matrices generated directly from NJOY (M.R. Gilbert et al. [18], Section IV);
- RASG - to generate PKA spectra from evaluated cross sections file in ENDF/B-6 format (J. Kwon et al., Section IV).

These codes also collapse the PKA spectra with user defined neutron-irradiation spectra.

Materials simulation data, Damage databases and Applications

The Primary radiation damage group of the OECD Nuclear Energy Agency has finalized and published its report [19]. It reviewed the current understanding of primary radiation damage from neutrons, ions and electrons with emphasis on the range of validity and shortcomings of the *dpa* concept in all main classes of materials (except organic ones). **The report introduced the "athermal recombination-corrected dpa" (*arc-dpa*) as well as a "replacements-per-atom" (*rpa*) equations** that account in a relatively simple functional form well-known issue that the *NRT*-dpa overestimates primary damage production and the actual atom relocations (ion beam mixing) in metals under energetic displacement cascade conditions.

The OECD report has delivered the recommended defect **surviving function parameters for *arc-* and *rpa-* equations** for Fe, Nd, Pd and Pt, which were fitted to the selected MD simulation results with feasible interatomic potentials.

The CRP participants have performed and continue the MD and BCA calculations of the in-cascade primary defects for Fe (M. Caturla et al., C. Ortiz et al.), W and Au (K. Nordlund), SiO_2 and Al_2O_3 (F. Mota, C.J. Ortiz, R. Vila), Ni_3Al and UO_2 (L. Luneville, J.P. Crocombette, D. Simeone) - see their Summaries in Section IV.

However for several crystalline materials (mono and especially multi-elemental: Cu, Zr, Ni, Al, Si, …) the available MD and BCA simulation results for the number of surviving defects are not sufficient (the overview of relevant published data are collected in this *summary* which helps to judge about the actual status).

To cover the typical **PKA energy range in the nuclear facilities** of interest the MD data are needed, e.g. in the case of Fe: up to **0.7 MeV (Fission Reactors), 1.0 MeV (Fusion), 3.8 MeV (IFMIF), 140 MeV (Spallation).** Just extrapolation of efficiency minimum value 0.2-0.3 to the higher energies could be wrong since the investigation at highest PKA energies has shown that damage production efficiency again increases for some interatomic potentials [20].

To simulate collision cascades generated by high-energy PKAs, C.J. Ortiz and P.G. Müller have developed a combined BCA-MD approach. In this model, the first stages of cascades are simulated using the BCA, which is more efficient than MD. When the energy of displaced SIAs drops below a certain threshold (e.g., 0.25 keV for Fe), the information from BCA is passed to MD, which simulates the last stages of cascade (see Section IV).

The results of the MD and BCA simulations for survived primary defects (total and cluster distributions) are expected from materials experts of this CRP. The fitted damage production efficiency as a function of PKA energy will then be included in the nuclear cross section data.

Quite recently the defect surviving functions were evaluated for **austenitic SS-316 and ferritic-martensitic Eurofer steels** (A. Konobeev, U. Fischer et al. [21, 22]) and were included in the DXS database.

The *arc-dpa* cross sections for the **ionic ceramic breeder materials Li_2O, for Li_2TiO_3 and Li_4SiO_4** with different ^{6}Li enrichments and at several ambient temperatures were calculated by D. Leichtle, who made these data available in the tabular form for CRP: https://www-nds.iaea.org/CRPdpa/Li_ceramics/ (see there additionally the short description and references).

On other hand the *arc-dpa* concept does not work for all crystalline or ordered materials. L. Luneville, J.P. Crocombette and D. Simeone have shown that this formula appears cannot be expected to work in concentrated ordered alloys such as Ni_3Al and UO_2 (in Section IV).

Damage accumulation depends on the radiation rate and accumulated fluence which results in the additional annealing of primary defects due to the spatial and temporal overlapping of the multiple cascades. In frame of this CRP this effect is studied by R.E. Stoller, K. Nordlund, C. Woo and others (see Section IV and [19]).

Being neglected in the *NRT* displacement model, it would be interesting to express the high-fluence effect numerically and use it as a supplementary parameter to the *arc*-dpa cross sections for specification of radiation conditions.

The **atom replacements in collision cascade** is another physical quantity describing the primary state of damage and accounts for the radiation-induced atom mixing [19]. The corresponding number of **replacements-per-atom (*rpa*)** is calculable by MD or BCA models and it is also experimentally measurable through the ion beam mixing at cryogenic temperatures. The *rpa*-correction factors for NRT model have been already evaluated for Ni, Pd and Pt and will be expanded for other materials (K. Nordlund et al., Section IV).

The **clustering of defects remained after cascade cooling can significantly change the character of radiation damage accumulation**, e.g. swelling. While the total amount of surviving Frenkel pairs are found to be similar in *fcc, bcc* and *hcp* metals, the size distributions of clusters essentially depend on the lattice type as it was shown for *hcp-bcc* phase in Zr at 1100 K (N. Lazarev et al., see [23] and Section IV).

The **database on primary damage effects** was extended **for metal alloys Fe-Cu, Fe-Ni, Fe-Mn and Fe-Cu-Ni-Mn**, which are relevant to the Reactor Pressure Vessels (PRV) steels (see D. Terentyev in Section IV). Particular focus was given to the impact of Mn, Ni and Cu solutes in the Fe matrix. The analysis of the results has shown that the addition of solutes in all explored configurations did not result in any significant change of the number of surviving defects over the whole range of the studied PKA energy as compared to pure Fe. On other hand, the fraction of clusterized vacancies and SIAs statistically increases in the matrix containing the dislocation loops of solutes.

The completion of a database on primary damage states in crystalline mono- and multi-elemental materials relevant for application in fusion and fission is expected. The damage has to be characterized by the total number of surviving Frenkel pairs and the size and density distribution of the defect clusters.

The demonstration of performance of primary damage as a scaling factor will be done by calculations of arc-, rpa-dpa, defect clustering, total fluence or accumulation rate in the nuclear facilities where

the microstructural material changes (stress yield, swelling, ...) were measured and shown to be a function of NRT dpa (see, e.g. L.R. Greenwood, Section IV).

Most of such neutron spectra were already collected and sent to the CRP participants for exercises.

The energy distributions of primary knock-on-atoms for many elements were calculated under DEMO first wall conditions using the FISPACT-II code and TENDL-20014 library. The data in graphical and tabular forms are presented in the CCFE Report available on-line [24].

The **SRIM code** [25] was considered so far as **a standard tool for the assessment of numbers of atoms displaced by protons and ions.** Its particularities and recipes for practical usage were summarised elsewhere [19,26]. Based on this, B. Marcinkevicius and S. Simakov (see Section IV) compared proton induced NRT displacement cross sections derived from SRIM with the same quantity from DXS. An agreement for proton energies between 1 and 10 MeV was observed. However SRIM overestimates the DXS by 30% at lower energies and increasingly underestimates the DXS above 15 MeV, where SRIM ignores the contribution of non-elastic reactions.

The usage of the SRIM code for calculation of defect production efficiencies by ions in metals was recently demonstrated by A. Konobeev *https://www-nds.iaea.org/CRPdpa/SRIM_MD.pdf* .

III. Recommendations of RCM-2 (List of Actions)

After discussions, the participants of RCM-2 came up with following recommendations for implementation during next period until RCM-3:

1. Include in the neutron data the different damage functions (primary defects surviving, atoms replacing functions etc.). The *arc*-dpa, as was already shown, may just be a factor of 3 or so lower than *NRT*-dpa. Check whether they may be used for data correlations in a similar fashion as the *NRT*-dpa (but be careful what we say in Introduction about their use in applications as a potential scaling parameter).

   It is of primary importance to include *arc*-dpa and *RPA* in the neutron data for Fe, W and other elements for which there are experimental data on radiation induced changes in materials.

2. Compare the results for different neutron spectra at various nuclear facilities collected within the framework of this CRP.

   For this collection, include numerical data for selected neutron spectra and spectral averages quantities. We need data for swelling or other properties in various irradiation facilities to compare versus *dpa* and other functions. If no data exits, we can compare ratios of damage rates.

   Include material testing and power reactors HFIR, FFTF, BOR-60, LWR 1/4T, BR-2, fusion ITER, IFMIF, and spallation (ESS, SNS, SINQ) as well as 1 MeV protons and 5 MeV Fe ion irradiations.

   Include material compounds such as SiC, UO_2, Li_2O, Fe-0.10Cr, Al_2O_3, and SiO_2. Generate the PKA spectra and calculate damage functions using different codes and approaches (NJOY, DART …).

3. Recommendations for displacement thresholds for materials including those in the Standard Practice for Neutron Radiation Damage Simulation by Charged-Particle Irradiation (ASTM 521) [27].

4. Collect *ab-initio* MD simulation data and relevant experimental data for validation.

3. Need to include experimental total and differential nuclear cross sections for gas production. List of data needed should include (also for the separated isotopes): Fe, Cr, Ni, W, Pb, C, Y, O, U (main structural or fuel elements), Ca (medical applications). The energy range from thermal (especially for elements/isotopes with positive Q-value for (n,α) reactions, e.g. Ni, Pb, Ca) up to several GeV.

   Make a request for new experimental data and specify the deficiencies in the main evaluated libraries (All, S. Simakov and A. Konobeyev).

4. We need to improve the accuracy and consistency of PKA spectra, including recoils from the neutron absorption reactions. Differences are seen currently between different evaluations. We need to try to establish the most reliable data, and this would be recommended by CRP, and provide a quantitative uncertainty estimate.

   Uncertainties are needed for the PKA spectra, KERMA, gas production and damage energy. PKA spectra are derived from all nuclear reactions, so their uncertainties are affected by the accuracy of the neutron cross section total and spectral data. Methods for their estimation should be established. The IAEA NDS should organize a meeting to address these issues.

5. We endorse the CIELO project working on H, O-16, Fe-56, U-235, U-238 and Pu-239 cross sections We encourage the expanding of the CIELO scope to include secondary reaction products and to include other key elements and isotopes such as Fe, Ni, Cr, W, etc., in the future.

6. Prepare input files for NJOY to derive KERMA, PKA, and gas production that will work with all nuclear data libraries. Put them on the *CRP web-site* so that they can be reviewed and improved as needed. The list of elements should include: Fe, Ni, Cr, Mn, Zr, Si, C, O, Al, U, W, Cu, Y, Pb, Ag, Pd, and Pt. The NJOY input files need to work for ENDF/B-VII.1, JEFF-3.2, JENDL-4.0,

FENDL-3 and TENDL-2014 libraries. These issues should be addressed at the Consultant's Meeting on processing codes organized by NDS in October 2015.

7. Direct measurements of resistivity for Al or W are planned at proton energies of 150 MeV in Japan. The improved estimates of the resistivity change for Frenkel pairs are needed to derive surviving primary defect.

References to Sections I-III

1. D.H. Abriola and R.A. Forrest (Eds.), Report of the IAEA Nuclear Data Section to the International Nuclear Data Committee for the period January 2010–December 2011, Report INDC(NDS)-0619, IAEA, April 2012
2. R.E. Stoller, K. Nordlund and S.P. Simakov, Summary Report of the Technical Meeting "Primary Radiation Damage: from nuclear reaction to point defects", Report INDC(NDS)-624, IAEA, Nov 2012
3. R.E. Stoller, L.R. Greenwood, S.P. Simakov, Summary Report of the First Research Coordination Meeting on Primary Radiation Damage Cross Sections, INDC(NDS)-0648, IAEA, Dec 2013
4. M.B. Chadwick et al., Nuclear Data for Science and Technology: Cross Sections, Covariances, Fission Product Yields and Decay Data, Nuclear Data Sheets, 112 (2011) 2887-2996
5. K. Shibata, O. Iwamoto, T. Nakagawa et al., JENDL-4.0: A New Library for Nuclear Science and Engineering, J. Nucl. Sci. Technol. 48 (2011) 1
6. JEFF-3.2 evaluated data library, http://www.oecd-nea.org/dbforms/data/eva/evatapes/jeff_32/
7. TENDL-2014: TALYS-based evaluated nuclear data library, http://www.talys.eu/home/
8. Y. Iwamoto et al., Measurement of the displacement cross-section of copper irradiated with 125 MeV protons at 12 K, J. Nucl. Mater. 296 (2015) 369
9. DXS: neutron and proton displacement and gas production cross sections database, available on line: https://www-nds.iaea.org/public/download-endf/DXS/
10. A.Yu. Konobeyev, U. Fischer, Complete gas production data library for nuclides from Mg to Bi at neutron incident energies up to 200 MeV, KIT Scientific Working Paper 36, Sep 2015
11. A.Yu. Konobeyev, U. Fischer, Reference data for evaluation of gas production cross-sections in proton induced reactions at intermediate energies, KIT Scientific Report KIT-SR 7660, 2014, available on-line: www.ksp.**kit**.edu/download/1000038463
12. S. Akça, A.Yu. Konobeyev and U. Fischer, Evaluated gas production cross-section data for natural titanium irradiated with protons at energies up to 3 GeV, Kerntechnik 79 (2014) 464
13. A.Yu. Konobeyev, U. Fischer, Further improvement of (n,p) and (n,α) reaction cross-sections calculated using the TALYS code, KIT Scientific Working Paper 35, 2015
14. A. Koning and D. Rochman, Modern Nuclear Data Evaluation with the TALYS Code System, Nuclear Data Sheets 113 (2012) 2841
15. P. Helgesson, H. Sjöstrand, A. Koning, D. Rochman, E. Alhassan, S. Pomp, Incorporating experimental information in the TMC methodology using file weights, Nuclear Data Sheets 123(2015)214
16. A.C. Kahler, Editor, The NJOY Nuclear Data Processing System, Version 2012, Report LA-UR-12-27079 , see at http://t2.lanl.gov/nis/codes/NJOY12/index.html
17. L. Luneville, D. Simeone, C. Jouanne, Calculation of radiation damage induced by neutrons in compound materials, Journal of Nuclear Materials 353 (2006) 89
18. M.R. Gilbert, J. Marian, J.-Ch. Sublet, Energy spectra of primary knock-on atoms under neutron irradiation, Journal of Nuclear Materials 467 (2015) 121
19. K. Nordlund, A.E. Sand, F. Granberg, S.J. Zinkle, R.E. Stoller, R.S. Averback, T. Suzudo, L. Malerba, F. Banhart, W.J. Weber, F. Willaime, S.L. Dudarev and D. Simeone, Primary Radiation Damage in Materials, Review of Current Understanding and Proposed New Standard Displacement Damage Model to Incorporate in Cascade Defect Production Efficiency and

Mixing Effects, Nuclear Science NEA/NSC/DOC(2015)9,
available on-line: https://www.oecd-nea.org/science/docs/2015/nsc-doc2015-9.pdf
20. X. Yi, A.E. Sand, D.R. Mason, M.A. Kirk, S.G. Roberts, K. Nordlund, and S.L. Dudarev, Direct observation of size scaling and elastic interaction between nano-scale defects in collision cascades, EPL 110, 36001 (2015), http://www.acclab.helsinki.fi/~knordlun/pub/Yi15preprint.pdf
21. A.Yu. Konobeyev, U. Fischer, Evaluation of atomic displacement and gas production cross-section for ^{9}Be irradiated with neutrons at energies up to 200 MeV, KIT Scientific Working Paper 37, Sep 2015
22. A.Yu. Konobeyev, U. Fischer, P.E. Pereslavtsev, Evaluation of advanced displacement cross-sections for the major EUROFER constituents based on an atomistic modelling approach, Kerntechnik 80(2015)1
23. N.P. Lazarev, A.S. Bakai, Atomistic simulation of primary damages in Fe, Ni and Zr, J. of Supercritical Fluids 82 (2013) 22
24. M.R. Gilbert, J.-C. Sublet, R.A. Forrest, PKA distributions of the elements simulated using TENDL-2014; FW Nuclear Fission plants, CCFE-R(15)26-supplement, Dec 2015; available on-line: http://www.ccfe.ac.uk/assets/documents/easy/CCFE-R(15)26_supplement.pdf
25. J.F. Ziegler, M.D. Ziegler and J.P. Biersak, "SRIM – The stopping and range of ions in matter", Nucl. Instr. Meth. B 268 (2010) 1818; code available from http://www.srim.org/
26. R. Stoller, M.B. Toloczko, G. Was, A. Certain, S. Dwaraknath and F. Garner, "On the use of SRIM for computing radiation damage exposure", Nucl. Instr. and Meth. in Phys. Research B, vol. 310, pp. 75 - 80, 2013
27. ASTM E521 "Standard Practice for Neutron Radiation Damage Simulation by Charged-Particle Irradiation", available on ASTM website www.astm.org

IV. Individual Summaries of the CRP participants

This section summarises the progress reached by the CRP Participants in the period from the RCM-1 and their further research plans.

Summary for Second Meeting of IAEA Coordinated Research Project on Primary Radiation Damage Cross Sections,

R.E. Stoller

Oak Ridge National Laboratory
Oak Ridge, TN, USA

Two presentations were made in this second meeting of the IAEA Coordinated Research Project (CRP) on Primary Radiation Damage Cross Sections. The first was intended to address the primary objective of the CRP, which is the assessment and development of possible new measures of radiation damage production and radiation damage correlation parameters. This presentation described some of the author's relevant research. In addition, because the author was chairing the meeting, he made a second presentation to address some of the controversial discussion which occurred during the meeting and to initiate the discussion on specific recommendations for the future work scope of the CRP. Information from both presentations is summarized below.

Research and Recommendations:

The two most common parameters used to characterize the cumulative exposure of a material to irradiation are the particle fluence and absorbed dose. The *particle fluence*, in units of $(\text{area})^{-2}$, depends only on the characteristics of irradiation source and can be determined at a point or averaged over a surface or volume. The *absorbed dose***,** in units of energy, depends on a variety of variables, including: particle fluence, particle type, particle energy spectrum, and the specific material being exposed. Thus, absorbed dose includes much more information about the irradiation environment, and it is material dependent. Both particle fluence and absorbed dose are used as independent variables to account for radiation exposure in experiments and for reactor components. They may also be used as a *damage correlation parameter* in attempts to correlate data from different irradiation environments. In this case, the particle fluence is of limited usefulness unless the particles are the same in each irradiation environment, e.g. the difference between neutron fluence and ion fluence prevents comparison on this basis. Absorbed dose (energy) is an exposure parameter that is better suited to comparing such different environments.

The primary damage formation mechanism in structural materials arises from what is called an atomic displacement cascade which involves many collisions among the atoms of a material following the introduction of an energetic particle, which could be a neutron, a charged particle, or even a high-energy photon. The cascade leads to the production of many stable vacancy and interstitial-type defects. The secondary displacement model of Norgett, Robinson, and Torrens (NRT) has been a de facto standard in the nuclear materials research community since its introduction in 1975 [1]. The primary physical parameter in the NRT model is the so-called *damage energy*, which is the energy dissipated in these collisions among the atoms. The damage energy is an absorbed dose, by the NRT model also provides a method of estimating of the number of atomic displacements per atom (dpa) generated by the damage energy.

The NRT displacements was not envisioned to be the actual number of vacancies and interstitials formed; but the model provided a simple scaling relationship that could be used in other computational models. Modern molecular dynamics (MD) simulations and cryogenic irradiation experiments have shown that the NRT model was well within an order of magnitude of the actual value. Such work indicates that the number of stable vacancies and interstitials formed in irradiated materials is about 20 to 40% of the NRT value [2].

Recently, efforts have been made to find an alternative to the NRT dpa that more accurately accounts for primary damage production and possibly improved damage correlation [3]. The work in Ref. [3] discusses two such parameters: the arc-dpa, which is intended to correct for the difference between MD simulations and the NRT dpa, and the number of replacements per atom (rpa) that accounts for the number of atoms which exchange positions during a displacement cascade. The arc-dpa was derived in a manner similar to previous work that led to spectrum-averaged displacement cross sections were based on the author's MD simulations.

A summary of the MD results are shown in Fig. 1a, spectrum-averaged values for a number of irradiation facilities are shown in Fig. 1b [2,4,5]. From the relative insensitivity to neutron energy spectrum shown in Fig. 1b, it appears that arc-dpa will not provide significantly different damage correlation properties than does the NRT dpa. More dependence on neutron energy spectrum is observed if a parameter such as the fraction of interstitials produced in large clusters is assessed as shown in Fig. 1c. For some measures of damage accumulation which may be more sensitive to the evolution of these clusters, a damage parameter that accounts for their formation may provide improved damage correlation [6]. Similarly, the rpa parameter may be useful for correlating damage mechanisms sensitive to atomic mixing rather than to vacancy and interstitial production.

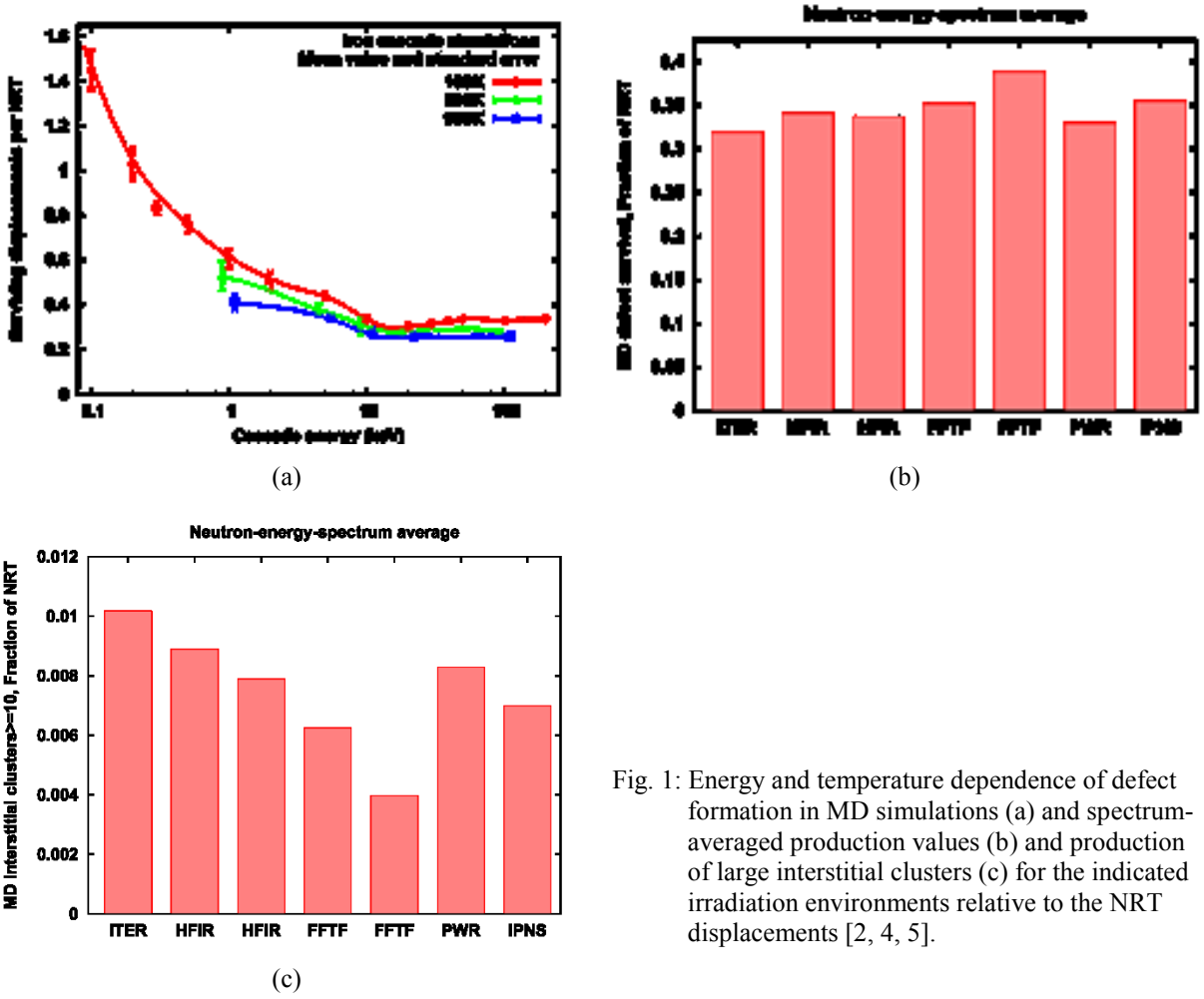

(a) (b)

(c)

Fig. 1: Energy and temperature dependence of defect formation in MD simulations (a) and spectrum-averaged production values (b) and production of large interstitial clusters (c) for the indicated irradiation environments relative to the NRT displacements [2, 4, 5].

However, additional factors must be kept in mind. First, MD simulations are effectively carried out using computationally pure metals which do not exist in nature. Results have been published that illustrated how the presence of defects, grain boundaries, and free surfaces can influence defect formation in displacement cascades [2]. In addition, the measurements of radiation-induced property changes such as swelling, irradiation creep or embrittlement typically irradiation experiments typically are obtained after irradiation which lasted from days to years, while a displacement cascade lasts about 10^{-11} sec. In this case, it is damage accumulation that is being measured and this can be far removed

from damage formation mechanisms. A broad range of phenomena such as long-range defect diffusion and defect aggregation, as well as transmutation production, occur after the cascade and ultimately determine the damage accumulation. As a result, it is unlikely that a single, simple radiation exposure parameter can function as a damage correlation parameter for the many radiation-induced phenomena of interest. Moreover, there a range of materials and material properties for which atomic displacements are not the primary source of damage, notably the physical properties of covalent and ionic materials for which the ionizing dose is more important than the displacement dose. Nuclear transmutation products, both gases and solids, are also critical in some cases.

ORNL Contribution to the CRP

One recent example from ORNL on the differences between damage formation and damage accumulation is shown in Fig. 2. In this work a sequence of MD simulations have been carried out in both pure Ni and a Ni-50%Fe binary alloy. This involved multiple cascades that were separated by a short period (1.4 ns) of inter-cascade annealing using a kinetic Monte Carlo approach. This annealing led to some additional point defect recombination and defect aggregation. The lines marked "Linear accumulation" indicate the number of Frenkel pair that would be expected if damage production from each succeeding cascade was the same as the first one. The lines marked with the annealing time show the actual damage accumulation which is significantly lower than the projected linear accumulation.

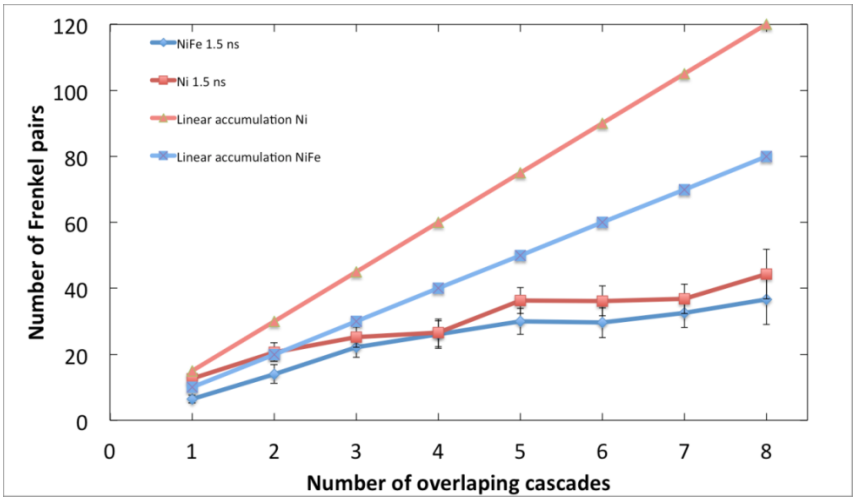

Fig. 2: Comparison of actual and projected linear production of defects from 10 keV cascades in Ni and Ni-50%Fe binary alloy.

References

1. M.J. Norgett, M.T. Robinson, and I.M. Torrens, Nucl. Engr. and Des. 33 (1975) 50-54.
2. R.E. Stoller, "Primary Radiation Damage Formation," in Comprehensive Nuclear Materials, R.J.M. Konings, T.R. Allen, R.E. Stoller, and S. Yamanaka, Editors, Elsevier Ltd., Amsterdam, 2012, pp. 293-332.
3. "Primary Radiation Damage in Materials", K. Nordlund, A.E. Sand, F. Granberg, S.J. Zinkle, R.E. Stoller, R.S. Averback, T. Suzudo, L. Malerba, F. Banhart, W.J. Weber, F. Willaime, S. Dudarev, D. Simeone, NEA/NSC/DOC(2015)-9, OECD Nuclear Energy Agency, Paris, pp. 1-86, 2015.
4. R.E. Stoller and L.R. Greenwood, J. Nucl. Mater.271 & 272 (1999) 57-62.
5. R.E. Stoller and L.R. Greenwood, "From Molecular Dynamics to Kinetic Rate Theory: A Simple Example of Multiscale Modeling", Multiscale Modeling of Materials, Vol. 538, V.V. Butalov, T. Diaz de la Rubia, P. Phillips, E. Kaxiras, and N. Ghoniem, Editors, Materials Research Society, Pittsburgh, PA, 1999, pp. 203-209.
6. R.E. Stoller and L.R. Greenwood, "An Evaluation of Through-Thickness Changes in Primary Damage Production in Commercial Reactor Pressure Vessels," *Effects of Radiation on Materials: 20th Intern. Symp.*, ASTM STP 1405, S.T. Rosinski, M.L. Grossbeck, T.R. Allen, and A.S. Kumar, Eds., American Society for Testing and Materials, West Conshohocken, PA, 2001, pp. 204-217.

Summary of the 2nd RCM of CRP on Primary Radiation Damage Cross-Section, K. Nordlund

University of Helsinki
Helsinki, Finland

1. Overview of work during 2013 - 2015

We have finalized the OECD Nuclear Energy Agency Primary radiation damage group report [1]. This report reviewed the current understanding of primary radiation damage from neutrons, ions and electrons (excluding photons, atom clusters, and more exotic particles), with emphasis on the range of validity of the dpa concept in all main classes of materials (except organic ones), and in particular discussed known shortcomings. The report introduced the "athermal recombination-corrected dpa" (arc-dpa) equation that accounts in a relatively simple functional form the well known issue that the dpa overestimates damage production in metals under energetic displacement cascade conditions, as well as a "replacements-per-atom" (rpa) equation that accounts in a relatively simple functional for the well known issue that the dpa severely underestimates the actual atom relocations (ion beam mixing) in metals.

The modified forms are:

$$N_d(E) = \begin{bmatrix} 0 & \text{when} & E < E_d \\ 1 & \text{when} & E_d < E < 2E_d/0.8 \\ \dfrac{0.8E}{2E_d}\xi(E) & \text{when} & 2E_d/0.8 < E < \infty \end{bmatrix}$$

where the efficiency function $\xi(E)$ is for the arc-dpa:

$$\xi_{arcdpa}(E) = \frac{1-c_{arcdpa}}{(2E_d/0.8)^{b_{arcdpa}}} E^{b_{arcdpa}} + c_{arcdpa}$$

and for the rpa:

$$\xi_{\mathrm{rpa}}(E) = \left(\frac{{b_{rpa}}^{c_{rpa}}}{(2E_d/0.8)^{c_{rpa}}} + 1 \right) \frac{E^{c_{rpa}}}{{b_{rpa}}^{c_{rpa}} + E^{c_{rpa}}}$$

The original NRT-dpa damage efficiency is obtained with $\xi_{NRT}(E) = 1$.

We emphasize that the arc-dpa and rpa equations are not intended to replace the NRT-dpa, which is still valid as a convenient energy deposition unit and can be used for e.g. comparing different kinds of irradiations. Rather, they are an alternative if one wishes to have a somewhat more accurate estimate of the actual damage production or number of replaced (mixed) atoms.

Within the IAEA CRP we have collected MD data on damage production and mixing for the metals in Fe, Ni, Cu, Ag, Au, Pd, Pt, W. We have fitted the data, including the uncertainty of the data if possible, using a least-squares Levenberg-Marquardt fitting algorithm for both the arc-dpa and rpa equations. The fits provide element-specific fitting parameters b_{arcdpa}, c_{arcdpa}, … including their statistical uncertainties to the data. The fits will be done to composite data for several different interatomic potentials, and as such the uncertainties of the parameters will also include an estimate of the systematic error with respect to the variation of the potentials.

The fits to data on both damage and mixing for Fe are shown in Figure 1, and to W - in Figure 2. The W case is particularly interesting in that a direct comparison on damage cluster sizes with experiments has recently been achieved, showing that some interatomic potentials in W give very good agreement

with experimental cluster sizes [1]. The resulting fitting parameters are given in Table 1 for Fe and W, the metals for which most data is available to date and hence a reliable fit can be provided.

Table 1. Fitting parameters of the *arc*-dpa and *rpa* equations for Fe and W.

Material	E_d	b_{arcdpa}	c_{arcdpa}	$b_{rpa\ [eV]}$	c_{rpa}
Fe	40	-0.568±0.020	0.286±0.005	1020 ± 140	0.950 ± 0.039
W	70	-0.564 ± 0.018	0.119 ± 0.005	12300 ± 1300	0.730 ± 0.010

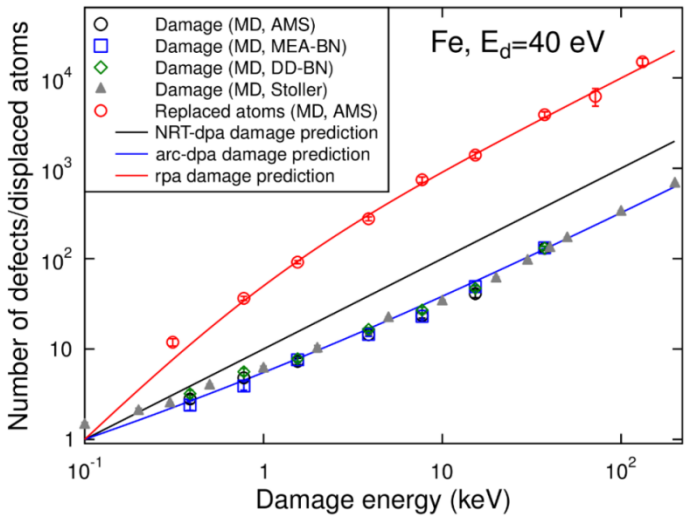

Fig. 1. Summary of fits of the arc-dpa and rpa functions to composite damage production and atom replacement (mixing) data in Fe.

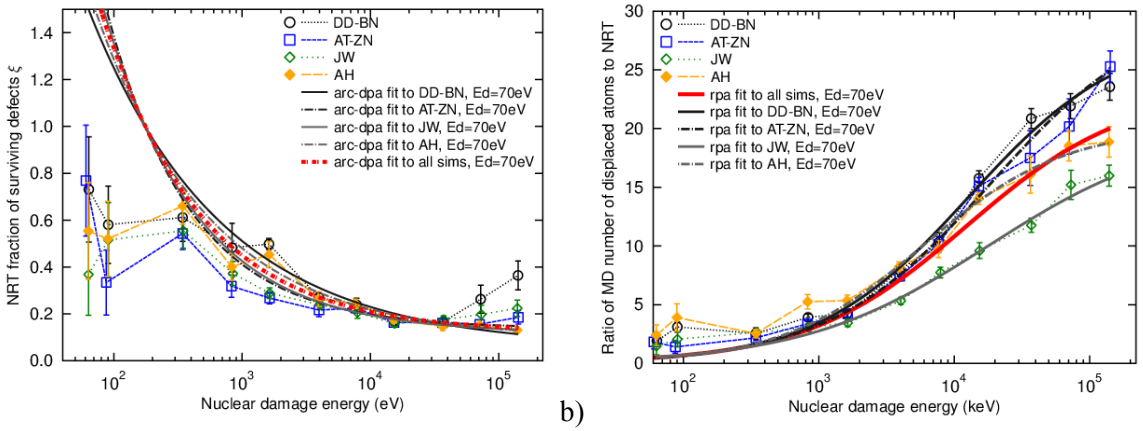

a) b)

Fig. 2. Fits of the a) arc-dpa efficiency function $\xi_{arcdpa}(E)$ and b) rpa efficiency function $\xi_{rpa}(E)$ to composite damage production data in W, as well as separate fits each individual potential data. The fact that the fits vary only slightly, even though the interatomic potentials are quite different in origin, indicates that the arc-dpa and rpa fits are quite reliable.

In figure 2, it seems that at the very highest energies, the damage production efficiency is in some potentials somewhat increasing again. This effect is observed to varying extent for certain potentials in several of the metals studied. It is most pronounced for the Sabochick-Lam potential ("KN modified"), see figure 3. Analysis of the nature of the damage at these energies showed that the reason is that,

within this potential, huge interstitial and vacancy loops are produced in the heat spikes at the highest energies, see figure 4. This effect is not necessarily to be considered a shortcoming of the arc-dpa model. The description of a large dislocation loop in terms of number of vacancies or interstitials is not very meaningful – dislocations are better described with quantities such as the habit plane and Burgers vector.

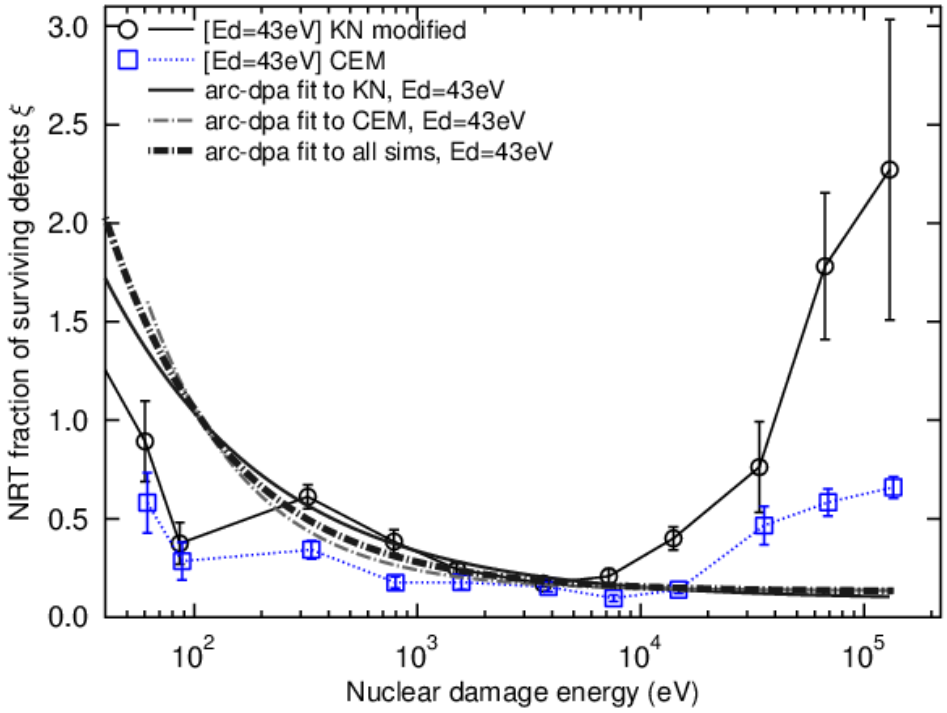

Figure 3. Damage production data and fits of the arc-dpa efficiency in Au.

Figure 4. Damage produced in a 200 keV cascade in Au. Red spheres show the positions of vacancies (empty Wigner-Seitz cells) and blue spheres positions of interstitials (Wigner-Seitz cells with two atoms).

2. IAEA CRP workplan 2015-2016

During the remainder of the IAEA work period, we plan, in collaboration with CRP partners, to:

1. Complete the fits by including literature data for the elements Cu, Ag, Au, Ni, Pd and Pt and publish the obtained fitting parameters for all the elements.

2. Calculate recoil spectra for 1 MeV p, 5 MeV Fe and 20 MeV W irradiation of Fe and W and evaluate the damage production using the NRT-dpa, arc-dpa and rpa models. A similar calculation is to be carried out for a few representative neutron spectra.

The aim is to give an idea whether the arc-dpa damage model gives a significant difference when comparing ion and neutron irradiation calculations. For comparison of neutron spectra with each other, discussions at the 2nd coordination meeting made it clear that, because these are dominated by energies of the order of 10 - 100 keV, the arc-dpa essentially will give a constant factor change c_{arcdpa} (about 0.3 in case of iron, see Table 1) of the damage production compared to the NRT-dpa.

Reference

[1] K. Nordlund, A.E. Sand, F. Granberg, S.J. Zinkle, R.E. Stoller, R.S. Averback, T. Suzudo, L. Malerba, F. Banhart, W. J. Weber, F. Willaime, S.L. Dudarev and D. Simeone, *Primary Radiation Damage in Materials,* OECD-NEA Report NEA/SC/DOC(2015)9

[2] X. Yi, A.E. Sand, D.R. Mason, M.A. Kirk, S.G. Roberts, K. Nordlund, and S.L. Dudarev, *Direct observation of size scaling and elastic interaction between nano-scale defects in collision cascades*, EPL **110**, 36001 (2015), http://www.acclab.helsinki.fi/~knordlun/pub/Yi15preprint.pdf

Calculations of PKA spectra using the PHITS code and measurement of displacement cross section of copper irradiated with 125 MeV protons at cryogenic temperature, Y. Iwamoto

Japan Atomic Energy Agency
Tokai, Ibaraki, Japan

Overview of IAEA CRP work 2013-2015

Based on the 1st CRP meeting recommendations, we calculated PKA spectra, kerma factors and gas productions for structural materials using the PHITS code and compared with other results. We also measured displacement cross section of copper irradiated with 125 MeV protons at cryogenic temperature.

1. Calculations of PKA energy spectra using PHITS code

To investigate discrepancy between different process steps and libraries for PKA calculations, we calculated PKA spectra for 5 and 14.5 MeV neutrons into ^{28}Si, ^{56}Fe, ^{90}Zr and ^{184}W using the combination of processing steps and ACE libraries indicated in Table 1.

Table 1. Processing steps and ACE libraries.

Processing step	ACE Library
PHITS-EG	JENDL4
PHITS-EG	ENDF/B-VII.1
SPKA	JENDL4
SPKA	ENDF/B-VII.1

PHITS event generator (EG) mode using reaction channel cross sections in JENDL4 and ENDF/B-VII.1 can determine all ejectiles with keeping energy and momentum conservation by Monte Carlo

method [1, 2]. On the other hand the PKA energy spectra or other relevant information are available in the evaluated cross section files and could be derived or calculated by the NJOY code. The SPKA code [3] was used to read the NJOY output files for the further processing of PKA data. Figures 1 and 2 show total recoil spectra for interactions of neutrons with ^{56}Fe and ^{90}Zr at the incident neutron energies of 5 and 14.5 MeV calculated using different data processing and libraries.

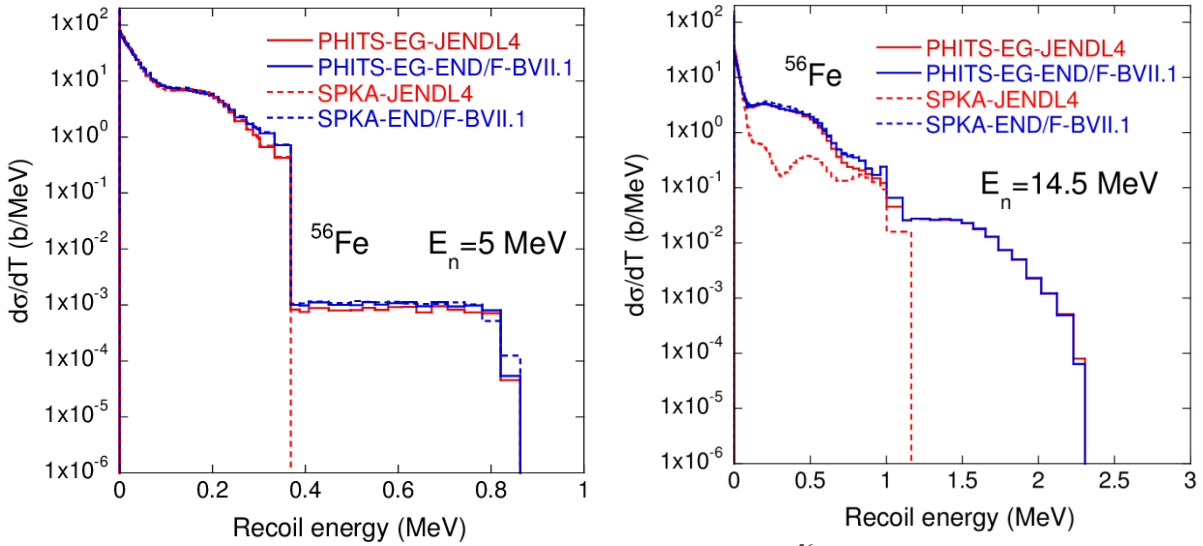

Fig. 1. Total recoil energy distributions for interactions of neutrons with ^{56}Fe at the incident neutron energies of 5 and 14.5 MeV calculated using different data processing and libraries.

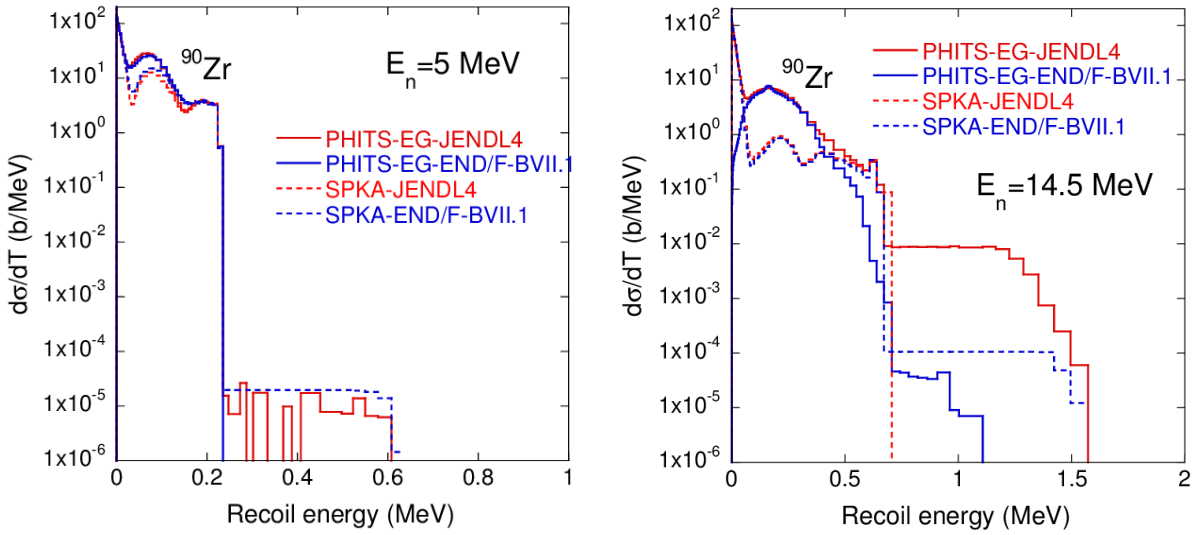

Fig. 2. Total recoil energy distributions for interactions of neutrons with ^{90}Zr at the incident neutron energies of 5 and 14.5 MeV calculated using different data processing and libraries.

For ^{56}Fe and ^{28}Si, there are good agreements except for SPKA-JENDL4 due to lack of PKA matrixes in JENDL4. For ^{90}Zr, there are discrepancies among PHITS-EG-JENDL4, PHITS-EG-END/F-BVII.1 and SPKA-END/F-BVII.1. This discrepancy results from the treatment of the reaction channel cross sections in JENDL4 and END/F-BVII.1. For example, END/F-BVII.1 includes cross sections of each excited state of (n,α) channels, however, JENDL4 has the inclusive (n,α) cross section only. As PHITS cannot read the cross sections of excited state ^{90}Zr correctly, calculated results using END/F-BVII.1 are not correct in Fig. 2. Therefore, it is necessary for PHITS to fix the problem of reading cross sections of excited state atoms in END/F-BVII.1. The same situation was observed in ^{184}W.

2. Calculations of kerma factors using PHITS code

The left graph and the right graph in Fig. 3 show the heating number related with the kerma factor of ^{208}Pb and the (n,α) cross section in JENDL4 and END/F-BVII.1, respectively. There are large differences in heating number of ACE libraries between JENDL4 and END/F-BVII.1 in the neutron energy region below 10^{-5} MeV. The difference mainly comes from the difference of (n,α) cross section in the both libraries. As the Q-value of (n,α) reaction of ^{208}Pb is 6.19 MeV, the reaction channel is opened in low energy region. The experiment data for the (n,α) reaction of ^{208}Pb is needed for the evaluation of not only kerma factor but also gas production.

3. Calculations of proton- and ^{4}He- production cross-section for iron at energies up to several GeV using nuclear models in PHITS

We calculated proton- and ^{4}He- production cross-section for iron at proton energies from 10 MeV to 3 GeV using INCL4/GEM [4,5] and Bertini/GEM models in PHITS for intercomparison and recommendation of gas production cross sections available in nuclear reaction models at higher energies over 100 MeV. Figure 4 shows the comparison among calculated results, experimental data and the evaluated cross section at KIT [6]. Calculated results with INCL4/GEM reproduce the experimental and evaluated data in the energy range between 80 and 500 MeV, while results with Bertini/GEM underestimates the experimental data. Helium is mainly produced by the evaporation process, GEM, in the proton energy region from 100 MeV to 3 GeV.

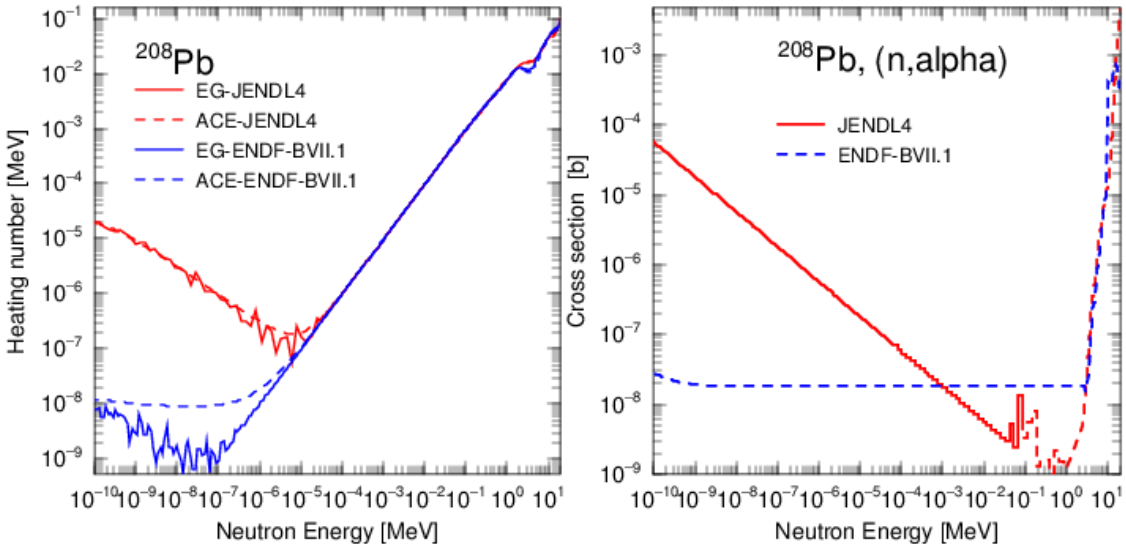

Fig. 3 Heating numbers of ^{208}Pb calculated with PHITS-EG and values in ACE files of evaluated nuclear data libraries (left side). Cross sections of ^{208}Pb (n,α) reaction in JENDL4 and ENDF/B-VII.1 (right side).

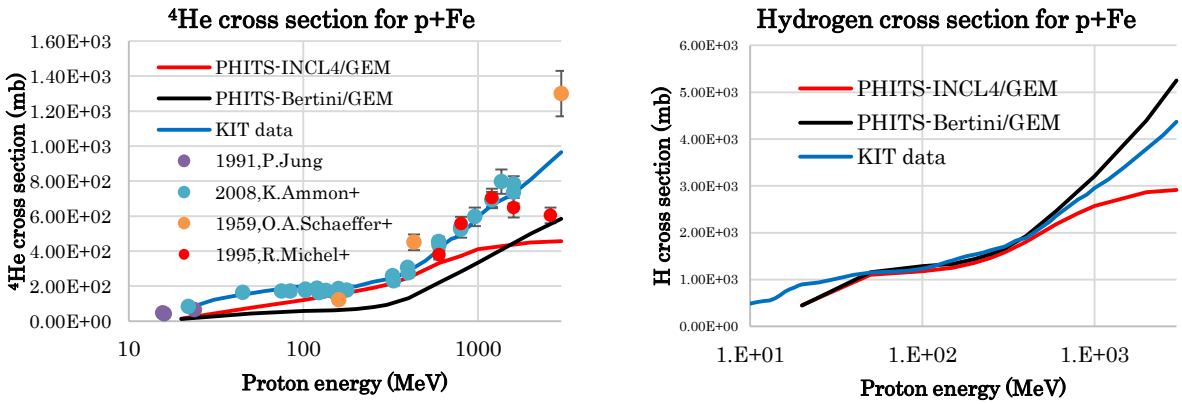

Fig. 4. Comparison among calculated results, experimental data and the KIT evaluated data of proton- and ^{4}He productions for the iron target.

4. Measurement of displacement cross section of copper irradiated with 125 MeV protons at cryogenic temperature

To validate Monte Carlo codes for the prediction of radiation damage in metals irradiated by >100 MeV protons, the defect-induced electrical resistivity changes related to the displacement cross-section of copper were measured with 125 MeV proton irradiation at 12 K in the FFAG accelerator facilities at the Kyoto University Research Reactor Institute (KURRI) [7]. The cryogenic irradiation system was developed with a Gifford–McMahon cryocooler to cool the sample via an oxygen-free high-conductivity copper plate by conduction cooling as shown in the left side of Fig. 5. The sample was a copper wire with a 250-μm diameter and 99.999% purity sandwiched between two aluminium nitride ceramic sheets as shown in the right side of Fig. 5.

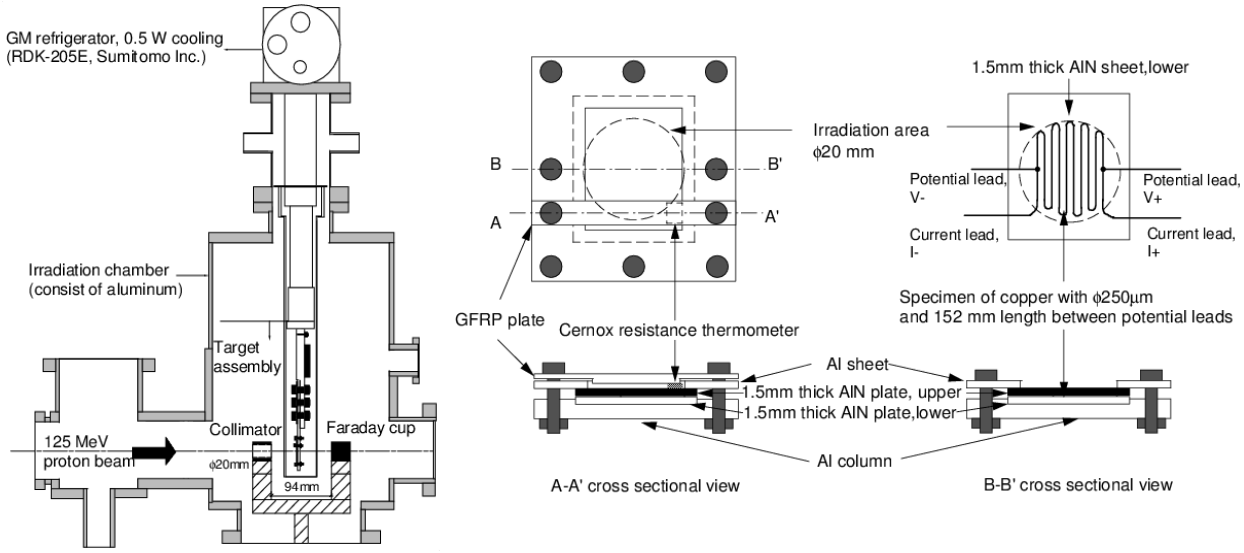

Fig. 5. Schematic of the irradiation chamber (left side) and drawing of the sample and its retention (right side).

The electrical resistivity changes of the copper wire were measured using the four-probe technique. After 125 MeV proton irradiation with 1.45 10^{18} protons/m^2 at 12 K, the total resistivity increase was 4.94 10^{-13} Ω m (resistance increase: 1.53 μΩ), while the resistivity of copper before irradiation was 9.49 10^{-12} Ω m (resistance: 29.41 μΩ). The resistivity increase did not change during annealing after irradiation below 15 K. The displacement cross-section can be easily related to the measured resistivity increase and the calculated damage energy in the metal. The experimental displacement cross-section σ_{exp} $\sigma_{\mathrm{exp}}$is obtained using the measured damage rate, which is the ratio of the resistivity change $\Delta\rho_{Cu}$ to the beam fluence Φ [8]:

$$\sigma_{\mathrm{exp}} = \frac{1}{\rho_{\mathrm{FP}}} \frac{\Delta\rho_{\mathrm{Cu}}}{\Phi} \quad ,$$

where ρ_{FP} is the resistivity change per Frenkel-pair density for a particular metal [9, 10]. In this work, ρ_{FP} was set to 2.0 10^{-6} Ω m, which was obtained by the Huang scattering of X-rays [10]. The same value was used in a previous paper for the measurement of the displacement cross-sections at 1.1 and 1.94 GeV [11].

Figure 6 shows the experimental data of the displacement cross-section for copper in this and previous studies [11]. The experimental displacement cross-section for 125 MeV irradiation shows similar results to the experimental data for 1.1 and 1.94 GeV. Comparison with the calculated results indicated that the defect production efficiency in PHITS gives a good quantitative description of the displacement cross-section in the energy region >100 MeV although the calculated results with the defect production efficiency are smaller than the experimental data.

5. IAEA CRP work plan 2015-2017

During the next two years, we have plans to calculate PKA spectra, gas production cross sections and displacement cross sections for structural materials using PHITS code in collaboration with CRP members. Calculations of PKA spectra will be carried out for a few representative neutron spectra in reactor and accelerator facilities. We will also find the difference of results among methods and point out the problem.

Another activity will be the measurement of displacement cross sections using the electrical resistance measurement method for 150 MeV protons on the Al or W wire targets in the FFAG accelerator facility at KURRI. To measure the displacement cross sections using various proton energies with 100 MeV < E_p < 400 MeV and various proton intensity with 1 nA < I < 100 nA, we will consider to move our device to the RCNP accelerator facility at Osaka university after the experiments at KURRI.

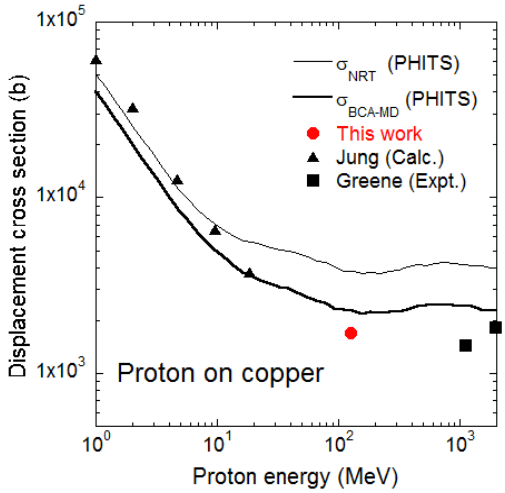

Fig. 6. Displacement cross-sections for proton irradiation of copper: this work (red circle), from the data measured in Ref. [11] (black squares), the cross-section calculated using the NRT model (thick solid line for PHITS), and defect production efficiency by the BCA-MD approach (thin solid line for PHITS).

Acknowledgments

This study was supported by a Japan Grant-in-Aid for Young Scientists (B) (25820450) and ‘‘Clarification of material behaviours in accelerator driven systems by an FFAG accelerator’’ carried out under the Strategic Promotion Program for Basic Nuclear Research of the Ministry of Education, Culture, Sports, Science and Technology of Japan.

References

[1] T. Sato et al., Particle and heavy ion transport code system PHITS, version 2.52, J. Nucl. Sci. Technol. 50 (2013) 913-923.
[2] T. Ogawa et al., Nucl. Instrum. Meth. A 763 (2014) 575-590.
[3] S.P. Simakov, SPKA code, FZK, 2007. Available from https://www-nds.iaea.org/CRPdpa/
[4] A. Boudard, J. Cugnon, J.-C. David, S. Leray and D. Mancusi, New potentialities of the Liege intranuclear cascade model for reactions induced by nucleons and light charged particles, Phys. Rev C 87 (2013) 014606.
[5] S. Furihata, "Statistical analysis of light fragment production from medium energy proton-induced reactions", Nucl. Instrum. Meth. B 171 (2000) 251-258.
[6] A.Yu. Konobeyev, U. Fischer, Advanced Evaluations of Displacement and Gas Production Cross-Sections for Chromium, Iron, and Nickel up to 3 GeV Incident Particle Energy, Int. Meeting on Nuclear Applications of Accelerators (AccApp'11), Knoxville, TN, April 3-7, 2011. Available from https://www-nds.iaea.org/public/download-endf/DXS/ .
[7] Y. Iwamoto et al., Measurement of the displacement cross-section of copper irradiated with 125 MeV protons at 12 K, J. Nucl. Mater. 296 (2015) 369-375.
[8] J.A. Horak, T.H. Blewitt, J. Nucl. Mater. 49 (1973/74) 161-180.
[9] C.H.M. Broeders, A.Yu. Konobeyev, J. Nucl. Mater. 328 (2004) 197-214.
[10] P. Ehrhart and U. Schlagheck, Investigation of Frenkel defects in electron irradiated copper by Huang scattering of x rays. I. Results for single interstitials, J. Phys. F: Metal Phys. 4 (1974) 1575-1588.

[11] G.A. Greene, C.L. Snead, C.C.Jr. Finfrock, A.L. Hanson, M.R. James, W.F. Sommer, E.J. Pitcher, L.S. Waters, Direct measurements of displacement cross sections in copper and tungsten under irradiation by 1.1-GeV and 1.94-GeV protons at 4.7 K. Proceedings of Sixth International Meeting on Nuclear Applications of Accelerator Technology (AccApp'03); 2004; Ja Grange Park, Illinois, USA. p. 881-892.

Assessment of uncertainties of recoil spectra and displacement cross-sections associated with the use of evaluated data files and results of model calculations,

A.Yu. Konobeyev, U. Fischer

Karlsruhe Institute of Technology
Karlsruhe, Germany

Introduction

The goal of the study is the estimation of uncertainty of recoil energy distributions and related damage energy cross-sections concerning the use of evaluated data and nuclear models. The questions to be answered are

- what is the degree of difference between recoil energy distributions obtained using actual versions of nuclear data libraries?
- can the comparative analysis of recoil spectra contribute to the validation of evaluated data?
- what is the possible impact of the difference in recoil spectra on the scatter of related displacement cross-sections?
- what is the likely deviation of recoil spectra from evaluated data files and spectra calculated using nuclear models at nucleon energies above 20 MeV?

Recoil energy distributions were calculated for further analysis using data from actual versions of ENDF/B, JENDL, JEFF, and TENDL libraries. The calculation was performed with NJOY and SPKA [1] codes. No difference was found using the last versions of NJOY-99 [2] and NJOY-2012 [3] codes.

Incident neutron energies below 20 MeV

Iron

The most interesting is the comparison of recoil spectra at the energies with a considerable variation of displacement cross-sections obtained using different evaluated data sets. Fig. 1 shows the ratio of displacement cross-sections σ_d obtained using JENDL-4, JEFF-3.2, and TENDL-2014 to cross-sections calculated applying ENDF/B-VII.1. The data are presented using SAND-II energy groups [4]. On the right, Fig. 1 shows the ratio for neutron energy range contributing more than 80 percent to spectrum- averaged σ_d values for most common applications [5]. The contribution of these energies to σ_d cross-sections calculated using the results of MD modelling [6] is a few percent less.

The following is typical examples of difference of recoil energy distributions from various data sets for energies with the largest scatter of displacement cross-sections (Fig. 1). The next figures show the recoil spectra for neutron incident energy 0.6 MeV (Fig. 2) and 10 MeV (Fig. 3). Fig. 3 also illustrates the contribution of elastic scattering and reactions in total $d\sigma/dT$ and $E_{dam}d\sigma/dT$ values at the example of ENDF/B-VII.1. The elastic scattering contributes about 23 percent and inelastic scattering about 69 percent to displacement cross-section calculated using the NRT model. When using the data from MD simulation [6] the contributions are about 21 and 70 percent, respectively. Examples of spectra multiplied by the damage energy corrected using MD results are given in the presentation [7].

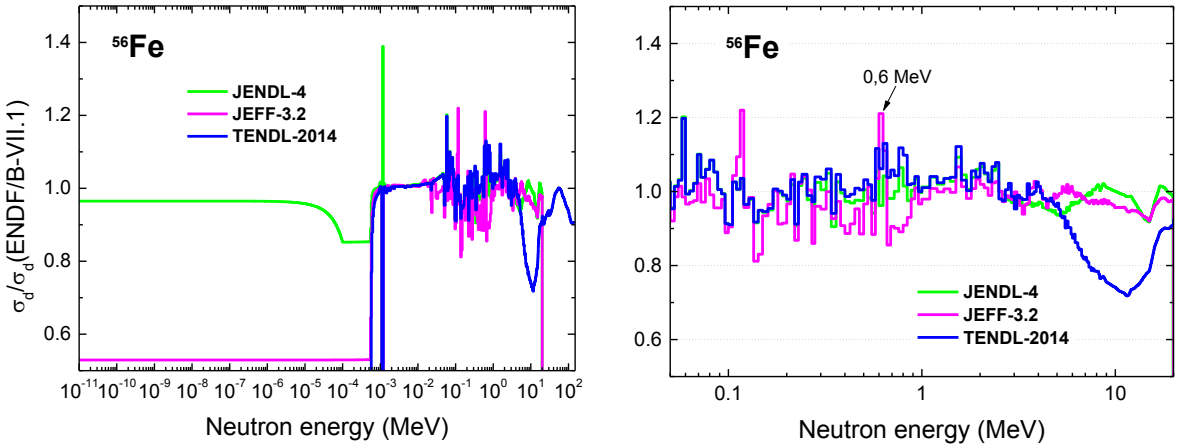

Fig. 1 The ratio of displacement cross-sections for neutron interactions with ^{56}Fe calculated using different data sets to cross-sections obtained using ENDF/B-VII.1. See details in the text.

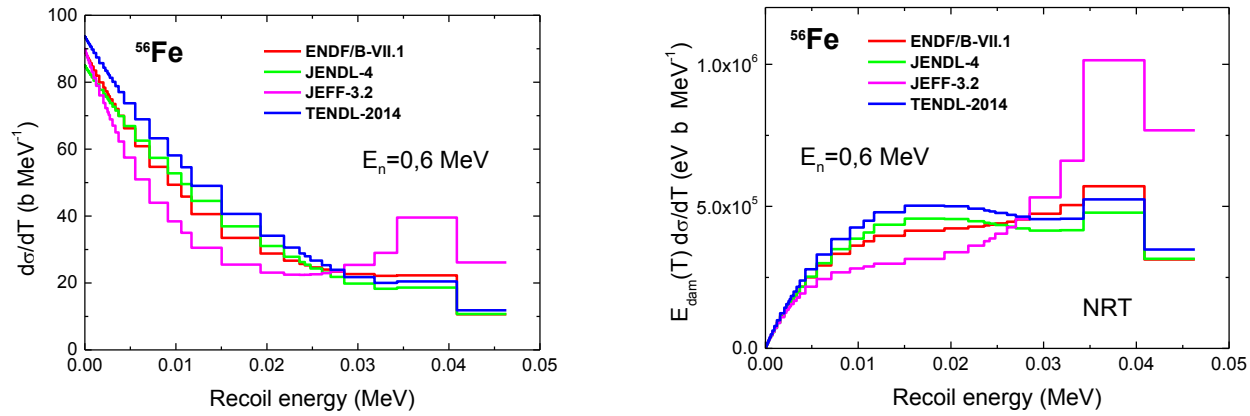

Fig. 2 The recoil energy distribution for ^{56}Fe for neutron incident energy 0.6 MeV (left) and the same multiplied by the damage energy (right).

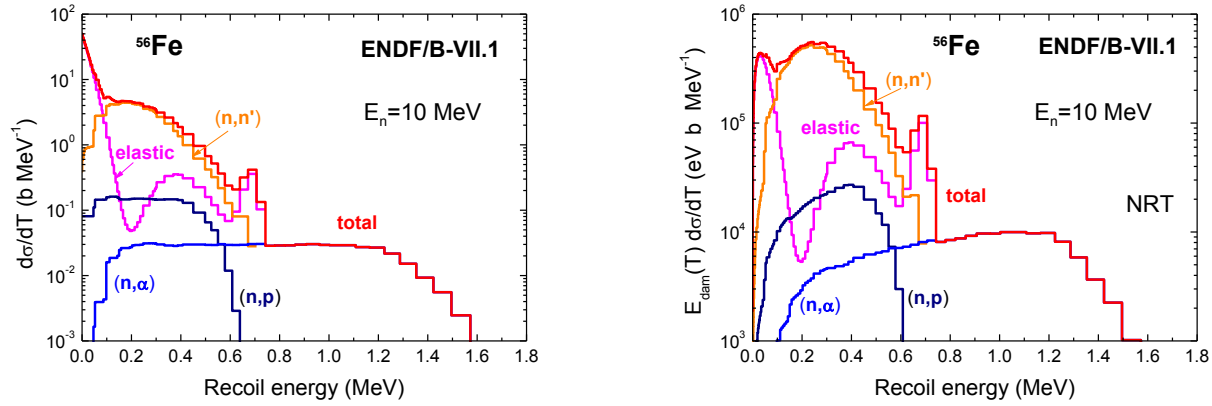

Fig. 3 The contribution of elastic scattering and reactions to the total recoil energy distribution (left) and to that multiplied by the damage energy (right) for ^{56}Fe for neutron incident energy 10 MeV.

Fig.4 shows recoil energy distribution obtained using ENDF/B-VII.1, JEFF-3.2, and TENDL-2014. Fig.5 illustrates the contribution of various energies in the total displacement cross-section and the ratio of dσ/dT values calculated using JEFF-3.2 and TENDL-2014 to values obtained using ENDF/B-

VII.1. The figure shows that the deviations of spectra at recoil energies above 0.7 MeV do not affect the value of σ_d. Substantial differences between $d\sigma/dT$ values below 0.7 MeV have a little impact on the variation of resulting displacement cross-sections. The difference in σ_d obtained using ENDF/B-VII.1 and JEFF-3.2 is about 4.4 percent and using TENDL-2014 is about 26 percent. The weak influence of deviations between recoil spectra on the discrepancy of calculated displacement cross-sections is typical for other neutron incident energies.

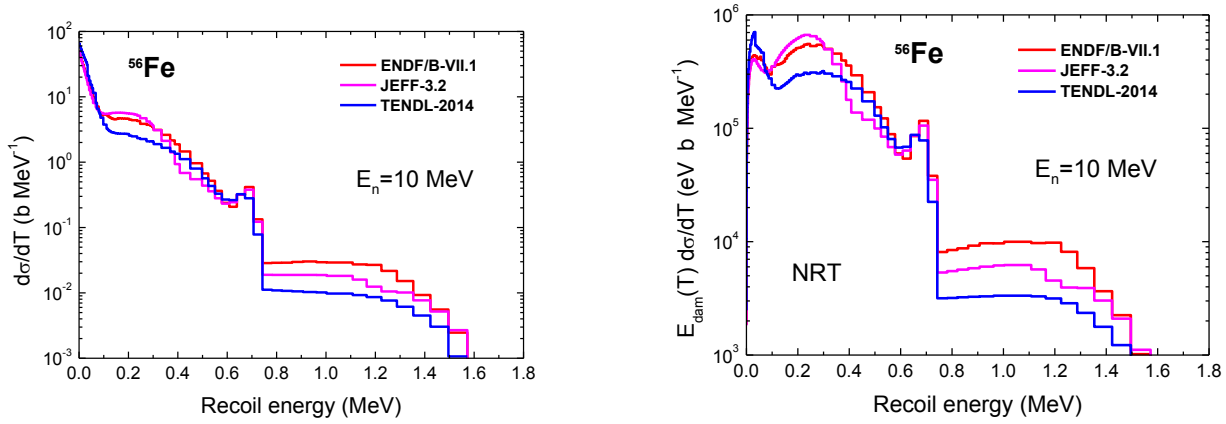

Fig. 4 The recoil energy distribution for ^{56}Fe for neutron incident energy 10 MeV (left) and one multiplied by the damage energy (right).

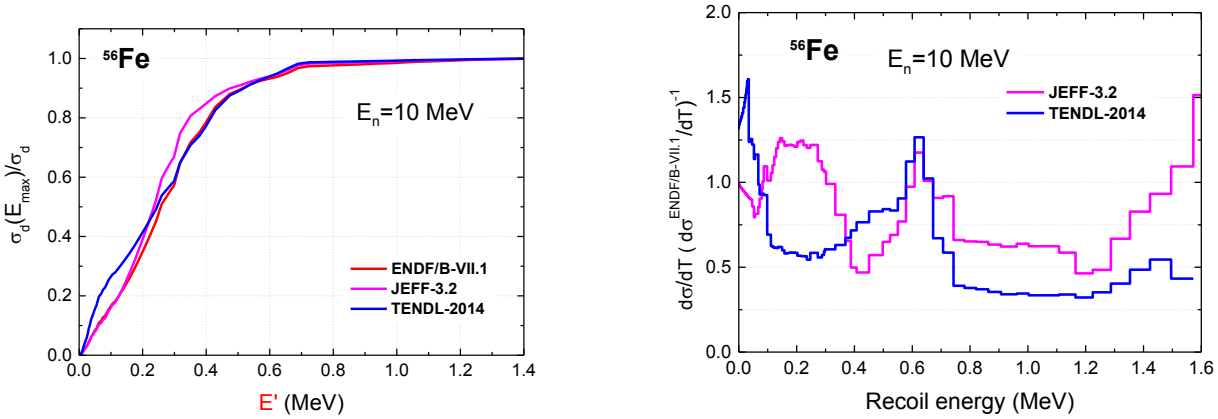

Fig. 5 The displacement cross-section depending on upper integration limit E_{max} (left) and the ratio of recoil energy distribution from JEFF-3.2 and TENDL-2014 to one from ENDF/B-VII.1 for ^{56}Fe for neutron incident energy 10 MeV (right).

Chromium and nickel

A marked difference in the value of σ_d for chromium is observed between values obtained using TENDL-2014 and ENDF/B-VII.1 at neutron energies up to 1 MeV and around 10 MeV and between σ_d values from JEFF-3.2 and ENDF/B-VII.1 at energies above 6 MeV. Because of the lack of information for recoil energy distribution for some reaction channels in libraries, the comparative analysis of spectra is not possible.

For nickel isotopes displacement cross-sections from TENDL-2014 and ENDF/B-VII.1 are markedly different at the neutron energy about 10 MeV. The difference of recoil spectra reaches 60 percent, while the discrepancy between corresponding σ_d values is about 28 percent. The maximal difference of spectrum-averaged displacement cross-sections for reactor and fusion applications [7] is about 13 percent.

Aluminium

The large difference in σ_d values is observed at neutron energies below 1 MeV and around 10 MeV. The difference of spectrum-averaged displacement cross-sections for most applications [7] is less than 2 percent. The estimated contribution of neutron energies above 0.1 MeV in $<\sigma_d>$ is more than 90 %.

At the neutron energy 10 MeV the recoil energies below 1.5 MeV contributes more than 95 percent of displacement cross-section. At these energies the difference between recoil spectra from TENDL-2014 and ENDF/B-VII.1 reaches 37 percent, which does not result in more than 6 percent difference in σ_d values.

Tungsten

The conclusion that the observable discrepancies in recoil spectra have a modest influence on the scatter of resulting values of displacement cross-sections is still valid for tungsten. The difference with other materials is a high degree of discrepancies of $d\sigma/dT$ and σ_d values. Fig.6 shows the ratio of displacement cross-sections for tungsten isotopes obtained using JENDL-4, JEFF-3.2, and TENDL-2014 data to cross-sections calculated with ENDF/B-VII.1. The large difference is observed at the neutron energy around 10 MeV.

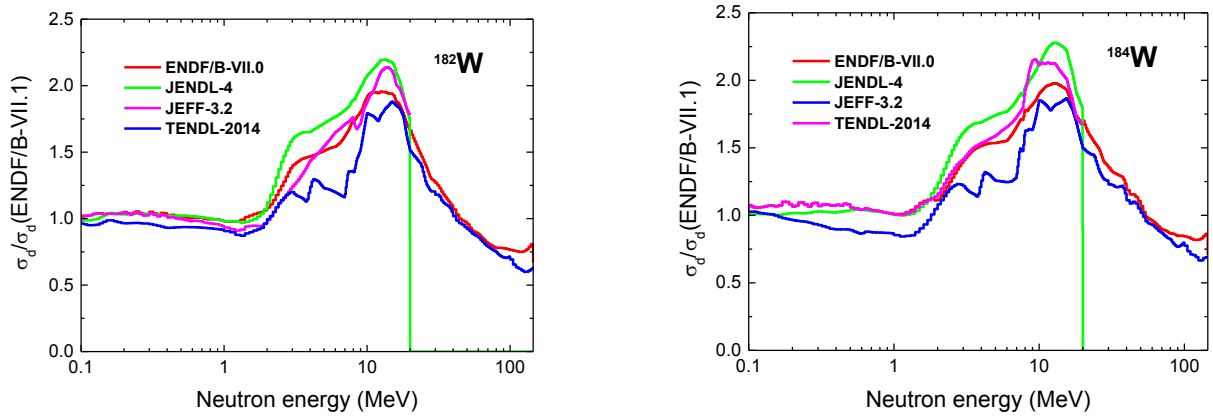

Fig. 6 The ratio of displacement cross-sections for neutron interactions with ^{182}W and ^{184}W calculated using different data sets to cross-sections obtained using ENDF/B-VII.1.

Fig. 7 shows the contribution of different recoil energies in the total displacement cross-section at the neutron incident energy 10 MeV and the ratio of $d\sigma/dT$ values calculated using TENDL-2014 data to values obtained using ENDF/B-VII.1 data. The large difference in the spectra results in high uncertainty in σ_d values at 10 MeV and in neutron spectrum averaged values $<\sigma_d>$ [7].

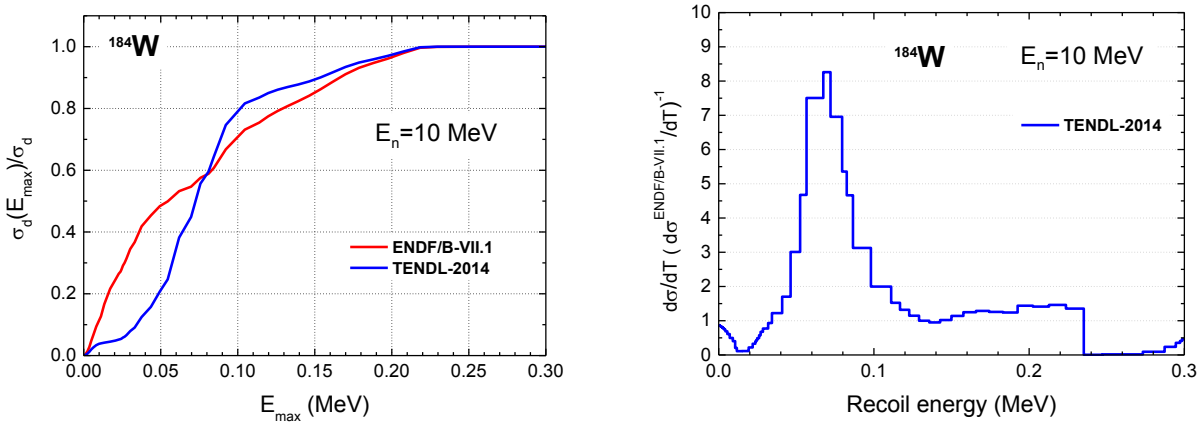

Fig.7 The displacement cross-section depending on upper integration limit E_{max} (left) and the ratio of recoil energy distribution from TENDL-2014 to one from ENDF/B-VII.1 for ^{184}W for neutron incident energy 10 MeV (right).

Incident neutron energies above 20 MeV

Recoil energy distributions were calculated using the nuclear models from MCNP [8] and data from ENDF/B-VII.1 and TENDL-2014. Fig. 8 shows the example of recoil spectra and spectra multiplied by the damage energy for n+^{56}Fe nonelastic interaction at neutron incident energy 150 MeV.

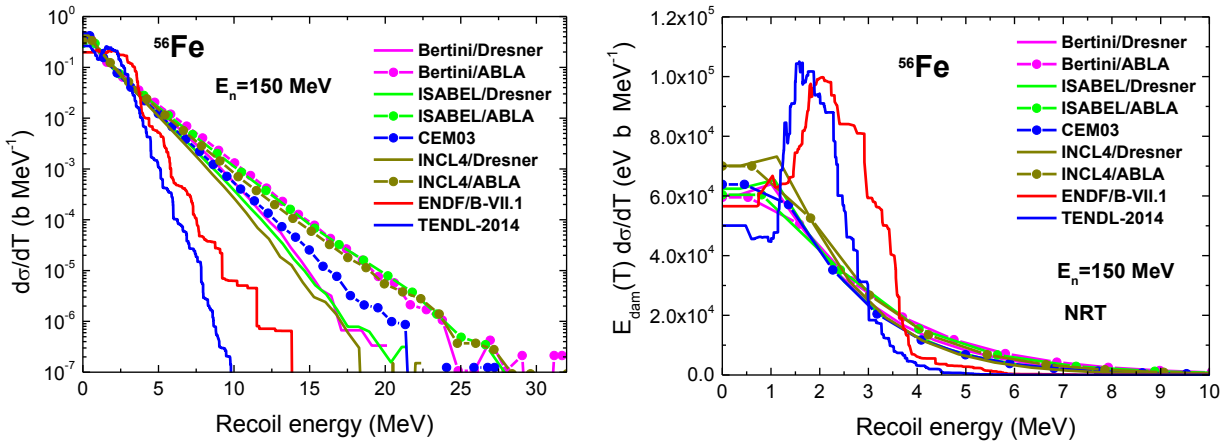

Fig. 8. The recoil energy distribution for ^{56}Fe for neutron incident energy 150 MeV (left) and that multiplied by the damage energy (right).

Fig. 9 illustrates the role of various energies of recoil spectrum for calculated displacement cross-section for neutron inelastic interactions with ^{56}Fe and the ratio of recoil spectra calculated using nuclear models and evaluated data to spectra obtained using the CEM03 code. The difference between displacement cross-sections is relatively small and is about 11 percent for data from ENDF/B-VII.1 and CEM03 calculations and 25 percent for TENDL-2014 and CEM03.

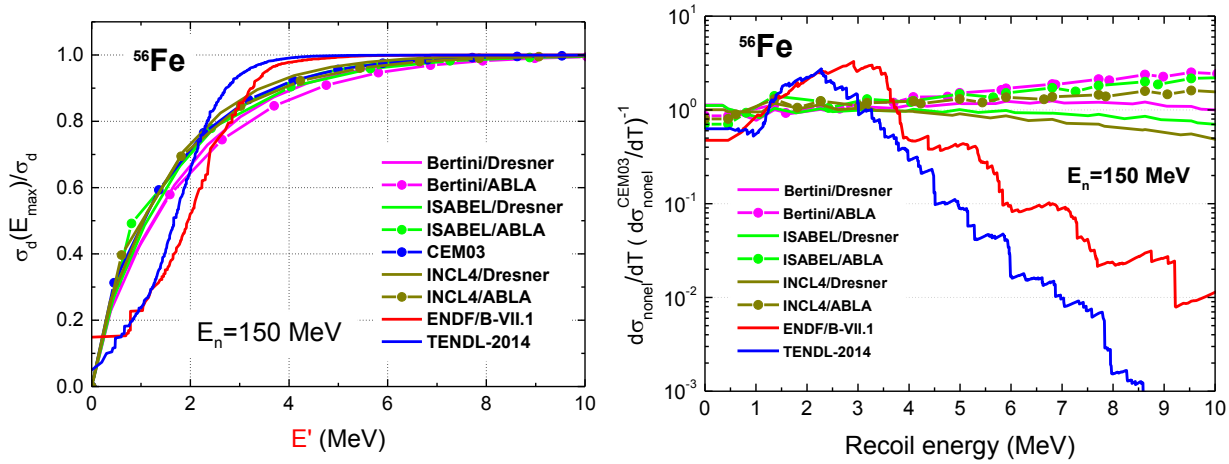

Fig. 9. The displacement cross-section for nonelastic neutron interaction with ^{56}Fe at neutron energy 150 MeV depending on upper integration limit E_{max} (left) and the ratio of recoil energy distributions calculated using different nuclear models and taken from ENDF/B-VII.1 and TENDL-2014 to ones calculated using CEM03 code (right).

Conclusion

The comparative analysis of spectra and displacement cross-sections shows:

- recoil energy distributions obtained using actual data from ENDF/B, JENDL, JEFF, and TENDL are in better agreement than before;
- the comparison of recoil spectra cannot recognize what data is “the best”;
- in most cases, differences in recoil spectra results in a relatively small variation of displacement cross-sections;
- the difference in recoil spectra and σ_d values for tungsten requires the further analysis.

References

[1] S.P. Simakov, SPKA code, 2015; https://www-nds.iaea.org/CRPdpa/
[2] NJOY-99, Data Processing System of Evaluated Nuclear Data Files in ENDF format; https://www.oecd-nea.org/dbprog/njoy-links.html
[3] NJOY 2012 Nuclear Data Processing System; http://t2.lanl.gov/nis/codes/NJOY12/index.html
[4] PREPRO 2015; https://www-nds.iaea.org/public/endf/prepro/
[5] A.Yu. Konobeyev, U. Fischer, P.E. Pereslavtsev, S.P. Simakov, Uncertainties in the Displacement Cross-Sections of Fe and W, EFFDOC-1180; https://www.oecd-nea.org/dbdata/nds_effdoc/effdoc-1180.pdf
[6] R.E. Stoller, Primary Radiation Damage Formation, In: Comprehensive Nuclear Materials, Ed: *R.J.M. Konings,* (Elsevier *2012), v.1, p.293*
[7] A.Yu. Konobeyev, U. Fischer, Presentation at this Meeting: https://www-nds.iaea.org/CRPdpa/RCM2_Presentations.htm
[8] MCNP6, https://mcnp.lanl.gov/

Calculation of primary radiation damage parameters using ENDF/B-VII: Recoil spectra and damage cross sections,

J. Kwon, Y.H. Choi*, G-G. Lee

Korea Atomic Energy Research Institute
*Seoul National University
Korea

Summary of work

Radiation damage in materials is caused by the energy transfer of a high-energy incident particle to the target atoms, which finally results in the redistribution of target atoms. During the nuclear reactor operation, wide energy ranges of neutrons are produced which ultimately affect the property changes of structural materials in a direct and/or indirect way. Energetic recoil atoms created by neutron-atom reactions will be able to induce the displacement cascade. In order to characterize the radiation damage, it is necessary to quantify the displacement damage including the number of surviving point defects and their clusters. The amount of damage is strongly dependent on the recoil energy spectra. In this proposed work, we will deal with two issues. One is to calculate the recoil energy distribution for given neutron spectra. Although there is a simple and convenient code, called SPECTER, for calculating the recoil spectra, we are going to develop the original code using the latest ENDF/B cross section library. The other is to generate the primary damage cross sections which implicates the net damage production. This work needs the molecular dynamics (MD) simulations to describe the surviving point defects following the displacement cascade reactions. We refer to the MD simulation results given in the published literature, which will be applied to the calculation of net damage production cross sections. This research will be performed for iron which is a main element of structural materials. The developed methods in this work will enable us to accurately predict the net damage production of Fe.

1. Calculation of displacement cross section of iron

In quantifying the primary radiation damage due to neutron irradiation, the basic parameter is the displacement cross sections. The displacement cross section σ_d, can be mathematically expressed such as:

$$\sigma_d(E) = \sum_i \sigma_i(E) \int_{T_{min}}^{T_{max}} f_i(E,T) \cdot \nu_{NRT}(T)\ dT \quad (1)$$

where E is the incident neutron energy, T the energy of recoil atom, $\sigma_i(E)$ the nuclear cross section for i-type interaction at neutron energy of E, $f_i(E,T)$ the neutron-atom energy transfer kernel, T_{min} and T_{max} are the lower and upper energy bound of a recoil atom, respectively and $\nu_{NRT}(T)$ represents the secondary displacement function which is calculated using the Norgett, Robinson, and Torrens formula [1]. Among several parameters of σ_d, the nuclear cross sections and the energy transfer kernel are included in the ENDF/B libraries.

The nuclear data processing system, NJOY, converts the ENDF/B format into forms which are useful for practical applications such as reactor analysis, radiation shielding and damage calculation [2]. The NJOY code consists of many modules for a specific task. One of many modules, called HEATR, generates point-wise heat production cross sections, KERMA (Kinetic energy release in materials) factors, and radiation-damage energy production cross sections. The latter cross section represents the recoil energy available to cause the displacement cascade, which is given in the unit of eV-barn. From the damage energy production cross section, we can readily derive the displacement cross section. Dividing the damage cross section by the displacement threshold energy gives us the displacement cross section. The damage energy production cross section (eV-barn) from the NJOY calculation and the displacement cross section (barn) for Fe are shown in Fig. 1. It is found that thermal neurons are capable of causing displacement damage as well as fast neutrons.

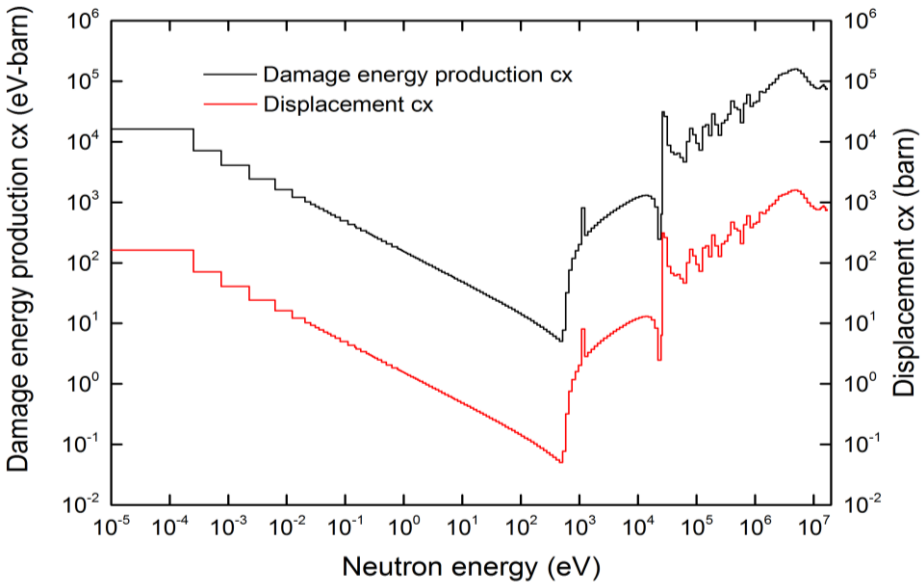

Fig. 1. Damage energy production cross sections (eV-barn) and displacement cross section (barn) for iron. (Displacement threshold energy for Fe = 40 eV).

Theoretically it is simple to derive the net damage production cross section from the displacement cross section, which can be expressed in a mathematical way such as,

$$\sigma_{dis}^{net}(E) = \sum_i \sigma_i(E) \int_{T_{min}}^{T_{max}} f_i(E,T) \cdot \nu_{NRT}(T) \cdot\ \eta(T)\, dT \quad (2)$$

As compare to Eq. (1), the function of $\eta(T)$ is inserted inside the integration. The function $\eta(t)$ represents the surviving defect fraction, which is a function of the recoil energy. Usually, the this

function is obtained from the MD simulation of displacement cascade, which can be described as a fraction of the NRT displacement. The surviving fraction is important since only these defect can make a contribution to radiation-induced microstructural evolution. We apply the MD calculation results produced by Stoller et. al. in this program [3]. The relationship between the recoil energy and the surviving fraction was obtained from a nonlinear least square fit to the MD calculation data. The fraction decreases with increasing the recoil energy. In the high recoil energy above 10 keV, the fraction tends to be saturated. This work will be carried out in the third year of this project.

2. Calculation of recoil atom spectra

The evaluation of recoil atom spectra is essential to quantify the primary radiation damage. The energy of primary knock-on atom (PKA), the initial recoil atom, is used as a major input to the MD simulation of displacement cascades. There are two ways of obtaining the recoil atom spectra. The first one is to use the SPECTER code, which generates neutron damage parameters including displacement cross section, dpa and gas production as well as the recoil atom spectra [4]. However, we cannot use the latest ENDF/B data in the SPECTER calculation because the code includes old ENDF/B library which was pre-processed and stored in the data file. The other method is to utilize the NJOY that can have an access to the ENDF/B-VII with ease. Since the NJOY does not provide the recoil atom spectra directly from ENDF/B data, we need to develop a new code for such calculation.

The recoil atom spectra can be expressed such as:

$$R(T)\,dT = \sum_i \int_0^{E_{\max}} \phi(E)\cdot\sigma_i(E)\cdot f_i(E,T)\,dE\,dT \qquad (3)$$

The recoil atom spectra stand for the probability that a recoil atom is created with its kinetic energy between T and T+dT for a given neutron spectrum. The recoil atom spectrum is also s function of microscopic cross section neutron flux and neutron-atom energy transfer kernel. Among the variables, the determination of energy transfer kernel is not straightforward. The kernel should be calculated by using the ENDF/B data split in the library. Depending on the file type (MF number) specified in the ENDF/B library, we can calculate the kernel in three different ways.

1) MF=4 (Angular distribution of emitted neutron)

This case corresponds to the elastic scattering and discrete-level inelastic scattering reactions. Since the relationship between the recoil atom energy and the scattering angle of the emitted neutron is unique, the kernel can be readily obtained. In general, the angular distribution of the scattered neutron is given in the Legendre polynomial series in the MF = 4 file.

2) MF = 6 (Energy-angle distribution of secondary particles)

File 6 contains subsections for all of the particles and photons produced by the reactions, including the recoil nucleus. The case is relevant to many reactions, including continuum inelastic scattering, (n,2n), (n,np), (n,nα), (n,p) and (n,α) reactions. Energy and angular distribution of secondary particles is expressed as a normalized probability function and is available directly from the ENDF/B. Therefore, we can readily obtain the transfer kernel without much mathematical treatment.

3) MF = 14/15 (Angular / Energy distribution of photon production)

This case corresponds to the radiative capture reaction (n,γ). Because the energy transfer kernel is not given in the ENDF/B completely, we need to derive the kernel by assuming that only one photon is emitted after (n,γ) reaction. When the energy of emitted photon is resolved, the data in MF = 14 can be applied. The data in MF=15 was applicable to the unresolved photon energy.

The RASG (Recoil atom spectra generation) code was developed to calculate the recoil spectra by combining the previous schemes with ENDF/B data. The RASG code is composed of three modules. Two module execute the generation of microscopic nuclear cross section and the calculation of the energy transfer kernel from the ENDF/B library using the NJOY system. The third computes the neutron spectra independently according to the environments. The recoil atom spectra was calculated for given neutron spectrum, which was included in the SPECTER code for demonstration.

The Fig. 2 (a) shows the neutron spectrum as an input to the RASG and the SPECTER and each recoil spectra were described in Fig. 2(b). The spectral-averaged recoil energy was 3.21 and 2.87 keV from the SPECTER and RASG code, respectively. The same procedure was applied to different neutron spectra. This spectra is the typical one in the core baffle region in the pressurized water reactor. The results are shown in Figs. 3.

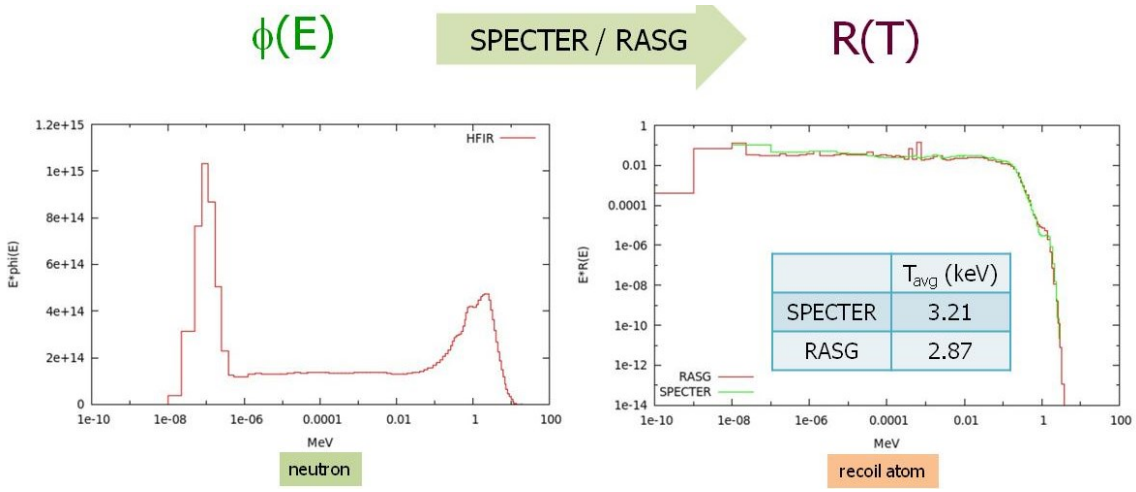

Fig. 2. (a) Neutron spectra in the HFIR for an input to the codes, (b) calculated recoil atom spectra & spectral-averaged recoil energy

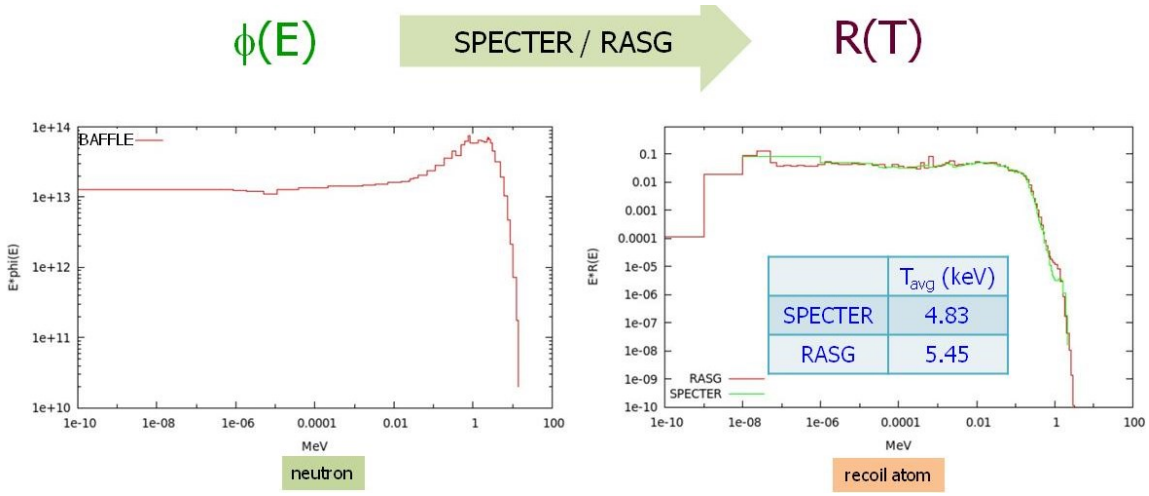

Fig. 3. (a) Neutron spectra in the core baffle region in PWR, (b) calculated recoil atom spectra & spectral-averaged recoil energy

Summary and Plan for 3rd Period

Based on the ENDF/B-VII library, we have developed the RASG code for obtaining the recoil atom spectra under neutron irradiation to Fe. Also, the net damage production cross sections are being evaluated with the NJOY code. Through the investigation of HEATR module in the NJOY code, the inclusion of the surviving defect fraction will enable us to derive the cross sections. This calculation will be continued in the 3rd period of the CRP. In addition, we are going to evaluate the recoil atom spectra for various neutron environments by using our own code RASG, which will be compared with the SEPCTER results. Although not a significant differences in the recoil spectra between the RASG and SPECTER are expected, the point of our interest is the use of the latest version of the ENDF/B library. We will perform the integration of the split RASG programs, which were originally made one by one in need. In addition, we will investigate other open codes which are available to generate the recoil atom spectra.

References

[1] M. J. Norgett, T. Robinson and I.Torrens. A proposed method of calculating displacement dose rates, *Nucl. Eng. Des*. 33 (1975) 50.
[2] R.E. MacFarlane and A.C. Kahler. Methods for processing ENDF/B-VII with NJOY, *Nucl. Data Sheets* 111 (2010) 2739.
[3] R.E. Stoller and L.R. Greenwood, Subcascade formation in displacement cascade simulations: Implications for fusion reactor materials, *J. Nucl. Mater*. 271&272 (1999) 57.
[4] L.R. Greenwood and K. Smither, SPECTER : Neutron Damage Calculations for Materials Irradiations, ANL/FPP/TM-197 (1985).

Development of TALYS and TENDL relevant for primary irradiation damage, A.J. Koning

Nuclear Data Sections of IAEA
Vienna, Austria

Introduction

NRG's TENDL library and its related uncertainty method, Total Monte Carlo (TMC), have been used by various parties in this CRP on primary radiation damage:

- KIT (Konobeyev and Fischer): comparison of TENDL recoils with other nuclear data libraries and gas production
- Sandia (Griffin): TENDL and TMC for displacement KERMA and damage energy in electronics
- CEA Saclay (Luneville, Crocombette and Simeone): damage energy calculations with DART using TENDL
- CCFE (Sublet and Gilbert): DPA calculations with FISPACT-II using TENDL
- UPM (Cabellos): TENDL and TMC for calculation of damage and its uncertainties
- NRG (Koning and Rochman): Maintenance and development of TENDL and TMC, specific for damage calculations.

As far as we know, TENDL is the only initiative in the world where nuclear data needed for damage calculations are provided on a consistent basis. It requires:

- nuclear data for all isotopes that could be of relevance for irradiation damage
- inclusion of recoil information for all relevant channels
- inclusion of all particle production channels (especially protons and helium)
- extension beyond the traditional 20 MeV limit
- provision of uncertainty data that is processable for damage calculations.

The main software package behind TENDL, certainly for damage calculations, is TALYS [Kon12], and we will first briefly summarize the code and some of its latest extensions. After that we give an overview of TENDL-2014.

TALYS

Many nuclear data evaluations and related validation methods revolve around TALYS. TALYS is software for the analysis and prediction of nuclear reactions that involve neutrons, photons, protons, deuterons, tritons, helions and alpha-particles, and formally for target nuclides of mass 5 and heavier, while results are expected to be reasonable for masses heavier than 20. To achieve this, a suite of

nuclear reaction models has been implemented into a single code system. This enables to evaluate nuclear reactions from the unresolved resonance range up to intermediate energies. TALYS is extensively used for both basic and applied science.

At the time of this writing, TALYS has been used in more than 600 different publications since its initial release in 2004. Fig. 1 shows a classification of these papers. An extensive description of TALYS and the nuclear data evaluation and validation software built around it has recently been published [Kon12].

One important recent extension to TALYS is the possibility to predict data up to 1 GeV. The Koning-Delaroche optical model potential from 2003 has been extended by two simple terms for the volume real and imaginary potentials. The resulting predictions have been tested against available experimental data above 200 MeV and now seem to provide reasonable results up to about 1 GeV. By means of logarithmic binning of the multiple decay scheme in TALYS it is now also possible to calculate non-elastic channels at higher energies. Emission spectra have not yet been validated, but preliminary results for residual production cross sections are shown.

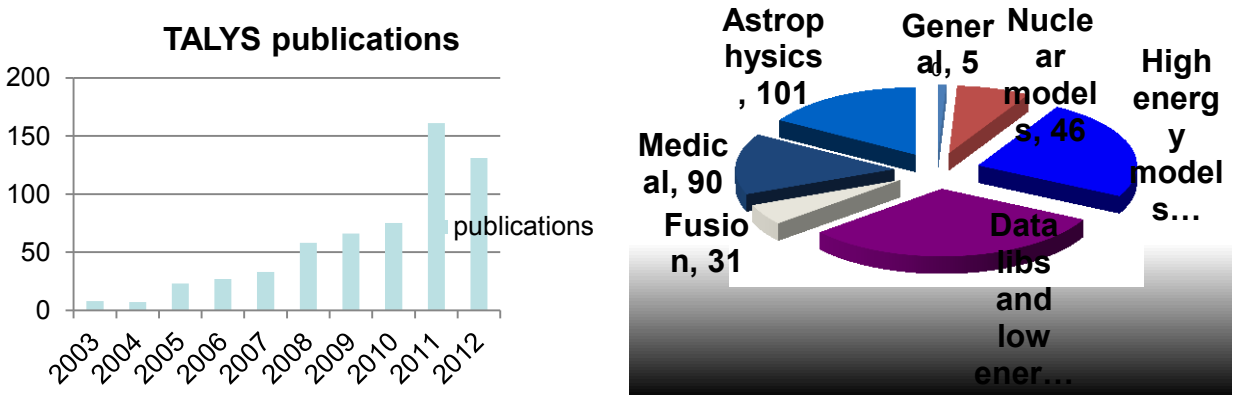

Fig. 1. Worldwide use of TALYS per year and per application area.

Fig. 2 shows some examples of residual production cross sections.

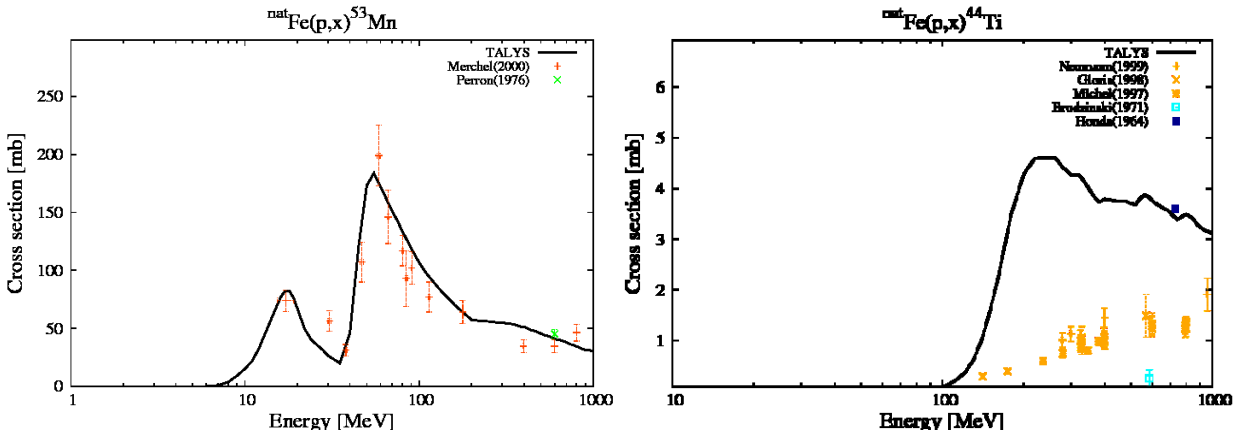

Fig 2. Some residual production cross sections up to 1 GeV calculated with TALYS-1.6.

TENDL

We will briefly discuss the latest version of the TALYS Evaluated Nuclear Data Library, TENDL. This TENDL-2014 library contains sub-libraries for incident neutrons, protons, deuterons, tritons, helium-3's, alphas, and photons. For all types of incident particle, nuclear data libraries for 2629 nuclides are produced. These are all isotopes, in either ground or metastable state, with a half-life

longer than 1 sec. from Z = 3 (Li) to Z = 110 (Ds). This is about 8 times more nuclides than in any other world library. All libraries extend up to 200 MeV, contain covariance information, and are as complete as the ENDF format allows it to be. Table 1 compares TENDL with the other world libraries for some quantities relevant for this CRP.

Table 1: Completeness of TENDL with emphasis on damage, compared to other world libraries.

Library	**# isotopes**	**# isotopes with recoils**	**# isotopes above 20 MeV**
TENDL-2014	2629	2629	2629
ENDFB-VII.1	423	121	47
JENDL-4.0	405	5	0 (separate JENDLHE file)
JEFF-3.1.2	381	65	34

Since its first version, TENDL-2008, it has been our aim to yearly produce nuclear data libraries which are complete from the nuclear reaction point of view. In ENDF language, this means a full nuclear reaction description from MF1 to MF40. Hence, every isotopic evaluation contains *all* possible nuclear reaction information, whether relevant for a particular application or not. The main challenge of the TENDL team now is to choose each year the right priorities for successive improvement, which obviously depends on many things, one of them being funding. Improvements could be better integral performance of criticality and reactor benchmarks, better overlap with differential data (EXFOR), more credible uncertainty information or, as relevant for this CRP, better description of particle production and recoil channels and proper streamlining of the related ENDF-6 formatting issues.

At the basis of this evaluation system is the TALYS nuclear model code, which produces nearly all these data. Only for fission quantities and resonance parameters other software is used, see Fig. 3. A statistics code, TASMAN, performing among others a Monte Carlo sampling loop around the entire system, to produce uncertainty information. The ENDF formatting code TEFAL, rivalling in programming complexity with TALYS, produces the nuclear data libraries. A full description of the system is given in [Kon12].

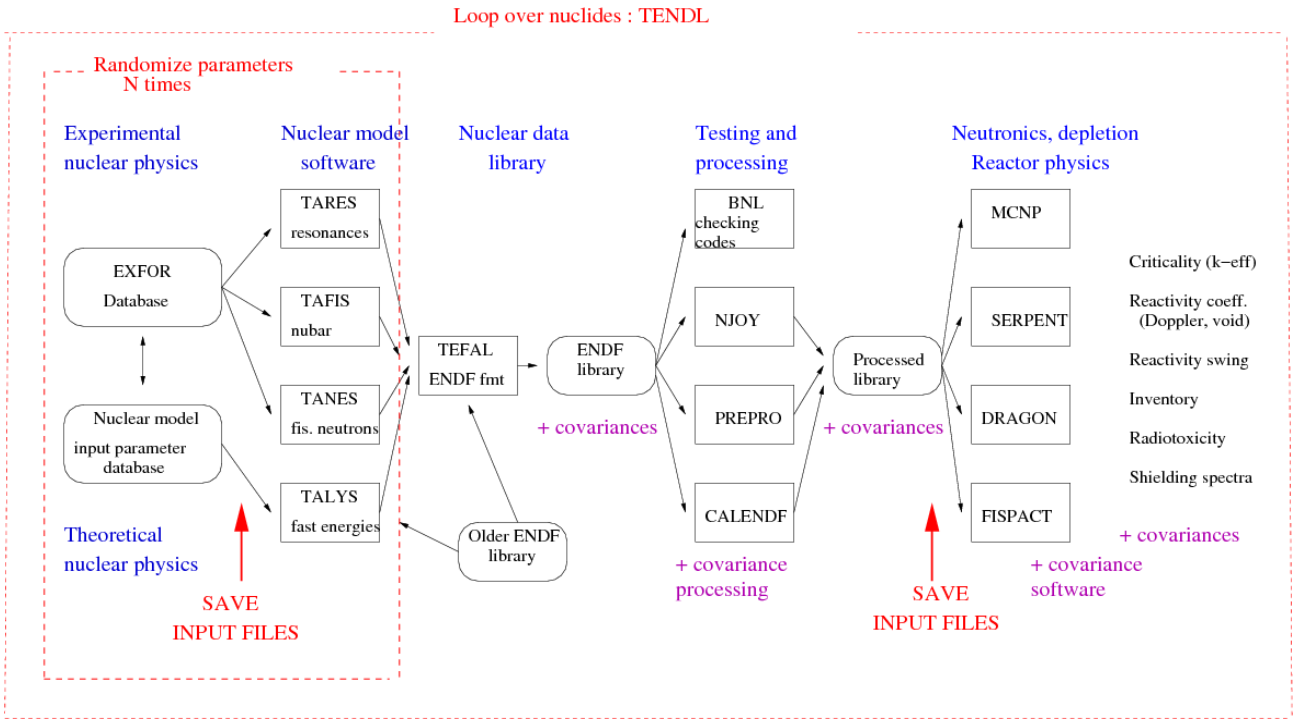

Fig. 3. Flowchart of the nuclear data file evaluation and production process with the TALYS system.

Total Monte Carlo

For the TENDL library described above, a single ENDF-6 covariance data file is created by averaging the hundreds of random nuclear data sets coming from TALYS or other codes, see the box at the lower left hand side of Fig. 3. An alternative approach [Kon08] is to take the effect of a single random sampling of nuclear model parameters all the way to the end, i.e. to create one ENDF-6 file per random set of input parameters, process it and perform an applied calculation. This process is depicted in Fig. 4. In other words, every random curve is stored in a different ENDF-6 file, while every ENDF-6 file is complete for all quantities, i.e. MF1-15 are used. This approach has later been coined (by M. Herman) "Total" Monte Carlo (TMC) and makes uncertainty propagation a lot easier (apart from the calculation time), and arguably more exact, than when using perturbation and covariance software. Covariance matrices simply do not appear in the entire process, with the exception of the extreme beginning, in the form of uncertainties and correlations of (model and experimental) input parameters, and the extreme end, e.g. an *average* DPA parameter, its uncertainty and covariance.

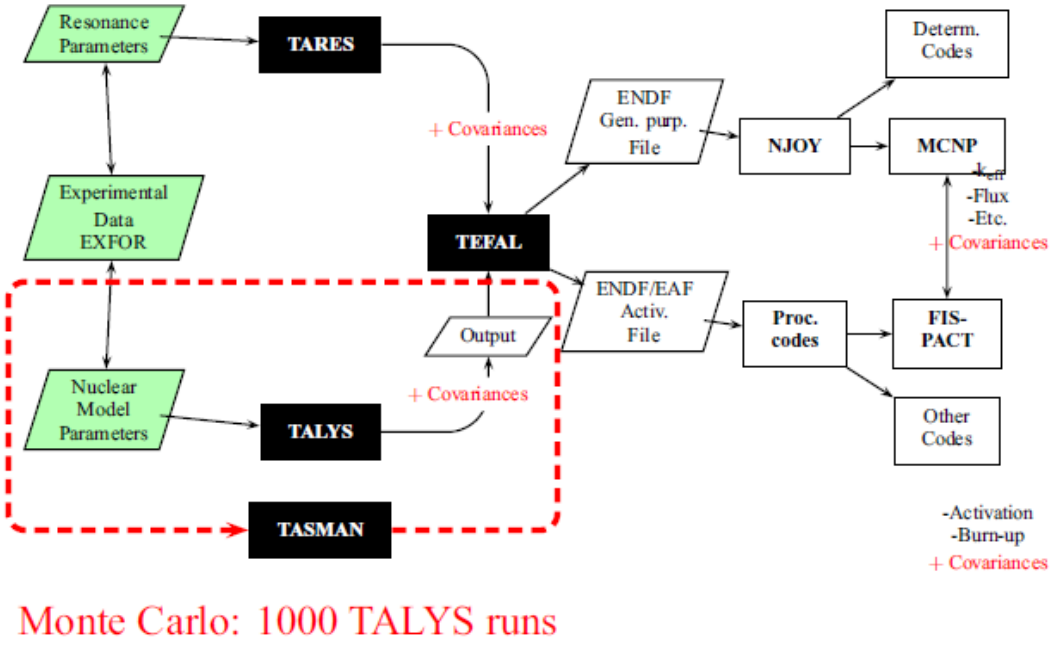

Fig. 4. Flowchart of automated, reproducible evaluation process used for TMC and the production of TENDL.

Conclusions

The quality of an isotopic evaluation is often *only* judged through comparison of existing experimental data, differential or integral. This means that the leading argument to adopt a certain isotopic evaluation over the other for any of the world libraries is probably *not* the existence of secondary reaction information (particle production, recoils etc.) that enables doing damage analyses. From the point of view of the maintenance method of these libraries (attempting to collect the best from many different contributing institutes) this is understandable. It does however lead to the statistics summarized in Table 1. The TENDL approach gets rid of that problem. TENDL-2014 is fully complete, in terms of reaction description. From now on it is zeroing in on the truth using differential and integral experimental data, and solving remaining glitches.

An important example of such a glitch is that at higher energies a discontinuity at 30 MeV showed up in the NJOY damage curves calculated with TENDL-2011 and TENDL-2012. This was due to erroneous residual production cross sections in certain cases and a discontinuity in the center of mass frame for which the data were tabulated. The problem is now gone [Kon13], at least for the individual cases for which we checked this.

References

[Kon08] A.J. Koning and D. Rochman, ``Towards sustainable nuclear energy: Putting nuclear physics to work", Ann. Nucl. Energy 35, p. 2024-2030 (2008).

[Kon12] A.J. Koning and D. Rochman, "Modern nuclear data evaluation with the TALYS code system", Nucl. Data Sheets 113, p. 2841 (2012).

[Kon13] Private communication with B. MacFarlane, S. Kahler, O. Cabellos and J.C. Sublet.

Uncertainty Analysis of Metrics Used for Assessing Primary Radiation Damage: Input to 2nd RCM,

P. Griffin

SAND2015-7151 O

Sandia National Laboratories, Radiation and Electrical Sciences
Albuquerque, NM, USA

Abstract. This report summaries the progress made by Sandia National Laboratories in its support of the International Atomic Energy Agency (IAEA) Nuclear Data Section (NDS) Coordinated Research Project (CRP) on primary radiation damage cross sections.

1. Planned Activities

This is the report from Sandia National Laboratories (SNL), presented at the 2nd Research Coordination Meeting (RCM) on the Primary Radiation Damage Cross Sections Cooperative Research Project (CRP), summarizing our first year's progress in this project. The 1st year plan submitted by SNL called for the following activities:

a) Review of validation data for displacement damage in crystalline silicon;
b) Use of TENDL cross sections to generate model-based uncertainty for the silicon displacement kerma;
c) Decomposition of the displacement kerma into its components based on main reaction channels;
d) Comparison of component-level displacement kerma uncertainties with reaction cross section uncertainty;
e) Investigation of uncertainty components due to model defect;
f) Investigation of the role of uncertainty in the recoil ion energy on the uncertainty in the damage metric.

The following sections of this report summarize actions taken in support of these areas of investigation.

2. Review of Validation Data for Displacement Damage in Semiconductor Materials

Validation evidence exists to support the proportionality, under neutron irradiation, of the inverse change in silicon bipolar junction transistor (BJT) gain degradation to the silicon displacement kerma. The proportionality is captured in the Messenger-Spratt relationship [1] for minority carrier lifetime degradation [2, 3]. The validation evidence includes measurements gathered for neutron spectra ranging from degraded fission spectrum to fast burst fission spectra, and includes data from DD neutron sources with energies ~ 2.5 MeV, and DT neutron energies near 14-MeV. This validation evidence is captured in ASTM standards [4, 5] for silicon bipolar junction transistors [6]. The ASTM standards indicate that, for silicon, typical reproducibility/precision in the ratio of damage in different neutron environments is within 2-3% and an overall uncertainty/accuracy in a damage ratio is ~8%. In silicon, deviations in the damage proportionality have been reported for thermal neutron energies. This deviation is probably related to the change in residual defect types from the point-like defects that result from thermal neutron interaction, i.e. isolated vacancy-oxygen (VO) defects, versus the cascade cluster damage from higher energy neutrons, i.e. divacancy (VV) defects.

For GaAs heterojunction bipolar transistors (HBTs), experimental evidence exists that the high energy neutron damage does not track with the displacement kerma. A thermal spike, i.e. defect recombination in cascade cluster damage areas, has been proposed as the explanation. A reformulated damage constant, one that applies a reduced damage efficiency with increasing primary knock-on atom (PKA) recoil atom, has been demonstrated to restore the damage ratio proportionality [4, 7]. Validation evidence in GaAs HBTs exists over a similar range of neutron spectra [7], i.e. degraded fission, fast fission, DD, and DT spectra.

Some work has been reported on damage equivalence in SiC devices using LEDs. No experimental validation evidence for damage ratios is available on GaN, InP, or AlN, or other III-V materials. No standard exists for the energy-dependent response function in these other semiconductor materials.

There is a need for validation evidence supporting the energy-dependent response in semiconductor materials for energies above the DT, ~ 14-MeV, energies. Such evidence may be obtained using facilities such as the Lawrence Berkeley National Laboratory and University of California Berkeley 88" cyclotron deuteron breakup beams [8]. Neutron beams at energies up to 60 MeV can be obtained from this facility.

3. Use of TENDL Cross Sections

A. Koning and D. Rochman provided the author with a set of random cross section libraries generated with the NRG (Petten, Netherlands) TALYS system of codes. 101 element samplings were provided for the ^{28}Si, ^{29}Si, and ^{30}Si isotopes. 301 element samplings were provided for ^{69}Ga, ^{71}Ga, and ^{75}As. The multi-element samples, representing random draws on the input parameters for TALYS nuclear data calculation, contained ENDF-6 format cross sections and File 6 residual recoil energy distributions for neutron energies up to 30 MeV. Work on this multi-element sampling of the variation in nuclear data evaluations produced by sampling of the input parameters in the nuclear physics codes has been restricted, so far, to an examination of the silicon isotopes. The sampling of the TALYS/TENDL cross sections [9] for the silicon isotopes were processed using the NJOY-2012 code [10]. This analysis enabled us to perform a Total Monte Carlo (TMC) analysis [11] of the non-linear uncertainty propagation from the model-based variation in the TALYS cross sections into the displacement kerma components. We performed analysis using a fine structure 640-group energy representation, going up to 20 MeV, for detailed energy-dependent responses and using a coarser 89-group representation which was focused on support for the energy-dependent covariance analysis. Figure 1 shows the ^{28}Si cross section components in the 640-roup representation plotted using both a linear and a logarithmic energy axes.

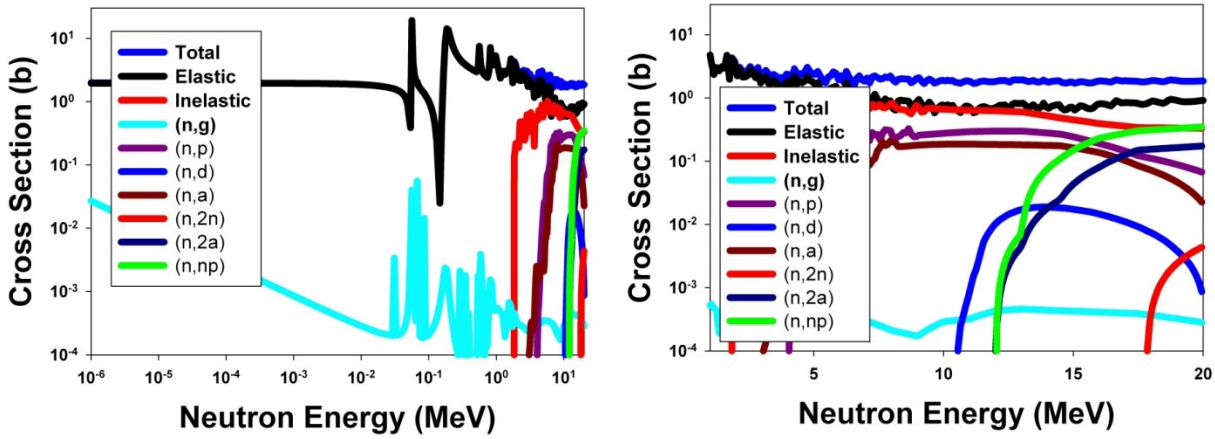

a) Logarithmic Energy Axis b) Linear Energy Axis

Figure 1: Baseline ^{28}Si Cross Section Components

The reaction channels in these isotopes can be grouped into four broad groups: elastic (MT = 2), inelastic (MT = 51 - 91), disappearance (MT = 102 - 120), and residual/other (MT = 16 - 45 except fission MT = 18, 19, 20, 21, 38). For the ^{28}Si TENDL evaluations, the important contributors to the "residual" group include the (n,nα), (n,np), (n.2n), (n,2nα) and (n,n2α) reaction channels (MT = 22, 28, 16, and 24, respectively).

In order to validate our 89-group Total Monte Carlo analysis approach to establishing the energy-dependent uncertainty and correlation matrix for the displacement kerma components, we first looked at the cross sections themselves, rather than the kerma components, and compared data derived from different data sets as well as different analysis methodologies. Figure 2 compares the cross sections and standard deviations that correspond to the following data/approaches: a) baseline ENDF/B-VI evaluation represented in a 640-group structure and using the data-driven File 32/33 covariance information to assess uncertainties; b) recent ENDF/B-VII.1 evaluation with a similar approach; c) TENDL-2013 baseline TALYS-produced evaluation with a File 33 covariance matrix to assess uncertainty; and d) a Total Monte Carlo approach based on using the 101 element random selection of TENDL-2014 ^{28}Si evaluations and an 89-group energy structure to assess variation/uncertainty.

The ENDF/B-VI covariance data for this elastic reaction are seen to be unreasonably small due to the approach used in the underlying nuclear data evaluation for the resonance region. The relative standard deviations are less than 0.5% and stop at 10^{-3} MeV. The standard deviations from the more recent ENDF/B-VII.1 are much more reasonable and, as noted in the file MT = 451 comments, the uncertainty in the scattering radius dominated the cross section uncertainty at low energies. The standard deviations from the baseline 640-group processing of theTENDL-2013 file and the associated TALYS-based 89-group processed TENDL-2014 statistical samples used in the TMC analysis are seen to be nearly identical. The differences seen near the 0.1 MeV anti-resonance can be attributed to the different group structure used in processing the two different analyses. In Figure 2b, the energy bin structure for the uncertainty data from ENDF-6 format evaluations (ENDF/B-VI, ENDF/B-VII.1, and TENDL-2013) are representative of the energy structure used by the evaluator in the File 33 representation of the uncertainty. The energy bin structure of the random/statistical analysis is taken from the 89-group energy bin structure used in the analysis. This 89-group energy bin structure was derived to support generic radiation shielding applications at Sandia.

The agreement between the baseline TENDL-2013 data and the random/statistical analysis is indicative that the 101 sample size used here was adequate for capturing the average elastic cross section and the associated standard deviations associated with the variation in input parameters of the nuclear physics code. The standard deviations from the TENDL-2013 and ENDF/B-VII.1 evaluations are seen to be fairly consistent for energies greater than $2\text{x}10^{-2}$ MeV and less than 2.75 MeV. Above the 2.75 MeV energy point, the ENDF/B-VII.1 evaluation does not report an uncertainty. Below 2×10^{-2} MeV the ENDF/B-VII.1 evaluation has a single point and the fidelity is suspect. The consistency of data seen in Figure 2 helps establish the validity of our implementation of mechanics for the TMC analysis. The variation seen in the standard deviations in Figure 2b is not a concern since the uncertainty is representative of the method used to generate the data and, thus, there is no reason to expect the covariance data from different libraries to have a similar characterization.

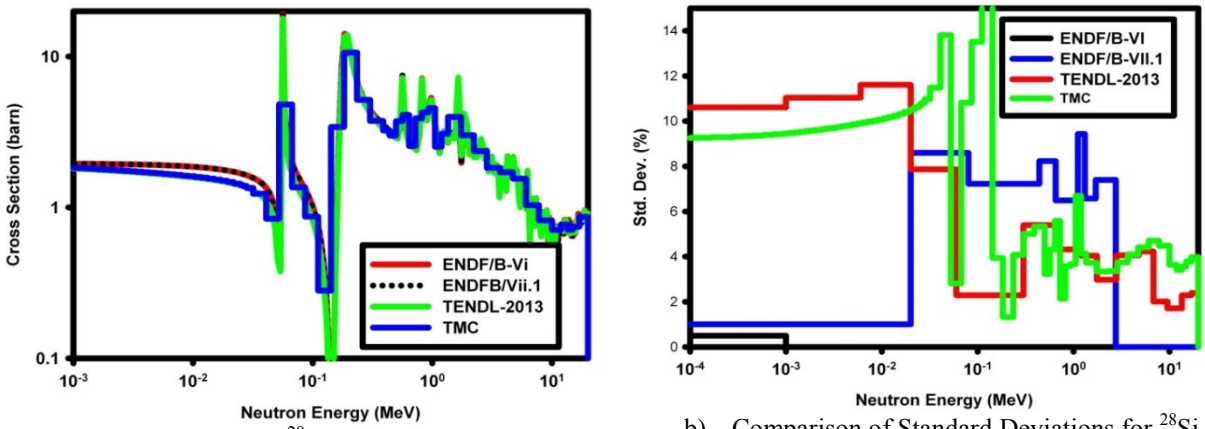

a) Comparison of ^{28}Si Elastic Cross Sections

b) Comparison of Standard Deviations for ^{28}Si Elastic Cross Section

Figure 2: Cross Section and Standard Deviation for ^{28}Si Elastic Reaction Channel as Derived from Various Data Sets/Methodologies

Figure 3 shows the TMC-based correlation matrix for the elastic ^{28}Si channel. The appearance of the correlated area is what one would expect, and what one sees in the File 33 representation from the baseline TENDL-2013 evaluation. The narrow uncorrelated region appearing in the figure just above 100 keV is probably related to the 89-group energy structure used in the analysis and its lack of sensitivity in capturing the variation in the narrow resonance structure in this energy region.

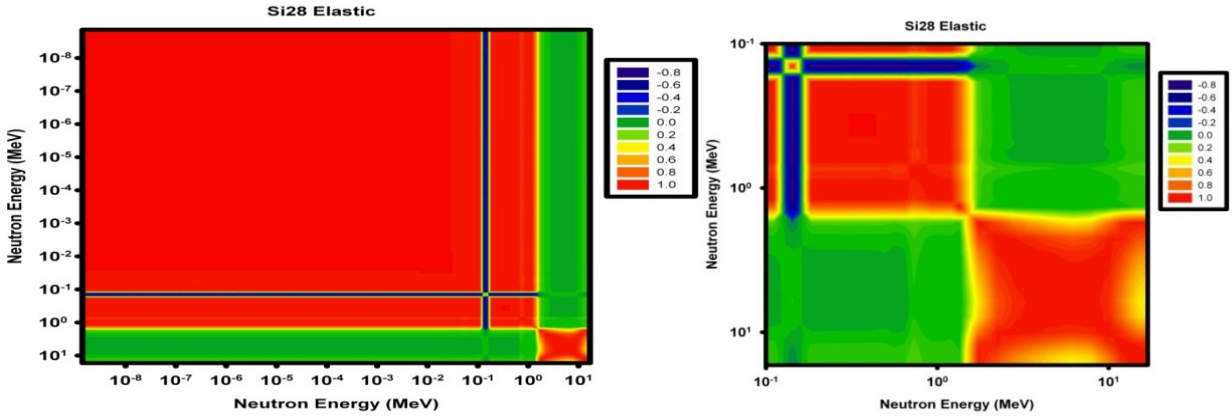

a) Broad Energy View b) Enlarged View of High Energy Portion

Figure 3: TENDL-2014 Elastic TMC Cross Section Correlation Matrix

When one considers the elastic channel over the total energy region, an examination of these various approaches and the comments found in the source evaluation files indicate that the model-based TENDL-2013 standard deviation, rather than the data-driven ENDF/B standard deviations, is probably the most representative of the actual underlying uncertainty in the elastic cross section. The data in Figures 2 and 3 support a position that, for the elastic channel, the 101-sample TMC approach adequately captures the covariance in the underlying random sampling.

Figure 4 shows the energy-dependent correlation matrix for some of the other reaction channels. i.e. the first inelastic reaction channel and the (n,p) transmutation/disappearance channel. These and the other higher energy reaction channels also exhibit the expected correlation structure and can be seen to be consistent with the File 33 covariance matrices seen in the baseline TENDL-2013 evaluation. This look at applying the 89-group TMC approach to the cross sections provides verification evidence for our implementation of the analysis process and establishes the foundation for applying this methodology to an examination of the energy-dependent covariance matrix for the displacement kerma and its components.

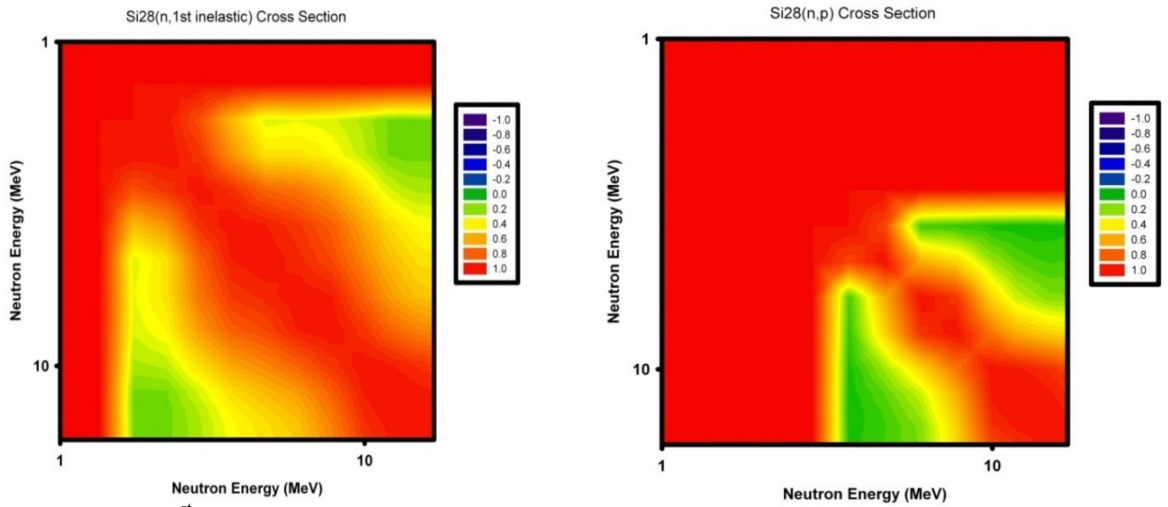

a) 1st Inelastic State (MF=51) b) (n,p) Transmutation Reaction (MF=103)

Figure 4: TENDL ^{28}Si TMC Correlation Matrix for Various Reaction Channels

4. Uncertainty in Recoil Atom Spectra

The calculation of a uncertainty in the displacement kerma in a material depends on a nonlinear propagation of underlying uncertainty from different aspects/features in the nuclear underlying data. The uncertainty in the displacement kerma depends not only on the uncertainty in the cross sections for the various reaction channels, but also in the variation in the recoil spectra and how the energy of the recoil particles is partitioned between ionization and displacement. This section addresses the variation seen in the recoil spectra for ^{28}Si reaction channels with different analysis methodologies.

While the analysis of the variation of recoil spectra seen in 101-sample draws from the TENDL-2014 random files has not yet been completely investigated, a first step was to examine the variation in the recoil spectra seen between different nuclear data evaluations. Figure 5 shows excellent agreement in the recoil atom spectra for the elastic recoil spectrum. The JEFF-3.1.2 and ENDF/B-VII.1 data evaluations adopted the same underlying evaluation and are identical for ^{28}Si. Figure 6 shows that higher energy transmutation reaction channels also exhibit fairly close agreement in the recoil spectra. Strong differences are observed between evaluations at neutron energies near the reaction threshold, but the agreement is fairly good for all reaction channels at energies well above the threshold energy. This good agreement may only reflect that the data-driven evaluation, like ENDF/B-VII, JENDL and JEFF, lack direct measurement data the spectra for recoil atoms and thus also rely on nuclear physics models and nuclear reaction codes to inform the data reflected in their File 6 representations of the recoil spectra.

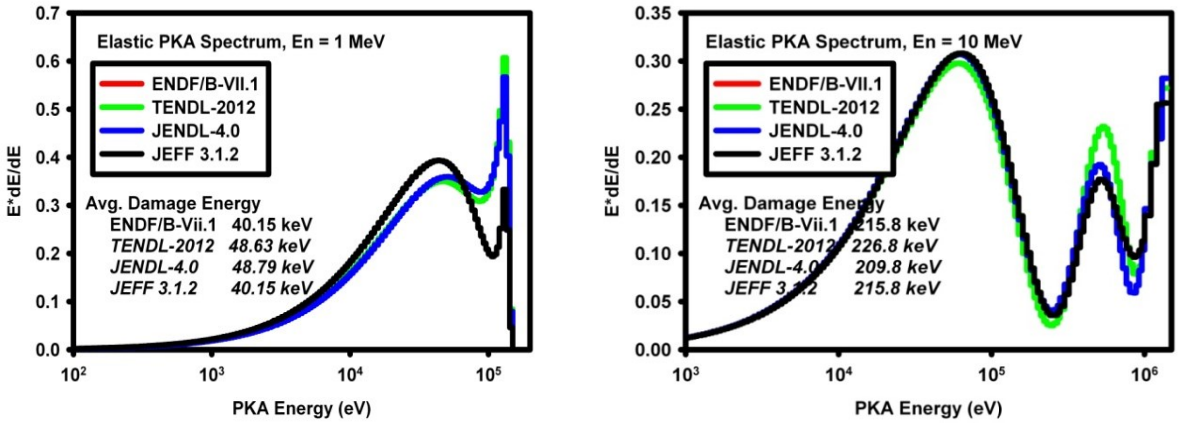

a) 1 MeV Incident Neutron Energy b) 10 MeV Incident Neutron Energy

Figure 5: Variation in the PKA Recoil Spectrum for ^{28}Si Elastic Reactions

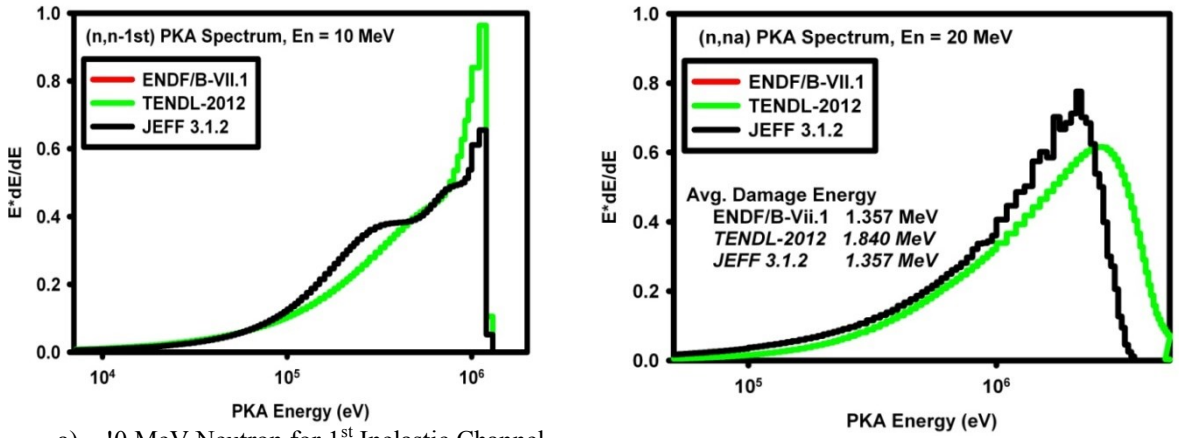

a) !0 MeV Neutron for 1st Inelastic Channel b) 20 MeV Neutron for (n,nα) Channel

Figure 6: Variation in the PKA Recoil Spectrum for Various ^{28}Si Reactions

To get another perspective on the variation that may be seen between different nuclear reaction modelling codes, a comparison was also made of recoil atom spectra generated by the EMPIRE code [12] and from the SPECTER code [13]. In this case consideration was given to the composite PKA spectrum rather than to the reaction-dependent PKA spectra and the normalized recoil spectra were examined in order to eliminate the influence from different magnitudes in the cross sections. Figure 7 shows the close agreement in shape of the overall PKA recoil spectrum between the nuclear models used in these two codes. When one compares the average recoil atom energy from the monoenergetic neutron cases depicted in Figure 7 close agreement is also seen. Comparing EMPIRE versus SPECTER the results are; at 1-keV 70 eV vs. 59 eV; at 1-MeV 41 keV vs. 39 keV; at 14-MeV 569 keV vs. 490 keV.

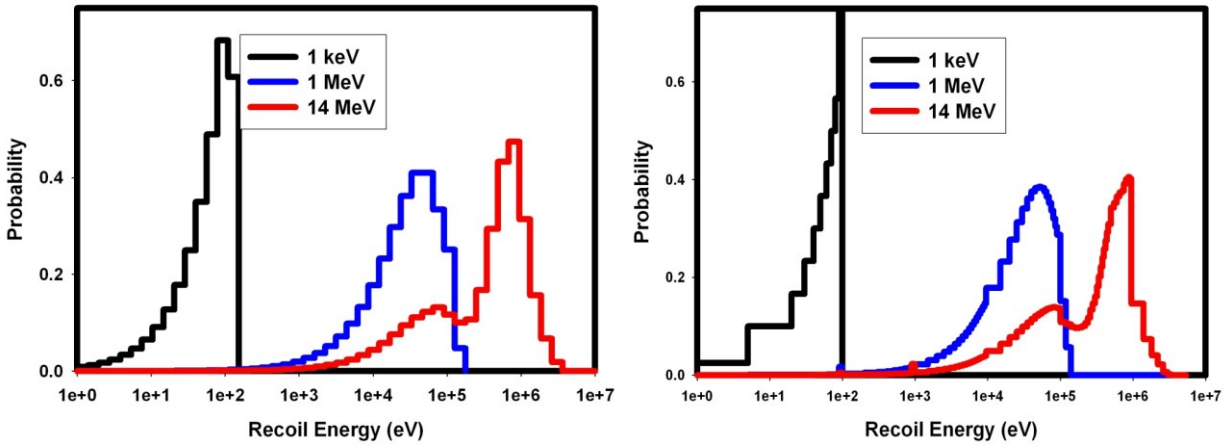

a) EMPIRE Recoil Spectra b) SPECTER Recoil Spectra

Figure 7: Comparison of EMPIRE and SPECTER Monoenergetic Recoil Spectra

5. Decomposition of Displacement Kerma and Component-level Uncertainties

The types of reactions can be divided into four broad categories, as previously discussed/defined in Section 3. Figure 8 shows the relative/fractional energy-dependent contribution of these four categories to the overall displacement kerma. When the TMC approach is used with the 101-sample TENDL random evaluations, the nonlinear uncertainty propagation is properly addressed and Figure 9 depicts the resulting energy-dependent uncertainties in the total displacement kerma and in its four displacement kerma components.

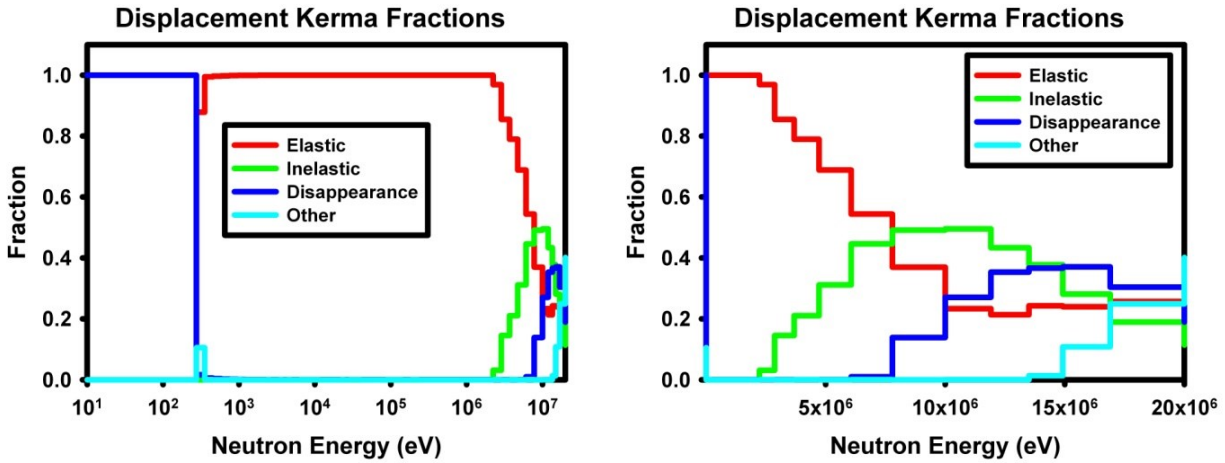

a) Logarithmic Energy View over a Wide Energy Region b) Linear Energy Perspective of High Energy Region

Figure 8: Contribution to the Total Displacement Kerma from Various Contributing terms

In Figure 9 the black curve depicts the uncertainty in the total displacement kerma. While this curve can be differentiated in the figure at high energies, it merges with the uncertainty seen in blue elastic component at mid-energies and then drops to the uncertainty seen in the green disappearance component at thermal energies. The contribution to the disappearance kerma at thermal energies comes entirely from the (n,γ) reaction channel. The abrupt decrease in the red inelastic displacement component uncertainty at an energy of ~2 MeV corresponds to the threshold energy for inelastic scattering events, i.e. 1.77903 MeV for the 1st inelastic channel in ^{28}Si. Below the threshold energy, the cross section is zero and associated standard deviation is also modeled as zero.

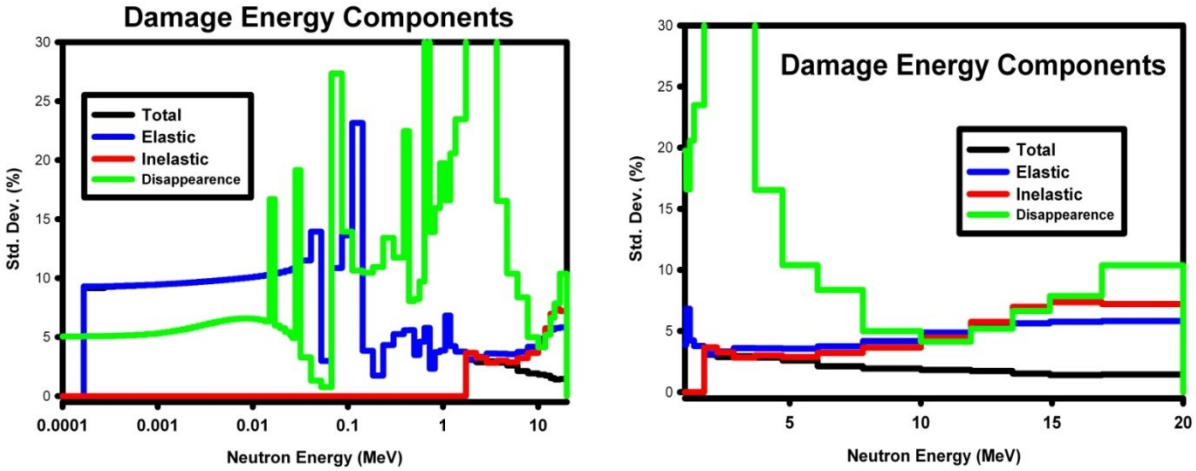

a) Logarithmic Energy Perspective

b) Linear Energy Representation of High Energy Region

Figure 9: Uncertainty from Various Displacement Kerma Components

Inspection of Figure 9 shows a surprising aspect to the uncertainty, namely that the uncertainty in the high energy total displacement kerma produced from this TMC treatment is much less than that obtained if the various reaction components are assumed to be uncorrelated and combined with a weighted root-mean-squared (rms) approach. This implies that the displacement kerma components are strong correlated at high energies. This was a very significant observation and it was confirmed by a more detailed investigation of the individual sample draws used in the analysis. A detailed analysis of a 9-element subsample of the 101 random TENDL library sample clearly showed, in each sample, a strong anti-correlation between the high energy displacement kerma components which enabled this small relative uncertainty in the total kerma while supported the larger uncertainty for each of the component categories. This implies that there are strong correlations in the nuclear physics models that are captured in the TENDL/TALYS code, which is an expected result when one considers the nature of the input parameters to the nuclear physics models, e.g. the optical model parameters, which generated the TALYS uncertainty. The observation of this strong high energy correlation indicates that this type of uncertainty analysis in the displacement kerma requires a treatment such as the TMC approach used here in order to address the correlation between reaction channels. Few approaches to uncertainty propagation, other than the TMC approach used here, can address the nonlinear propagation of correlated uncertainty contributions.

6. Uncertainties Due to "Model Defect"

The analysis in the previous section addressed the uncertainty contribution to the displacement kerma from a parameter variation of the inputs in the underlying nuclear physics models used to generate the nuclear data representations. There is another element of uncertainty that must be captured, that due to "model defect" [14], i.e. the uncertainty in the underlying nuclear reaction models that cannot be captured with accessible model parameter variation. One flag for the presence of a "model defect" contribution to the uncertainty is a difference between the uncertainty elicited by parameter variation and the uncertainty seen in the variation between analysis using state-of-the-art nuclear data evaluation [15].

There are many possible contributors to model defect that should be investigated. One of the most important contributors was expected to be the damage partition model. The above analysis used the damage partition model built into the NJOY-2012 code, which is the Robinson fit [16, 17] to the Lindhard, Scharff, and Schiott (LSS) partition function [18]. The LSS energy partition used a Thomas-Fermi screening function over the Coulomb potential to model the elastic interactions and a non-local free uniform electron gas model for the inelastic electronic scattering. The LSS model assumes the local density approximation (LDA); that is, material can be represented as a "structureless" solid, referred to as a "lattice gas". Thus the LSS theory does not account for any crystal effects upon the lattice displacement nor does it account for any complications due to the cascade development [19]. The Lindhard model is limited to energies less than about $24.8*Z^{4/3}*A$ (in keV) [20, 21] where A is the atomic mass of the incident ion and Z is the atomic number of the incident ion. In iron this limitation translated to a maximum permissible ion energy of 107 MeV. In silicon, the limitation translates to a maximum permissible ion energy of 23 MeV. These limitations are relevant when considering the equivalence of charged particle induced damage and neutron-induced damage. This energy limitation is related to the LSS assumption that the stopping power is related to the ion velocity. When collisions impart more than the Bohr velocity to the lattice recoils, $e^2/\hbar$ = ~25 keV/amu, this assumption is violated [22, 23]. It must be noted that while this energy limitation applies to the Lindhard LSS model, codes such as MARLOWE [22] that incorporate the LSS model often are augmented to also use the semi-empirical Ziegler potential to address "the transition from the Lindhard to the Bethe regime governed by Rutherford scattering" [24] through the use of this "heavy ion scaling rule" to capture the stopping poser of atoms with energies greater than 25 keV per amu. In MARLOWE, this has been implemented by several different people and is typically accomplished by augmenting the MARLOWE code with new interaction potentials based on the ZBL potential [24, 25, 26].

Recent work by Akkerman [27], has used updated potentials for silicon to derive a new energy partition in silicon valid for recoil ion energies < 500 keV. Akkerman used the Ziegler, Biersack, and Littmark (ZBL) [28] potential for the elastic Coulomb scattering and used a combination of a local (impact parameter dependent) model and a non-local model for the inelastic ion-atom scattering. Their results used a displacement threshold energy of 21 eV for silicon.

Figure 10a compares the Robinson fit to the LSS damage partition function and this more recent Akkerman partition function. The Akkerman partition function results in about a 15% high lattice displacement damage component for low energy incident particles. At high energy the difference between the Akkerman and Robinson energy partition functions is not clearly depicted in Figure 10a due to the small values of the damage energy. To clarify the comparison and to indicate the fractional difference at high recoil ion energies, Figure 10b shows the ratio between the two damage partition functions. This figure shows that the Akkerman partition results tend to smaller damage energies at higher energies (> 100 keV), with an 8% lower value for 2 MeV incident silicon ions, and then the ratio tends back to higher values again with the damage energy being about 8% higher than unity for 100 MeV silicon ions. Future work will investigate how this component of "model defect" translates into any increased uncertainty in the total neutron displacement kerma.

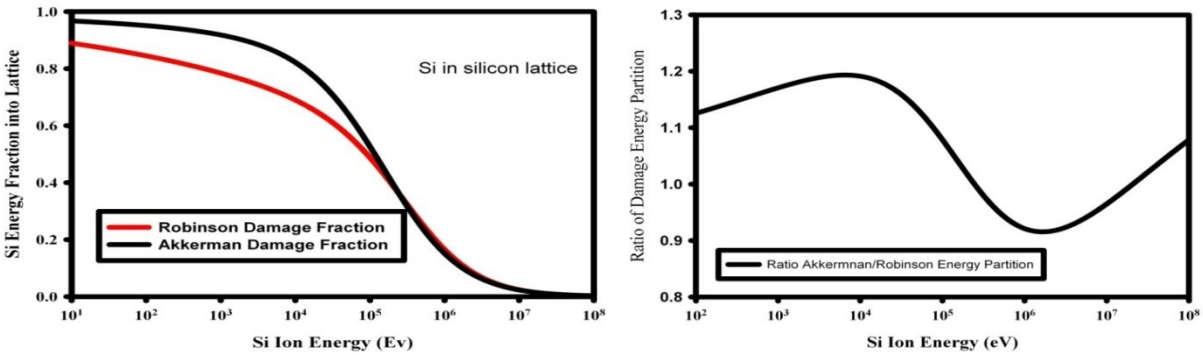

c) Energy-dependent Damage Partition Functions d) Ratio of Damage Partition Functions

Figure 10: Comparison of Robinson and Akkerman Damage Partition Functions

Another aspect of "model defect" applies to the selection of the potential used to generate the damage partition function. Some aspects of this variation were captured as part of the above comparison between the LSS (Thomas-Fermi potential) and the Akkerman (ZBL potential). When the MARLOWE code is used to isolate just this dependence on the ion interaction potential, Table 1 shows the variation, as a function of the recoiling silicon atom, between the LSS partition and the MARLOWE binary collision approximation (BCA) modelling of the partition with the Moliere and ZBL potentials. The variation in potential is seen to induce changes in the partition of energy into ionization of about 10% for silicon ion energies less than ~50 keV, decreasing to less than 1.5% for ion energies greater than 500 keV. When one looks at the percentage of energy into displacement rather than into ionization, the change is less than 7% for energies less than 100 keV, decreases to less than 4% for energies through 1 MeV, then jumps to about 30% for energies of 10 MeV.

Table 1: Comparison of Effect of Various the Interaction Potentials on the Partition of Damage into Ionization in Silicon.

Silicon Ion Energy (keV)	MARLOWE BCA Code Using:		LSS
	Moliere Potential	ZBL Potential	
30 keV	29.1	32.9	38.5
50 keV	35.1	38.9	43.3
100keV	44.0	47.8	53.0
500 keV	72.0	72.9	74.5
1 MeV	82.7	82.7	83.5
10 MeV	94.7	95.0	97.6
Entries show percentage of energy going into ionization			

Another parameter whose variation was not considered in the above analysis is the uncertainty in the displacement threshold energy. The latest ASTM E722-14 standard [4] recommends using a value of 20.5 eV. Changes here may not have any effect if the displacement kerma is defined in a manner that only considers displacement and ionization terms [29]. Changes in the displacement threshold energy will have an effect on the number of displaced atoms, also called the dpa. These changes in the dpa are expected to provide a variation that is totally correlated over the energy region.

7. Conclusions and Future Work

The above discussion has captured the work performed at Sandia National Laboratories over the past year in support of this IAEA Cooperative Research Project (CRP) focused on an examination of primary radiation damage in semiconductor materials, and, in particular, on quantifying the energy-dependent uncertainty in the silicon displacement kerma. Over the next year this work will be expanded to address more areas of "model defect" in the parameter variation uncertainty contribution that was captured in this work with silicon. In particular, the influence of the uncertainty in the energy partition function will be placed on a solid mathematical foundation using the TMC approach. We will also address the need to add an empirical uncertainty term to address deviation between the TMC covariance matrix and the variation seen between displacement kermas derived from different state-of-the-art silicon evaluations. Work will also start to expand this analysis to address the uncertainty in the displacement kerma in GaAs and to address an approach for addressing the deviation between the displacement kerma and the displacement damage seen in GaAs electronic devices (i.e. for a damage metric related to the change in minority carrier lifetime).

References

1. G.C. Messenger, J.P. Spratt, "The effects of neutron irradiation on silicon and germanium", *Proc. IRE*, Vol. 46, pp. 1038-1044, 1958.
2. G.C. Messenger, M.S. Ash, The Effects of Radiation on Electronic Systems, Van Nostrand Reinhold Company, New York, NY, 1986, p. 103.
3. V.A.J. Van Lint, T.M. Flanagan, R.E. Leadon, J.A. Naber, V.C. Rogers, Mechanisms of Radiation Effects in Electronic Materials, Volume 1, Wiley-Interscience Publications, 1980.
4. ASTM E722-09, Standard Practice for Characterizing Neutron Fluence Spectra in Terms of an Equivalent Monoenergetic Neutron Fluence for Radiation-Hardness Testing of Electronics, ASTM International, West Conshohocken, PA, 2014.

5. ASTM E1855-10, Standard Test Method for Use of 2N2222A Silicon Bipolar Transistors as Neutron Spectrum Sensors and Displacement Damage Monitors, , ASTM International, West Conshohocken, PA, 2014.
6. J.G. Kelly, and P/J. Griffin, "Comparison of Measured Silicon Displacement Damage Ratios with ASTM E-722-87 and NJOY Calculated Damage," *Proceedings of the Seventh ASTM-EURATOM Symposium on Reactor Dosimetry*, Strasbourg, France, Aug. 1990, p. 711, Kluwer Academic Publishers, Boston, (1992).
7. P.J. Griffin, J.G. Kelly, T.F. Luera, A.L. Barry, and M.S. Lazo, "Neutron Damage Equivalence in GaAs," *IEEE Transactions on Nuclear Science*, NS-38, No. 6, 1991.
8. http://cyclotron.lbl.gov/
9. A.J. Koning, D. Rochman, "Modern Nuclear Data Evaluation with the TALYS Code System," *Nuclear Data Sheets*, Volume 113, pp. 2841-2934, December 2012.
10. R.E. MacFarlane, A.C. Kahler, D.W. Muir, R.M. Boicourt, The NJOY Nuclear Data Processing System, Version 2010, LA-UR-27079, Los Alamos National laboratory, Los Alamos, NM, December 20, 2012.
11. A.J. Koning, D. Rochman, "Towards sustainable nuclear energy: Putting nuclear physics to work," *Annals of Nuclear Physics*, Volume 35, pp. 2024-2030, November 2008.
12. M. Herman, R. Capote, B.V. Carlson, P. Oblozinsky, M. Sin, A. Trkov, H. Wienke, V. Zerkin, "EMPIRE: Nuclear Reaction Model Code System for Data Evaluation", *Nucl. Data Sheets*, 108 (2007) 2655-2715.
13. L.R. Greenwood, R.K. Smither, SPECTER: Neutron Damage Calculations for materials Irradiations, Argonne National Laboratory, report ANL/FPP/TM-197, January 1985.
14. Oakley, Probability is Perfect, but We Can't Elicit it Perfectly, *Reliability Engineering and System Safety*, Vol. 85, pp. 239-248, October 2002.
15. M.B. Danjaji, P.J. Griffin, "Uncertainty of Silicon 1-MeV Damage Function" Proceedings of the 9th International Symposium of Reactor Dosimetry, World Scientific, 1998, pp. 611-618
16. M.T. Robinson, O.M. Torrens, "Computer Simulation of Atomic-Displacement Cascades in Solids in the Binary-Collision Approximation," *Physical Review* B, Vol. **9**, pp. 5008-5024, June 1974.
17. M.T. Robinson, "Binding Energy Effects in Cascade Evolution and Sputtering," *Nuclear Instrumentation and Methods in Physics Research* B 115, pp. 549-553, 1996
18. J. Lindhard, M. Scharff, H. Schiott, "Range Concepts and Heavy Ion Ranges," *Mat. Phys. Medd. Dan. Vld. Selsk*, Vol. **33**, pp. 1-40, 1963
19. J. Helm, Reactor Vessel Irradiation Damage: Absorbed Dose Estimates, Columbia University, published by Electric Power Research Institute, report EP 89-21, second edition, October **18**, 1993
20. M.J. Norgett, M.T. Robinson, I.M. Torrens, "A Proposed Method of Calculating Displacement Dose Rates," *Nuclear Engineering and Design,* Vol. 33, pp. 50-54, 1975.
21. T. Robinson, The dependence of neutron irradiation damage in solids, R.N.E.S. nuclear fusion reactor conference at Culham Laboratory, September, 1969, Nuclear Fusion Reactors, pages 364-378, British Nuclear Energy Society, London, 1970.
22. F. Mota, C.J. Ortiz, R. Vila, "Primary Displacement Damage Calculation Induced by Neutron and Ion Using Binary Collision Approximation Techniques (MARLOWE code)", presentation to the First Technical Meeting on Primary Radiation Damage, IAEA Vienna, October 1-4,2012
23. J.F. Ziegler, The Stopping of Energetic Light Ions in Elemental mater, *J. Appl. Phys*. / *Rev. Apply. Phys*. Vol. 85, pp. 1249-1272, 1999.
24. M. Hou, C.J. Ortiz, C.S. Becquart, C. Domain, U. Starkae, A. Debacker, "Microstructure evolution of irradiated tungsten: Crystal effects in He and H implantation as modelled in the Binary Collision Approximation," *Journal of Nuclear Materials*, Vol. **403**, pp. 89-100, 2010.
25. M.T. Robinson: MARLOWE Binary Collision Cascade Simulation Program, Version 15b, A Guide for Users, December 5, 2002.
26. M. Robinson, "Computer simulation studies of high-energy collision cascades1", *Nuclear Instruments and Methods in Physics Research Section* B Vol. 67, 1992.
27. A. Akkerman, J. Barak, "New Partition Factor Calculations for Evaluating the Damage of Low Energy Ions in Silicon," *IEEE Transactions on Nuclear Science*, Vol. 53, pp. 3667-3674, December 2006
28. J.F. Ziegler, J.P. Biersack, U. Littmark, The Stopping and Range of Ions in Solids, Pergamon Press, Inc., New York, 1985.
29. P.J. Griffin, Relationship between Metrics Used to Represent Displacement Damage in Materials, Sandia National Laboratories, Albuquerque NM, report SAND2014-3341, April 2014.

Improved spectrometer for the (n,α) reaction study and first experimental results,

V. Khryachkov, A. Gurbich, I. Bondarenko, T. Khromyleva, P. Prusachenko, A. Sergachev

Institute for Physics and Power Engineering
Obninsk, Russia

Radiation resistance of materials is mainly determined by helium/hydrogen-producing nuclear reactions. Especially this problem is actual for construction materials, as they are most commonly used for manufacturing of different mechanisms and units of nuclear power plants. However, in spite of the great practical importance of these elements, according to our literature review, for a number of them, such as isotopes of chromium, iron and nickel, the set of experimental studies on the cross section measurement of the (n,α) reaction is extremely poor and is limited to works performed for neutrons with energies of 14 MeV. The data obtained by different authors for this energy may differ by tens of percents. The experimental data for the neutron energies close to the reactor spectrum are completely absent. This results in the large spread (up to several hundred percents) in the estimates of the cross section energy dependence. Existing differences between evaluations can be eliminated only with the appearance of new experimental data.

Such situation with the experimental data for structural materials is due to the fact that these nuclei are extremely inconvenient for studies by existing methods. The reaction cross sections for charged particles emission are usually small (a few millibarns) and the reaction Q-value is low. The most accurate and widely used method, based on the analysis of gamma-spectra emitted by the daughter nuclei, may not be used in this case since the reaction products are stable. The only way to measure the reaction cross section in this case is a direct measurement of the alpha particles yield from a thin target.

Methods that allow carrying out such measurements must have a high sensitivity and high selectivity to the products of the studied reaction. To solve this problem, we apply a method based on the usage of an ionization chamber with a Frisch grid and solid target, located on the cathode. This technique has been successfully used in laboratories in Dubna [1], Obninsk [2] and Japan [3] for the measurement of different reaction cross sections. However, this method is not free from drawbacks: in some cases the background of the chamber electrode is much greater than the effect of the investigated thin spectrometric target.

A new spectrometer was designed and created, wherein a solid target made of the investigated structural material is placed in the middle of the ionization chamber sensitive volume. Figures 1 and 2 illustrate the design and target location. For this target arrangement, usage of digital techniques for evaluation of anode and cathode signals makes possible to distinguish events happened at the chamber cathode, in the working gas and on the surface of the investigated layer. Indeed the drift time of the most remote from the anode electrons depends from the place of particle birth in a cathode-grid gap, when the drift velocity is constant (see Fig. 3).

A block diagram of the electronics used in the experiment is shown in Fig. 4. Signals from the anode and cathode of the ionization chamber, after their amplification, fed to the digitizer which transformed analog signals to the digital form.

The typical shape of digital signals received from the spectrometer is shown in Fig. 5. The digital signals were stored on the hard disk of a computer for further processing.

This way of signal accumulation and processing allows determining a number of parameters of the recorded event at once. During the processing the signal amplitude, the drift of electrons to the anode, the length of the projection of the particle track on the axis of the camera were determined.

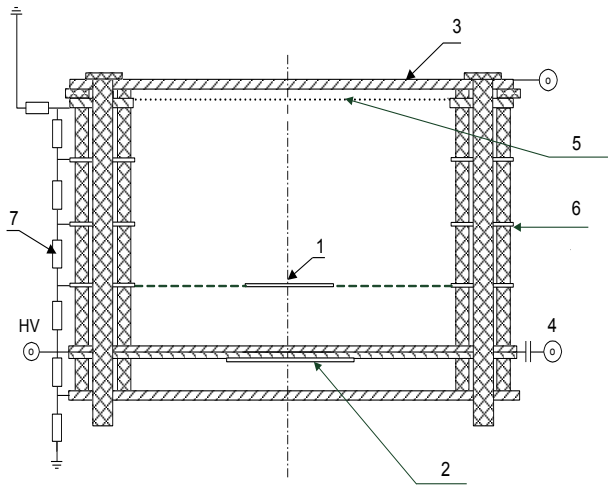

Fig. 1. Schematic detector design. 1 - solid target; 2 - ^{238}U target; 3 - IC anode; 4 - common cathode; 5 – Frisch greed; 6 - guard electrodes; 7 - divider.

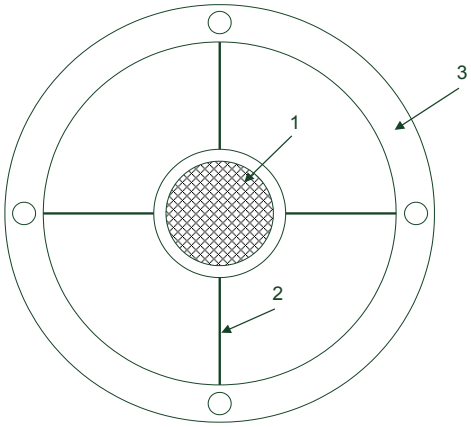

Fig. 2. The target scheme. 1 - solid target, 2 - golden threads, 3 - guard ring.

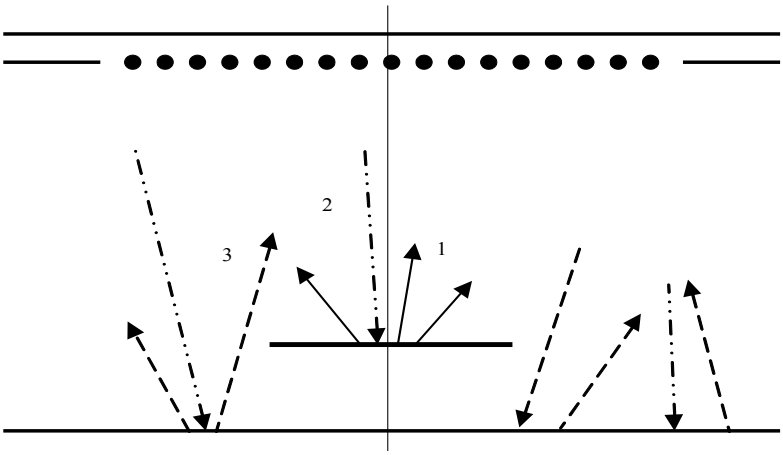

Fig. 3. Scheme of α-particle tracks, which can be realized in the ionization chamber irradiated by fast neutrons. 1 - "cathode" particles, 2 - "false cathode" particles, 3 - "gas" particles.

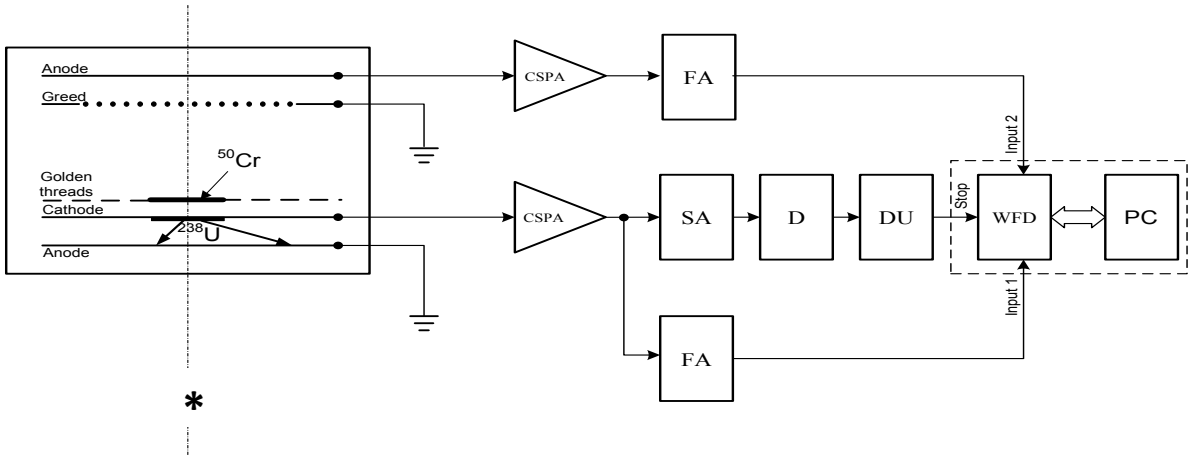

Fig. 4. Block diagram of the detector and electronics. CSPA - charge sensitive preamplifier; SA - spectrometric amplifier; D - discriminator; DU - delay unit; WFD - waveforms digitizer; FA - fast amplifier.

Figure 6 shows the two-dimensional spectrum, where the X-axis is amplitude of the anode signal, the Y-axis is the electron drift time. From the figure, it is clear that all of the events are divided into 3 groups - events that took place at the cathode (upper part of the spectrum), events that took place in the studied target (the middle part of the spectrum), and events happened in the working gas (the lower part of the spectrum). By choosing the window for "electron drift time" parameter we can select events originated on the target (shown on the Fig. 6 by the dashed line). This method allows us to suppress significantly the contribution of background reactions, occurring on the structural elements of the camera and in its working gas.

Figure 7 shows the two-dimensional spectrum, where the X-axis is the amplitude of the anode signal and the Y-axis is the rise time of the anode signal. The rise time parameter of the anode signal allows us to make separation of the particles of different type. Indeed the rise time parameter of the anode signal is directly connected with the particles path projection on the symmetry axis of the camera. At the same amplitude of the anode signal (particle energy), the lighter particles will have the longest range.

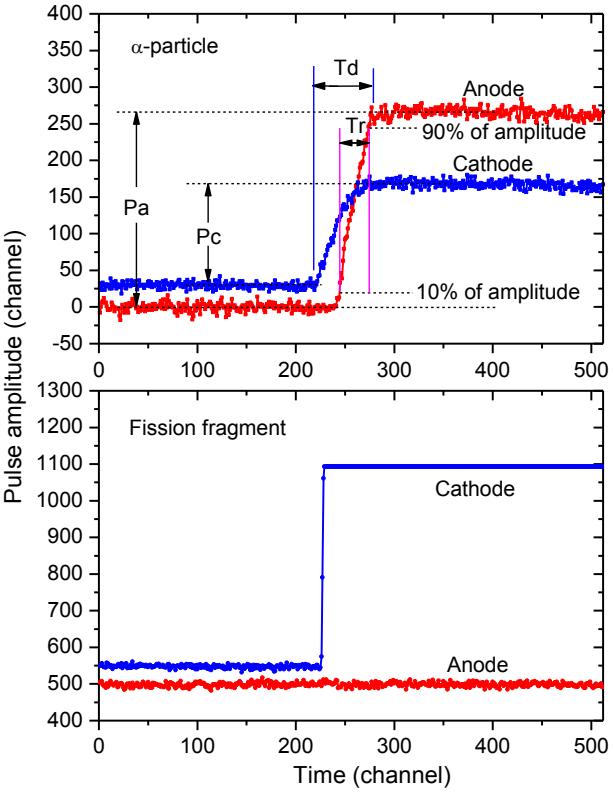

Fig. 5. Typical signals from the spectrometer. Figure at the top – α-particle in the main chamber. Figure at the bottom - fission fragment in a chamber without a grid.

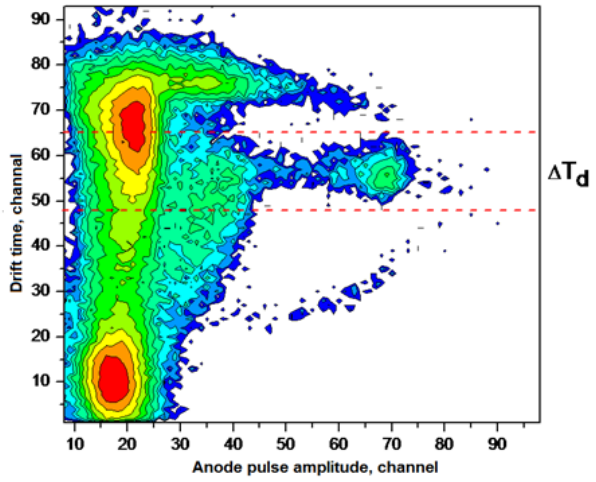

Fig. 6. A two-dimensional spectrum, where the X-axis is the amplitude of the anode signal, the Y-axis is the electrons drift time obtained after background suppression.

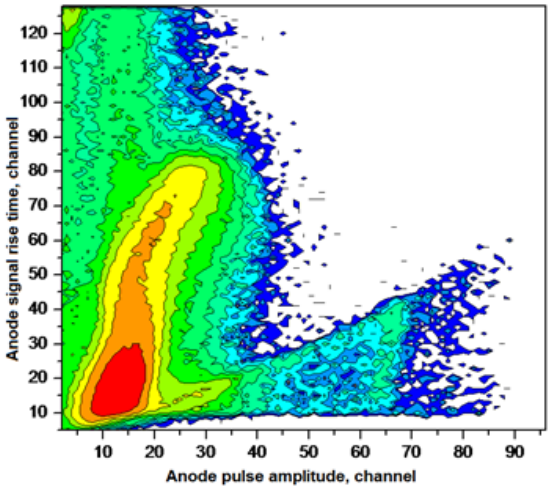

Fig. 7. A two-dimensional spectrum, where the X-axis is the amplitude of the anode signal, the Y-axis is the rise time of the signal obtained for neutron energy of 6.5 MeV.

In Figure 7 we can see a group of particles with short range (α-particles) and with long range (protons and electrons). For α-particles (due to their short range in the gas) there is a small value of the "rise time of the anode signal" parameter. Cutting particles with large values of the rise time of the anode signal we discriminate events caused by the particles other than α-particles. This way of selection of events allows to reduce the background and to distinguish the events corresponding to the investigated reaction.

Traditionally, the electrodes of the ionization chamber are made of stainless steel. This material is corrosion resistant and it allows achieving a good vacuum in the chamber. However, to study the (n,α) reaction of iron, chromium and nickel isotopes such electrode is obviously not suitable as it contains incomparably greater amount of studied nuclei than in a thin spectrometer target. To solve this problem cadmium covers were used, they closed the side of the electrodes that faced the sensitive volume of the chamber.

The excitation functions of α-production for natural iron and cadmium are shown in Figure 8. The figure shows that use of cadmium can significantly reduce the background caused by electrodes in the whole range of interest-energy neutrons.

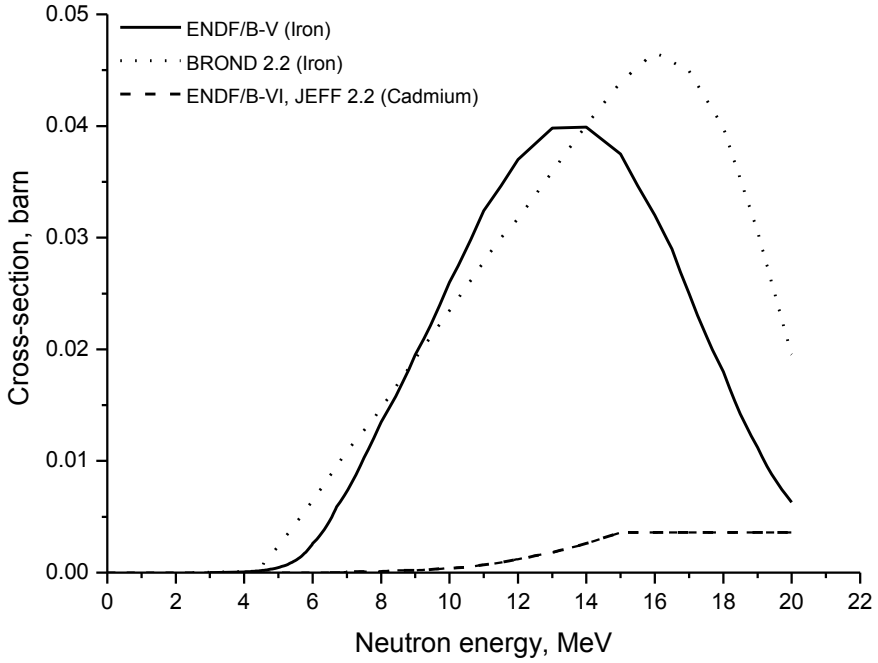

Fig. 8. Theoretical estimates of the cross section of (n,α) reaction on natural iron and cadmium.

Detailed studies of the excitation function of the reaction $^{50}Cr(n,\alpha)^{47}Ti$ in the neutron energy range from 4.5 to 7.2 MeV were performed with the use of the developed spectrometer. The results are shown in Figure 9. It should be noted that the results are in a good agreement with the data given in [3]. For the evaluated data given in the different libraries there is a huge discrepancy. Our data are in satisfactory agreement with estimates given by the library JENDL-4.0 and BROND-3, and disagree significantly with the ENDF/B-VII.1 evaluation.

Figure 10 shows the results of measurements of the cross section for the reaction $^{52}Cr(n,\alpha)^{49}Ti$ carried out in IPPE. The experimental data of other authors for this energy region do not exist. The closest cross sections were predicted by the ENDF/B VII.1 library. Data of other libraries are significantly lower than experimentally observed values.

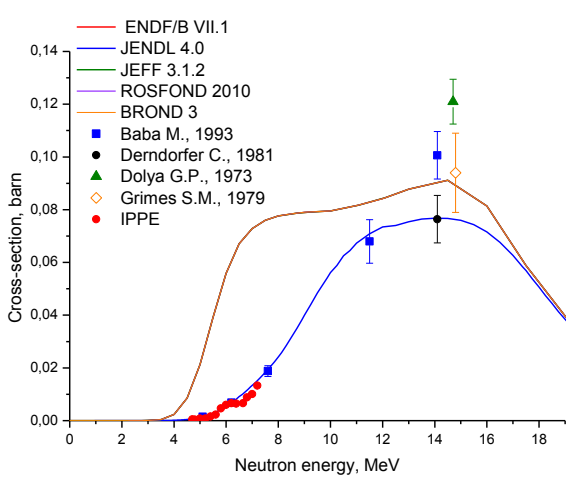

Fig. 9. The cross section of the reaction $^{50}Cr(n,\alpha)^{47}Ti$ compared with evaluated data libraries ENDF/B-VII.1, JENDL-4.0, JEFF-3.1.2, ROSFOND-2010 and BROND 3 and the experimental data of other authors.

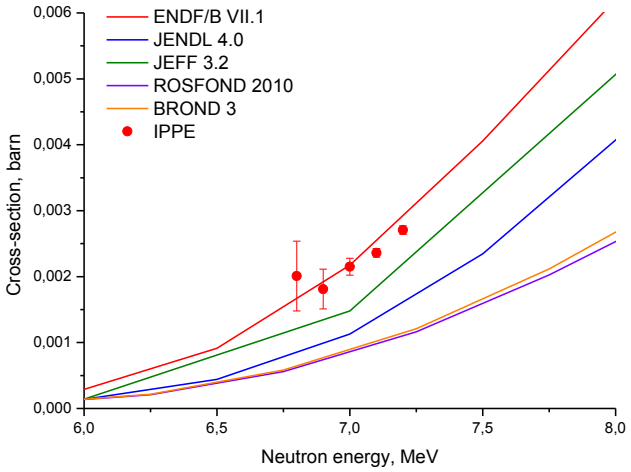

Fig. 10. The results of the measured cross section of the $^{52}Cr(n,\alpha)^{49}Ti$ compared with evaluated data libraries ENDF/B-VII.1, JENDL-4.0, JEFF-3.1.2, ROSFOND-2010 and BROND-3.

Data for ^{50}Cr and ^{52}Cr were obtained for the targets evaporated on a thick gold substrate, the mass of studied materials was known. For a number of isotopes, that interested us, we had the samples in the form of thin self-sustaining films, exact mass of which was unknown.

In this case, the thickness of self-sustaining iron and chromium targets (number of atoms per square centimeter) was measured by Rutherford backscattering of protons. The experimental scheme is shown in Fig. 11. The error of target thickness measurement with the help of this method does not exceed 7 - 8%, it is determined by the accuracy of the detector solid angle measurement and the charge of the particles passed through the target. By means of this method, the homogeneity of the target can be determined as well as its thickness.

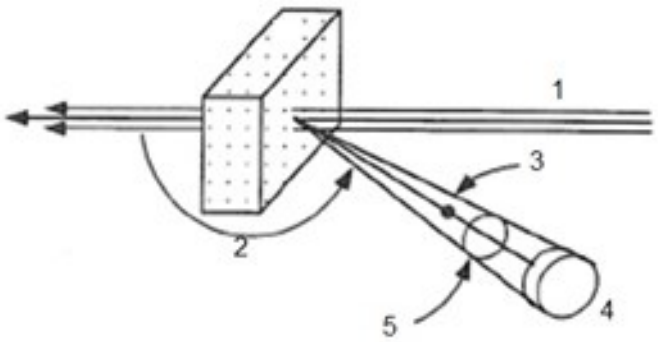

Fig. 11. Experimental set-up for determination of number of nuclei in the solid target: 1 - incoming particles, 2 - scattering angle, 3 - scattered particle, 4 - detector, 5 - solid angle of the detector.

This method was used to determine the number of atoms in a target made of ^{54}Fe. For this target the preliminary measurements of the cross section of $^{54}Fe(n,\alpha)^{51}Cr$ were made. The measured results are shown in Figure 12. For this reaction, there are a number of experiments carried out with the help of the activation method, their results are in a good agreement with each other. That allows us to use the reaction as a standard to confirm the correctness of the procedures of determining the number of nuclei in the target and the number of registered events. As seen in Figure 12, our data coincide with the data of other authors, that allows us to make a conclusion about the correctness of the entire process of the cross-section determining of the studied reaction.

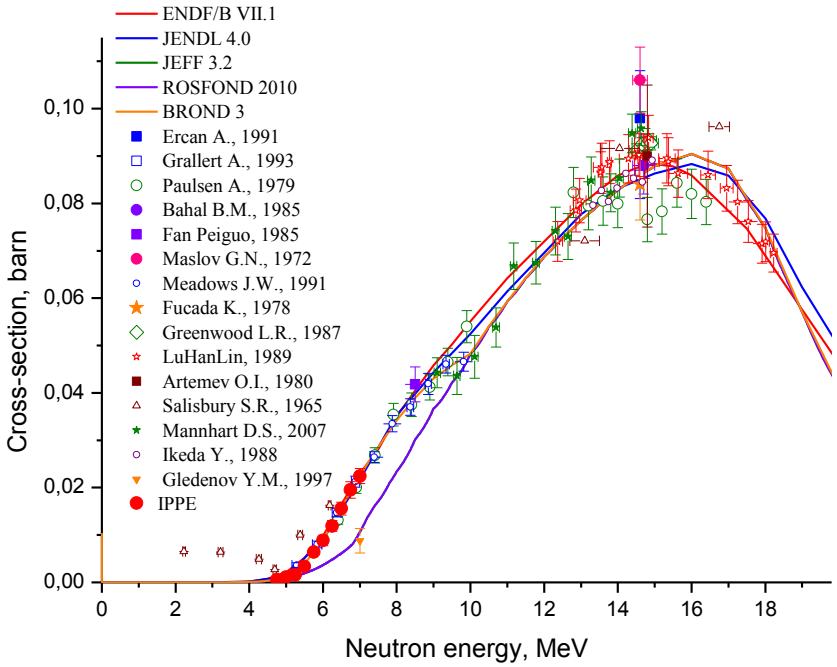

Fig. 12. The results of the measured cross section for reaction $^{54}Fe(n,\alpha)^{51}Cr$ in comparison with the evaluated data libraries ENDF/B-VII.1, JENDL-4.0, JEFF-3.1.2, ROSFOND-2010 and BROND-3 and the experimental data of other authors.

Over the past year the spectrometer of the (n,α) reaction products has been modified. The aim of the modernization was to make it possible to work with thin solid targets of structural materials and to reduce the detector's background. The spectrometric layers were made of a number of isotopes and method of the Rutherford backscattering was used to determine their masses.

The measurements of the (n,α) reaction cross section for ^{50}Cr and ^{52}Cr were made. The first experimental results for the ^{54}Fe target were obtained.

Plans for the second year of the investigation:

- measurement of the number of nuclei in solid targets made of ^{57}Fe and ^{53}Cr by means of the beam ion scattering method on the investigating target;
- measurements of the (n,α) reaction cross section for ^{57}Fe and ^{53}Cr;
- analysis of the experimental data uncertainties;
- preparation of a detailed plan of works for the third year of CRP project.

References

1. Y.M. Gledenov, M.V. Sedysheva, G. Khuukhenhuu et al. "Study of the fast neutron induced (n,α) reaction for middle-mass nuclei", Int. Conf. Nucl. Data for Sci. & Techn., Trieste 1997, v. 1, p. 514
2. A.A. Goverdovskiy, V.A. Khryachkov, V.V. Ketlerov et al. "(n,α) reaction studies using a gridded ionization chamber", Int. Conf. on Nucl. Data for Sci. and Techn., Gatlinburg 1994, v. 1, p. 117
3. M. Baba, N. Ito, I. Matsuyama et al. "Measurement of double-differential (n,α) cross sections of Fe, Ni and ^{50}Cr for 4.5 – 14.1 MeV neutrons", Int. Conf. Nucl. Data for Sci. & Techn., Gatlinburg 1994, p. 94

Generation of justified and complete nuclear data and associated uncertainties for material damage applications - gas-production cross-sections and their uncertainties for ^{59}Ni and their consequences for stainless steel,

P. Helgesson and H. Sjöstrand

Department of Physics and Astronomy, Uppsala University
Uppsala, Sweden

Background

In the work for this CRP, we will connect macroscopic fuel and aging parameters to the fundamental nuclear physics processes by using the nuclear model code TALYS and the Total Monte Carlo Method (TMC) method [1]. With a TALYS based code package, nuclear data libraries can be produced for the entire nuclide map, with all reaction channels and secondary particle production. This so called TENDL library is in that respect superior to classical libraries such as ENDF/B-VII and JEFF3.1. Furthermore, the TENDL library has the advantage that it can produce complete covariance information.

We are using and improving the TENDL library to improve basic damage nuclear data, e.g. KERMA, damage energy, dpa- and gas-production cross sections for different structural elements. In order to obtain justified best estimates and uncertainties in damage nuclear data derived from nuclear modeling, a proper calibration of the nuclear data with respect to experimental data is necessary. A rigorous treatment of experimental uncertainties will improve the predictive power of damage modeling.

So far we have investigated ^{59}Ni, since the two-step thermal neutron reaction sequence ^{58}Ni(n,γ)^{59}Ni(n,α)^{56}Fe, (Q_value = 5,1 MeV) results in non-linear He production rates and is an important contribution to the He production in steel in thermal spectrum. The reaction sequence is also an important contribution to the damage energy. We are also investigating the hydrogen producing reaction sequence: ^{58}Ni(n,γ)^{59}Ni(n,p)^{59}Co (Q_value = 1.9 MeV). Currently, existing evaluated data has no uncertainty information, neither for ^{59}Ni(n,α)^{56}Fe, nor for ^{59}Ni(n,p)^{58}Co reactions, in the thermal region. Furthermore, the TENDL evaluation disregards the resonance structure for these reaction types.

Results

One of the main goals is to develop methods that better takes into account the experimental differential data to calibrate the nuclear data and its uncertainties and to apply these methods for reactor relevant structural materials. The TMC method for nuclear data ND uncertainty propagation has been subject to some critique because the nuclear reaction parameters are sampled from distributions which have not been rigorously determined from experimental data. We are addressing this by weighting random ND files with likelihood function values computed by comparing the ND files to experimental data, using experimental covariance matrices generated from information in the experimental database EXFOR and a set of simple rules. The results are presented in [2, 3], where, inter alia, ^{56}Fe, is investigated. The results have so far not been propagated to damage parameters, however.

To improve the He production prediction and to provide nuclear data uncertainty estimates, new ^{59}Ni cross section data has been developed. As opposed to existing evaluated data (for nuclides in general) the helium and hydrogen production cross sections have been produced using relevant resonance parameters using R-matrix theory with the Reich-Moore approximation. The lack of well documented measurements on these cross sections in the resonance region however makes the actual values of these resonance parameters very uncertain. The cross-sections are generated from average unresolved resonance parameters and sampled with a high uncertainty, after which they are adjusted to the experimentally known thermal cross sections and their uncertainties. In this particular case we have used the values in the Atlas of resonances [4] for the thermal cross sections. Thus, this new cross section data is more complete and has physically motivated uncertainties. The cross-sections will soon be published in ENDF-6 format, including so called random files, for usage by the nuclear community.

The distributions of some of the cross sections in the current random files are shown in Figure 1. It should be noted that this is still preliminary data.

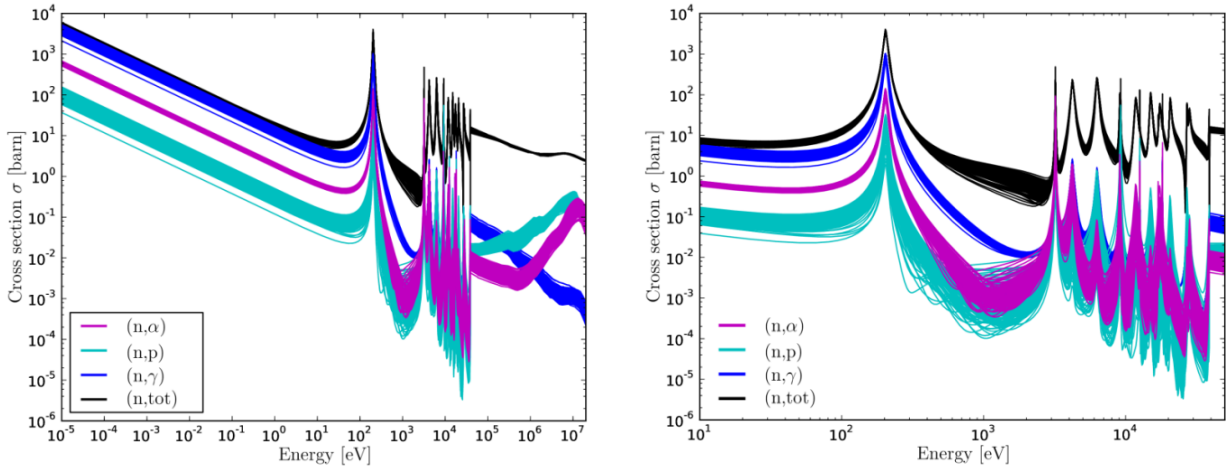

Figure 1. Plot of preliminary random files for the different ^{59}Ni reaction channels. Left: full energy range; right: zoomed at the resonances.

So far, the produced random files only contain pointwise cross sections. In resonance range and below: (n,tot) and (n,γ) are produced using TARES and NJOY-12.32. The gas producing channels (n,α), (n,p) are produced as described above, and (n,el) is obtained by subtracting the absorption reactions from the total cross-section. Finally, (n,tot) is adjusted such that (n,el) $> 10^{-8}$ b.

The random files have been processed with NJOY-12.32. However, it was not possible to directly process the random files with this NJOY version. The number of "particle pairs" used in the LRF = 7 format is limited to 11 (including the compound + gamma-pair) in current versions of NJOY-2012.XX [5]. However, for ^{59}Ni(n,α)^{56}Fe, 22 states of ^{56}Fe are possible and for ^{59}Ni(n,p)^{59}Co, 4 states of ^{59}Co are possible. Including the two particle pairs necessary to describe the neutron and gamma widths, 28 particle pairs are necessary for a full description of the open channels in the resonance range, i.e. more than the allowed number in NJOY. This has been solved by producing partial (n,α) cross sections (to a maximum of 9 levels), which has subsequently been summed up, and the sum has been used for the adjustment to the thermal cross section. An update of NJOY can be helpful to avoid this workaround and a version of the ENDF file that could not be processed has been sent to A. Kahler (who develops NJOY) for further investigation.

In order to check the performance of the random files they have been tested on an MCNP-6 model. The model consists of a cylinder with r = 100 cm and h = 1 cm, containing stainless steel with 69.5% Fe, 19% Cr, 9.5% Ni, and 2% Mn. A surface source at one side of the cylinder was applied with typical LWR spectrum [6]. The ^{59}Ni and ^{58}Ni content was modified to the values in the ^{59}Ni peak in Ref. [7]. The results were compared to He and H production rates in a reference case, i.e., the same model but with natural Ni instead of modified Ni content. It was found that the inclusion of ^{59}Ni increased the helium production rate with a factor of five. The uncertainty on the He production rate due to ^{59}Ni data was estimated to 5.7 +/- 0.2 %. It was also found that there were some discrepancies between the results obtained with these new files and the result which was obtained using ENDF/B-VII.1. In particular, the helium production rate increase was significantly larger using ENDF/B- VII.1 – this can however be explained by a significantly larger thermal (n,α) cross section in ENDF/B- VII.1 (not agreeing with the recommendation in the Atlas of resonances [Mughabghab]).

Planned activities

It is planned to include more differential data for ^{59}Ni(n,α) and (n,p) cross sections, e.g., re-evaluate thermal cross sections including experimental correlations. We also plan to reconsider the distributions for the unknown resonance parameters (URR), e.g. including uncertainty of URR parameters from TALYS.

We aim to apply the data to some more advanced applications, possibly some He-production benchmark. In the planned work we also aim to include transmutation in the simulation, i.e. starting from natural Ni and including the nuclear data uncertainty of other nuclides.

The angular distribution, the emitted spectrum, and the excitation of the residual are important for the damage energy. The quantification of these quantities and their uncertainties will be a priority. We intend to propagate the uncertainty of the ^{59}Ni nuclear data to damage relevant parameters, such as damage energy, KERMA, and PKA-spectra.

Finally, contributions from other isotopes, such as the reactions in ^{55}Fe (via capture in ^{54}Fe), to the He production in the thermal region may be investigated.

Conclusions

TENDL and the TMC method have a great potential to address damage relevant macroscopic quantities. We are working on improving TENDLs calibration against experimental data.

The two-step thermal neutron reaction sequence, ^{58}Ni(n,γ)^{59}Ni(n,α)^{56}Fe results is an important contribution to the He production in steel in thermal spectrum and can be an important contribution to the damage energy. We have performed a preliminary evaluated the ^{59}Ni(n,α)^{56}Fe and ^{59}Ni(n,p)^{58}Co reactions and their uncertainties using the TMC method. Random files have been produced and processed with NJOY-2012.32.

The He production rate in stainless steel in a thermal spectrum has been determined using MCNP. Its uncertainty has been estimated to 5.7% . More calibration against experimental data is planned.

Acknowledgment

The performed work is part of a research project (MÅBiL) in collaboration with the main stakeholders in the Swedish nuclear sector with the aim to improve nuclear materials for LWR. We acknowledge the funding from Ringhals AB, Forsmarks Kraftgrupp AB, OKG AB and Westinghouse.

References

[1] A. Koning and D. Rochman, Nucl. Data Sheets 113, 2841 (2012)
[2] P. Helgesson, H. Sjöstrand, A. Koning, D. Rochman, E. Alhassan, S. Pomp, Incorporating experimental information in the TMC methodology using file weights, Nuclear Data Sheets, Volume 123, 214–219, 2015
[3] P. Helgesson, H. Sjöstrand, A.J. Koning, J. Rydén, D. Rochman, E. Alhassan, S. Pomp, *Including experimental information in TMC using file weights from automatically generated experimental covariance matrices,* submitted to Annals of Nuclear Energy, 2015
[4] S. Mughabghab, *Atlas of Neutron Resonances,* (Elsevier 2006), 5th ed.
[5] Personal communication with A.C. Kahler (NJOY developer), July 2015.
[6] M. Pescarini et al., *ENEA-Bologna Multi-Group Cross Section Libraries for LWR Shielding and Pressure Vessel Dosimetry Applications*, Tech. rep., ENEA (2011)
[7] M. Griffiths, *The Effect of Irradiation on Ni-containing Components in CANDU Reactor Cores: A Review*, AECL Nuclear Review 2 (2013)

Advanced nuclear observables processing for materials sciences and PKA spectra under neutron irradiation: time and spatial variation, and contributions from radioactive decay,

J.-Ch. Sublet and M.R. Gilbert

United Kingdom Atomic Energy Authority, Culham Science Centre,
Abingdon, Oxfordshire, UK

The concept of dpa, whether NRT, ARC or otherwise, is limited in its ability to describe radiation damage. In particular, it does not properly account for the evolution of defects. A complete picture must, desirably, include simulation and modelling of the time evolution in defect structures and population changes. Computational simulations, such as atomistics with molecular dynamics, can simulate the cascade of damage caused by an initial recoil event (the "primary knock-on atom" or PKA) and track subsequent evolution. With modern computers it is now possible to build up a statistical picture of defect creation under cascades as a function of PKA energy, which is then suitable for further modelling (at larger length and timescales) to understand defect evolution and perhaps explain the experimentally observed changes in material character. For the former, atomistic simulations, a more useful direct link is needed to the results of neutron transport simulations – giving a complete picture of the population of PKAs as a function of energy – so-called PKA recoil spectra.

As part of the United Kingdom Atomic Energy Authority's contribution to the CRP, we have used the latest techniques to evaluate up-to-date nuclear data to develop a consistent and robust methodology to produce the complete set of recoil spectra, including the correct differentiation as function of recoiling species, for a given material, whether a single isotope or complex alloy, in a given neutron irradiation field. Additionally, the latest version of the inventory package EASY-II [1] can calculate the time evolution in NRT dpa/year and other damage indices for the complete inventory of nuclides, as well as gas production rates using in-built cross section libraries processed through NJOY heatr and gaspr modules. Uniquely, the full energy dependence of each quantity is properly taken into account.

For example, the figures 1 and 2 below show the cross sections for various gaseous species from Fe-056 and W-186 as well as total dpa cross section for Fe, Fe-56 and W, W183. The high computational efficiency inherent to the current FISPACT-II [2] inventory code in EASY-II [1], together with dedicated libraries [3, 4, 5, 6], has enabled rapid comparison, via simple indices like dpa/year values, dpa/He ratios or above 1 MeV fluence, of different irradiation conditions and/or different materials.

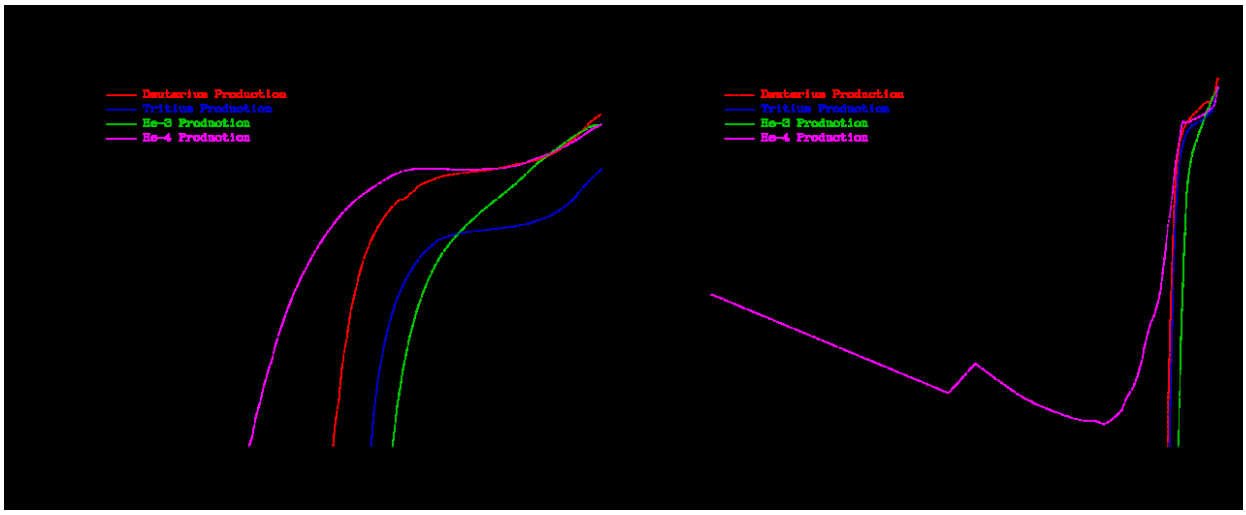

Figure 1: Gas production cross-sections on Fe-56 (left) and W-186 (right).

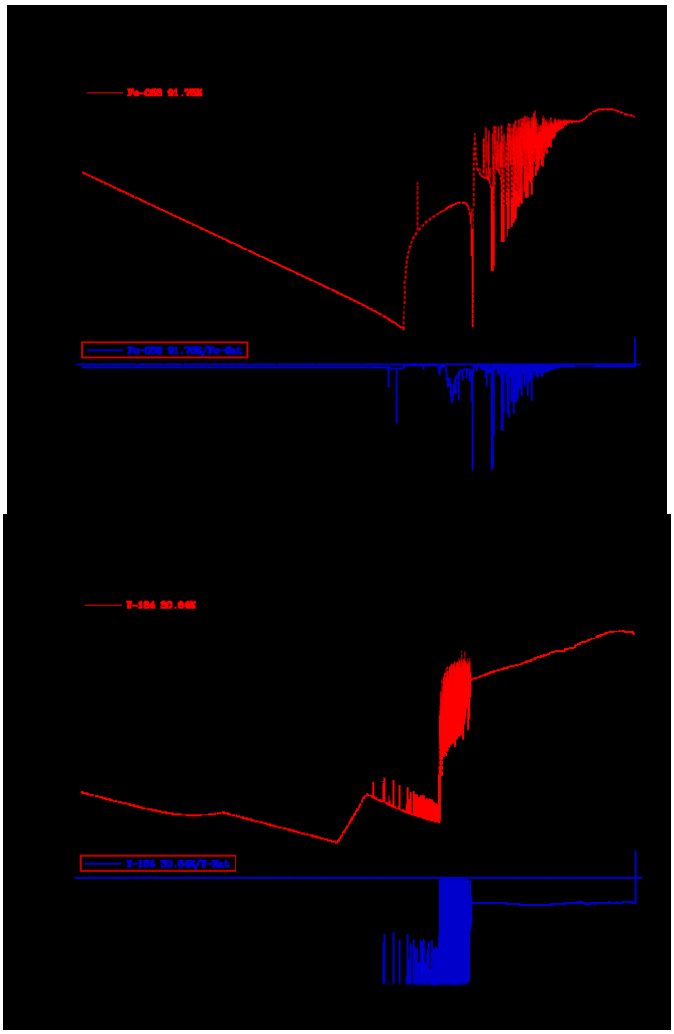

Figure 2: DPA cross-sections on Fe, Fe-56 and W, W184.

Detailed PKA cross section matrices are derived from the TENDL-2014 evaluations and depicted in fig 3 for (n,α) reactions on W-184 and (n,p) reactions on Fe-56. One may notice that the positive Q value (7.3 MeV) for the charged particle (n,α) reaction on W-184 means that the alpha energy can be much higher than the energy of the incident neutron, while the energy on the recoil atom Hf-181 stays below 1 MeV.

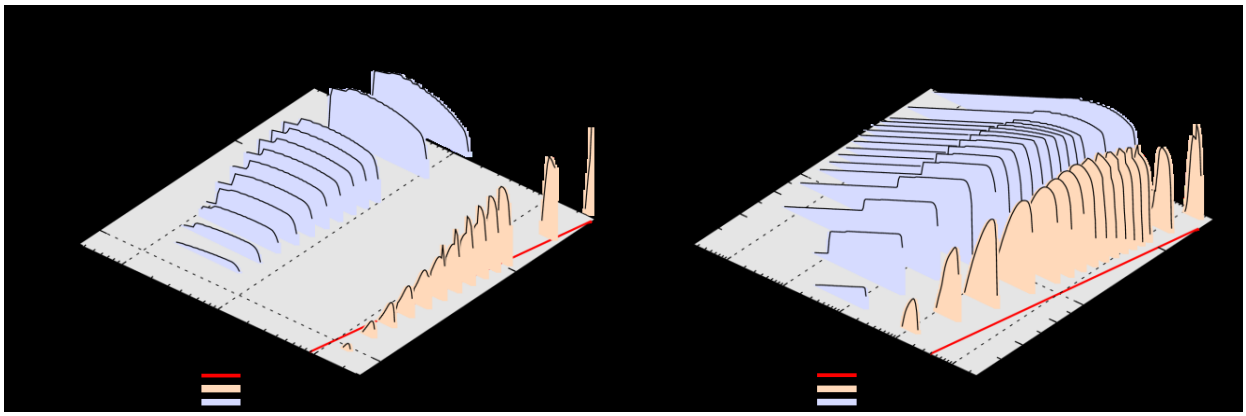

Figure 3. Recoil spectra from (n,a) on W-184 (left) and Fe-056 (right). The distributions in blue are for the heavy recoils – in this case Hf-181 and Mn-056 from W-184 and Fe-056, respectively. The orange distributions are for the recoiling light particles (alphas or protons in these examples).

We have developed a computational routine, called SPECTRA-PKA, which takes these PKA recoil cross section matrices, output from NJOY with a fine group structure (660 groups below 30 MeV), collapses them with a given neutron irradiation field, performs any necessary summing as a function of recoiling nuclide or element over a given set of input parent nuclides (for example the four naturally occurring isotopes of Fe, with appropriate weighting), and outputs the resulting (set of) PKA distributions as a function of energy. Figure 4 shows a typical output from SPECTRA-PKA, for Eurofer irradiated under DEMO fusion first wall (FW) conditions, using both TENDL2014 (left) and ENDFB/VII (right) libraries.

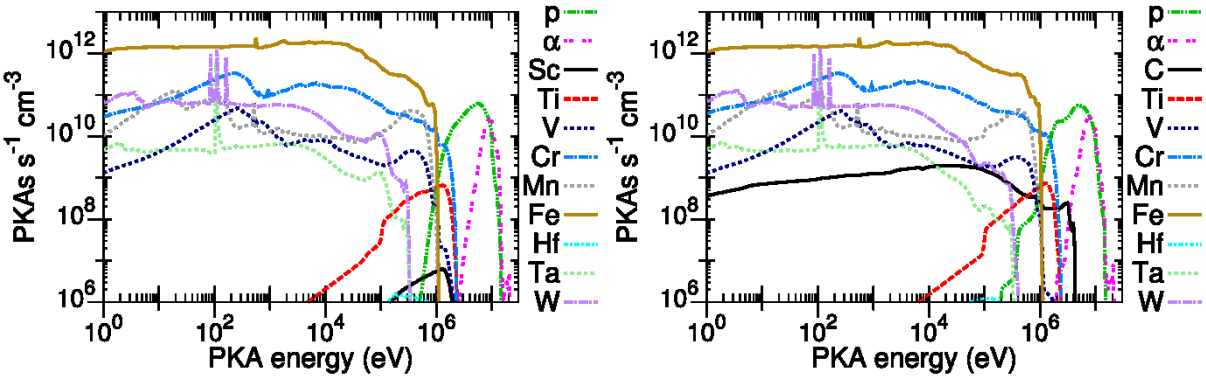

Figure 4. Eurofer elemental-sum PKA spectra under DEMO fusion FW conditions. Left: using TENDL2014 nuclear data; Right: ENDFB/VII.

Figure 4 illustrates the flexibility and robustness of the new computational routines. Eurofer is a fairly complex alloy, but SPECTRA-PKA is perfectly able to read NJOY output for any number of target nuclides (around 15 contribute more than 0.1 atomic % in the Eurofer, which was used as a cut-off for inclusion in the results). This ability to consider complex materials is a significant advance over earlier codes, and can, for example, be used to investigate how the PKA distributions vary as a function of irradiation in a highly transmuting material or irradiation environment (all of the results here are presented for the time, t = 0 composition).

Notice that the results in figure 4 are summed as a function of different recoiling element. In reality the raw results from collapsing the PKA cross section matrices with a neutron irradiation spectrum is a curve for every single channel, which means that even a single nuclide may have multiple curves associated with it – especially in a real material. Thus SPECTRA-PKA merges the data into more useful forms. As well as sums as the sums as a function of element shown in the figure, which might be the starting point for certain atomistic modelling approaches, it also outputs nuclide sums.

Additionally, the total PKA rate distributions are also produced, such as those given in Figure 5 as cumulative functions for several important fusion materials under the same DEMO FW conditions used for Eurofer above. These total distributions might be particularly useful as sampling functions in atomistic simulations where only one atomic species (hopefully the primary one) is considered.

Figure 4 also illustrates that, for this particular material, there is very little difference between the two nuclear library evaluations, other than for some of the minor recoil components (such as carbon).

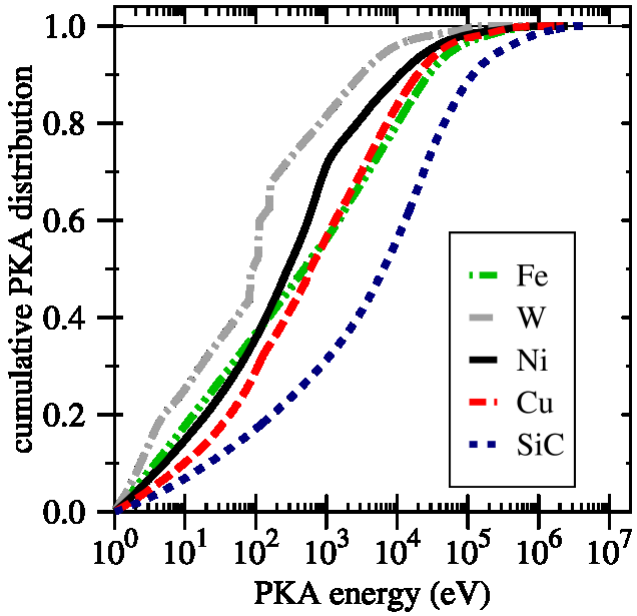

Fig 5. Cumulative total PKA distributions for several materials under DEMO FW conditions using recoil cross sections derived from TENDL-2014.

As part of our contribution to the CRP, SPECTRA-PKA has so far been used to produce a large database of PKA distributions for all naturally occurring elements (up to Bi by mass) under fusion FW conditions. These are part of a much larger nuclear physics handbook [7], but are given special attention in a supplement [8], where the elemental sum distributions are presented in tabular format.

Reference

[1] EASY-II, European Activation System, http://www.ccfe.ac.uk/EASY.aspx

[2] J.-Ch. Sublet, J.W. Eastwood, and J.G. Morgan, "The FISPACT-II User manual" CCFE-R(11)11 Issue 6 (2014), http://www.ccfe.ac.uk/EASY.aspx

[3] A.J. Koning, D. Rochman, S.C van der Marck, J. Kopecky, J. Ch. Sublet, S. Pomp, H. Sjostrand, R. Forrest, E. Bauge and H. Henriksson, "TENDL-2014; TALYS-based evaluated nuclear data library", Available from ftp://ftp.nrg.eu/pub/www/talys/tendl2014/tendl2014.html

[4] M.B. Chadwick et al., "ENDF/B-VII.1 Nuclear Data for Science and Technology: Cross Sections, Covariances, Fission Product Yields and Decay Data", Nuclear Data Sheets Volume 112, Issue 12, December 2011, Pages 2887–2996.

[5] The JEFF team, "JEFF-3.2: Evaluated nuclear data library", http://www.oecd-nea.org/dbdata/jeff , 2014

[6] K. Shibata, O. Iwamoto, T. Nakagawa, N. Iwamoto, A. Ichihara, S. Kunieda, S. Chiba, K. Furutaka, N. Otuka, T. Ohsawa, T. Murata, H. Matsunobu, A. Zukeran, S. Kamada, and J. Katakura, "Jendl-4.0: A new library for nuclear science and engineering," J. Nucl. Sci. Technol., vol. 48, pp. 1–30, 2011

[7] M.R. Gilbert, J.-Ch. Sublet and R.A. Forrest, "Handbook of activation, transmutation, and radiation damage properties of the elements simulated using FISPACT-II & TENDL-2014; Magnetic Fusion Plants" CCFE-R(15)26 (2015), http://www.ccfe.ac.uk/easyii_handbooks.aspx

[8] M.R. Gilbert, J.-Ch. Sublet and R.A. Forrest, "PKA distributions of the elements simulated using TENDL-2014; Magnetic Fusion Plants" CCFE-R(15)26-supplement (2015), http://www.ccfe.ac.uk/easyii_handbooks.aspx

NJOY2012 Summary,
A.C. (Skip) Kahler

Los Alamos National Laboratory
Los Alamos, NM, USA

The NJOY2012 Nuclear Data Processing code system is the latest in a long line of NJOYxx code releases, dating back to 1977.

NJOY2012 was released in December, 2012 and was updated to NJOY2012.8 in August, 2013 and NJOY2012.50 in February, 2015. Code features of interest to this group include gas production and heating/radiation damage calculations. Gas production is calculated in NJOY's GASPR module while heating/radiation damage is calculated in the HEATR module. In Evaluated Nuclear Data File (ENDF) terminology these data are called "derived" quantities as they are not included in an original ENDF evaluation.

Gas production, in NJOY, refers to any reaction that produces one or more of a proton, deuteron, triton, helion (^{3}He) or alpha particle among the outgoing reaction products. There are many possible reactions that are defined in the ENDF system that include such products and NJOY's GASPR module will search through the User specified ENDF input tape and previously created "PENDF" tapes to sum these cross sections, including an appropriate multiplicity factor, to produce the desired total production cross section for these particles. These cross sections are then inserted into the User specified output tape for use by subsequent NJOY modules. Users are cautioned that if that output tape already contained gas production data from an earlier NJOY job that those data will be overwritten.

The NJOY2012.50 release corrects a long-standing error in calculating heating at low incident energy following n+^{1}H capture. Up through ENDF/B-VI.8 the emitted photon was described using MF12/MT102 and the heating contribution from recoil following photon emission was properly calculated. For ENDF/B-VII.0 and later the photon description was moved to MF6/MT102. This change was not recognized by any version of NJOY and so the calculated heating cross section below about 10 eV was increasingly in error. We acknowledge our JAEA colleagues for noticing this deficiency.

As stated previously, NJOY has included coding for several decades that calculates heating and radiation damage. Current coding is little changed from what was originally programmed. Radiation damage is calculated in terms of a "displacements per atom", DPA, cross section. DPA is given by

$$DPA = \frac{\xi E_a}{2E_d},$$

where E_a is the available energy from the various reaction products and depends upon the incident neutron energy while E_d is the energy needed to produce a displacement. ξ is an empirical factor, typically set to 0.8, that improves the model prediction.

In addition, DPA is zero when $E_a < E_d$. NJOY's original coding used a single constant value of 25 eV for E_d. That was changed in the late 1990s when a table of E_d values for selected elements was defined (values vary from a low of 25 eV for Si to a high of 90 eV for W). Undefined elements default to 25 eV but in all instances Users may override the code default with their own input value. These values do not always agree with the current literature; see, for example, "Primary Radiation Damage in Materials, NEA/NSC/Doc(2015)9, Table 2.4. A future NJOY2012 code revision will incorporate these newer data.

Two other aspects of NJOY usage were summarized. First, when processing ENDF covariance data with ERRORR it was noted that Users have the option of running the GROUPR module and feeding those multigroup data to ERRORR, or letting ERRORR calculate multigroup data based upon the energy mesh available from the underlying covariance data. When using GROUPR to precompute multigroup cross sections it is best to use a dense energy mesh so that details of the underlying cross

section are more accurately represented. Use of too coarse a group structure can distort the resulting cross section uncertainty calculation.

Users were also reminded that when passing output files from one NJOY module to another they can use ASCII format or binary format. The data in a binary file contain more significant figures and so use of binary tapes is recommended until all NJOY calculations are complete. At that time NJOY's "MODER" module may be used to convert the final binary tape to ASCII.

Status of work committed by CIEMAT for the IAEA CRP on Primary Radiation Damage,

F. Mota, C.J. Ortiz, R. Vila

Laboratorio Nacional de Fusión, Unidad de materiales, CIEMAT
Madrid, Spain

1. Introduction

Fusion neutron radiations will generate a number of defects in the material affecting their physical properties. Therefore, present pathway to fusion reactors includes a rigorous material testing program. To reach this objective, irradiation facilities must produce the displacement damage per atom (dpa, primary knock-on atom (PKA) spectrum and gaseous elements (He, H) by transmutation reactions as closely as possible to the ones expected in the Fusion Power Reactor (FPR). In order to emulate the neutron irradiation that would prevail under fusion conditions is contemplated to use the nowadays or futures neutron sources to emulate the extreme fusion irradiation conditions (Current neutron sources like fission reactors or spallation neutron sources; or futures neutron sources like IFMIF or DONES).

In the last few years new Fusion Roadmaps have been developed in a number of countries [1 -4]. Generally speaking, the tendency is to speed up the design and construction phase of DEMO (in the case of EU it is foreseen to start its construction early in the 2030 decade) and, at the same time, to reduce the neutron dose requirements on the materials. In the case of the EU Roadmap an initial DEMO phase is foreseen with a maximum dose around 20 dpa, for components integration testing, and a second DEMO phase with a maximum dose around 50 dpa [5]. Specifications and requirements on materials irradiation data for future Power Plants remain unchanged but the time required to gather the information is much longer than for DEMO [6]. This new approach reduces the requirements for the early phase of the neutron source, maintaining the long term ones, and opens the possibility of a staged approach to IFMIF in which its construction can be developed in different phases. In this framework the IFMIF-DONES (DEMO-Oriented Neutron Source) facility has been proposed focused on DEMO needs [7].

Other option to emulate the extreme fusion irradiation condition is by means of three ion accelerators: One used for self-implanting heavy ions to emulate the displacement damage induced by fusion neutrons and the other two for light ions (H and He) to emulate the transmutation induced by fusion neutrons.

2. Methodology

Therefore, in order to emulate fusion neutron effects in materials is needed to be able to design equivalent irradiation experiments. As the methodologies used so far to calculate the primary displacement damage induced by neutrons or ions have not anything in common, we decided to develop comparable methodologies to calculate it for both kinds of radiations. So, our main objective was to find the way to calculate the primary displacement damage induced by neutron irradiation and by ions irradiation starting from something in common, i.e. the PKA spectrum.

This methodology to calculate the primary displacement damage generated in materials due to the combined effects of fusion neutrons and PKA spectra was developed [8]. This methodology is based on a methodology previously developed by KIT Laboratory [9, 10] and consists of a combination of Nuclear Data Libraries Processing, neutronics transport, and Monte Carlo Binary Collision codes. This methodology allows for the calculation of several damage parameters such as the PKA spectrum, displacement cascades, damage profile, damage function, and damage dose rate in materials under neutron irradiation. The block diagram is shown in Figure 1.

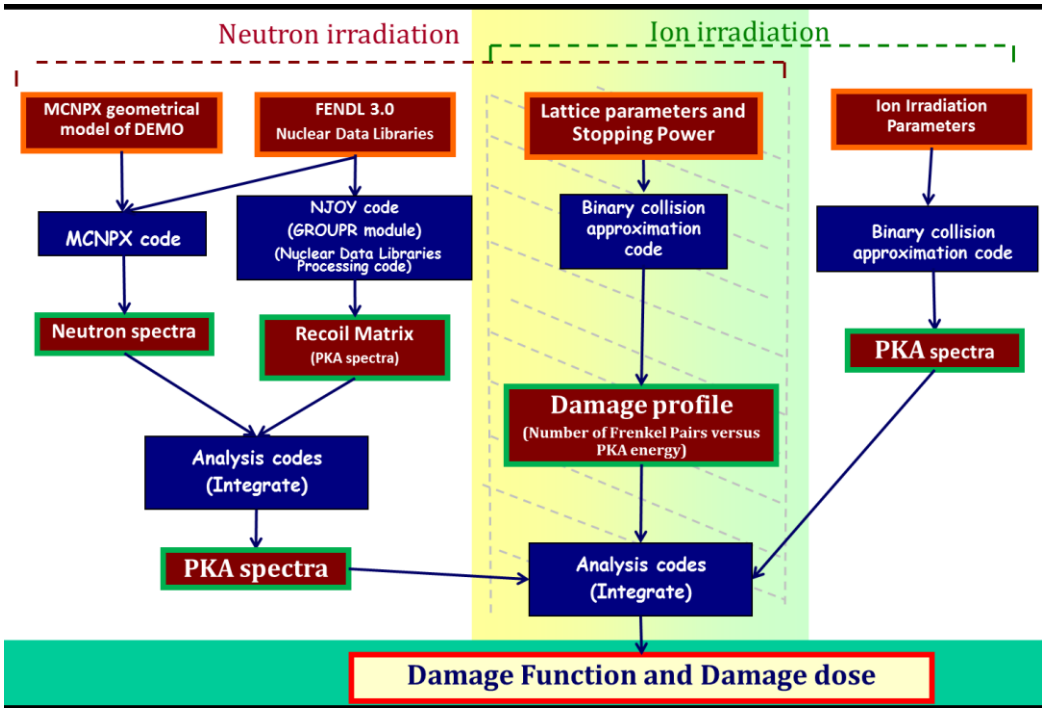

Figure 1. Methodology block diagram.

The damage profile, i.e. the number of Frenkel pair vs PKA energy was calculated with MARLOWE code since is more realistic than SRIM code. MARLOWE code is a displacement damage simulation code based on binary collision approximation [11,12]. MARLOWE code shows to be of high interest to simulate displacement cascades in monocrystal, polycrystal or amorphous materials. It allows exploring higher energies (up to GeV) in a much shorter time than MD. It represents thus an interesting alternative to MD to simulate the effects of energetic fusion neutrons in materials. In order to accurately predict the number of stable Frenkel pairs produced in cascades, those that will contribute to the long-term evolution of defects, the I-V capture radius must be first calculated. This can be done using MD results obtained for low-medium PKA energies (~ keV). As an example, the capture radius of I-V pairs in Fe as a function of PKA Energy has been calculated [13]. MARLOWE is able to account for the recombination of defects that occur during the cooling phase of a cascade by means of the concept of capture radius. A constant capture radius of about $3.3a_o$ was obtained for energies higher than 5 keV. MARLOWE can thus be used to simulate displacement cascades with energies higher than 5 keV in Fe with this calibrated value of the capture radius. For lower PKA energies it was observed that the capture radius is variable and must be determined for each PKA energy [14]. However, the capture radius has to be adjusted for each materials under study.

3. Status of the work committed for this year

The work plan for the first year was to use MARLOWE code to determine the capture radius in Fe, SiO_2, Al_2O_3 as a function of PKA energy. However, due to several reasons it has been impossible to fulfil the objectives:

On one hand, for strategy reasons of my department I have been involved in a lot of neutronics tasks related with the development of diagnostics for ITER. I was involved in a neutronics analyst contract for the diagnostic department of ITER IO under supervision of Luciano Bertalot (luciano.bertalot@iter.org).

On the other hand, in order to adjust the capture radius for MARLOWE, it is necessary to find enough molecular dynamics simulation. However, finding in the literature enough MD data to adjust the capture radius for Al_2O_3 and SiO_2 has been impossible. Therefore, so far, we have not been still able to fulfil the objectives committed for the first year.

During the next year, our planning is to solve this issue and reach the objectives committed for the first year.

4. PKA spectra for different facilities and using several nuclear data libraries

As fulfilling with the targets planned for the first year has been impossible, we decided to begin with the calculations committed for the second year. The target for the second year was to determine the PKA spectra for Fe, SiO_2 and Al_2O_3 induced by different neutron sources an ion sources. In addition, it would be performed using different nuclear data libraries (FENDL3.0_r2, ENDF\B-VII.1, JEFF 3.2), in order to evaluate the sensitivity of the results to them. Here, only preliminary results are shown in this section, because it is needed to extent this study to other nuclear data libraries (e.g. JENDL and TENDL).

So far, the neutrons spectrum-weighted total PKA's differential cross sections (named in the rest of this report, PKA spectrum) for the isotopes ^{56}Fe, ^{27}Al, ^{16}O, ^{28}Si and ^{12}C induced by different neutron sources have been calculated. The neutron sources considered for this comparison are the following: two kind of DEMO (DCLL and HCLL), two fission reactors (BR-2 and HFR-Petten), and IFMIF-HFTM.

Figure 2 shows the PKA spectra calculated for the FW of DEMO-DCLL using different nuclear data libraries. The neutron spectrum corresponds to the FW in the equatorial and inboard zone. The DEMO-DCLL MCNP geometrical model used is the current model which was developed during this year (2015) in EUROFUSION [15].

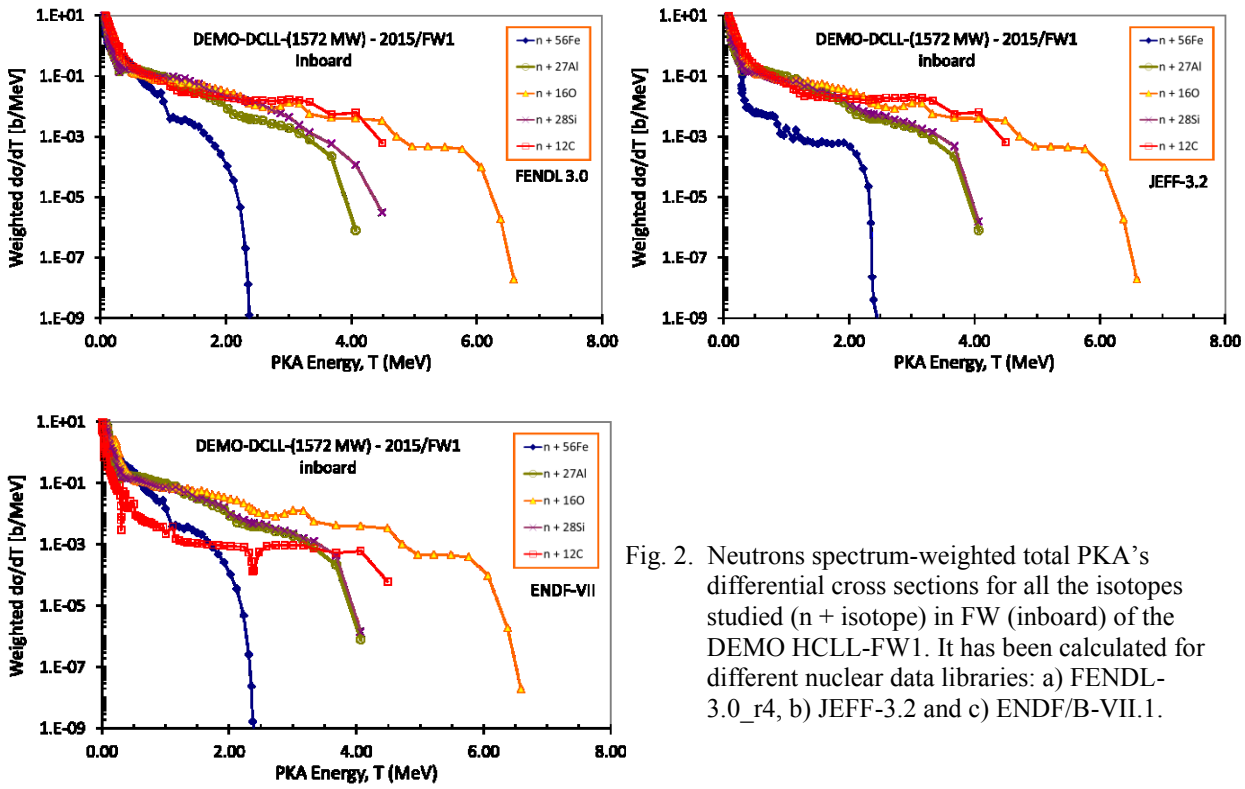

Fig. 2. Neutrons spectrum-weighted total PKA's differential cross sections for all the isotopes studied (n + isotope) in FW (inboard) of the DEMO HCLL-FW1. It has been calculated for different nuclear data libraries: a) FENDL-3.0_r4, b) JEFF-3.2 and c) ENDF/B-VII.1.

It is possible to observed clear differences in the PKA spectra, which depend on the nuclear data libraries used. For example, important differences have been found in the PKA spectrum calculated for ^{56}Fe. When it is calculated with JEFF-3.2 the cross section decreases more quickly than using FENDL-3.0 and ENDF/B-VII. In addition, something similar occurs for the PKA spectrum calculated for ^{12}C. In this case, the cross section is very different when is calculated with ENDF/B-VII. Although, it is necessary to add other nuclear data libraries to complete this study, we can conclude from this preliminary study, it is very important to perform a broad study in order to be able to recommend the proper nuclear data libraries to determine the more realistic PKA spectrum, as much as possible, to each isotope.

Figure 3 shows PKA spectra induced by neutron spectrum from the FW (inboard) of the DEMO-HCLL (model of 2013) [16]. The nuclear data library used was FENDL-3.0_r4. Figure 4 shows PKA spectra induced by neutron spectrum from two fission reactors, the BR2 and HFR-PETTEN. The nuclear data library used is FENDL-3.0_r4.

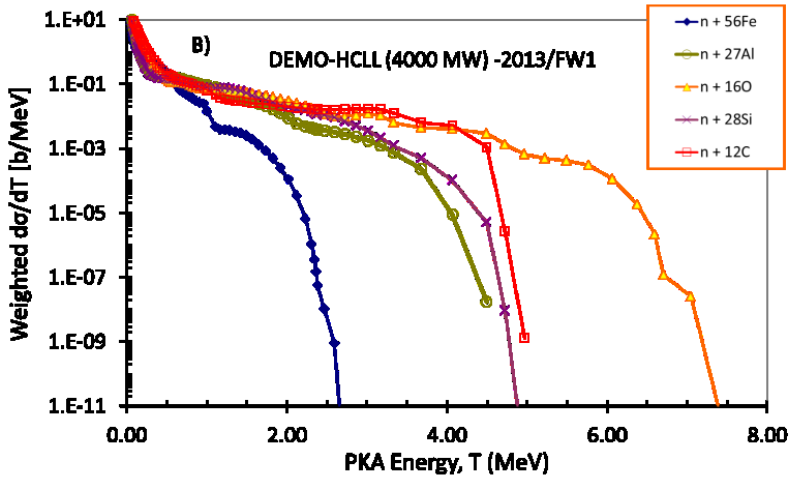

Fig. 3. Neutrons spectrum-weighted total PKA's differential cross sections for all the isotopes studied (n + isotope) in FW (inboard) of the DEMO-HCLL.

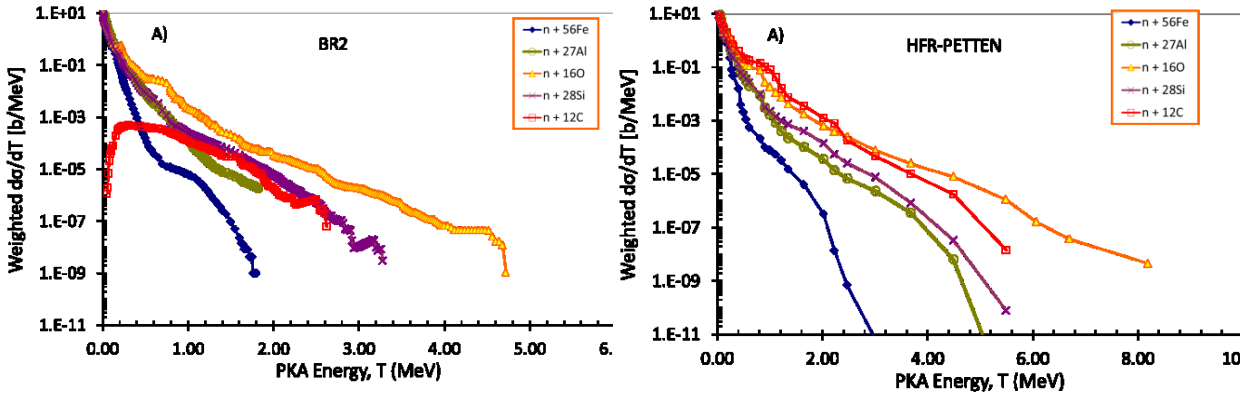

Fig. 4. Neutrons spectrum-weighted total PKA's differential cross sections for all the isotopes studied (n + isotope) for two different nuclear fission reactors; a) BR2 and b) HFR-Petten.

Finally, figure 5 shows the PKA spectra induce by the neutron spectrum from the IFMIF-HFTM. The nuclear data library used was FENDL3.0_r4. It is possible to note that for IFMIF-HFTM the maximum PKA energy reaches values higher than the rest of the neutron sources assessed.

For the next meeting, the calculations of the Figures 3, 4, and 5 will be extended to the rest of nuclear data libraries evaluated in Figure 2, and, in addition, adding, at least, the nuclear data libraries

TENDL-2014 and JENDL. We start using the FENDL-3.0_r4 because our initial objective was to compare with IFMIF results, the results obtained for the rest of the nuclear facilities evaluated. Then, for IFMIF, it is very difficult to find other nuclear data libraries up to neutron energies about 55 MeV.

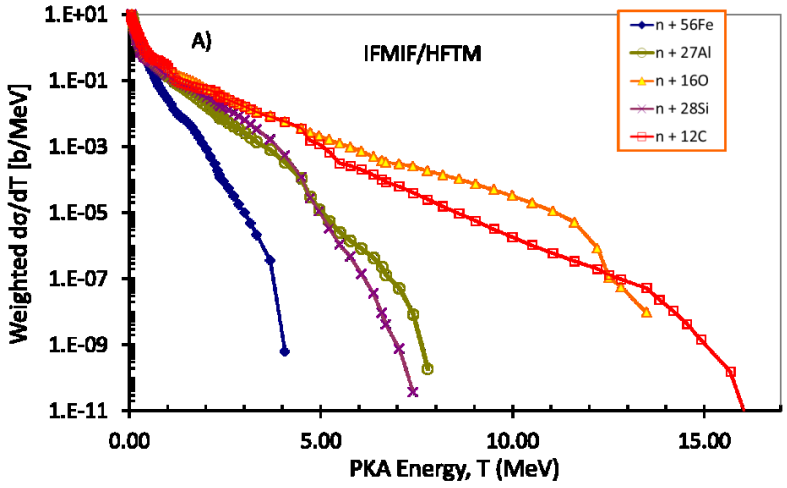

Fig 5. Neutrons spectrum-weighted total PKA's differential cross sections for all the isotopes studied (n + isotope) for High Flux Test Module (HFTM) of IFMIF.

5. Plan for the next year

During the next year, our planning is to sort out the troubles found to reach the objectives committed for the first year. We will try to sign a collaboration agreement with some research institutes to perform the molecular dynamics calculations needed to adjust the capture radius for MARLOWE code.

Once, we can adjust the capture radius for MARLOWE, the calculation of the damage dose and the damage functions for the different neutron sources assessed for different nuclear data libraries is planned.

Reference

1. F. Romanelli et al, "A Roadmap to the realisation of fusion energy", EFDA Report 2012.
2. Kunihiko Okano, Gianfranco Federicib, Kenji Tobita "DEMO design activities in the broader approach under Japan/EU collaboration", 89, (2014) 2008–2012
3. G.S. Lee, "K-DEMO Design, R&D and International Collaboration on behalf of K-DEMO Team", In proceedings ISFNT-11 Barcelona-Spain. September 2013.
4. Yican Wu, "China's plan for design and R&D activities of multi-functional fusion test reactor", In proceedings ISFNT-11 Barcelona-Spain. September 2013.
5. G. Federici et al, "Overview of EU DEMO Design and R&D activities". Fusion Engineering and Design, to be published. 2014.
6. D. Stork et al, "Materials R&D for a timely DEMO: key findings and recommendations of the EU Roadmap Materials Assessment Group", Fusion Engineering & Design, to be published. 2014.
7. A. Ibarra, R. Heidinger; P. Barabaschi, F. Mota et al. "A Stepped Approach from IFMIF/EVEDA toward IFMIF", FUSION SCIENCE AND TECHNOLOGY, 66 (2014) 252-259
8. F. Mota, R. Vila, C. Ortiz, A. Garcia, N. Casal, A. Ibarra, D. Rapisarda, V. Queral, Fusion Eng. Des., 86 (2011), pp. 2425–2428
9. P.V. Vladimirov, Yu.D. Lizunov, A.I. Ryazanov, Rad. Eff., 139 (1996), pp. 109–123
10. P.V. Vladimirov, S. Bouffard, C.R. Physique, 9 (2008), pp. 303–322
11. M.T. Robinson, Phys. Rev B 40 (1989) 10717-10726
12. M.T. Robinson, Rad. Eff. Def. 130-131 (1994) 3-20

13. D.A. Terentyev, L. Malerba, R. Chakarova, K. Nordlund, P. Olsson, M. Rieth, J. Wallenius "Displacement cascades in Fe–Cr: A molecular dynamics study" Journal of Nuclear Materials 349 (2006) 119-132
14. F. Mota, C.J. Ortiz, R. Vila, "Beyond NRT concept: using BCA codes to design irradiation experiments to emulate neutron fusion effects in materials", Summary Report of the First Research Coordination Meeting on Primary Radiation Damage Cross Sections, pp. 44-46, https://www-nds.iaea.org/publications/indc/indc-nds-0648.pdf
15. I. Palemo, DEMO-DCLL MCNP geometrical model: https://idm.euro-fusion.org/?uid=2KZTEM
16. J. Jordanova, U. Fischer, P. Pereslavtsev, Y. Poitevin, A. Li Puma, A. Cardella et al., Fusion Eng. Des. 75–79 (2005) 963–967.

A BCA-MD approach to simulate high-energy PKAs,

C.J. Ortiz, P.G. Müller

Laboratorio Nacional de Fusión, Unidad de materiales, CIEMAT
Madrid, Spain

Introduction

It is well-known that Binary Collision Approximation (BCA) allows simulating collision cascades in much shorter times than Molecular Dynamics (MD). However, BCA is not able to accurately predict last stages of cascades since it does not take into account the long-range potential and neither solves for the equation of motion of each atom as MD does. As a consequence, BCA cannot account for the recombination of defects and for the formation of clusters during thermal spike. The objective of this work is to simulate collision cascades with BCA up to some criterion - to be defined - and pass the state of the cascade to MD to simulate last stages. Our goal is to accelerate MD calculations in order to obtain large cascade statistics, in particular for high energy PKAs.

Description of the work

Given an interatomic potential, MD solves for the equations of motion of each atom in the system, whether they are at equilibrium position or displaced, as they are under irradiation. Under irradiation, two potentials are necessary; a short-range potential to account for collision events and a long-range potential to account for interactions between atoms. This allows taking into account multi-body interactions and simulating complex processes such as the thermal spike or the formation of clusters intra-cascade. However, this accuracy has a cost since the higher the initial PKA energy, the larger the simulation box must be. This implies that for large PKA energies, the number of Newton equations to solve for significantly increases, and so does computational effort. Therefore, obtaining large statistics for high PKA energies becomes unrealistic.

The objective of this work is to combine both advantages - of BCA and MD - to obtain accurate results in a short computational time. The idea is to simulate first stage of collision cascades with BCA, until some criterion has been reached, and then the state of the cascade is passed to MD as initial conditions. MD predicts then final stages of cascade. First of all, we must ensure that BCA reproduces well MD results in the range of validity of BCA, i.e. for energies above 10 eV. Then, some criterion must be found to decide when to switch from one theory to the other.

In order to test BCA and compare it to MD calculations, we simulated PKAs with an energy of 10 keV in Fe, in random directions as well as in the <111> direction. The short-range potential used in BCA as well as in MD calculation is the so-called ZBL [1]. For long-range interactions in MD, the potential Acklan04 [2] was used. In Fig. 1, we report the evolution of the PKA energy as a function of time for the case of a <111> direction, as calculated by BCA and by MD. As we can see, results are in

excellent agreement. Clearly, BCA is able to predict the energy loss as a function of time down to low kinetic energies.

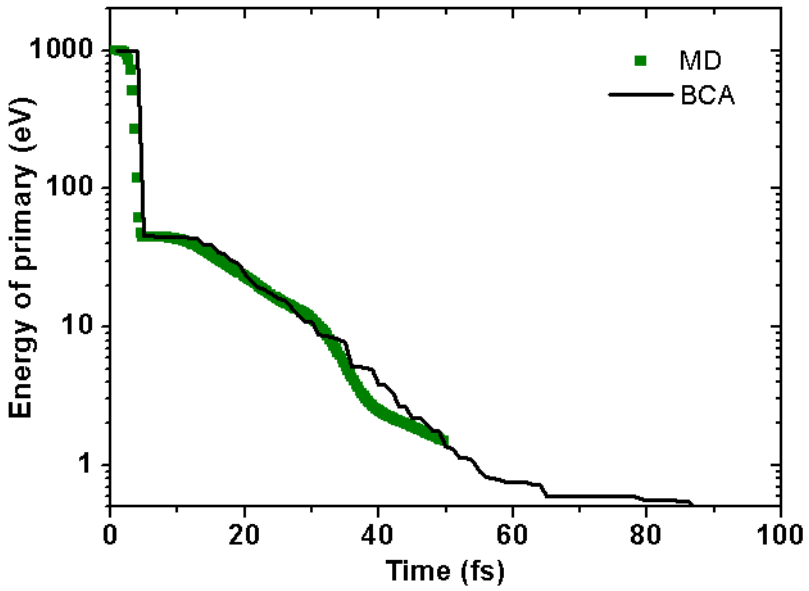

Fig. 1. Evolution of the PKA energy vs time as calculated by MD (green squares) and by the BCA (black line).

In Fig. 2, we compare the evolution of the number of SIAs displaced with a certain energy. As it is evidenced, BCA reproduces very well the number of displacements with an energy higher than 10 eV, in comparison to MD calculations. In contrast, we can see in Fig. 2 that BCA is not able to predict the number of SIAs with a kinetic energy larger than 4 eV. This is due to the fact that at these energies, multi-body interactions cannot be neglected. This confirms that BCA breaks down below a threshold energy, here in Fe, at 10 eV.

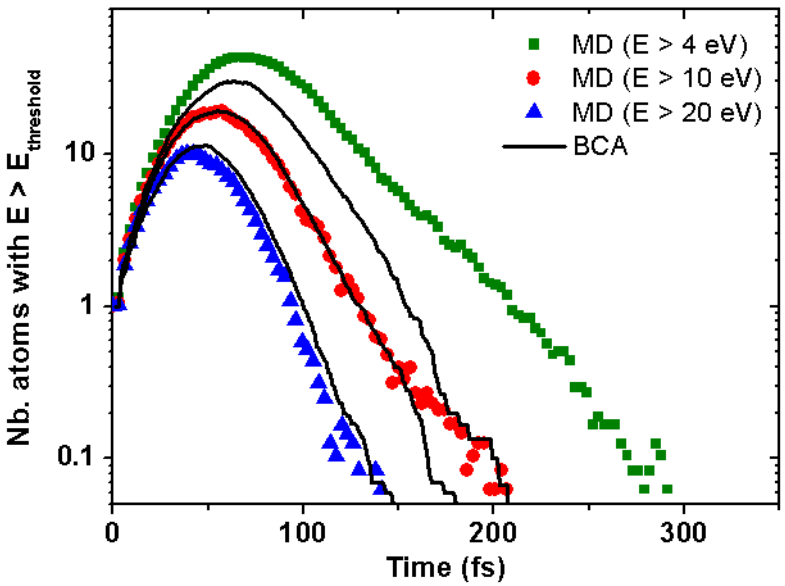

Fig. 2. Comparison between MD (symbols) and BCA (lines) of the numbers of SIAs displaced during cascades with a certain energy.

This suggests that the criterion when to stop BCA calculations in order to transfer the state of the cascade to MD should take into account the energies of the SIAs in motion. Clearly, the criterion imposes a threshold energy below which, the results obtained with BCA are incorrect and cannot be passed to MD.

Assuming an energy threshold of 250 eV we built a hybrid BCA-MD model in which first stages of cascades are simulated using the BCA, and, when SIAs have an energy below the fixed threshold, the information is transferred to the MD.

In Fig. 3 we show the evolution of defects during a cascade generated by a PKA of 80 keV in the 111 direction in Fe. As we can see, our hybrid BCA-MD model reproduces very well results obtained with pure MD calculations.

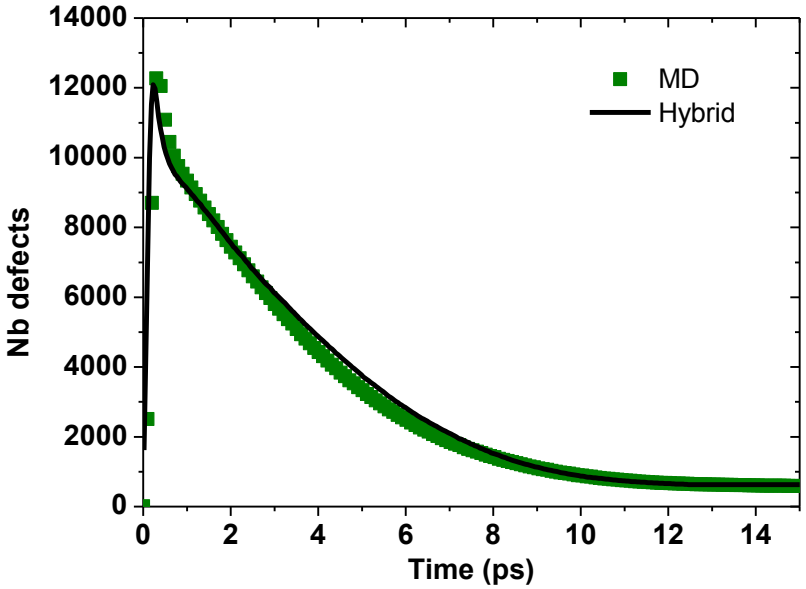

Fig. 3. Evolution of defects during a cascade generated by a PKA of 80 keV in Fe. Green squares represent results obtained with pure MD calculation; black line represents the result obtained with our hybrid BCA-MD model.

Conclusions

In this work we have developed a BCA-MD approach to simulate collision cascades generated by high-energy PKAs. In this model, the first stages of cascades are simulated using the BCA, which is more efficient than MD. When SIAs that are displaced during collisions have an energy below a fixed energy threshold, the information obtained with the BCA is passed to the MD, which simulates last stages of the cascade. Our model is in very good agreement with results obtained with pure MD calculations.

References

1. J.F. Ziegler, J.P. Biersack and U. Littmark, The Stopping and Range of Ions in Matter, Pergamon, New York, 1985
2. G.J. Ackland, M.I. Mendelev, D.J. Srolovitz, S. Han and A.V. Barashev, J. Phys.: Condens. Matter 16 (2004) S2629

Contribution to the second RCM of the IAEA CRP on Primary Radiation Damages, L. Luneville, J.P. Crocombette, D. Simeone

CEA Saclay
Gif-sur-Yvette Cedex, France

When a material is subjected to a flux of high-energy particles, its constituent atoms can be knocked from their equilibrium positions with a wide range of energies, depending on the exact nature of the collision. The spectrum of damage energy, derived from the exact knowledge of the recoil spectra for each nuclear reaction occurring in the solid, constitutes a vital data set required for understanding how materials evolve under irradiation**.** The project will be aimed at using the latest, most modern nuclear data to produce, evaluate and assess the damage energy spectra for a range of nuclear-relevant materials. The knowledge of such damage energy is relevant to compare the impact of different facilities on the structural behaviour and relevant properties of materials. The second part of this work is devoted to the applicability of the arc-dpa formula for concentrated ordered alloys.

1. Overview of work during 2013 - 2015

The DART [1] code was developed to compute both the primary spectra produced by neutrons, ions and electrons as well as the energy damage deposited by these particles in a poly atomic material. The ultimate goal of this work is to mimic radiation damage induced in nuclear plants with experimental reactors as well as ion beam facilities.

For a mono atomic material, the energy damage produced by neutrons of a given energy E_n can be written as:

$$E_d(E_n) = \int dT \frac{d\sigma_{nx}(E_n,T)}{dT} E_d(T) \qquad (1)$$

Where $\frac{d\sigma_{nx}(E_n,T)}{dT}$ is the sum of all the cross sections associated with all open channels (elastic, inelastic, …) between the neutron of energy E_n and an isotope forming the material.

Summing the cross section of all isotopes over all open channels, this equation can be written as:

$$E_d(E_n) = \sigma_{nx}(E_n) \int dT\, p(T) E_d(T) \qquad (2)$$

Where $\sigma_{nx}(E_n)$ is the total cross section summed over all open channels and all isotopes. p(T) is the density probability function responsible for the creation of a PKA with a kinetic energy T set in motion by a neutron of energy E_n.

Normalizing p(T) allows to compute the fraction of atoms set in motion by the incident particle. P(T) is the cumulative function associated with p(T) and is usually called the primary Knocked-on atom spectrum. Sampling p(T) with ions allows simulating the fraction of primary damage produced by a nuclear plant.

Such an analysis can be extended to compounds:

$$E_d(E_n) = \sum_{i=1}^{Natci} f_i\, \sigma_{ni}(E_n) \int dT\, p_i(T) E_{di\to mat}(T) \qquad (3)$$

Where f_i is the atomic fraction of the i^{th} chemical species in the compound and *Natci* is the total number of species forming the compound.

To select the best ion to mimic the primary damage production in a compound, recoil spectra, the cumulative function associated with $\int dT\, p_i(T) E_{di\to mat}(T)$ must be computed. This calculation is included in the DART code. Whereas the DART code does not take into account the attractive part of the interatomic potential, it calculates the energy damage induced by each recoil by solving *Natci* integro-differential equations [2, 3]. The damage energy does not thus result from an averaging over the atomic fraction of the damage energy given by Robinson [4].

Dividing the damage energy given by Eq. (3) by the displacement threshold energy Ed_i for each species, it is possible to compute the dpa produced in a poly atomic target as well as replacements in

different sub lattices. Obviously these replacements are meaningless because only the repulsive part of the interatomic potential is taken into account. Integrating Eq. (3) over the neutron flux allows computing the "dpa" production rate and then a more direct comparison of different facilities taking into account both the neuron flux and the material.

2. Impact of the different cross section libraries

To illustrate the interest of the DART code, figure 1 displays the comparison of the of PKA spectra in pure lithium as a function of the ^{6}Li enrichment. As (n,α) reactions occur with ^{6}Li, the n-^{6}Li cross section is quite different from the n-^{7}Li cross section for low neutron energies. For neutron with kinetic energies above 100 keV, this absorption becomes negligible and cross sections for the two isotopes are of the same order of magnitude. Even if these two cross sections are largely different (4 orders of magnitude for neutrons below 100 keV), the PKA spectra of the two isotopes are similar.

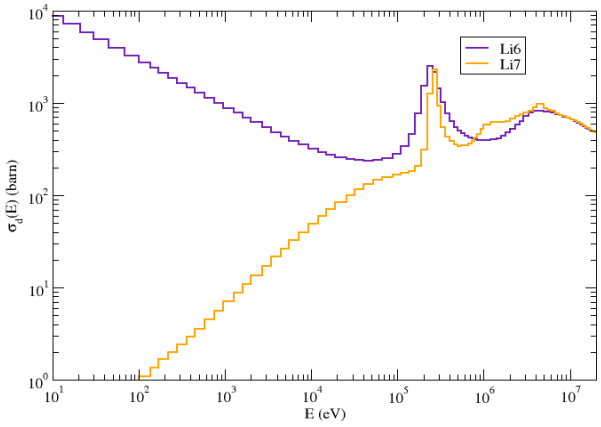

Fig. 1a: Comparison between the neutron Li cross section for ^{7}Li and ^{6}Li isotopes (ENDF/B-VI library).

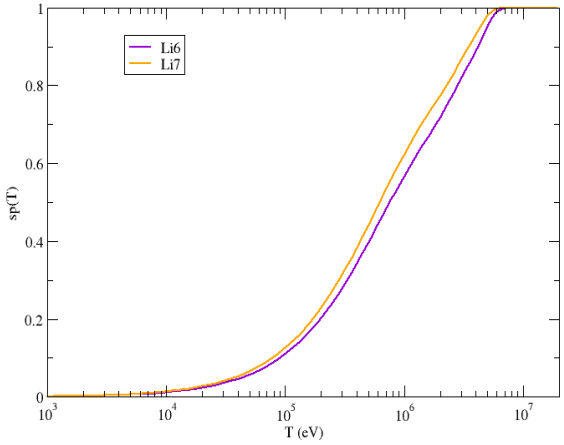

Fig. 1b: PKA spectra computed for Li pure element composed of ^{7}Li and ^{6}Li isotopes ($Ed_{7Li} = Ed_{6Li}$ = 25 eV and ENDF/B-VI library).

However, the dpa cross sections are largely different because the recoil of atoms due to fission products (^{6}Li + ^{1}n -> ^{4}He + ^{3}H, Q = 4.8 MeV) are computed by the DART code. Figure 2 displays for instance the evolution of the dpa cross section as a function of the ^{6}Li enrichment in LiO_2.

Table 1 displays the different dpa production rates in Li as a function of the ^{6}Li enrichment. The dpa production rates were calculated for a typical PWR neutron flux. Moreover, this dpa rate was also computed for a 1 MeV Li irradiation. The fluxes were all equal to 2.6 10^{11} cm^{-2} s^{-1} (E_d(Li) = 25 eV) in all calculations.

Table 1: Comparison of the dpa rate produced in nuclear plant on pure Li as a function of the ^{6}Li enrichment. For comparison, the dpa rate induced by 1 MeV Li ions on lithium is also calculated.

	n-7Li	**n-6Li**	**n-Li**	**1 MeV Li on Li**
Rate (dpa/s)	3 10^{-11}	1.5 10^{-9}	1.4 10^{-10}	5.6 10^{-8}

As the dpa rate is an estimation of the amount of the energy deposited in the solids, it appears that the simulation of primary damage by an ion beam induces an energy deposition rate two orders of magnitude larger than the rate produced in a nuclear plant.

In order to study the impact of different cross sections for evaluating the "damage" function, we have computed the total displacement cross section in SiC from the DART using ENDF/B-VI and

computed with SPECOMP using ENDF/B-V library, Fig. 3. As Si and C exhibit similar mass and charge, the energy damage calculated solving the Lindhard equations (DART) or extracted from Robinson formulae (SPECOMP) are equivalent and the main part of the discrepancy between displacement cross sections results from the cross section evaluation for Si.

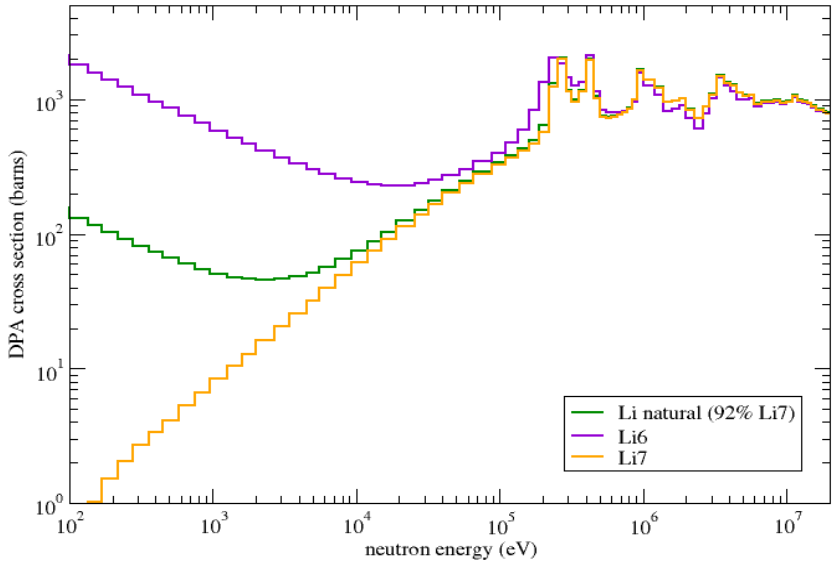

Figure 2: Comparison between the different cross section in LiO_2 as a function of the ^6Li enrichment.

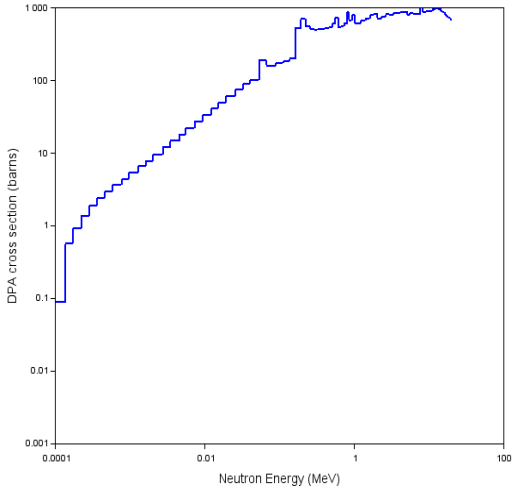

Fig. 3a: Total displacement cross section in SiC calculated using ENDF/B-VI library (DART)

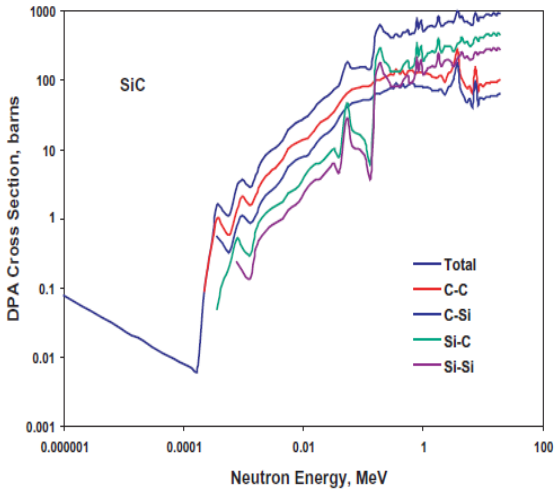

Fig. 3b: Total displacement cross section in SiC calculated using ENDF/B-V library (SPECOMP)

Direct comparison between the two calculations clearly shows that the discrepancy in the calculation of the "dpa" cross section differs from one order of magnitude for 100 eV neutrons. This point illustrates the impact of the library cross section for the calculation of the damage energy, recoil spectra as well as displacement cross sections. For all these calculations, displacement threshold energies were equal to respectively 20 eV and 35 eV for C and Si.

3. Calculation of the energy deposition

The second interest of the DART code is related to the calculation of the energy deposition. This calculation is performed using the full Lindhard theory. The damage energy is calculated from the

Molière approximation for the interatomic potential within the Lindhard theory framework. This function differs from the Robinson formula as well as the SRIM calculation derived from the Ziegler approximation of the Thomas-Fermi interatomic potential. In order to estimate the errors induced by the calculation of the damage energies calculated within these different approximations, we computed these energy damages for different pure elements and compounds. For a comparison of these damage energies with Frenkel pairs extracted from MD simulations, we divided this energy damage by 0.8/2Ed for SRIM and DART.

Figure 4 displays the comparison between different calculations of the damage energies.

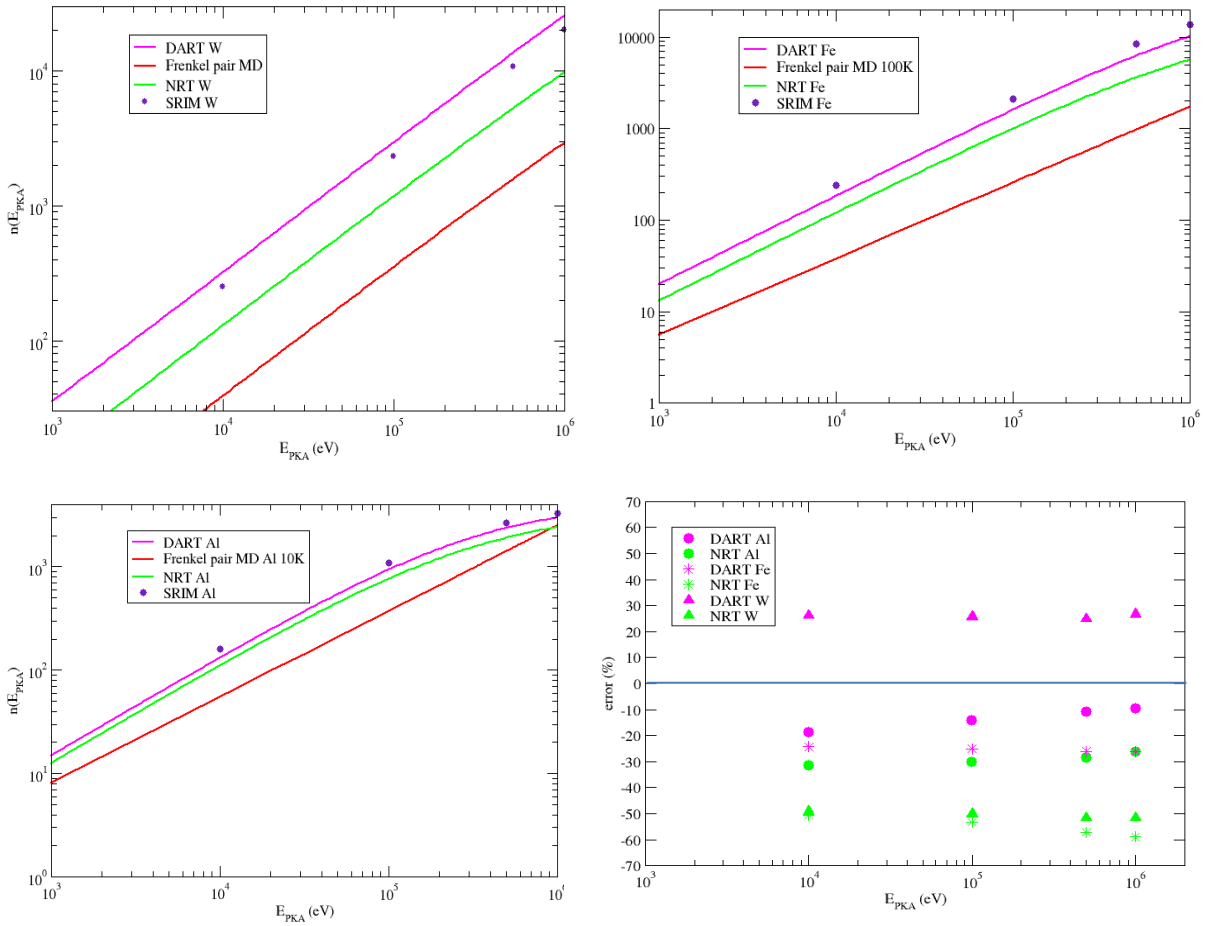

Fig. 4: Comparison of the different damage energies (divided by 0.8/2Ed) from SRIM, DART and application of the Robinson formula for pure material (NRT dpa) for W, Fe and Al. The red lines display the fraction of Frenkel pairs produced in these material using MD simulations (Radiation damage: Mechanisms and Modelling, Stoller TN (2012) for W, Calder, Bacon, JNM 207, 25 (1993) for Fe and M.Caturla, JNM, 296, 90 (2001) for Al). The graph on the right bottom displays errors between these calculations as a function of the PKA energy (damage energy calculated by SRIM was taken as the reference).

For studied materials, it appears that all these formulations exhibit the same almost linear evolution of the energy damage versus the projectile energy. What is more surprising is that the damage energy computed averaging the damage energy obtained from the Robinson formula by the atomic fraction (SPECOMP) gives an accurate estimation of the damage energy produced by self ions in a compounds as pointed on figure 5 for different compounds

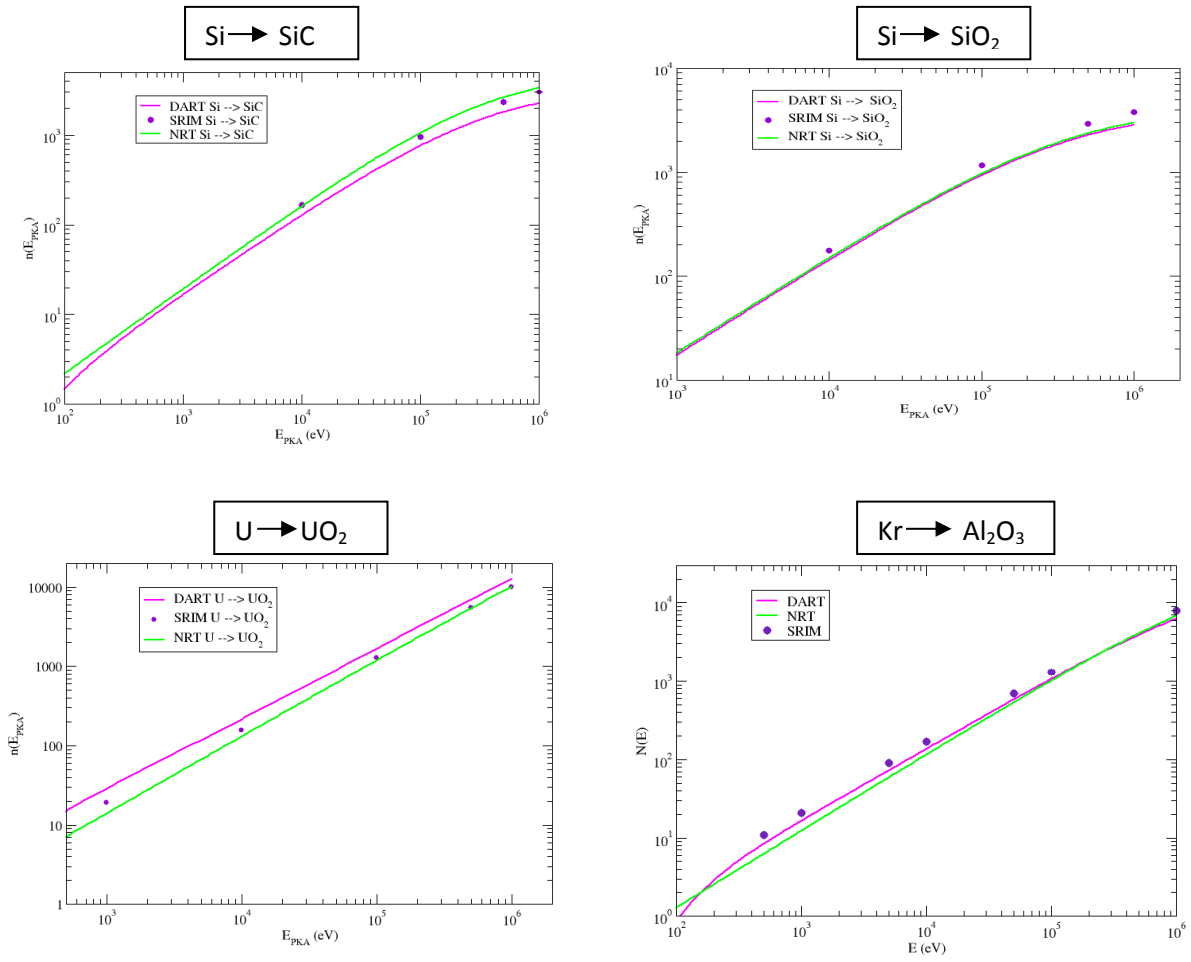

Fig. 5: Comparison of the damage energies (divided by 0.8/2Ed) computed with various approximations in some compounds (SiC, SiO_2, UO_2 and Al_2O_3) composed of atoms with different masses. The Robinson formula (NRT dpa) seems more accurate than the DART formulation for self ions. However, DART seems to give more realistic results for irradiation of compounds with ions (right bottom graph).

Even if the damage energies are different, it appears that the NRT formula gives an accurate estimation of the damage energy even for compounds with different masses when projectiles are self ions. Moreover, all these damage energies display the same almost linear evolution with the energy of the incident particles insuring similar recoil spectra.

A direct comparison of the damage energies extracted from DART and given according to the NRT formula over the PKA energy varying from 100 eV to 1 MeV clearly point out these values are proportional. However, the ratio evolves with Z ($0.67 + 0.036*Z - 1.59E\text{-}4*Z^2$). This dependence comes from the fact that the inelastic stopping power used by DART is derived from SRIM-2013 and does not evolve as the LSS electronic stopping power used by Robinson to compute its damage function.

4. Validity of the arc-dpa formalism for the calculation of the damage energy

A supposedly universal formula has recently been proposed by an OECD expert group [6] to estimate the number of Frenkel Pairs (FP) produced by a PKA of a given ballistic energy (E_b). This formula is a correction to the NRT-dpa formula. It is indeed well known that the NRT-dpa formula tends to overestimate the number of created defects. The NRT formula states that the number of defects, for ballistic energies larger than two times the threshold displacement energy (E_d) is simply proportional to E_b/E_d as:

$$N_{FP}^{NRT} = 0.4\frac{E_b}{E_d}$$

To correct this error, the so called athermal recombination corrected dpa (arc-dpa) uses an expression for the efficiency, i.e. the ratio of the actual number of defects to the one predicted by the NRT-dpa formula. It is based on the observation made in simple metals, especially in [7] that the number of FP can expressed as a sum of a linear and a sublinear term, as follows:

$$N_{FP} = a_1 E_b + a_2 E_b^{\alpha}$$

The arc-dpa relies on the assumption that the number of created FP is equal to one at $E_d/0.4$. This reasonable assumption is verified in the case of iron. With this constraint the arc-dpa efficiency is:

$$\chi^{arc-dpa} = c + (1-c) * \left(0.4\frac{E_b}{E_d}\right)^b$$

The number of number of FP created by a PKA of ballistic energy E_b is then expressed as:

$$N_{FP}^{arc-dpa} = 0.4\frac{E_b}{E_d} * \left(c + (1-c) * \left(0.4\frac{E_b}{E_d}\right)^b\right)$$

The arc-dpa formula introduces two additional parameters beyond the threshold displacement energy: c which is the constant efficiency observed at high energy with respect the NRT formula and b which is a negative number expressing the rate at which the efficiency goes from 1 to c.

In this report we present the results of Molecular Dynamics (MD) cascade calculations performed on two ordered, concentrated alloys (Ni_3Al and UO_2). The goal of these calculations was to check the applicability of the arc-dpa formula on such non amorphizable alloys. The first part of the report briefly presents the technicalities of the work, especially the principles of the Cell Molecular Dynamics for Cascade (CMDC) code which has been used in these simulations. The second part presents the obtained results.

4.1. Technicalities

We consider Ni_3Al and UO_2 as examples of concentrated ordered alloys. It is well known that UO_2, being an insulator, the irradiation damage goes far beyond the simple ballistic effects. This is however not our concern in the present report as we deal only with the number of created defects by ballistic processes. Ni_3Al is described by an Embedded Atom Model of [8] while UO_2 is described by a real space pair potential [9]. Once again the quality of these potentials is not our concern, as we do not aim to study in detail the response of these two materials to irradiation.

Cascade simulations have been performed with the CMDC code which is a MD code designed specifically to accelerate the MD calculations of displacement cascades. CMDC is based on the observation that many parts of the usual MD boxes do not take part in the cascade. They are just present in case the cascade would go there and to make a tri-periodic box. The core principle of CMDC is then to perform a regular MD simulation but just where and when necessary to properly describe the cascade unfolding. The first point of the code is to build the MD box during the unfolding of the cascade. Crystalline cells are added and removed on the fly from the calculation based on a local kinetic energy criterion. The second point of the code is to use a space variable time step for the simulation, applying a different time step for each active cell. CMDC includes electronic stopping as a slowing term; PKA energies are thus total kinetic energies: ionizing plus ballistic. A detailed description of the CMDC code has been published elsewhere [10]. On the whole, CMDC allows making cascade calculations which scales linearly with the projectile energy thus ensuring a huge speed-up compared to MD, of about 5 orders of magnitude for 1 MeV cascades in iron.

Tests calculations in iron have shown that the number of defects predicted with CMDC agree well with standard MD results. However the clustering of defects, especially interstitials, is not reproduced. This is not a problem in the present work, as we are only interested with the number of created FP. As explained below, CMDC calculations end in each cell when the local kinetic energy becomes low enough. With this algorithm (hereafter denoted as short runs), total simulated time proves to be of the

order of 0.5 ps. Such a simulated time proves too small to allow the recombination of metastable FP produced at the end of the cascade. Tests calculations for selected cascades with U PKA in UO_2 with a simulated time of 5 ps (hereafter denoted as long runs) have shown that these metastable defects recombine. The number of created defects in then identical to the one predicted by standard MD for the same cascade [11].

We have performed cascade calculations of U or O PKA in UO_2 and Ni or PKA Al in Ni_3Al. 16 different energies from 100 eV to 580 keV have been considered, except for U PKA in UO_2 for which additional calculations at 1 MeV were done for reasons detailed below. These total energies correspond to various ballistic energies depending on the PKA and material. In the following, results are shown as functions of the corresponding ballistic energy as calculated with the SRIM code. For instance, 580 keV total energy corresponds to 367, 307, 165 and 82 keV for U, Ni, Al and O PKA respectively (in Ni_3Al or UO_2). Except for U in UO_2, all calculations were of the short run type.

4.2. Results

a. Choice of the effective displacement energy

To test the arc-dpa formula, one must compare the number of created FP at the end of the cascades to the NRT prediction. A difficulty arises for alloys. Indeed there is no obvious definition of the displacement threshold energy entering the dpa and arc-dpa formulas. Displacement energies can be calculated for each component of the alloy. With the present potentials, we obtain values of 15 and 41 eV for Ni and Al respectively in Ni_3Al and 40 and 20 eV for U and O respectively in UO_2. Based on a paper by Ghoniem [12], a standard exists to obtain the effective displacement energies from the threshold energies of the components of an alloy:

$$E_d^{eff} = \frac{1}{\sum_i S_i (E_d)^{-1}}$$

In essence, this formula corresponds to partitioning the ballistic energy among the various components according to stoechiometry and applying the NRT formula for each component using its own displacement energy. With this formula, the effective displacement energy (E_d^{eff}) is 17.8 eV and 24 eV for Ni_3Al and UO_2 respectively. BCA calculations using SRIM and DART point to different values of E_d^{eff}, most of the time smaller than the Ghoniem formula. However as this latter formula is a standard, we choose to stick to it in our analyses.

The number of produced FPs is given in figure 6 for all considered cases.

The points in figure 7 shows the efficiency of production of defects in the four cases considered in the present work. For U PKA in UO_2, two sets of points are given. The blue (resp. red) ones corresponds to the short (resp. long) runs, see above. All cases exhibit a decrease of efficiency with increasing ballistic energy. Beyond this common point noticeable differences appear.

a. Ni PKA in Ni_3Al

In the case of Ni PKA in Ni_3Al, the efficiency though slightly irregular decreases from around 1 to about 0.3. The data points can be satisfactorily fitted with the arc-dpa formula with the fixed displacement energy Ed = 17.8 eV and the obtained fitted parameters: c = 0.29 and b = -0.34.

b. U PKA in UO_2

The efficiency observed for U PKA in UO_2 exhibits a regular decrease down to values of 0.37 or 0.26 for short or long runs respectively. The corresponding number of FP follows a power law up to very large energies (E_b < 270 keV) with

$$N_{FP}^{CMDC} \sim E_b^{0.76}$$

The number of FP then switches to linear. We checked the linearity with calculations up to1 MeV of total energy (E_b = 597 keV).

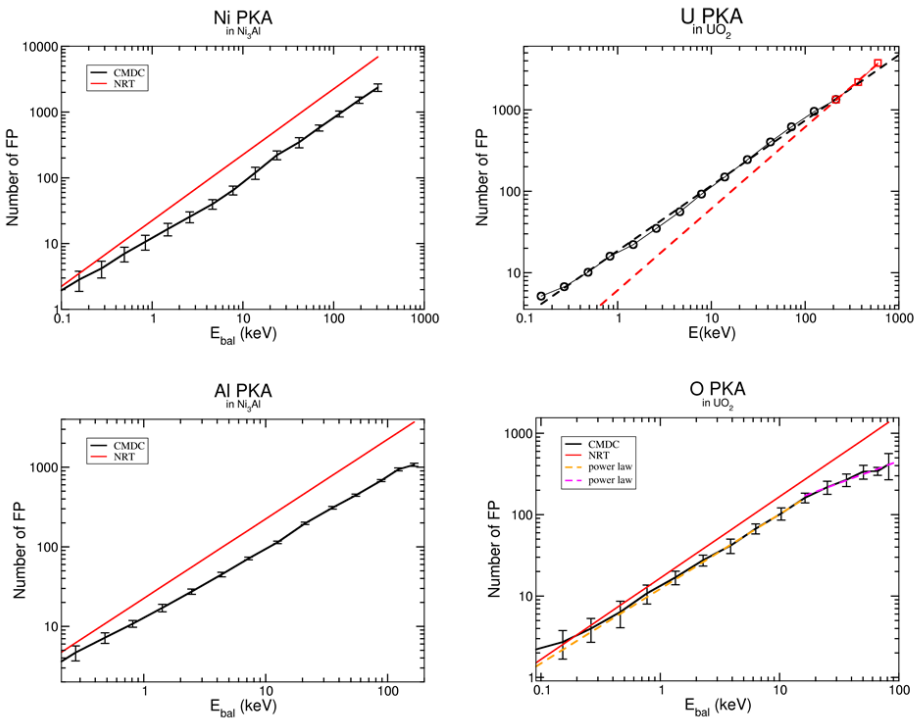

Fig. 6: Number of created FP calculated with CMDC for total energies from 100 eV to 580 keV. Straight lines are the prediction of the NT law. Upper right: U in UO_2 case (short runs). The NRT law is not shown; instead the dashed lines show the power law and linear fits (see text). Lower right: O in UO_2 case. The two subsequent power law fits are shown as dashed lines.

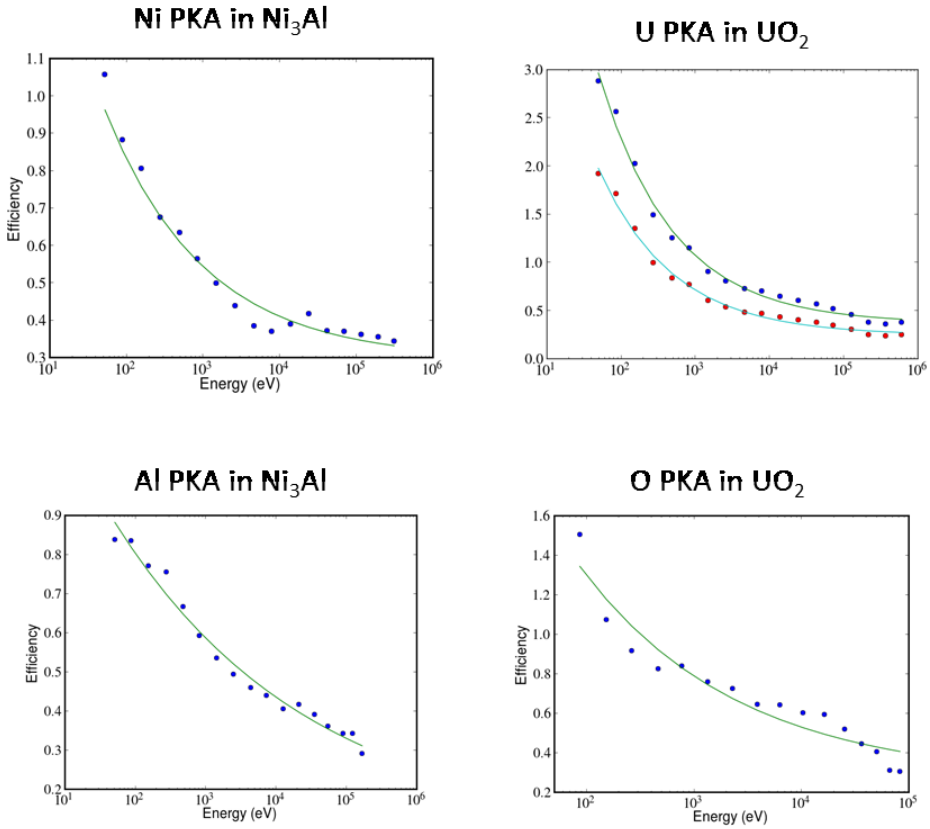

Fig. 7: Efficiency of FP creation with respect the NRT law. Straight lines are fits by the arc-dpa law for Ni case and by the modified formula including E_a for the other cases. Upper right: U in UO_2 case. Short runs (resp. long runs) are blue (resp. red points).

One should note that in both cases the efficiency at low energies is much larger than one, i.e. the number of created defects is 2 or 3 times larger than predicted by the NRT formula. Because of this large number of defects at low energy it is not possible to fit the observed efficiency with the arc-dpa formula. Indeed, as indicated before, this formula relies on the assumption the efficiency equals one at $E_d/0.4$ = 60 eV. It is clear from figure 1 that χ is much larger than 1 at 60 eV for both types of runs. The shape of the efficiency curve is nevertheless close to the one observed in the Ni case or in the seminal case of Fe PKA in iron. However to be fitted with a formula close to the arc-dpa one, one has to lift the assumption χ = 1 at $E_d/0.4$. Doing so, one can fit the efficiency with

$$\chi = c + (1-c) * \left(0.4\frac{E_b}{E_a}\right)^b$$

In the above formula the displacement energy E_d has been replaced by a new parameter E_a. Introducing E_a amounts to coming back to the general formula of Stoller:

$$N_{FP} = a_1 E_b + a_2 E_b^{\alpha}$$

The curves in the figure are the results obtained for the fit with this modified formula (including E_a) with the following parameters:

E_a = 508 eV; c = 0.37; b = -0.43 for short runs and

E_a = 133 eV; c = 0.26; b = -0.43 for long runs.

The total number of created defects eventually varies as:

$$N_{FP} = 0.4\frac{E_b}{E_d} * \left(c + (1-c) * \left(0.4\frac{E_b}{E_a}\right)^b\right)$$

It is worth stressing that this formula depends on 4 different parameters (E_d, c, b, E_a) while the NRT formula involves only one (E_d).

c. Al PKA in Ni_3Al and O PKA in UO_2

The cases of Al PKA in Ni_3Al and O PKA in UO_2 are close and can be discussed together. In both cases the efficiency exhibits a continuous decrease. There is no sign of a possible saturation of the decrease of χ, thus no sign of a linear regime in the production of defects.

For Al the number of FP evolves continuously as a power law of the ballistic energy as

$$N_{FP}^{CMDC} \sim E_b^{0.83}$$

For O PKA the situation is even worse as there seems to be two different power law regime. For $E_b < 16keV$, N_{FP}^{CMDC} scales as $E_b^{0.91}$; then for larger ballistic energies up to PKA energies of 580 keV (i.e. E_b=82keV) N_{FP}^{CMDC} scales as $E_b^{0.54}$ which is even less linear.

In both cases a fit of the efficiency with the arc-dpa formula is not possible. For Al, χ is always smaller than one even at $E_d/0.4$ = 45 eV while for O it starts from larger than one values. The efficiencies are poorly fittable using the modified formula with the following parameters

for Al: E_a = 8.5 eV, c = 0.08, b = -0.15; and for O: E_a = 126 eV, c = 0.26, b = -0.29.

These fits while rather poor allow estimating the ballistic energy that would be needed to reach linearity of defect production. One could estimate that linearity is reached when the linear term is five times larger than the power law term in the modified arc-dpa formula for χ. This leads to a value of the ballistic energy of 1.8 MeV and about 1 TeV for Al. None of these ballistic energies corresponds to any real total energy. There is no total PKA energy that corresponds to 1.8 MeV ballistic energy for O in UO_2 or 1 TeV for Al in Ni_3Al. Therefore it appears that the linear regime will never be reached for these PKAs.

The arc-dpa formula has been tested for two examples of concentrated ordered alloys. We found that while the efficiency χ with respect the NRT law decreases with ballistic energy, the arc-dpa formula is only applicable for Ni PKA in Ni_3Al. At the opposite, it proves unusable for the other types of PKAs.

There appears to be two reasons for this inapplicability of the arc-dpa formula. First it is based on the assumption that the efficiency with respect to the NRT law equals 1 at $E_d/0.4$. While this assumption appears valid for Fe in iron and Ni in Ni_3Al, it proves false for the other cases. The energy at which $\chi = 1$ may be much larger than $E_d/0.4$ (U and O PKA in UO_2 case) or there may be no energy at which $\chi = 1$, the efficiency being always smaller than 1 (Al case in Ni_3Al). We introduced a revised formula with an additional parameter *Ea* substituted for *Ed* in the efficiency formula. With this new formula the efficiency can be fitted, tough rather poorly in the Al and O cases. This poor fit is linked to the second reason the arc-dpa formula is unusable, namely the fact that for these two types of PKAs the efficiency never saturates so that the number of defects is never linear with the ballistic energy. Both reasons of inapplicability relates to the noticeable mass difference which exists between the two components of each of the two tested alloys.

The arc-dpa formula is an interesting attempt to correct the NRT dpa formula based on the observation of a decrease of the efficiency with increasing energy. However, it appears that this formula cannot be expected to work in concentrated ordered alloys. Moreover it requires 3 additional parameters beyond the displacement energy or even 4 if one contemplates using the new formulation introduced in the present report. We therefore advocate against using it as a "new" or "improved" norm for the dpa. The flaws of the NRT dpa are more and more documented but it nevertheless has a few major advantages:

- it is well known and relies on a unique parameter
- it scales linearly with the ballistic deposited energy which is the more physically sound parameter to count ballistic damage.

5. Conclusion and IAEA workplan for period 2015 - 2017

The DART code is a freeware and can be downloaded from OECD (www.oedc-nea.org).

The arc-dpa formula has been tested for two examples of concentrated ordered alloys. We found that while the efficiency χ with respect the NRT law decreases with ballistic energy, the arc-dpa formula is only applicable for Ni PKA in Ni_3Al. At the opposite, it proves unusable for the other types of PKAs. There appears to be two reasons for this inapplicability of the arc-dpa formula. First it is based on the assumption that the efficiency with respect to the NRT law equals 1 at $E_d/0.4$. While this assumption appears valid for Fe in iron and Ni in Ni_3Al, it proves false for the other cases. The energy at which $\chi = 1$ may be much larger than $E_d/0.4$ (U and O PKA in UO_2 case) or there may be no energy at which $\chi = 1$, the efficiency being always smaller than 1 (Al case in Ni_3Al). We introduced a revised formula with an additional parameter *Ea* substituted for *Ed* in the efficiency formula. With this new formula the efficiency can be fitted, though rather poorly in the Al and O cases. This poor fit is linked to the second reason the arc-dpa formula is unusable, namely the fact that for these two types of PKAs the efficiency never saturates so that the number of defects is never linear with the ballistic energy. Both reasons of inapplicability relates to the noticeable mass difference which exists between the two components of each of the two tested alloys.

The arc-dpa formula is an interesting attempt to correct the NRT dpa formula based on the observation of a decrease of the efficiency with increasing energy. However, it appears that this formula cannot be expected to work in concentrated ordered alloys. Moreover it requires 3 additional parameters beyond the displacement energy or even 4 if one contemplates using the new formulation introduced in the present report. We therefore advocate against using it as a "new" or "improved" norm for the dpa. The flaws of the NRT dpa are more and more documented but it nevertheless has a few major advantages:

- it is well known and relies on a unique parameter
- it scales linearly with the ballistic deposited energy which is the more physically sound parameter to count ballistic damage.

During the remainder of the IAEA work period, we plan in collaboration with CRP partners to:

- Improve the DART code in order to compute recoils, PKA spectra and dpa rate including different neutron libraries (ENDF/B-VII, TENDL …). The basic idea is to compute PKA spectra in Fe and W for typical neutron fluxes (FBR, PWR…) in order to determine the impact of

evaluations on the calculation of PKA spectra. These calculations will be performed at different temperatures on Ni pure element with and without ^{59}Ni isotope.

- Determine recoils spectra for 1 MeV proton, 5 MeV Fe and 20 MeV W and some nuclear plants neutron fluxes with different libraries for pure Fe and W materials. The basic idea is to compare these spectra with similar spectra calculated using the arc dpa to point out the impact of this formulation of the damage energy to mimic the primary defects of solids in nuclear plants with ion beam facilities.
- In order to point out the effect of high accumulation dose on the PKA and recoil spectra, the DART code will be used to calculate these spectra in Fe including different amounts of Cr (5%, 10%, 15%) for a typical PWR spectrum [5].
- Calculate displacement cascades in iron at very high energies (at least 10 MeV) using the CMDC code. The goal is to calculate the efficiency at these large energies to check whether its re-increase observed in MD-BCA calculations is also observed in pure MD simulations.

References

[1] L. Luneville, D. Simeone, C. Jouanne, Journal of nuclear Materials 353, 89 2006
[2] J. Lindhard, V. Nielsen, M. Scharff, Mat. Fys. Medd. Dan. Vid. Selsk 36, 1 1968
[3] D. Parker and C. Coulter, Journal of Nuclear Materials 101, 216 1981
[4] M. Robinson, Journal of Nuclear Materials 216, 1 1994
[5] K. Vortler, C. Bjorkas, D. Terentyev, L. Malerba, K. Nordlund, J. of Nucl. Mater. 382, 24 2015
[6] K. Nordlund, A.E. Sand, F. Granberg, S.J. Zinkle, R.E. Stoller, R.S. Averback, T. Suzudo, L. Malerba, F. Banhart, W. J. Weber, F. Willaime, S.L. Dudarev and D. Simeone, *Primary Radiation Damage in Materials*, OECD-NEA Report NEA/SC/DOC(2015)9
[7] R.E. Stoller, *The role of cascade energy and temperature in primary defect formation in iron,* Journal of Nuclear Materials **276**: 22-32 (2000)
[8] G.P. Purja Pun and Y. Mishin, *Development of an interatomic potential for the Ni-Al system,* Philosophical Magazine **89**: 3245-3267 (2009)
[9] N. Morelon, D. Ghaleb, J. Delaye and L. Van Brutzel, *A new empirical potential for simulating the formation of defects and their mobility in uranium dioxide,* Philosophical Magazine **83**: 1533-1550 (2003)
[10] J.-P. Crocombette and T. Jourdan, *Cell Molecular Dynamics for Cascades (CMDC): A new tool for cascade simulation,* Nuclear Instruments and Methods in Physics Research Section B: Beam Interactions with Materials and Atoms **352**: 9-13 (2015)
[11] L. Van Brutzel, M. Rarivomanantsoa and D. Ghaleb, *Displacement cascade initiated with the realistic energy of the recoil nucleus in UO_2 matrix by molecular dynamics simulation,* Journal of nuclear materials **354**: 28-35 (2006)
[12] N.M. Ghoniem and S.P. Chou, *Binary collision Monte Carlo simulations of cascades in polyatomic ceramics,* Journal of Nuclear Materials **155-157, Part 2**: 1263-1267 (1988)

Comparative Simulation of Primary Damages in Polymorphous Zirconium,

N. Lazarev

National Science Center Kharkiv Institute of Physics and Technology
Kharkiv, Ukraine

Summary

We study the effect of lattice symmetry on the production efficiency and morphology of primary radiation damages. Molecular dynamics simulation of the primary defect formation in various allotropic forms of zirconium is performed.

Introduction

Different swelling behaviour of fcc, bcc, and hcp alloys under irradiation is one of today's challenges. The fcc alloys generally have the swelling rate of about 1%/dpa at steady state after some incubation dose. The bcc alloys are more swelling-resistant having a typical swelling rate of about 0.1-0.2%/dpa [1,2]. Alloys with hcp lattice are found to be weakly susceptible to swelling.

By comparing the defect formation efficiencies in Ni, Fe, Zr, and some other pure metal lattices, it was found that the lattice type and chemical composition have a minor effect on the *total number* of point defects formed in cascades [3,4]. At low primary knock-on atoms (PKA) energies the ratio of the formed Frenkel defects N_{FP} to the defect number in the Norgett, Robinson and Torrens (NRT) formulation [5], N_{NRT}, is close to 1. With the energy increase, this ratio decreases according to the power law, but approaching 10 keV it reaches approximately 0.15 - 0.3 and further stays nearly constant. Such dependence occurs in all simulated lattices and the number of surviving Frenkel defects at the end of the post-collision phase of the cascade appears to be substantially system-independent [6]. In this context the complex cooperative processes at cascade development are reduced to a simple binary collision model.

Most likely, different macroscopic properties of crystals with different symmetries under irradiation can be attributed to the nature of the recombination of defects and the features of the microstructure evolution inherent to crystal symmetry. The correlation properties of the formed radiation defects show that the distinctions are already observed on the early stages of primary defects formation in cascades. A probable reason for such behaviour is the in-cascade clustering and size distributions of point defect clusters. The comparison of cluster size distributions in metals possessing fcc (Ni), bcc (Fe), and hcp (Zr) symmetries has shown that the tendency of lattices to the swelling correlates with the increase of the fraction of clustered self-interstitial atoms (SIAs) [7].

This gives rise to the question: are the observed distributions a consequence of the properties of the chemical elements or the lattice symmetry?

Results

To answer this question, we consider the effect of the lattice symmetry independently of chemical features. With this aim in view we simulate the system which exhibits the polymorphism of the lattice. Zirconium is the suitable pure metal. It undergoes the martensitic transformation in the appropriate temperature range. Moreover, we can simulate this transformation by the MD method to obtain the proper structures for the study of primary radiation damages [8].

Classical molecular dynamics with the empirical potential of Mendelev-Ackland for Zr [9] was used for the simulation. An appropriate computational technique was employed to get sufficient accuracy and to speed up the simulations [10]. A typical time of cascade simulation was equal to 0.15 ns. Intermediate and final configurations of the formed vacancies and self-interstitial atoms were analyzed by the Wigner-Seitz cell method, see details e.g. in [11]. A simple definition of a cluster of point defects is used. If two point defects are in the adjacent Wigner-Seitz cells, they are considered to be connected. Continuous chain of connected point defects forms a cluster. At least 150 cascades were generated for each temperature-energy point.

Figure 1 shows the temperature dependence of the reduced enthalpy of simulated Zr initially arranged in a perfect bcc lattice. The calculated enthalpy was shifted by 6.5 eV which is approximately equal to the magnitude of cohesive energy in a perfect Zr. Stepwise cooling results in a β→α transformation at the temperature M_F = 500 K, and subsequent heating brings the system back to the austenite bcc structure at A_F = 1550 K. Transition temperatures M_F and A_F depend on the cooling/heating rates. For the larger rate the hysteresis becomes broader. A local structure analysis of the phase transformation indicates that the new phase is nucleating in the vicinity of an external surface and then rapidly extends into the bulk. Such heterogeneous nucleation is observed for both β→α and reverse α→β transformations. Due to the unconstrained nature of the dynamics and relatively small sizes of the simulated systems all twin boundaries are annealed in short times. The thermodynamic hcp-bcc martensite transition temperature of about $T_{\alpha\beta}$ = 1230 K was derived from the simulation of coexisting phases [12].

Periodic boundary conditions significantly inhibit the phase transitions: the temperature M_F is shifted below 200 K and A_F rises above the melting temperature T_m. A wide hysteresis of properties of the simulated Zr opens sufficient temperature window for the study. In fact, a nanosecond time scale both bcc and hcp Zr lattices are quite stable in the temperature range from 500 to 1500 K. Furthermore, the generically metastable fcc lattice of zirconium is also sufficiently stable at the simulation conditions. To ensure the stability of bcc and hcp allotropic forms of zirconium the simulation temperature should be close to the transition temperature $T_{\alpha\beta}$. Considering the stability of the fcc lattice the simulation temperature was taken as 1100 K. Test runs at 900 K and 1200 K demonstrate very similar results.

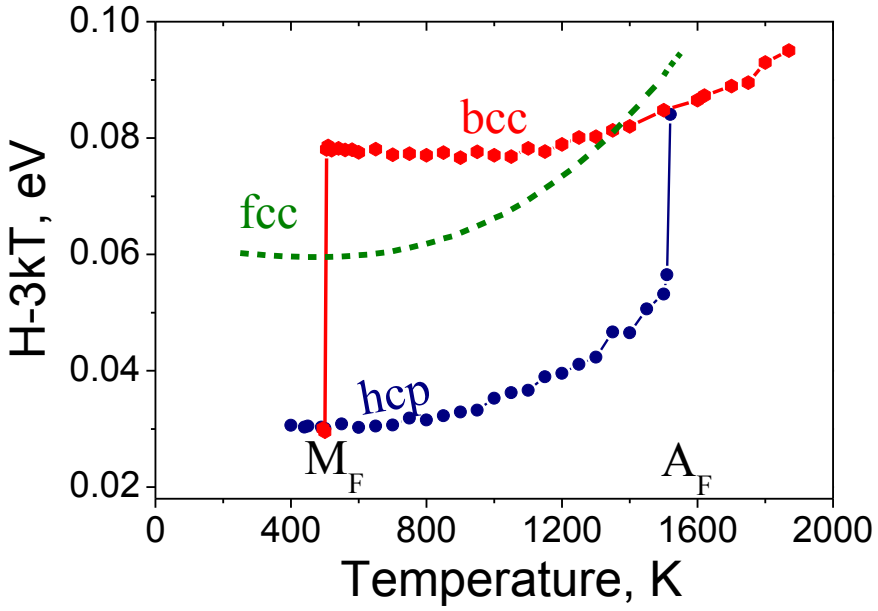

Fig. 1. Temperature dependence of the reduced enthalpy for a finite size system. Contributions of surface and near-surface atoms are ignored here. The annealing time was 0.08 ns at each temperature point. At a temperature step of 10 K this corresponds to the effective cooling/heating rate of 10^{11} K/s. Dashed line shows the same dependence for fcc lattice. The solid lines are drawn as guides for the eyes only.

Figure 2a shows the dependence of the average number of surviving Frenkel pairs on the cascade energy for different Zr lattices. The data is conveniently presented as the ratio to the NRT number of displacements, Fig. 2b. These dependencies for bcc and hcp lattices are found to be very close, particularly for high-energy cascades with E_{PKA} > 1 keV. The numbers of Frenkel pairs in fcc lattice are always below bcc data. It seems that this difference is simply due to lower threshold displacement energy in fcc crystal. We can conclude that a lattice type has a weak effect on the total number of point defects generated in cascades.

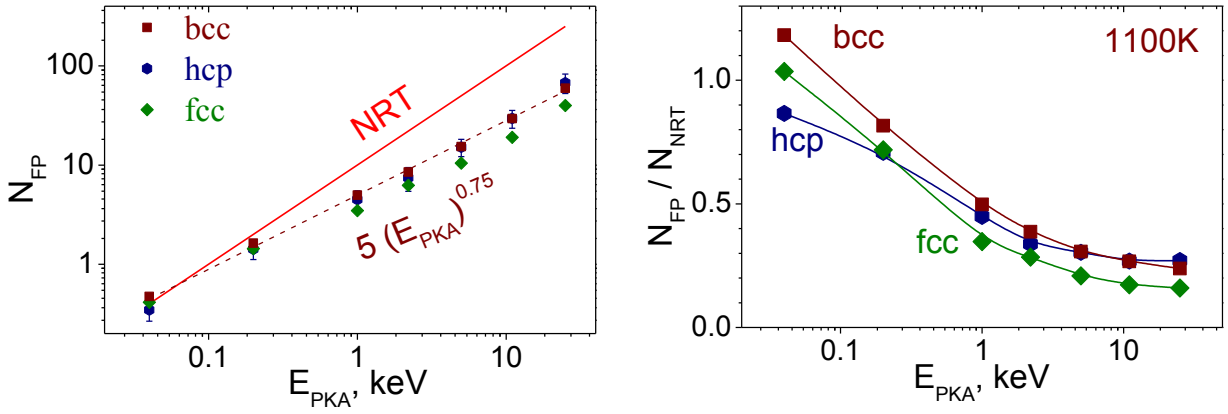

Fig. 2. (a) The number of Frenkel pairs vs the PKA energy in Zr lattices. Dashed lines show best-fit for hcp by the relations $N_{\mathrm{FP}} = 5 \cdot (E_{\mathrm{PKA}})^{0.75}$. The solid line shows the NRT dependence at the recommended values of the effective displacement energy $E_d = 40$ eV. (b) Defect formation efficiencies in bcc, fcc and hcp Zr lattices. The lines are drawn as guides for eyes only.

According to the generally accepted view, the point defects initially generated in the collision stage of the cascade are likely to be partitioned into three portions during the cooling down stage: those that recombine; those that cluster; and those that escape the cascade region and undergo long range migration [13]. Clustered defects can significantly change the character of radiation damage accumulation. As a rule, vacancy clusters appear in the form of immobile 3-dim voids while self-interstitial clusters are highly mobile and they migrate in a highly anisotropic, one-dimensional manner [14].

By *P(n)* we denote the average number of clusters per cascade, containing *n* point defects. Positive *n* are assigned to SIAs and negative *n* correspond to vacancies. Let the total number of formed Frenkel pairs be N_{FP}, then the numbers *P(n)* are related as:

$$\sum_{n=-\infty}^{-1} |n| P(n,E) = \sum_{n=1}^{\infty} n P(n,E) = N_{\mathrm{FP}}(E).$$

Here, we explicitly highlighted the dependencies $P(n,E)$ and $N_{\mathrm{FP}}(E)$ on the PKA energy E. Let us write the density of clusters of size n as

$$\rho(n,E) = \frac{1}{N_{\mathrm{FP}}(E)} |n| P(n,E).$$

The distribution $\rho(n,E)$ is normalized so that the sum over all positive or negative n is equal to one. In other words, the magnitude of $\rho(n,E)$ is the fraction of created vacancies (SIAs) in clusters of size n. For instance $\rho(-1,E)$ is the fraction of freely migrating single vacancies, whereas $1-\rho(-1,E)$ is the fraction of clustered vacancies.

Figures 3a-3c show the simulated distributions of cluster sizes in different Zr lattices depending on the PKA energy. In the *hcp* lattice the majority of both vacancies and SIAs are collected in clusters. This takes place for all cascade energies presented in Fig. 3a, i.e. about 70% of vacancies and 60% of SIAs are found to be clustered at $E \geq 5$ keV. With decreasing PKA energy the clustered fraction decreases, but even for $E = 1$ keV it is still about 50%. Visual inspection shows that both vacancy and SIA clusters form dislocation loops. No perceptible fraction of 3-dim voids was detected.

In the *bcc* lattice, single vacancies and single SIAs are the majority of formed point defects. The total fraction of clustered SIAs is found to be only about 1% at high PKA energies. The distribution

$\rho(n,E)$ decreases sharply for negative n (vacancies) up to n = -3 (tri-vacancy) and then stays nearly invariable up to the cluster sizes n = -40. Large vacancy clusters form 3-dim voids.

In the *fcc* lattice the fraction of clustered vacancies is about 70%, i.e. as many as in the hcp lattice, however large vacancy clusters form 3-dim voids as in bcc lattice. The fraction of the clustered SIAs is about 40%, more than 5% of which belong to SIA loops with sizes n >10. These loops are slidable and demonstrate fast 1-dim diffusion.

It should be noted that the defect distributions in all the lattices shown in Figs. 3a-3c are only weakly dependent on cascade energy for small cluster sizes. For example in the fcc lattice, for PKA energies E > 2 keV, the distributions $\rho(n,E)$ nearly coincide in the range of cluster sizes $(-10<n<5)$ within the statistical accuracy of the simulation. Differences between distributions for these energies are manifested only in the extension of distribution tails with increasing the PKA energy. This observation is valid for all allotropic forms of zirconium and confirmed by known data for iron and nickel. We assume that distributions have approximate invariance with respect to PKA energy E.

Fig. 3d clearly shows the distinctive difference between point defect distributions in bcc and fcc lattices. The existence of a large fraction of mobile SIA loops in the fcc lattice supports an effective separation of vacancy and SIA fluxes through the so-called 'production bias' [13], which may explain the greater susceptibility of fcc lattice to swelling as compared to bcc lattice.

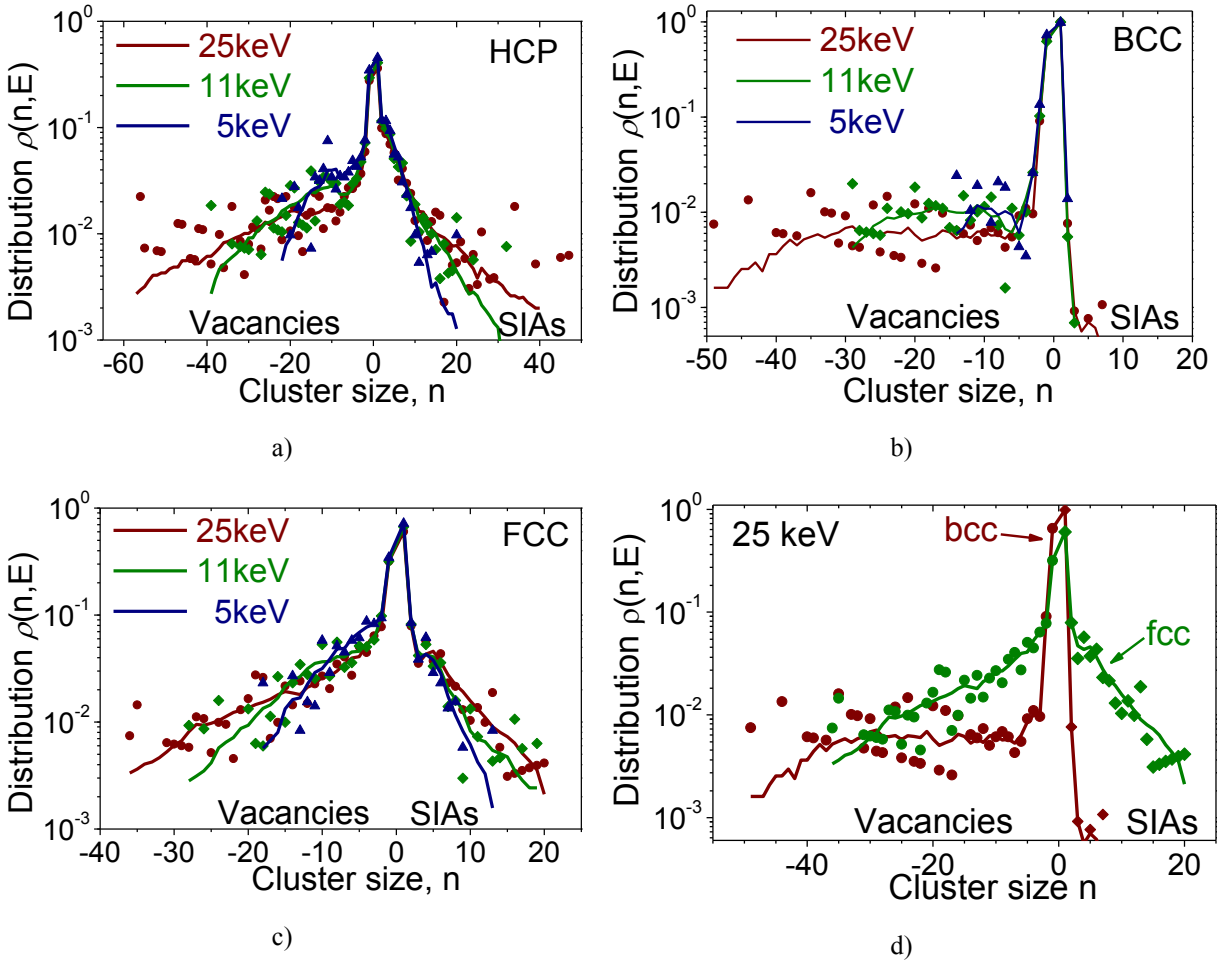

Fig. 3. Cluster size distributions in a) hcp, b) bcc, c) fcc Zr lattices at PKA energies of 5, 11 and 25 keV; d) comparison of distributions in bcc and fcc lattices at PKA energy 25 keV. The lines depict smoothed data calculated by simple moving average method.

Conclusions

- the simulation of primary damages in hcp, bcc and fcc Zr lattices directly demonstrates the effect of lattice symmetry on the morphology of the created defects;
- the size distributions of the created defect clusters were calculated for various allotropic forms of Zr; the approximate invariance of these distributions with respect to PKA energy was observed;
- the tendency of lattices to swelling correlates with the relative fraction of movable SIA loops in total primary damages.

References

1. F.A. Garner, M.B. Toloczko, B.H. Sencer, J. Nucl. Mater. 276 (2000) 123-142.
2. M.B. Toloczko et al, J. Nucl. Mater. 453 (2014) 323–333.
3. D.J. Bacon, F. Gao, Yu.N. Osetsky, J. Nucl. Mater. 276 (2000) 1-12.
4. R.E. Stoller, in: Comprehensive Nuclear Materials. Vol. 1. Elsevier Press. 2012. 293–332.
5. M.J. Norgett, M.T. Robinson, I.M. Torrens, Nucl. Engineering and Design 33 (1975) 50-54.
6. L. Malerba, J. Nucl. Mater. 351 (2006) 28–38.
7. N.P. Lazarev, A.S. Bakai, J. Supercrit. Fluids 82 (2013), 22-26.
8. N.P. Lazarev, C. Abromeit, R. Schäublin, R. Gotthardt, J. Appl. Phys. 100 (2006) 063520.
9. M.I. Mendelev, G.J. Ackland, Phil. Mag. Lett. 87 (2007) 349–359.
10. K. Nordlund, Computational Materials Science 3 (1995) 448-456.
11. R.E. Voskoboinikov, Yu.N. Osetsky, D.J. Bacon, J. Nucl. Mater. 377 (2008) 385–395
12. J.R. Morris, C.Z. Wang, K.M. Ho, C.T. Chan, Phys. Rev. B49 (1994) 3109-3115.
13. C.H. Woo, B. N. Singh, Phil. Mag. A65 (1992) 889-912.
14. B.D. Wirth, G.R. Odette, D. Maroudas, G.E. Lucas, J. Nucl. Mater. 244 (1997) 185-194.

Summary of 2nd RCM meeting of CRP on Primary Radiation Damage Cross-Section, D. Terentyev

SCK-CEN, Belgian Nuclear Energy Research Centre
Mol, Belgium

1. Overview of work 2013-2015

a. Executive summary

Primary damage due to displacement cascades (10 - 100 keV) has been assessed in Fe-1%Mn-1%Ni-0.5%Cu and its binary alloys by molecular dynamics (MD), using a recent interatomic potential, specially developed to address features of Fe-Mn-Ni-Cu system in dilute limit. The latter system represents the model matrix for reactor vessel pressure steels. The potential applied reproduces major interaction features of solute with point defects in the binary, ternary and quaternary dilute alloys. As compared to pure Fe, the addition of one type of a solute or all solutes together does not change the major characteristics of primary damage. However, the chemical structure of the self-interstitial defects is strongly sensitive to the presence and distribution of Mn in the matrix. 20 keV cascades were also studied in the Fe-Ni-Mn-Cu matrix containing <100> dislocation loops (with density of 10^{24} m^{-3} and size 2 nm). Two solute distributions were investigated: random and obtained by Metropolis Monte Carlo in our previous work. The presence of the loops did not affect the defect production efficiency but slightly reduced the fraction of isolated self-interstitials and vacancies. The cascade event led to the transformation of the loops into ½<111> glissile configurations with a success rate of 10% in the matrix with random solute distribution, while all the pre-created loops remain stable in the Monte-Carlo "relaxed" crystal.

b. Background

The displacement cross section is a reference measure used to characterize and compare the radiation damage (in terms of lattice defects) induced by neutrons and charged particles in crystalline materials. Norgett-Torrens-Robinson (NRT) standard [1] proposed 40 years ago has been recently revisited with the aid of modern computer simulation techniques such as combination of Molecular Dynamics and Monte Carlo simulations (for review in Iron see [2]), based on the interatomic models fitted using first principle calculations and experimental data. In the case of such important nuclear material as body centred cubic Iron (BCC Fe), it has been shown that the number of survived defects as compared to the NRT prediction is systematically lower and the discrepancy depends on the recoil energy [3]. A similar result was obtained for BCC Fe-Cr solid solution [4]. These and many other studies done by now have clearly demonstrated how modern computational material science techniques may contribute to the upgrade of nuclear cross-section database and to the understanding of primary radiation damage processes in metallic materials.

Most of the studies performed in bcc Fe were in fact addressing Fe-based structural alloys among which there are high-Cr steels (for fusion and GEN IV reactors) and Reactor Pressure Vessel (RPV) steels. The primary radiation damage phenomenon (PRD) in the latter type of steels is the subject of the present contribution. The need to understand radiation damage in RPV steels is driven by the radiation-induced hardening which must be kept at the acceptable level for the safe exploitation of the vessel (see e.g. [5]). Historically, the hardening was associated to the formation of Cu-containing precipitates (accelerated by the radiation produced defects), hence Fe-Cu binary was conventionally taken as model material for RPV steels [6]. With the appearance of fine microstructural characterization techniques it has been recognized that Cu-precipitates formed under irradiation contain significant amount of vacancies [7, 8], so pure Cu precipitates formed upon thermal ageing are not representative to study embrittlement of RPV steels. At the same time, an in-depth mechanical and microstructural characterization concluded that experimentally measured hardening in RPV steels cannot be explained by the detectable microstructural features and further detailed investigation of the invisible damage needs to be assessed [9]. Application of Topographic Atom Probe and Positron Annihilation Spectroscopy provided new information on chemical composition of agglomerates, possibly responsible for the hardening. Analysis of different types of RPV steels revealed the presence of Mn and Ni enrichment [10]. That information has totally fitted in the conventional correlation models applied to assess the hardening in RPV surveillance programme [11]. However, the particular atomic structure of the solute-rich containing high percentage of Mn and Ni remains unclear.

A massive campaign combining experimental and theoretical studies has been initiated in the frame of FP7 European programme (EP 'Perform60'), addressing the issues of safety of Light Water Reactors and prolongation of their lifetime. A number of experiments, addressing evolution of microstructure and subsequent hardening in Fe, Fe-Cu, Fe-Mn-Ni, PRV steel, was performed [9]. The experiments did not reveal the presence of visible damage in RPV steels, in line with previous work, while dislocation loops were observed in all model alloys. The numerous formation Mn-Ni-rich clusters was confirmed in model alloys and RPV steel. Importantly, the density and size of invisible defects is comparable in the model alloys and RPV steel. Eventually, hardening in pure Fe and model alloys is severely determined by the formation of TEM-visible dislocation loops, while their growth is somehow suppressed in RPV steel (which nevertheless shows essential hardening). One may therefore assume that solute-rich clusters containing Mn and Ni atoms are associated with small but numerous dislocation loops (with spacing of ~10 nm), which at the end significantly contribute to the hardening of RPV steels.

If one accepts the above proposed picture, every high energy cascade event will occur in the material containing a high density of pre-existing nano-voids and dislocation loops. What could be the role of the pre-existing nanostructural defects (significantly enriched with solutes) in the establishment of the primary damage state is the subject of this work. To address this question it is necessary to understand how the primary damage evolves in pristine (i.e. defect-free) RPV-model alloy and in the matrix with pre-existing solute-decorated loops. Naturally, these atomic scale studies will require a reliable interatomic potential, which is now available as a result of the above mentioned project.

In this work, we extend the database on primary damage effects by considering Fe-Cu, Fe-Ni, Fe-Mn and Fe-Cu-Ni-Mn alloys. The composition of the alloying elements will be chosen so as to be relevant for the RPV steels. A parametric MD study will be done to investigate the evolution of collision cascades in the crystals containing Ni-Mn(-Cu) solutes associated with dislocation loops by taking the physically-relevant initial atomic configurations, obtained in the recent studies. The effect of the solute-rich nano-structures on the total number of survived Frenkel pairs, their clustered fraction, morphology of point defect clusters, etc. is studied.

c. Applied interatomic model

The details of the fitting procedure and validation of the Embedded Atom Method (EAM) interatomic potential for Fe-Ni-Mn-Cu system used in this work can be found elsewhere. Herein only the highlights will be summarized.

All details regarding the development of the interatomic potential are described in our recent work [12]. Here we concentrate only on the essential features that were considered in the process of the derivation. The potential is made using Embedded Atom Method formalism [13] and itself it is a central force many body potential. The Fe-Cu and Fe-Ni-Cu potentials were developed in the preceding years and the main accent was made on the correct solubility limit of Cu and Cu-Ni, and in general on the consistence with the thermodynamic behaviour [14]. A number of Monte Carlo studies has shown that the precipitation of Cu in Fe-Cu and in Fe-Cu-Ni alloys is very well described by the potentials, concluded on the basis of the agreement with experiments [15, 16]. The Fe-Cu-Ni potential was also exploited for the investigations of the hardening due to Cu-vacancy-rich clusters (with and without Ni) [17]. There it was concluded that hardening due to Cu-rich vacancies is not sufficient to explain the experimental result in RPV steels. The interaction of point defects and solutes was carefully fitted using ab initio data (and some limited experimental evidence). The quaternary FeCuNiMn potential is based on the extensive DFT dataset on solute–solute and solute-point defect interaction. Certain experimental data (e.g. phase diagrams) were used to validate the potential. The reference DFT data on solute–solute interaction reveal that, while Mn–Ni pairs and triplets are unstable in bcc Fe matrix, larger clusters are actually kept together by the collective attractive interaction. That implies that initial seeds for the nucleation of Mn-Ni clusters is necessary to induce a considerable segregation (as obtained experimentally). Thus, the formation of thermodynamically stable Mn–Ni-rich phases in Fe is actually possible under cascade damage irradiation, which generate nanometric dislocation loops, proven to be strong enough defects to induced heterogeneous nucleation of solute clusters [12].

To investigate the effect of solute-rich clusters we have considered several crystals specially prepared by introduction of dislocation loops and solutes. The decoration of the solutes by loops was obtained by performing Metropolis Monte Carlo (MMC) simulations in relevant temperature range, following our early works [18-20]. Summary of the crystals used in the present study is given in Table 1.

Table 1. Nomenclature of the crystals used in MD simulations.

Name	**Composition**	**Remark**
RPV	Fe-1.3Mn-0.7Ni-0.05Cu	Random distribution of solutes
Binary	Fe-1Ni, Fe-1Cu, Fe-1Mn	Random distribution of solutes
M1	Fe-1Mn-1Ni-0.5Cu	Random distribution of solutes
M2	Fe-1Mn-1Ni-0.5Cu	MMC at 500K to get Mn-Ni-Cu precipitate
M3	Fe-1Mn-1Ni + <100> loop	MMC at 600K
M4	Fe-1Mn-1Ni-0.5Cu + <100> loop	MMC at 600K
M5	Fe-1Mn-1Ni-0.5Cu + <100> loop	Random distribution of solutes

By inserting the dislocation loop in a crystal, a strain field is generated around the edge of the dislocation and on its habit plane. Previous MMC calculations have shown that depending on ambient temperature, solute concentration and Burgers vector, different solute arrangement may form on the loop habit plane [12]. Example of such solute segregation is given in Fig. 1, where both solute enrichment and stress-state near the loop is shown.

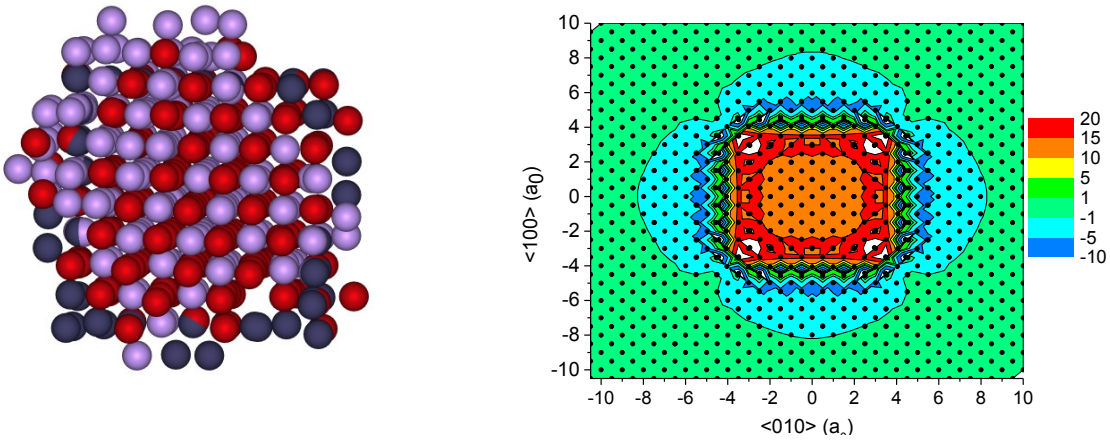

Fig. 1. (a) Representative examples of heterogeneous Mn-Ni precipitation on a <100> loop, blue and red are Mn and Ni solutes respectively; (b) – Pressure maps calculated from the potential a 2 nm <100> dislocation loop.

Since here we are primary interested in the low concentration mode, it is convenient to draw the solubility limit for the formation of Mn-Ni-Cu clusters in the ternary system with and without the dislocation loop. One can see that in the defect-free random alloy the solubility limit is already above 500K, meaning that no formation of solute clusters is expected in the range of reactor vessel temperature. However, if the high density (10^{24} m^{-3}) of dislocation loops is added – the solubility threshold shifts up to 700K, at least. This information was put as a basis for the selection of different crystals where the primary damage was explored. Thus, Table 1 summarizes five different types of crystals, which exhibit principally different types of solute-formed microstructures.

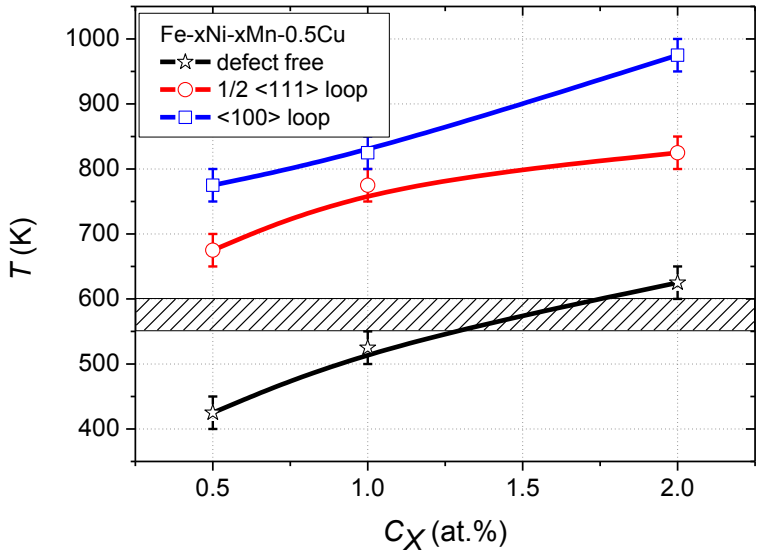

Fig. 2. Local solubility limit of Fe-xNi-xMn-0.5Cu with and without dislocation loop present.

Finally, we would like to note that solutes explored in the present study exhibit rather different interaction sign and strength with point defects. The binding energy for solute-defect interaction in BCC Iron is summarized in Table 2. One sees that Cu and Ni exhibit weak to moderate binding to a vacancies. At this, Cu atom has a stronger binding energy in the 2nd nearest neighbour site, which makes it a stronger (and "wider") trap for vacancies as compared to Ni. Mn has neutral interaction with vacancies but very strong attractive energy with SIAs forming mixed Fe-Mn dumbbells as well as forming Mn-Ni foreign dumbbells and <111> Fe-Mn crowdions. Contrary to that Ni and Cu do not favour the formation of mixed SIAs with <110> dumbbell or <111> crowdion configuration.

Table 2. Binding energy (eV) of solutes with point defects.

	Vacancy	Self-interstitial
Cu	0.1 - 0.2 (1st and 2nd nearest neighbour)	Repulsive
Ni	0.1	0.1 (in tensile region)
Mn	0.02	0.37

d. Cascade simulation

The above-described potential was implemented in the classical MD code Dymoka, which is suitable for the simulation of displacement cascade [21]. Prior to initiating the cascade, a block was equilibrated for 1 ps at 300 K. This initial atom block was then used as starting point for cascade simulation and reference for defect analysis. The cascade was initiated by imparting a kinetic energy E_{MD} to the selected primary knock-on atom (PKA) along a high-index direction such as ⟨135⟩ following the standard practice. The cubic box size, simulated time and number of cascades versus E_{MD} are summarised in Table 3. No electronic stopping or electron-phonon coupling was included in the simulations and all results were obtained in the NVE microcanonical ensemble, with periodic boundary conditions. It is indeed accepted that the final simulation temperature rise scarcely influences the defect population generated in displacement cascades in Fe. This temperature rise, which varies as a function of E_{MD} and the produced defect distribution, was at any rate in no case seen to exceed about 100 K.

Table 3. Summary of MD cascade simulation setup.

Energy (keV)	Simulation time (ps)	No. (successful) cascades	Box side (in a_0)	Atoms in the box (10^3)
10	30	10	50	432
20	30	10	65	~550
50	30	10	73	~780
100	50	10	100	2000

The evolution of the cascades was followed by studying selected representative snapshots. Intermediate and final atomic configurations were analysed to detect and count defects, using a Wigner-Seitz cell method: an empty cell corresponds to a vacancy, while two (or more) atoms in the same cell correspond to a self-interstitial configuration. Chemical composition of individual and clusterized SIAs was identified and recorded as well. The morphology of defects was monitored using appropriate visualization tools.

Clusterization of vacancies and SIAs was defined using a 3rd nearest neighbour (nn) and 2nd nn criterion truncation distance, respectively. The application of a sharp cut-off distance for the identification of SIA clusters has been seen to underestimate by about 10-20% the fraction evaluated through visual inspection. The trend remains however unaffected, so that its use allows a consistent and rigorous comparison between different cascade events.

Following the previous works in Fe and Fe-Cr alloys, the interstitial clusters were identified to form in cascades according to at least three mechanisms, namely: at the end of the thermal spike, as a consequence of collective atomic motion due to the enhanced defect diffusion; SIA coalescence driven by elastic interaction. A considerable solute-SIA interaction is expected to influence both of these mechanisms and therefore, we expect to see the difference in the clusterized SIA fraction and chemical composition depending on the matrix composition and spatial solute arrangement. In addition, large interstitial clusters may form when a high-density part of the liquid is isolated by a recrystallization front, which should not be affected by the presence of solutes.

At the end of the cascade, after relaxation, only a reduced fraction of the Frenkel pairs produced at peak time survives the thermal-spike-enhanced recombination process. We shall report the final number of survived Frenkel pairs, ν_{FP}, and so called production defect efficiency, η, referring to the NRT value. Thus, $\eta = \nu_{FP}/\nu_{NRT}$, where $\nu_{NRT} = 0.8E_{PKA}/2E_d$, and E_d is the average threshold displacement energy (40 eV) and E_{PKA} is the damage energy.

The evolution of ν_{FP} as a function of E_{PKA} has been proven to follow the empirical power law proposed by Bacon and co-workers, so as $\nu_{FP}^{end} = A \cdot E_{MD}^{m}$. The MD results are approximated by this formula, the coefficients are given in Annex 1. The defect production efficiency, on the other, is known to reduce from unity down to 0.2 - 0.3, as soon as the PKA energy is above 1 keV.

Finally, for the MD cascades initiated in the crystals containing the <100> loops, we have applied visual inspection to reveal the impact on the structure and possible displacement of the loops.

e. Results

The analysis of the results have shown that addition of solutes in all explored configurations did not results in any significant change of the number of survived defects over the whole range of the studied PKA energy as compared to pure Fe. To demonstrate this we limit ourselves to presenting the results for pure Fe and Fe-1%Ni-1%Mn-0.5%Cu random alloy, see Fig. 3. Further comparison between the features of the primary damage state will be shown on the example of the results obtained in the 20 keV cascades, as the principal observations and conclusions were found to be independent on the PKA energy (not surprising given that we studied only the range of high PKA energies).

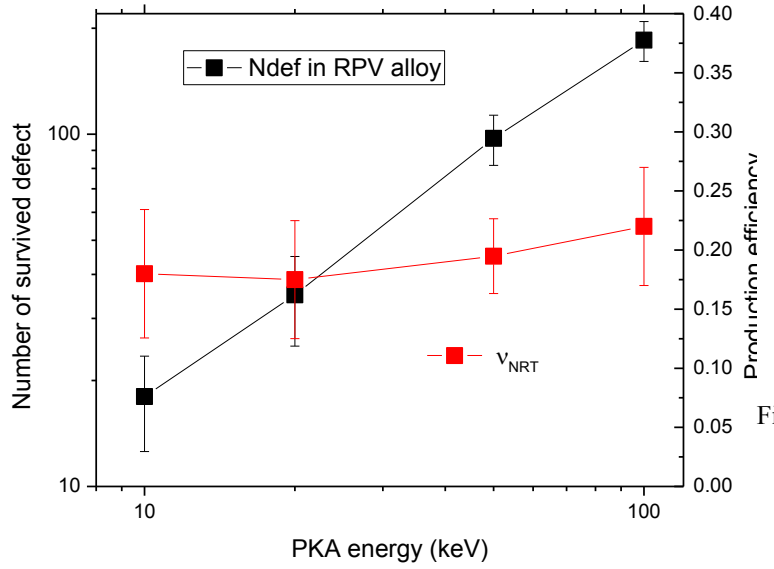

Fig. 3. Number of survived Frenkel pairs and the NRT production efficiency versus PKA energy in random Fe-1%Ni-1%Mn-0.5%Cu alloy.

Fig. 4 demonstrates that the average number of survived defects and production efficiency do not vary (remain within the standard deviation value) irrespective of the presence of solutes (random or ordered state) and pre-existing dislocation loops.

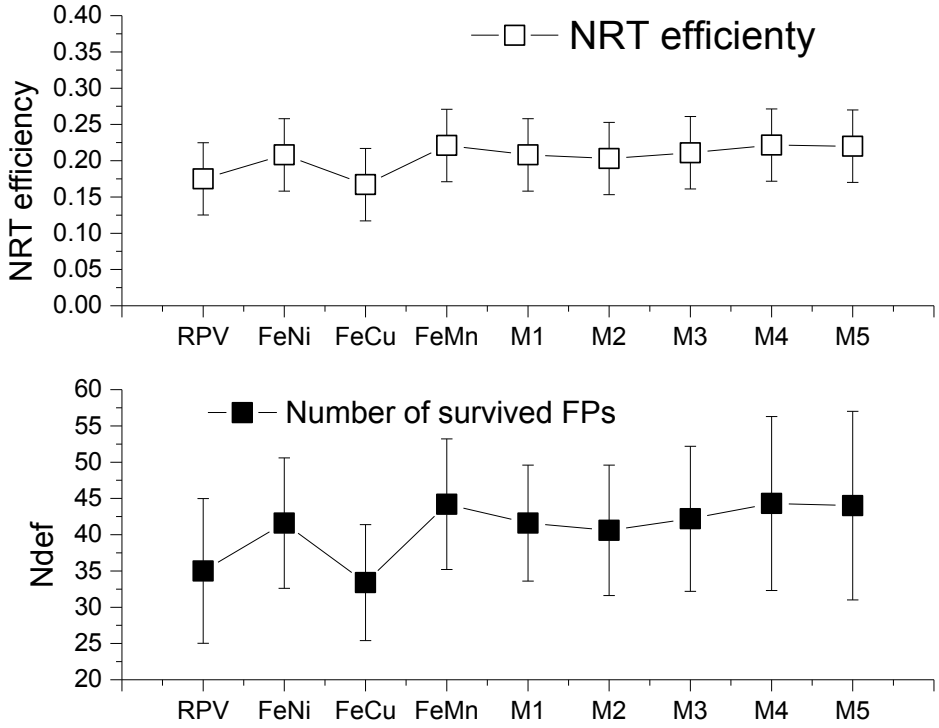

Fig. 4. Number of survived Frenkel pairs and the NRT production efficiency in 20 keV cascades.

Fig. 5 reports the fraction of clusterized vacancies and SIAs. The figure reveals that the fraction of clusterized vacancies and SIAs statistically increases in the matrix containing the dislocation loops (M3, M4, M5). We attribute this effect to the enhancement of recombination of isolated point defects on pre-existing dislocations loops. Clearly pronounced minimum in SIA clustering took place in FeMn alloy, where apparently the trapping of SIAs and their clusters by Mn atoms suppressed the clusterization already at the cascade cooling stage, since Mn is the strongest trap for SIAs among other solutes present in the system. Visible reduction of the vacancy clustering was also observed in Fe-Cu and random RPV-alloy, which also correlates with the fact that Cu is the strongest trap for vacancy. Note that, the vacancy clustering is much higher in the MMC-ed RVP-alloy, which can be explained by the depletion of matrix with Cu, being gathered into Cu-Ni clusters. Maximum of the SIA clustering is observed in Fe-Ni, where the migration of Fe-Ni SIAs was apparently enhanced by the mixed SIA migration.

To facilitate the above discussion, we present the total fraction of foreign SIAs in Fig. 6. The figure reveals that: (i) no mixed SIAs are formed in Fe-Cu binary; (ii) 70-80% of SIAs contain solute in the Fe-Mn system and random RPV-alloy; (iii) fraction of the foreign SIAs is about 10% in Fe-Ni, i.e. ten times higher than the content of randomly distributed solute atoms. In the case of specially prepared matrixes, the content of solutes in SIA clusters is about 20%, again about ten times higher than the solute concentration, but still much lower than in Fe-Mn random alloy. The latter result shows clearly that Mn segregation to dislocation loops or to MN-Ni-Cu clusters does have a statistically measurable effect on the chemical morphology of SIAs in the end of the cascade.

The exact fraction of different types of dumbbells depending on chemical content is presented in Fig. 7. We see that irrespective of the alloy preparation, the most frequent state for SIA is the Fe-Mn dumbbell. A considerable fraction of Fe-Ni and Mn-Ni SIAs is observed in random RPV-alloy. Finally, we must note that mainly Fe-Mn and Mn-Ni SIAs are present in the alloys M1 and M2, while the fraction of Fe-Ni SIAs is negligible.

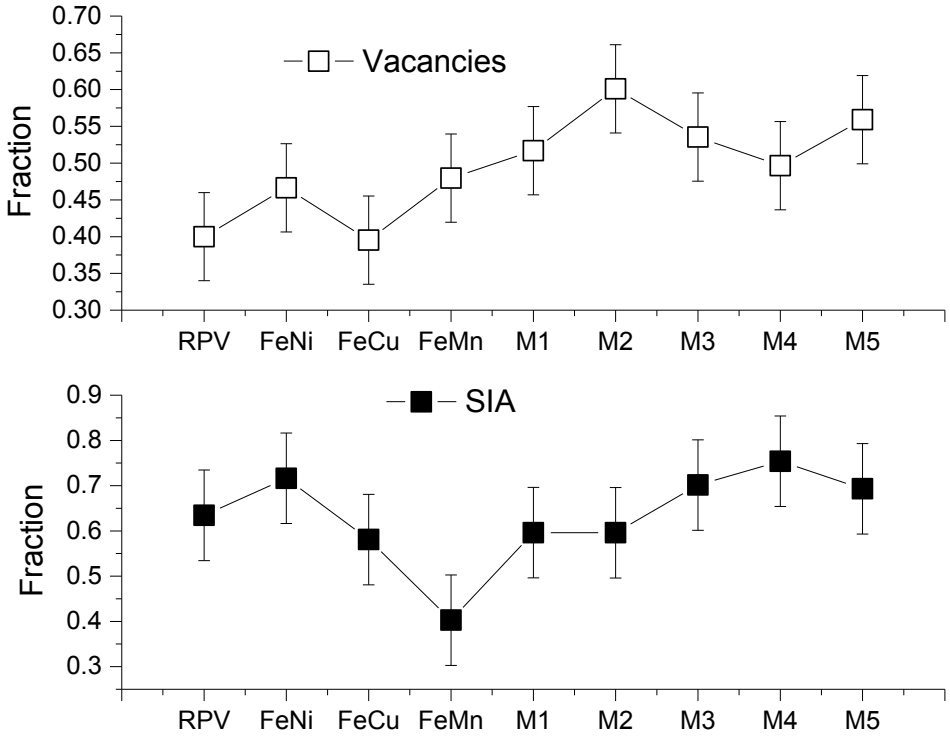

Fig. 5. Clustered fraction of SIAs (above) and vacancies (below) in 20 keV cascades.

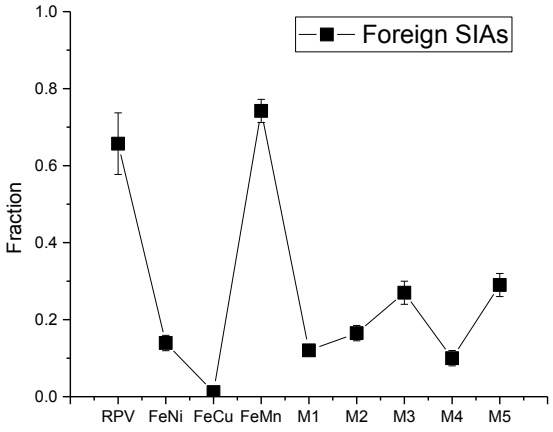

Fig. 6. Fraction of foreign SIAs in 20 keV cascades.

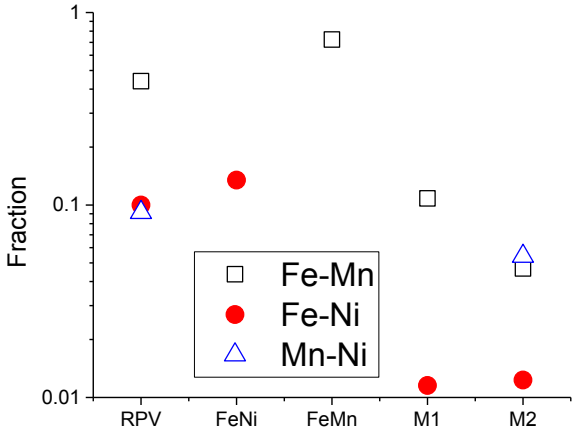

Fig. 7. Fraction of Fe-Mn, Fe-Ni and Mn-Ni SIAs in 20 keV cascades.

Analysis of the impact on the dislocation loop pattern in M3, M4 and M5 alloys was performed by means of visualization tools. Note that all pre-existing loops were of <100> type with the same particular orientation of the Burgers vector. In most of the cases (80-90%) no effect of the collision cascade was seen and the final loop structure was nearly the same initial one, except that some SIAs and small SIA clusters were seen to be attached to the loops (see Fig. 8a). In about 10% of the simulated cascades, the types of microstructural modification were observed, namely: (i) rotation into ½<111> loop (Fig.7b); (ii) coalescence of two loops in one (Fig. 8c); (iii) split of one <100> loop into two of ½<111> type (Fig. 6d).

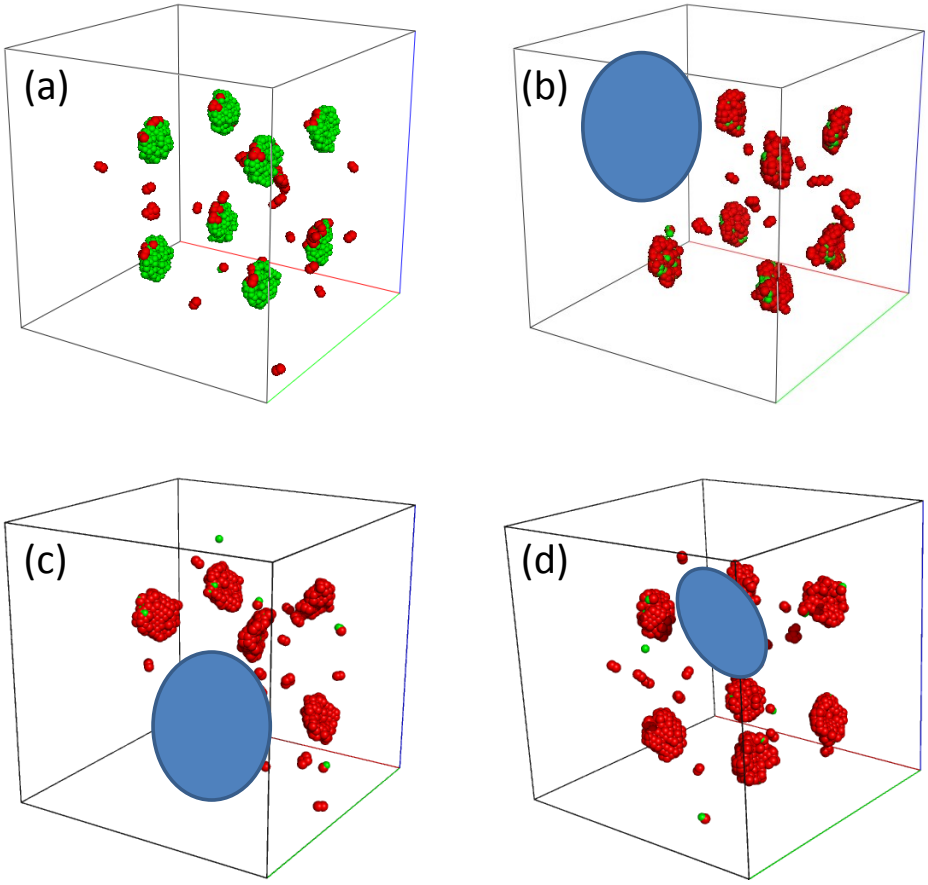

Fig. 8. Examples of final primary damage state (SIA defects shown only) in the matrix containing <100> dislocation loops before and after Monte Carlo relaxation. (a) RPV-alloy MMC 600K, no cascade induced modification to the loop structure; (b) Fe-1Mn-1Ni MMC 700K, transformation into ½<111> orientation; (c) RPV-alloy random distribution (800K MMC), two loops were merged in on; (d) RPV-alloy random distribution, split into two ½<111> clusters.

Probability of these three events (i.e. frequency divided by total number of trials) is drawn in Fig. 9. The analysis revealed that the probability to split the loop is nearly independent on the arrangement of solutes, while the loop rotation and coalescence is fully suppressed in M4 – where the strongest segregation of Mn and Ni is obtained after MMC treatment at 600K. Contrary to that, the highest frequency of the loop transformation occurs in M5 – where solutes are randomly distributed. For that matrix, the cumulative probability of the loop morphology modification as a result of 20 keV cascade is about 20%. These results demonstrate that local arrangement of solutes in the matrix plays a role of "stabilizer" of the <100> loops against their coalescence or transformation into ½<111> type.

Major conclusions, which were made on the basis of the analysis of defect structure and chemistry at the end of the cascade cooling stage (30 ps):

1. Major features of primary damage state are not modified by the alloying, not even by adding high density of dislocation loops.
2. Chemical composition and spatial arrangement of Mn, Ni and copper do affect the fraction of clusterized defects.
2. In-cascade induced loop coarsening, or in-cascade loop destroy.
3. Segregation of Mn and Ni leads to the stabilization of loops against cascade-induced morphologic changes.

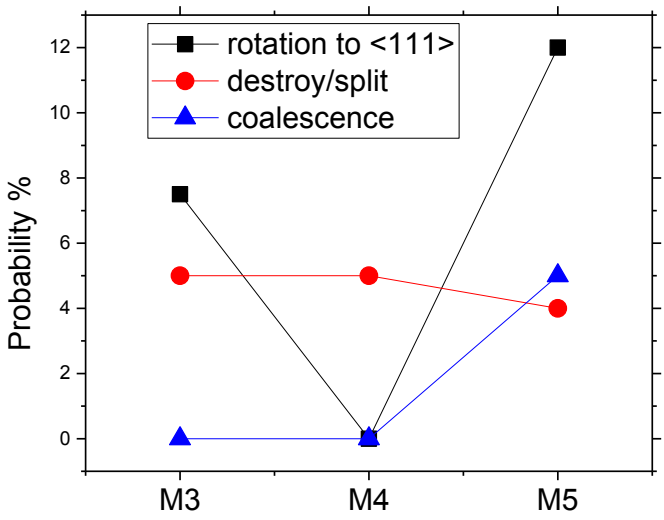

Fig. 9. Statics of the transformation of loops as a result of 20 keV cascades.

f. Summary and conclusions

Displacement cascades in Fe-Ni-Mn-Cu system and its binary alloys have been simulated by molecular dynamics in a range of PKA energies from 10 up to 100 keV. It has been observed that:

- The presence of solutes in all explored configurations does not affect the final population of Frenkel pairs. Fraction of clusterized self-interstitials and vacancies is, however, sensitive to the presence of Ni, Mn and pre-existing dislocation loops.
- It has been observed that the presence of Cu in solution leads to reduction of the vacancy clustering (by about 20%). The presence of Mn leads to the reduction of SIA clusterized fraction by about 20%. The variation in the clusterized fraction in both cases is statistically meaningful.
- Analysis of the interaction of point defects with solute atoms suggests that the above conclusions are connected to the strong affinity of Mn atoms to bound with self-interstitial defects, which manifests itself in a large population of Fe-Mn dumbbells, in proportion well above the Mn concentration in the alloy, as well as in a preferential association of Mn atoms to interstitial clusters. A similar conclusion can be made for Cu-vacancy interaction, which is apparently strong enough to suppress the short range migration of SIA clusters.
- Stability of pre-existing dislocation loops depends strongly on the PKA energy. The higher the PKA energy the more frequent the loop rotation and loop break takes place. Nevertheless, one could clearly see that solute segregation, stabilizes the loops and overall suppresses their rotation and migration.

2. IAEA CRP workplan 2015 - 2016

Within the remaining CRP timeframe 2015-2017, we plan, in collaboration with CRP partners, to:

1. Complete the database on primary damage state in concentrated BCC Fe-Cr and FCC Fe-Ni-Cr alloys relevant for application in fusion and fission. These two alloys are being the model materials for high-Cr ferritic martensitic steels (such as T91, Eurofer, F82H, etc.) and austenitic steels (316, 304, 15-15-2Ti, etc.).

2. Primary damage will be characterized by number of produced Frenkel pairs, size and density distribution of defect clusters and cluster structure. This information will be summarized and collected along the well established data for bcc Fe and fcc Cu.

This way, the database for the primary damage state in the range of damage energy 10 - 100 keV and temperature range 300 - 600K for RPV, ferritic martensitic and austenitic steels will be established.

Annex 1. Fit parameters for the number of Frenkel pairs (N_{FP}) produced in cascades

Number of Frenkel Pairs is approximated as $N_{FP} = A \times E_{MD}^{B}$, and the coefficients are given in the Table below.

Table A1. Coefficients entering the expression to fit the Number of Frenkel pairs survived in cascades, defined as $N_{FP} = A \times E_{MD}^{B}$. The nnomenclature of the crystals used in MD simulations is listed in Table 1.

$N = A \times E_{MD}^{B}$	Fe-Ni	Fe-Mn	Fe-Cu	M1	M2	M3	M4	M5
A = 4.05 (Fe)	4.21	4.78	4.34	4.3	4.1	3.98	4.5	4.23
B = 0.86 (Fe)	0.85	0.83	0.91	0.9	0.93	0.86	0.95	0.94

References

[1] M. Robinson, I. Torrens, Physical review B, 9 (1974).
[2] L. Malerba, Journal of Nuclear Materials, 351 (2006) 28-38.
[3] D. Bacon, A. Calder, F. Gao, Radiat Eff Defect S, 141 (1997) 283-310.
[4] D. Terentyev, L. Malerba, R. Chakarova, K. Nordlund, P. Olsson, M. Rieth, J. Wallenius, Journal of Nuclear Materials, 349 (2006) 119-132.
[5] R. Chaouadi, R. Gerard, Journal of Nuclear Materials, 345 (2005) 65-74.
[6] A. Calder, D. Bacon, Materials research Society Symp. Proc., 439 (1997).
[7] Y. Nagai, K. Takadate, Z. Tang, H. Ohkubo, H. Sunaga, H. Takizawa, M. Hasegawa, Physical Review B, 67 (2003) 224202.
[8] M. Lambrecht, L. Malerba, A. Almazouzi, Journal of Nuclear Materials, 378 (2008) 282-290.
[9] E. Meslin, M. Lambrecht, M. Hernandez-Mayoral, F. Bergner, L. Malerba, P. Pareige, B. Radiguet, A. Barbu, D. Gomez-Briceno, A. Ulbricht, A. Almazouzi, Journal of Nuclear Materials, 406 (2010) 73-83.
[10] T. Toyama, A. Kuramoto, Y. Nagai, K. Inoue, Y. Nozawa, Y. Shimizu, Y. Matsukawa, M. Hasegawa, M. Valo, Journal of Nuclear Materials, 449 (2014) 207-212.
[11] J.D. Varsik, S.T. Byrne, Americal Society for Testing and Materials, ASTM STP 683 (1979) 252-266.
[12] G. Bonny, D. Terentyev, A. Bakaev, E.E. Zhurkin, M. Hou, D. Van Neck, L. Malerba, Journal of Nuclear Materials, 442 (2013) 282-291.
[13] M. Daw, M. Baskes, Physical Review B, 29 (1984) 6443.
[14] G. Bonny, R.C. Pasianot, N. Castin, L. Malerba, Philosophical Magazine, 89 (2009) 3531-3546.
[15] N. Castin, M.I. Pascuet, L. Malerba, J Chem Phys, 135 (2011) 064502.
[16] F.G. Djurabekova, R. Domingos, G. Cerchiara, N. Castin, E. Vincent, L. Malerba, Nucl Instrum Meth B, 255 (2007) 8-12.
[17] D. Terentyev, L. Malerba, Journal of Nuclear Materials, 421 (2012) 32-38.
[18] G. Bonny, D. Terentyev, A. Bakaev, E.E. Zhurkin, M. Hou, D. Van Neck, L. Malerba, Journal of Nuclear Materials, 442 (2013) 282-291.
[19] G. Bonny, D. Terentyev, E.E. Zhurkin, L. Malerba, J. of Nuclear Materials, 452 (2014) 486-492.
[20] D. Terentyev, X. He, G. Bonny, A. Bakaev, E. Zhurkin, L. Malerba, Journal of Nuclear Materials, 457 (2015) 173-181.
[21] C. Becquart, C. Domain, A. Legris, J. Duysen van, J. of Nuclear Materials, 280 (2000) 73-85.

Neutron Spectral Dependence of Radiation Damage Calculations,

L.R. Greenwood

Pacific Northwest National Laboratory
Richland, WA, USA

Introduction

There are many factors that influence the accuracy, applicability, and utility of primary radiation damage calculations such as NRT damage energy and the derived displacements per atom (dpa) or more advanced functions. Such factors must be considered in comparisons of the effectiveness of using alternate damage functions beyond the standard NRT damage energy for the correlation of accumulated radiation damage effects. Some of these considerations are discussed in this report, including reactor dosimetry and fluence and spectral calculations, flux gradients, irradiation history, irradiation temperature, gas production, transmutation, and damage rate effects.

The introduction of NRT damage energy and dpa (displacements per atom) in the 1980s has proven to be very useful for the correlation of radiation damage observed in materials irradiated in very diverse facilities including light water reactors, fast reactors, 14 MeV sources, and higher energy neutron sources such as Be(d,n) and spallation facilities. This correlation is illustrated in Figure 1. From a physics point of view, the reason for the success of such simple functions may be due to the fundamental concept of damage energy, which is defined as the energy available for creating displacement damage in materials following the interaction with a neutron or other particle. The damage energy (T_{dam}) is calculated from the nuclear part of the stopping power. Displacements per atom are then calculated as $0.8 \times T_{dam}/(2 \times E_d)$, where E_d is the average energy required to remove an atom from its lattice site. For any given value of E_d, dpa is simply a constant factor times the damage energy. Consequently, the use of dpa to characterize a given irradiation is completely equivalent to just using the damage energy.

The SPECTER computer code [1] was developed to calculate the damage energy and dpa for over 40 different elements. The code was later extended to include compounds using the SPECOMP computer code [2]. Both the SPECTER and SPECOMP codes are available on the NDS/IAEA web-site https://www-nds.iaea.org/irdf2002/codes/index.htmlx .

Neutron Spectral Considerations

The calculation of dpa for any given irradiation simply involves multiplying the damage cross sections times the neutron spectrum. The accuracy of this calculation is thus directly determined by how well we know the neutron spectrum. The best method for determining the neutron spectrum requires calculation of the neutron spectrum for any given irradiation coupled with neutron dosimetry derived from activation measurements. Spectral adjustment codes such as STAYSL PNNL [3, 4] (also available on the NDS/IAEA web-site https://www-nds.iaea.org/irdf2002/codes/index.htmlx) can then be used to determine the best estimate of the neutron spectrum at the exact location of the irradiation experiment. It is not sufficient to simply use a generic neutron spectrum for a given reactor due to radial and azimuthal flux and spectral gradients.

Authors of papers regarding material irradiation effects should thus provide sufficient detail to document the neutron spectrum used as the basis of dpa (or more advanced damage functions) calculations. The lack of such information in the extensive literature on radiation effects makes it difficult to determine if new proposed damage functions such as arc-dpa or RPA are more useful in correlating radiation damage effects than NRT dpa or damage energy. Other factors such as shielding of materials in a given experiment, the irradiation history, and uncertainties further complicate the reevaluation of prior experiments.

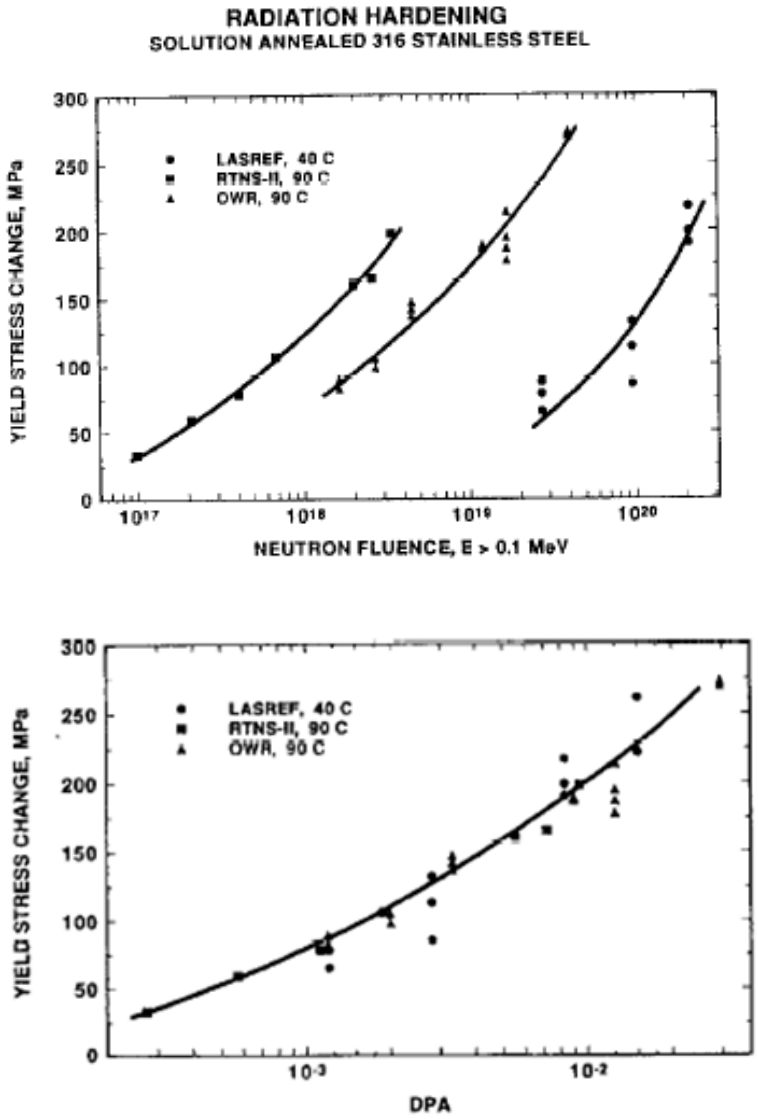

Fig. 1. Comparison of yield stress change in 316 stainless steel following irradiation in three radically different facilities, the Omega West Reactor (OWR) at LANL, the 14 MeV neutron source Rotating Target Neutron Source at LLNL, and the spallation neutron source Los Alamos Radiation Effects Facility at LANL. Note the good correlation with dpa, demonstrating the usefulness of this concept.

Consideration of Other Effects

There are a number of other effects that can strongly influence the evolution of materials damage that may be just as important as dpa. Temperature strongly influences damage accumulation since at very low temperatures damage is "frozen in" whereas at elevated temperatures a lot of the damage is annealed. Consequently, the correlation of radiation damage in different neutron spectra can only be performed if all the damage was generated at the same temperature.

Helium generation is known to strongly influence swelling and embrittlement at higher levels. The ratio of helium generation to dpa was recognized many years ago to be one of the main differences between fission and fusion reactors due to the higher helium generation in fusion reactors from the 14 MeV neutrons. This effect is enhanced in facilities that have been proposed for simulating the higher helium to dpa rations such as the Li or ^{9}Be(d,n) type (IFMIF) and spallation neutron sources. There is also a well-known effect in alloys containing nickel which can generate very high levels of helium from the ^{58}Ni(n,γ)^{59}Ni(n,α) two-step reaction since ^{59}Ni has a high thermal neutron cross section for helium generation. This reaction produces energetic 340 keV ^{56}Fe recoil which leads to a significant increase in damage energy and dpa [5].

This non-linear effect can have a very large impact on damage in nickel-bearing alloys as was seen recently with the unexpected early failure of springs in CANDU reactors, as shown in Figure 2 [6].

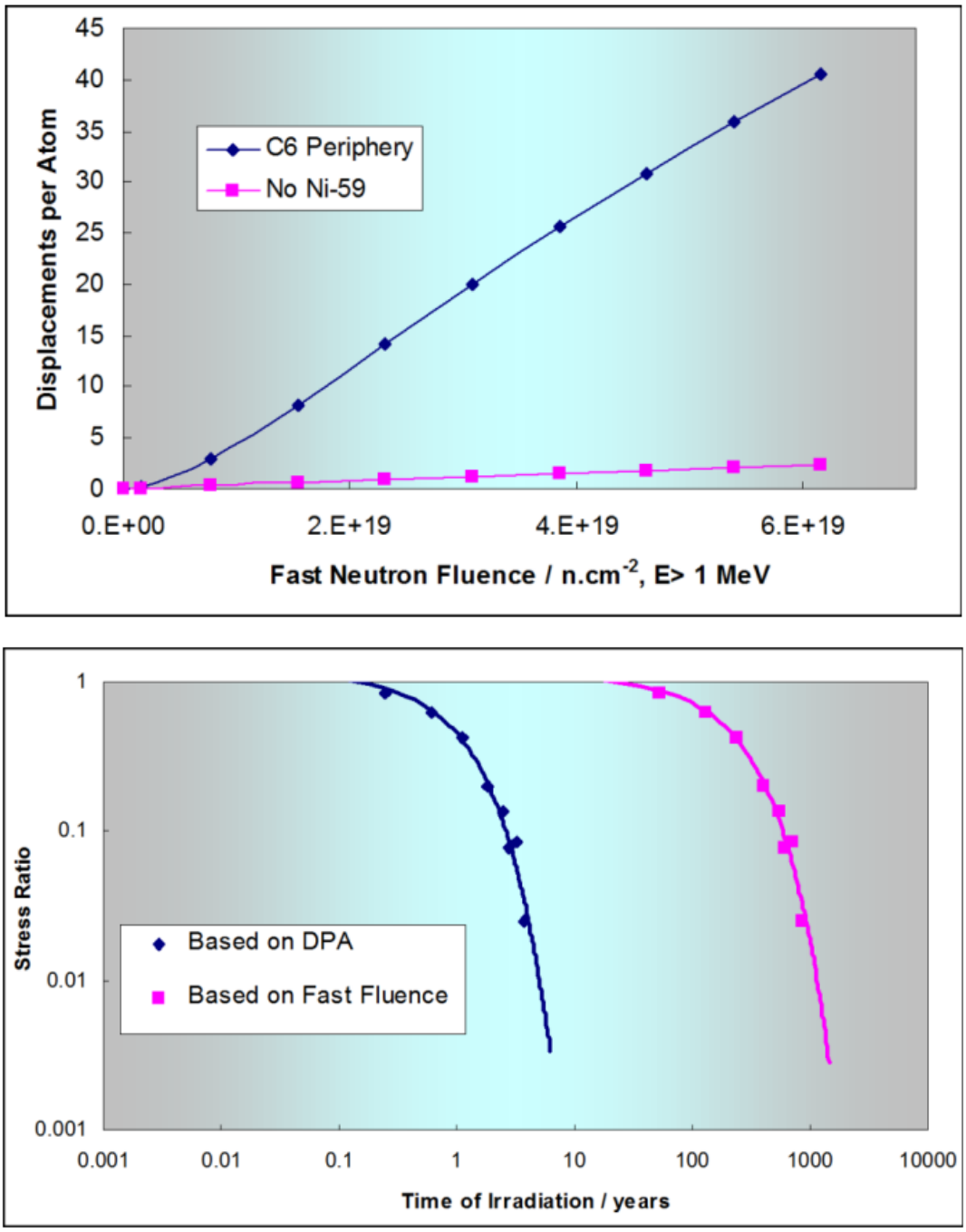

Figure 2. Ni-59 helium production in X-750 increases the dose more than an order of magnitude (top figure) such that the spring is 90% relaxed in a few years, many years before predicted (bottom figure).

Whereas dpa cannot be directly observed in materials, gas production can be easily measured and compared with calculations such that the accuracy can readily be determined, as shown in Figure 3 [7]. Other thermal neutron helium production reactions are well known for ^{6}Li, ^{10}B, ^{55}Fe, ^{65}Zn.

Nuclear transmutation is also a very important consideration since it changes the basic composition of metals or alloys during the course of the irradiation. It should be noted that the highest levels of transmutation are due to thermal neutrons and thus such effects do not correlate with damage energy or dpa which is primarily caused by fast neutrons. For example, the high rate of transmutation of W to

Re and Os varies significantly for different reactors. The thermal to fast neutron ratio can change by large factors both between different neutron facilities as well as at different positions within a facility, especially at out of core locations, as shown in Figure 4.

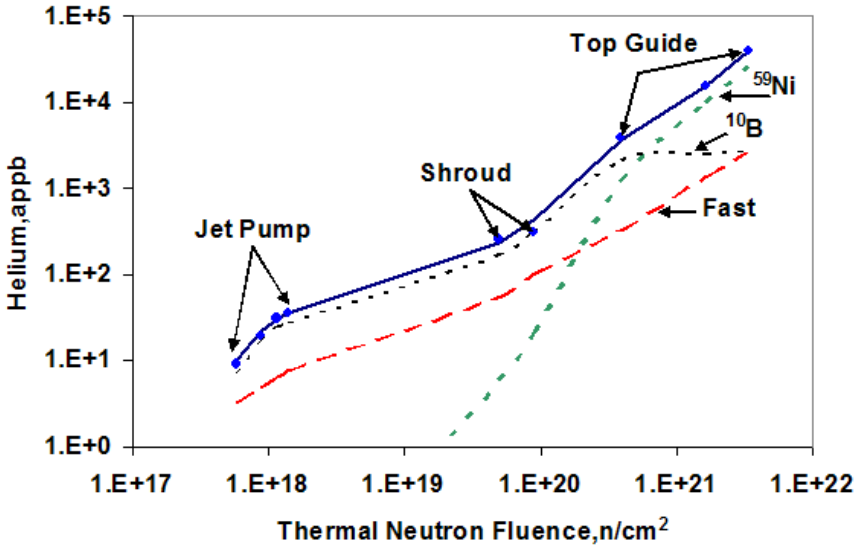

Figure 3. Helium measurements agree very well with calculations for samples removed from BWR reactors over a wide range of neutron fluences [7]. At low fluence the helium is produced by boron; at intermediate fluence fast neutron reactions; and at higher fluences the ^{59}Ni reaction dominates gas production. The solid line at the top is the total helium production for all three reactions.

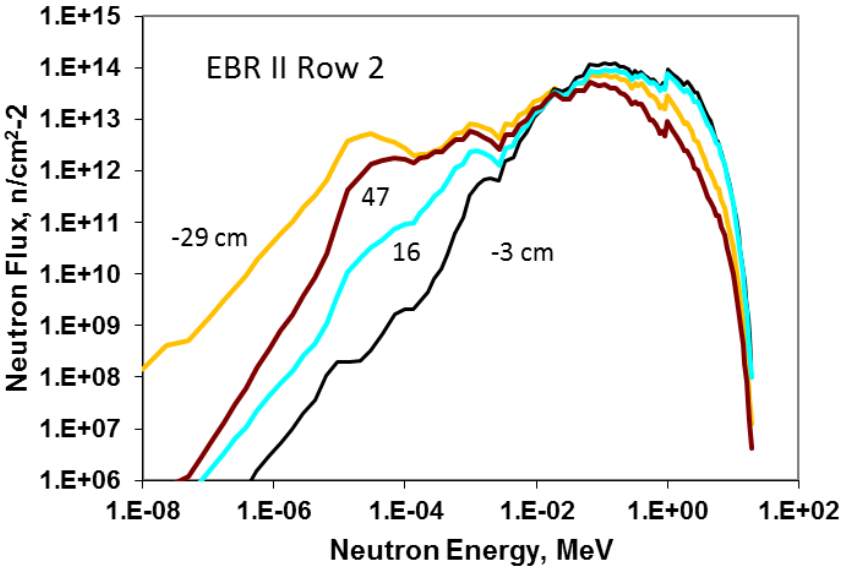

Figure 4. Neutron spectra change significantly at various locations in the Experimental Breeder Reactor II. The increase in the lower energy flux greatly enhances helium production from ^{59}Ni even in a fast reactor.

Damage rate effects also have been shown to strongly influence damage accumulation. This effect is clearly shown in Figure 5 in the recent study of materials irradiated at different rows in EBRII [8].

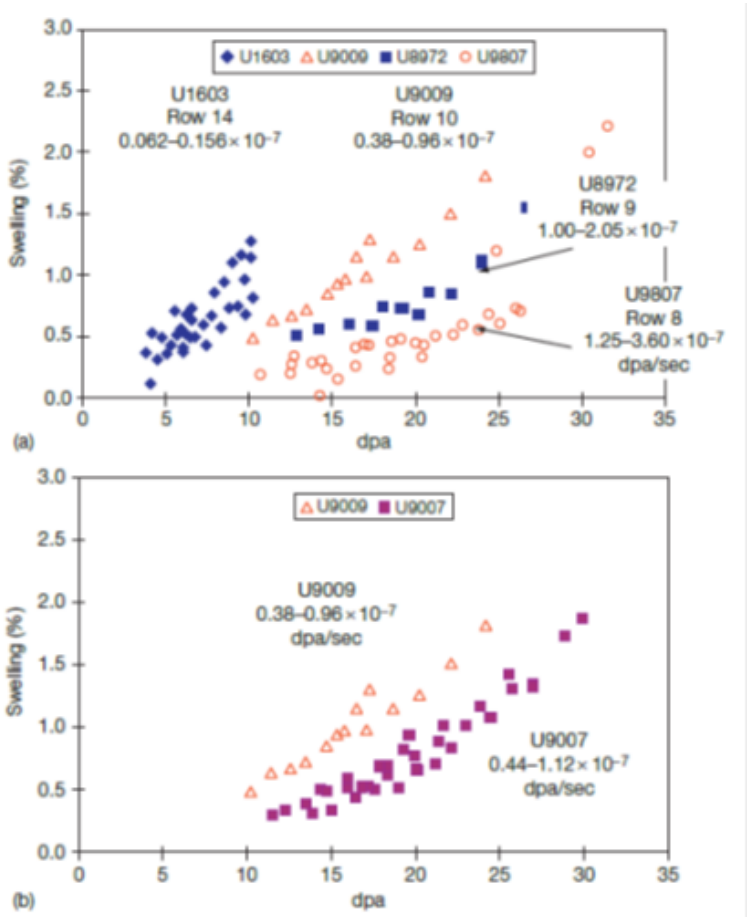

Fig. 5. Swelling of annealed 304 stainless steel in the range 373 – 388°C measured by density changes in the lower halves of EBR-II reflector subassemblies, designated by identification numbers such as U9807. Note that each data set spans a range of dpa rates. (a) Comparison of four subassemblies in different rows of the reactor. (b) Comparison of two subassemblies in Row 10 but on opposite sides of the reactor, with dpa rates varying only rv16%, showing that lower dpa rates lead to an earlier acceleration of void swelling. Reproduced from F.A. Garner, B.J. Makenas, *In Proceedings of Fontevraud-6 Symposium on Contribution of Materials Investigations to Improve the Safety and Performance of LWRs; 2006; p. 625.*

References

1. L.R. Greenwood and R. K. Smither, ANL/FPP/TM-197, (1985).
2. L.R. Greenwood, Radiation Damage Calculations for Compound Materials, Effects of Radiation on Materials, ASTM STP 1046, N.H. Packan, R.E. Stoller, and A.S. Kumar, Eds, ASTM, 1990, p. 633.
3. L.R. Greenwood and C.D. Johnson, User Guide for the STAYSL PNNL Suite of Software Tools, Pacific Northwest National Laboratory Report PNNL-22253, January 2013.
4. L.R. Greenwood and C.D. Johnson, Least-Squares Neutron Spectral Adjustment with STAYSL PNNL, proceedings of the 15th International Symposium on Reactor Dosimetry, Aix en Provence, France, May 2014.
5. L.R. Greenwood, A New Calculation of Thermal Neutron Damage and Helium Production in Nickel, Journal Nucl. Mater. 115, pp. 137-142 (1983).
6. F.A. Garner, L.R. Greenwood, M.N. Gusev, O.P. Maksimkin, "Second-order phenomena in austenitic internal components growing to first order importance at the higher damage levels associated with PWR plant life extension", presented by F.A. Garner at Contribution of Materials Investigations to Improve the Safety and Performance of LWRs, Avignon, France, 27 Sept, 2010
7. L.R. Greenwood and B. M. Oliver, Comparison of Predicted and Measured Helium Production in US BWR Reactors, Journal of ASTM International, JAI13490, Vol. 3, No. 3, March 2006.
8. F.A. Garner, Radiation Damage in Austenitic Steels, Comprehensive Nuclear Materials, Amsterdam, Elsevier, 2012.

Primary damage in pure bcc Fe and FeCr alloys, including the presence of impurities such as He, from molecular dynamics simulations,

M.J. Caturla

Universidad de Alicante
San Vicente del Raspeig, Spain

Introduction

The IAEA CRP working plan for the first year included:

- Damage produced in bcc Fe by recoils of energies between 50 keV and 100 keV.
- Results for bulk cascades as well as thin films.
- Calculations performed with two different interatomic potentials.

During this first year we have performed and analyzed the damage produced by recoils of energies 50 keV and 100 keV in pure b.c.c. Fe using molecular dynamics simulations. Calculations were done for two different situations. On one hand we studied the damage produced in bulk b.c.c. Fe, which would correspond to the damage produced by a recoil generated by neutron irradiation. On the other hand we studied the damage produced by Fe ions irradiating a thin b.c.c. Fe sample. The reason for undergoing this comparison is that *in situ* TEM analysis is often performed to study radiation damage. This analysis is done in very thin films (50 to 100 nm thickness) irradiated with ions of different types and energies. In this work we show how the damage produced under these conditions is quite different from that produced in the bulk. *In situ* TEM irradiation experiments are an extremely valuable source of information on defect production and evolution in metals. However, if this information is to be extrapolated to the case of neutron irradiation the effects described in this report should be taken into account.

This work is part of the PhD thesis of María José Aliaga, from the University of Alicante, Spain and it has been performed in collaboration with Profs. R. Schäublin and J. Löffler of ETH, Zurich, Switzerland.

Methodology

Calculations have been performed using the parallel molecular dynamics code MDCASK, developed at LLNL [1]. Two different type of interatomic potentials are used for comparison, the one developed by Dudarev and Derlet [2] and the one by Ackland et al [3], (DD and AM from now on). Both potentials were modified for short range interactions following the procedure used in [4]. These same potentials have been used previously to study cascade damage in bulk samples [4]. They were selected because they reproduce fairly well the stability of different point defects as compared to DFT calculations. But also, the cluster size distribution obtained with these potentials seems to better reproduce the experimental observations, compared to other potentials [5]. We should mention that bulk cascades in α-Fe have been performed by many different groups and different interatomic potentials [6-9]. For a review see reference [10].

Two types of simulations were performed: simulations of implantation of energetic ions in thin films (from now on 'thin films') and simulations of energetic recoils inside a periodic crystal (from now on 'bulk'). For the implantation calculations, periodic boundary conditions are used along two axes while free surfaces are considered in the third axis. The energetic atom is launched from the outside of the crystal towards the surface with the selected implantation angle. In the case of cascades in the bulk, periodic boundaries conditions in all directions are used. We report here simulations with the two interatomic potentials (DD and AM), two energies, 50 keV and 100 keV and two incident angles, 10^o and 22^o. Note that the critical angle for channelling according to the Lindhard expression [11] is 21º for 50 keV and 15º for 100 keV ions. Most calculations are performed in system sizes of 180 a_0 × 180 a_0 × 180 a_0 simulation cells, where a_0 is the lattice parameter for Fe (a_0 = 2.8665 Å). For the case of implantation, this corresponds to thin films of about 50 nm. This size is, in fact, comparable to those used experimentally in implantation of thin films [12]. Table 1 describes all the different conditions simulated.

Table 1. Simulations performed. The table shows the energy of the ion, angle of incidence, interatomic potential, number of cascades performed, whether it is a thick film or bulk simulation, and the thickness of the sample (for thin films).

Case #	Energy (keV)	Angle of incidence	Interatomic potential	Number of cases	Thin film or bulk	Thickness (nm)
1	50	10	DD	14	Thin film	45.7
2	50	22	DD	17	Thin film	51.4
3	100	10	DD	20	Thin film	51.4
4	100	22	DD	20	Thin film	51.4
5	50	10	AM	14	Thin film	51.4
6	50	22	AM	30	Thin film	51.4
7	100	10	AM	20	Thin film	51.4
8	100	22	AM	30	Thin film	51.4
9	50	10	DD	14	Bulk	51.4
10	50	22	DD	14	Bulk	51.4
11	50	10	AM	14	Bulk	51.4
12	50	22	AM	14	Bulk	51.4
13	100	22	AM	14	Bulk	70

Results

Figure 1 shows two examples of the damage produced in a b.c.c. thin film after irradiation with an Fe ion of energy 50 keV (Figure 1(a)) and 100 keV (Figure 1(b)). The green dots represent the location of the vacancies while the red dots are the locations of the self-interstitials. The arrow indicates approximately the initial location of the energetic atom. The location of the atoms at the surface are also represented in the figure. In figure 1(a) the damage results - in two interstitial clusters with 23 and 27 defects, and two significantly larger vacancy clusters with 108 and 148 defects. The total number of vacancies in this case is 448 while the total number of self-interstitials is 140. In this cascade 79% of all vacancies are in clusters and 57% are in clusters with more than 55 defects, which correspond to a loop of 1 nm radius. Interstitials are also in clusters (58%) although there are no large clusters (with more than 55 defects). As can be observed in the figure, in this particular case most of the damage is below the surface, however, the total number of self-interstitials is significantly lower than the number of vacancies. This is due to the attraction of self-interstitials to the surface, that can be seen as ad-atoms at the surface in Figure 1(a). This unbalance between vacancies and self-interstitials when damage is created close to the surface was already pointed out by Stoller et al. for lower energy recoils started below the surface [13].

Figure 1(b) shows the damage produced by a 100 keV Fe ion with incidence angle 10^{o} implanted in a thin film, after 20 ps (case 7 on Table I). The total number of vacancies in this particular case is 662 while the total number of self-interstitials is 187. As in the case of figure 1(a), a significant number of atoms end up at the surface, as ad-atoms, 469, while 6 atoms are sputtered. The inset in figure 1(b) shows the location of these surface atoms seen from the top. In this case a large vacancy loop can be observed right below the surface with a total of 480 defects. The dimensions of the cluster are approximately 9 a_0 × 5 a_0 × 14 a_0 (3 nm × 1 nm × 4 nm). These vacancies are arranged in a loop oriented along the <100> plane. It is noticeable that the <100> vacancy loops we obtain, like this one in Figure 2, have rectangular shape, in agreement with the stability calculations by Gilbert et al. [14, 15] which show that rectangular <100> vacancy loops are more stable than circular ones so they should form preferentially. The formation of <100> vacancy loops in bulk cascades was already shown by Soneda et al [8] as well as Kapinos [16], however, their formation was rare.

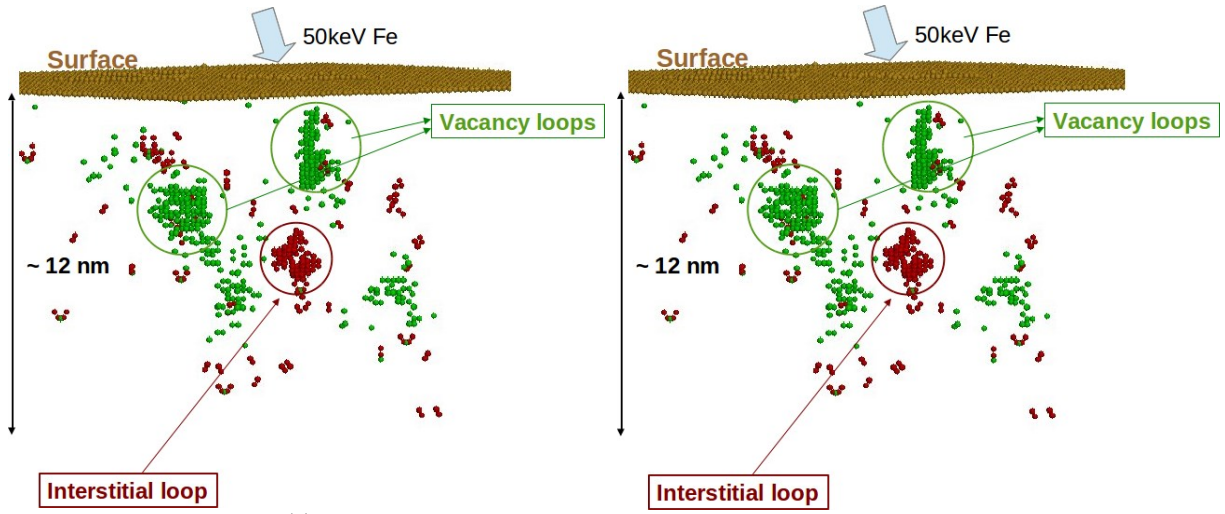

(a) (b)

Fig. 1. Damage produced by Fe ion implanted in a thin film of bcc Fe for (a) 50 keV and (b) 100keV ion energies. Red dots are the location of interstitials and green dots the location of vacancies.

In figure 2 we show, for comparison, the damage produced by a 50 keV recoil in bulk alpha-Fe using the same interatomic potential (case 10 on Table 1), as well as the damage produced by a 100 keV recoil in bulk alpha-Fe. Comparing figures 1 with figures 2, the difference in the damage distribution and configuration between bulk cascades and implantation are clearly seen. Notice the production of subcascades in the case of 100 keV recoils.

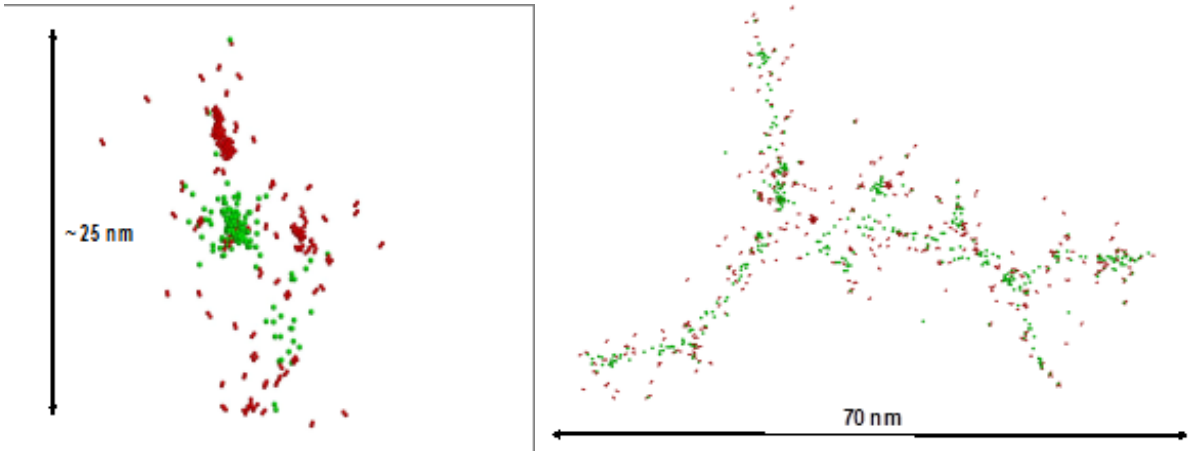

(a) (b)

Fig. 2. Damage produced by a recoil in bulk bcc Fe for (a) 50keV and (b) 100keV energies. Red dots are the location of interstitials and green dots the location of vacancies.

A statistical analysis has been performed to compare the results of bulk irradiation and ion implantation. We observe two important differences, besides the unbalance between the number of vacancies and self-interstitials observed in thin films. On one hand the results in terms of number of defects, clustering fraction or ion range are much more dispersed in the case of thin films that in bulk irradiation. On the other hand the formation of large vacancy loops close to the surface is much more efficient in thin films than in bulk irradiation. This is in good agreement with experimental observations, where <100> loops have been identified for irradiation at low doses and close to the surface [5, 17].

Figure 3 shows the number of clusters produced of different sizes comparing bulk irradiation and thin films. Figure 3(a) compares vacancy clusters and it is quite clear that the size of vacancy clusters in thin films is much larger than in bulk. Figure 3(b) compares self-interstitial clusters and in this case, clusters are larger in bulk than in thin films due to the strong interaction between self-interstitials and the surface. Other quantities have been analyzed statistically such as the number of defects produced (vacancies and self-interstitials), their clustering fraction, ion range, etc. A scaling law has been obtained for the frequency of formation of self-interstitial and vacancy clusters as a function of size.

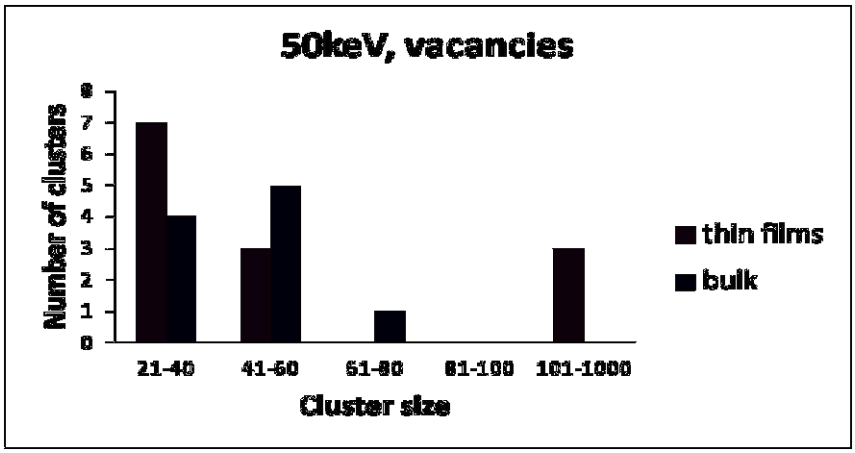

(a)

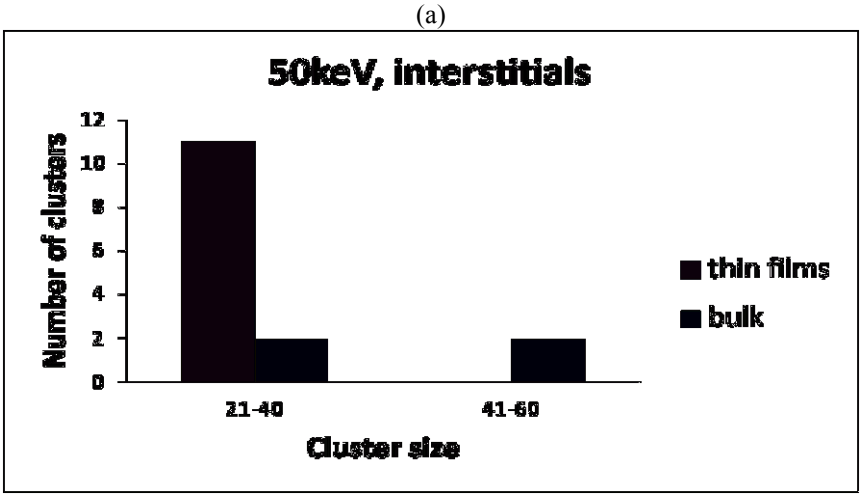

(b)

Fig. 3. Histogram of number of vacancies (a) and self-interstitials (b) comparing bulk cascades with thin films.

We have been able to fit the data to one single power law for the case of self-interstitials but two power laws are needed for the case of vacancies. We think this result is due to the formation of two types of vacancy clusters in the case of thin film irradiation: those deeper in the bulk and unaffected by the surface and those closer to the surface which are much larger. Moreover, simulations have been performed with Ga ion irradiating Fe thin films which show the formation of much larger vacancy loops, of sizes that can be easily resolved under TEM.

Conclusions

The calculations presented here show that the damage produced by ion implantation in alpha-Fe thin films by low energy ions (50 keV and 100 keV) is significantly different from that produced by recoils of the same energy in the bulk. Surface damage gives rise to an unbalance in the number of vacancies with respect to self-interstitials, with a much larger number of vacancies than self-interstitials due to

the trapping of these at the surface, becoming ad-atoms. It also shows a large dispersion in the number of defects produced for the same irradiation conditions. While in the bulk, results from two cascades of the same characteristics (energy, recoil angle) are very similar in terms of the total number of defects or the percentage of defects in clusters, in the case of surface damage the total number of defects can be very different from one case to another, as well as the morphology of the damage produced. In particular, two type of structures can be identified. Most of the cases show large vacancy clusters, mostly loops of <100> type, and small self-interstitial clusters right below the surface. In a few cases, large surface damage is produced. For low doses and damage close to the surface, the formation of <100> vacancy loops directly in the cascade is revealed by these simulations, in agreement with the experiments [12, 17].

Some important conclusions can be extracted from these simulations. As we have shown in previous works [5, 18], the initial damage distribution and configuration has important consequences in damage accumulation and damage evolution. The initial damage in the cascade, together with defect mobilities, defines how damage will grow with dose. This has consequences for modeling radiation effects. In the quest of developing a model that is able to describe neutron damage, ion implantation experiments using thin-films are often used to validate these models. These results show that one should be careful with the treatment of surfaces in these models.

These results have been submitted for publication to Acta Materialia and are currently under review. The database of cascades in the form of x,y,z coordinates for the location of vacancies and self-interstitials from the molecular dynamics simulations is available under request. Please send an email to mj.caturla@ua.es .

References

[1] T. Diaz de la Rubia, M.W. Guinan, Phys. Rev. Lett. 66 (1991) 2766.
[2] S. Dudarev, P. Derlet, J. Phys: Condens. Matter. 17 (2005) 1-22.
[3] G.J. Ackland, M.I. Mendelev, D.J. Srolovitz, S. Han, A.V. Barashev, J. Phys.: Condens. Matter 16 (2004) S2629.
[4] C. Björkas, K. Nordlund, Nucl. Instr. And Meth. In Phys. Res. B 259 (2007) 853-860.
[5] C. Björkas, K. Nordlund, M. J. Caturla, Phys. Rev. B 85 (2012) 024105.
[6] D.J. Bacon, A.F. Calder, F. Gao, J. Nucl. Mater. 251 (1997) 1.
[7] R.E. Stoller , G.R. Odette, B.D. Wirth, J. of Nucl. Mat. 25 1 (1997) 49-60
[8] N. Soneda, S. Ishino, T.D. de la Rubia, PHILOSOPHICAL Magazine Letters 81 (2001) 649
[9] E. Zarkadoula, S.L Daraszewicz, D.M Duffy, M.A. Seaton, I.T. Todorov, K. Nordlund, M.T. Dove and K. Trachenko, J. Phys.: Condens. Matter 25 (2013) 125402.
[10] L. Malerba, J. Nucl. Mater. 351 (2006) 28-38.
[11] L.-P. Zheng et al., Nucl. Instr. and Meth. in Phys. Res. B 268 (2010) 120-122.
[12] Z. Yao, M. Hernández Mayoral, M.L. Jenkins, M.A. Kirk, Phil. Mag. 88 (2008) 2851.
[13] R.E. Stoller, Comprehensive Nuclear Materials, vol. 1, ed. R.J.M. Konings (Elsevier), p. 293 (2012).
[14] M.R. Gilbert, S.L. Dudarev, P.M. Derlet and D.G. Pettifor, J. Phys.: Condens. Matter 20 (2008) 345214.
[15] M.R. Gilbert, Z. Yao, M.A. Kirk, M.L. Jenkins, S.L. Dudarev, J. Nucl. Mat. 386–388 (2009) 36–40.
[16] V.G. Kapinos, Y.N. Osetskii, P.A. Platonov, J. of Nucl. Mat. 173 (1990) 229.
[17] M.L. Jenkins, C.A. English, B.L. Eyre, Nature, 263, 400-401 (1976).
[18] M.J. Caturla, N. Soneda, E. Alonso, B.D. Wirth, T.D. de la Rubia, J.M. Perlado, J. of Nucl. Materials 276 (2000) 13.

Quantifying primary irradiation damage from cascades to characterize the long-term behaviour of its accumulation: Second Report,

C.H. Woo

Department of Physics and Materials Science
City University of Hong Kong
Hong Kong SAR, China

1. Introduction

Fast neutrons produce high-energy recoils, leading to the production of a large number of atomic displacements. Partial annealing then follows during the subsequent cooling down of the highly heated cascade region. The residual damage participates in the ongoing irradiation damage accumulation process as an elemental component of the source (production) term in the kinetic description of the evolving microstructure.

In terms of spatial and temporal scales, investigation of the kinetics of cascade evolution naturally fits within the realm of atomistic modeling using techniques such as molecular dynamics (MD) or spin-lattice dynamics (SLD). However, macroscopic manifestation of damage effects occurs through multiple development stages, and has to be considered in a global perspective through the accumulation of an astronomical number of events occurring with infinitesimal probabilities, with overall spatial dimensions and time scales much larger than those accessible to atomistic simulations. In this perspective, the multi-scale nature of irradiation damage modeling must be recognized, and the foremost role of the collision cascade is that of a source term of point defects and primary clusters.

In my first report (2013) of this series, effects due to the strong temporal and spatial correlations of point-defects produced in the same cascade are studied. As a result of random cascade occurrence, production of point-defects occurs probabilistically and in discrete packages, which cannot be adequately represented in kinetic models by a deterministic and continuous source term. Fluctuations in point-defect concentrations are known to be important in nucleation processes that involve only a small number of point-defects. We have clarified the role played by the strongly correlated production of point-defects in cascades, and have constructed a physically transparent and easy to use model to account for this effect.

In the present report, two issues are considered:

1. How does ferromagnetism in bcc iron affect the evolution of collision cascades?
2. How and to what extent does correlated production in cascade damage affect cluster dynamics?

2. Role of ferromagnetism in the evolution of collision cascades in bcc iron

To magnetic alloys such as ferritic steels, effects of ferromagnetism in the evolution of collision cascades are obviously relevant. The weight carried by the spin component in the thermodynamics of bcc iron may be assessed by comparing the phonon and magnon contributions to the specific heat calculated using MD and SD (Spin Dynamics) shown in the following graphs.

It is immediately apparent that the two contributions have comparable magnitudes, but vastly different temperature dependencies, particularly near the Curie temperature (1043K). Unlike the lattice component which obeys the Dulong and Petit's law, the anharmonic spin component strongly deviates from it. Comparison between the lattice and spin components of the activation enthalpies and entropies of vacancy formation and migration in bcc iron [1] yield the same conclusion that the spin component is important to its activation thermodynamics. A similar assessment has not been made in the case of dynamic simulations of cascade evolution in bcc iron. Nevertheless, there seems to be little valid reason to support the neglect of the spin component in this case, in which the cascade spends a substantial part of its lifetime in the ferromagnetic phase, particularly near the Curie temperature.

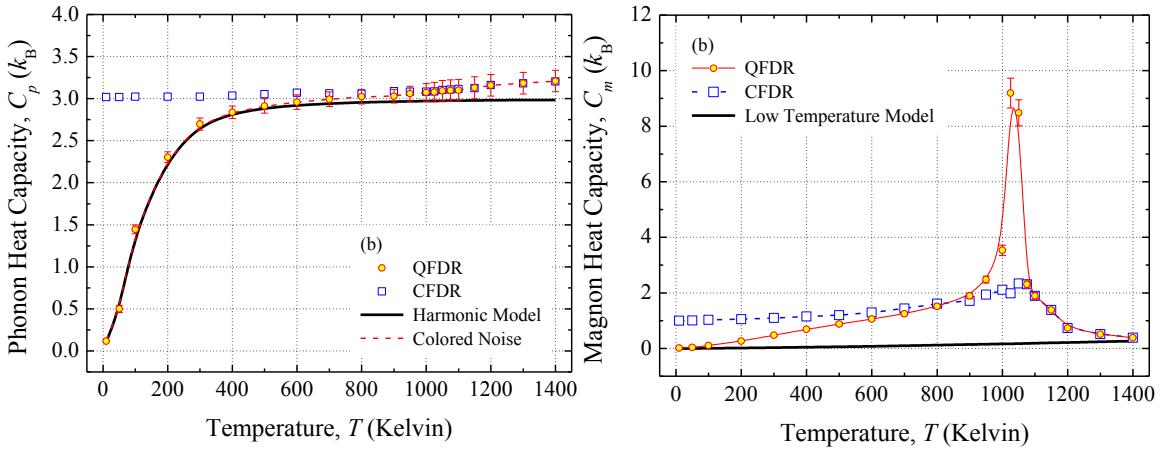

Modeling the coupled spin-lattice system is a challenging task, particularly near the FM/PM transition boundary, where the magnon frequencies significantly slow down to the phonon level and the coupling of the spin and lattice dynamics is the strongest. In this temperature regime, one needs to be equipped to describe the stability/instability of long-range magnetic ordering in the presence of magnon softening on the basis of the strong anharmonicity caused by the amplitude-dependent spin-spin interaction. In contrast, the vibrational thermodynamics of the coupled spin and lattice components are mostly treated within harmonic or quasi-harmonic approximations. Anharmonicity may sometimes be taken into account, but because of the limited size of the model, contributions from the most easily accessible low-energy long-wavelength excitations are sacrificed. This kind of approximations cannot give a good representation of the dynamical crystal in this sensitive regime near the Curie temperature.

To properly simulate the dynamics of a large-scale atomistic system with interacting spins, Ma, Woo and Dudarev [2] generalized molecular dynamics into a spin-lattice dynamics (SLD) scheme, in which the coupled spin and lattice systems could be simulated dynamically on equal footing. The equation of motion of the spins is derived from the Heisenberg Hamiltonian, in which spins interact through the exchange interaction that depends on the interatomic separation [3]. The dynamics of the ensemble of atoms with spins with fully anharmonic spin-spin, spin-lattice and interatomic interactions can be simulated using methodologies similar to conventional MD models. Canonical thermodynamics simulations of the strongly quantized magnons are achieved with increased accuracy in subsequent works [4] via a heat bath constructed based on a quantum fluctuation-dissipation relation linking the stochastic dynamics with the heat-bath temperature. The following shows the magnetization, the specific heat, and the diffusivity of self-diffusion as functions of temperature calculated over a wide temperature range using SLD with quantum heat bath (QFDR). Comparison with experimental data shows that, as a simulation tool for ferromagnetic materials, SLD is capable of producing a sufficiently accurate representation, at least in the case of ferromagnetic bcc iron.

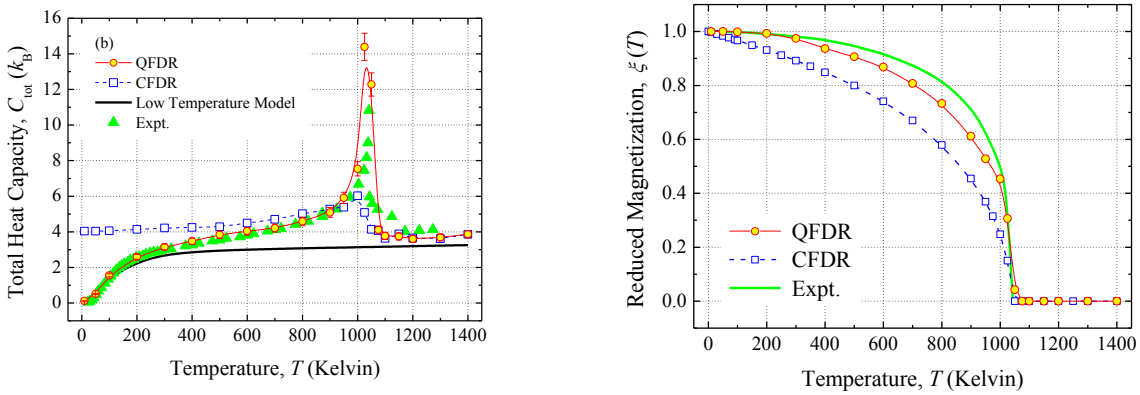

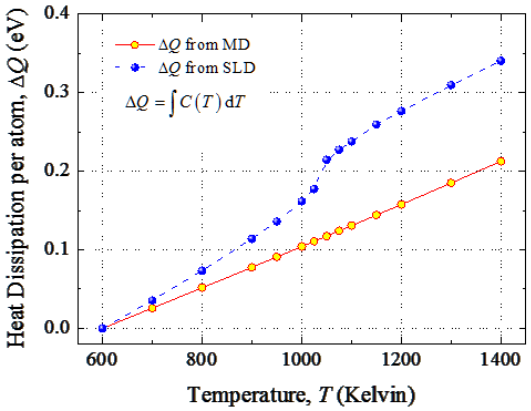

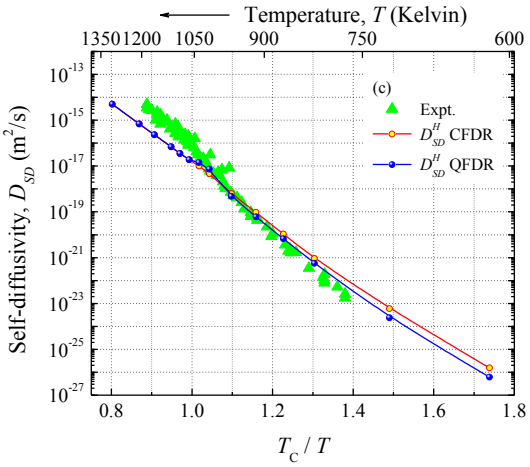

The amount of heat removal needed to cool a bcc iron sample from temperature T to, say, 600K can be calculated from the heat capacity by integration. We compare in the figure below the results calculated with SLD (blue), in which the contribution from the spin component is included, and results with MD (red), without the spin component. Without the spin system, cooling from 1400K to 600K requires heat removal of 0.2 eV, compared with 0.35 eV including the spin contribution. With the same heat removal mechanism by electrons, cooling time is ~70% longer with spins. Cooling from 1100K to 1000K with no spins only needs 0.2/8 eV of heat to be removed, less than a third of the quantity if spins are involved.

Indeed, in this temperature range, the cascade region undergoes an order/disorder transformation from the paramagnetic to the ferromagnetic state. The ordering requires an entropy or heat loss from the spin system to the environment before the spin system can be cooled below the Curie temperature to attain the ferromagnetic state. This heat loss has a physical origin similar to the latent heat released from a sample during condensation, which must be absorbed by the environment before the vapor state is transformed to the liquid state. In the case of a cascade cooling down from the paramagnetic to the ferromagnetic phase, the slower cooling may allow more times for clustering. These features are demonstrated in the following figure that shows the preliminary results of a 15 keV cascade in iron at 600K simulated by SLD, with and without spins.

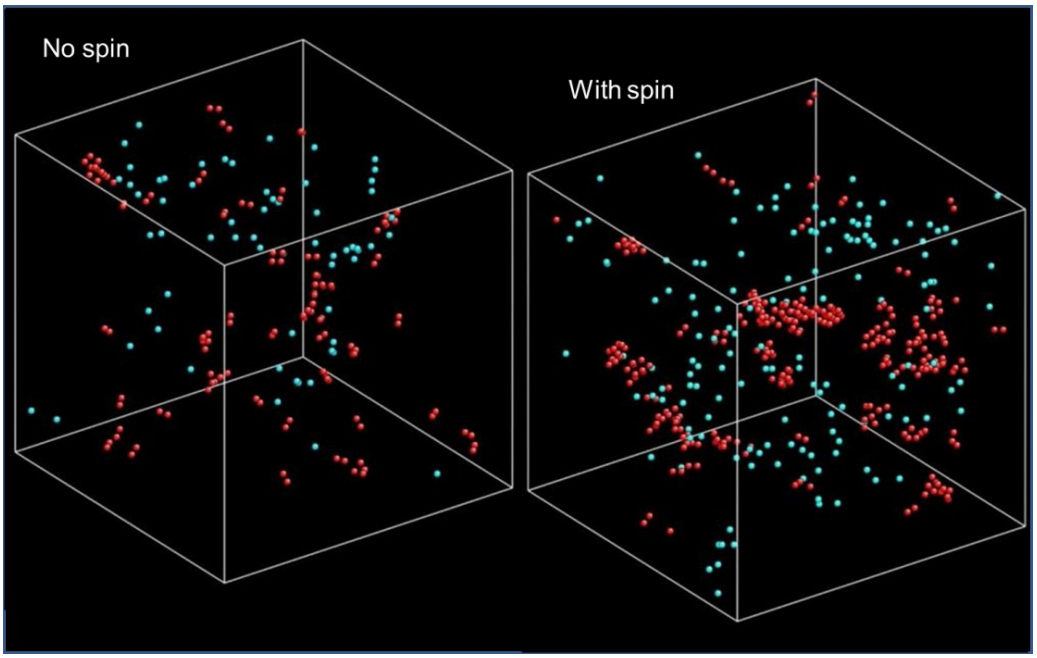

3. Effect of cascade damage production on cluster dynamic

Kinetic theory of bulk diffusion-mediated reactions has been a main tool for irradiation-damage modeling, which provides the link between the evolution of the underlying microstructure and mechanisms at the atomistic scale. For several decades, simplified versions of the kinetic theory based on the mean-field approximation provided the mainstream approach of irradiation-damage modeling, under the name of rate theory. Many useful models have been developed for use as technological tools of analysis and interpretation for reactor design and operation. However, the neglect of stochastic effects due to thermally-induced concentration fluctuations limits the usefulness of mean-field rate theory in treating primary events of evolution relating to nucleation and stochastic coarsening, involving the evolution of small subcritical clusters.

The classical treatment of the growth and dissolution of clusters of the nucleating phase is described as an evaporation-condensation mechanism in which particles are added or lost from a cluster one at a time. The evolution kinetics of the clusters, sometimes known as cluster dynamics, can then be represented in terms of a system of hierarchical conservation equations (master equations) for clusters of increasing sizes first derived by Becker and Döring [5].

$$\frac{dP(n,t)}{dt} = \sum_{m\neq n} J_{m\to n} - \sum_{q\neq n} J_{n\to q};\ \text{with}\ J_{m\to n} = w^{+}_{m\to n}P(m,t); J_{n\to q} = w^{-}_{n\to q}P(n,t)\,. \tag{1}$$

Using the Kramers-Moyal expansion [6, 7] in a continuous approximation and truncating in second order, the master equation (1) can be cast in the form of the following Fokker-Planck equation (FPE),

$$\frac{\partial P(n,t)}{dt} = -\frac{\partial}{\partial n}\left\{ w^{+}(n,t) - w^{-}(n,t) - \frac{1}{2}\frac{\partial}{\partial n}\left(w^{+}(n,t) + w^{-}(n,t)\right)\right\} P(n,t) \tag{2}$$

where $w^{\pm}(n,t)$ designates the forward and backward kinetic coefficients describing particle absorption by and emission from the cluster. Eq. (2), however, does not yield the equilibrium distribution of the original master equation (1).

Via an alternate route, the Zeldovich-Frenkel (Z–F) equation is another FPE that can be derived from eq. (1), which avoids this problem. The original Z-F equation is derived for reaction-controlled kinetics assuming quasi-equilibrium across the cluster/solution interface. For irradiation damage modeling, our calculations are based on a modified Z-F equation [8], reformulated to treat non-equilibrium diffusion-controlled kinetics. In addition, in the presence of both vacancies and self-interstitials, the modified Z-F equation for the probability distribution of an evolving void ensemble under irradiation reads

$$\frac{\partial P(n,t)}{\partial t} = -\frac{\partial}{\partial n}\left\{ \frac{4\pi R(n)}{\Omega}\left[D_v\left(C_v - C_s^e(R)\right) - D_i C_i\right] - \frac{\partial}{\partial n} D(n)\right\} P(n,t)\,, \tag{3}$$

Here $R(n)$ is the radius of void formed with n vacancies, Ω is the atomic volume, D_v and C_v are the diffusion coefficient and the concentration of vacancies, respectively, $a = (3\Omega/4\pi)^{1/3}$. The concentration $C_s^e(n)$ of vacancy solution, which is in equilibrium with a void of radius $R(n)$, is given by

$$C_s^e(R) = C_\infty \exp\left(\frac{2\gamma_s \Omega}{k_B T R}\right), \tag{4}$$

where C_∞ is the equilibrium vacancy concentration, γ_s is the surface tension coefficient, k_B is the Boltzmann constant, and T is the absolute temperature. The diffusion coefficient $D(n)$ in the space of void sizes in eq. (3) is given by

$$D(n) = \frac{4\pi R^2}{2\Omega a}\left[3D_v C_R + \frac{a}{R}\left(D_v(C_v - C_s^e(R)) + D_i C_i\right)\right], \tag{5}$$

where D_i and C_i are the diffusion coefficient and the concentration of self-interstitials, respectively.

The very substantial correction due to the non-equilibrium nature of the diffusion-controlled kinetics of cluster growth is shown in the figure below, in terms of the ratio of steady-state nucleation rates plotted (in log scale) as a function of cluster critical size $n_{cr}^{1/3}$ at different values of supersaturation C/c_∞.

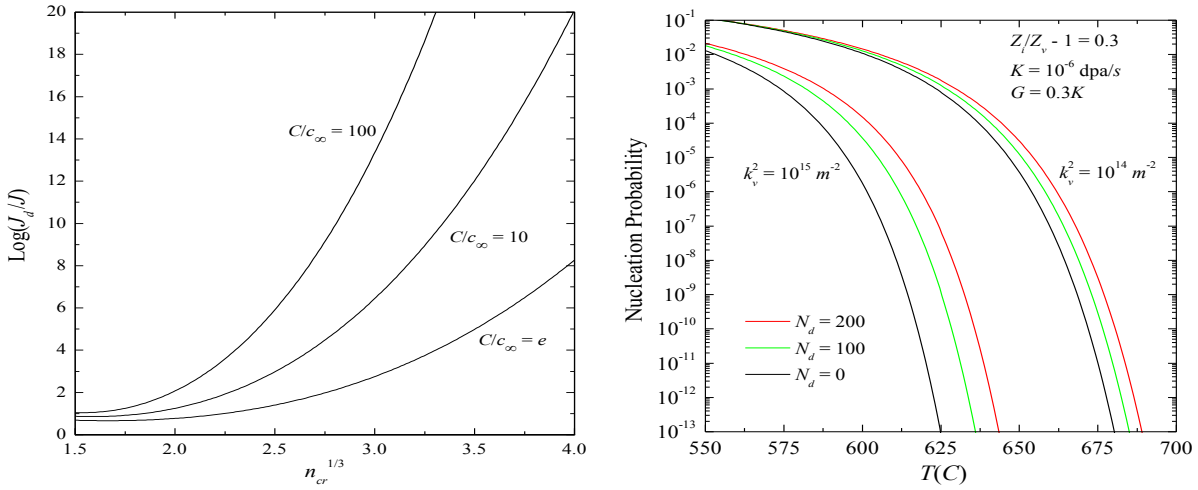

In eq. (3), the growth of subcritical clusters is driven by noise term $D(n)$. In eq. (5), only the noise due to the fluctuation of point-defect diffusion and emission are included. We must also recognize the stochastic nature of cascade damage production in $D(n)$, which we have discussed in the first report. Accordingly, the term $D_c(n)$ must be added to $D(n)$ in eq. (5), where

$$D_c(n) = \frac{3n^{2/3}}{4a}\left[\frac{G_v\left\langle N_{dv}^2\right\rangle}{k_v N_{dv}} + \frac{G_i\left\langle N_{di}^2\right\rangle}{k_i N_{di}}\right]. \tag{6}$$

Here G_j is the mean generation rate of free point defects, N_{dj} and $\left\langle N_{dj}^2\right\rangle$ are the average number and the average square number of free point defects generated in a single cascade, respectively, and k_j^2 is the total sink strength for point defects of the type j.

The nucleation probability is then given by

$$P_m \cong \sqrt{\frac{2\gamma_s\Omega}{2k_BT\pi a^3 n_{cr}}}\frac{(D_vC_v - D_iC_i)}{D(n_{cr})}\exp\left[\int_{n_0}^{n_{cr}} V(n)/D(n)\,dn\right](n_0 - n_{\min}), \tag{7}$$

from which we can estimate the effect of cascade size and sink strength on the void density at different temperatures (see figure above), where the large sensitivity of the nucleation rate to the cascade size, total sink strength and temperature is clear. The role of this sensitivity to designing for irradiation-damage resistance is obviously important.

References

[1] H. Wen and C.H. Woo, J. Nucl. Mater. **455** (2014) 31; also unpublished (with quantum heat bath).
[2] P.-W. Ma, C.H. Woo, and S.L. Dudarev, Phys. Rev. B**78**, 024434 (2008).
[3] H. Wang, P.W. Ma, C.H. Woo, Phys. Rev. B**82**, 144304 (2010).
[4] C.H. Woo, H. Wen, A.A. Semenov, S.L. Dudarev and P.-W. Ma, Phys. Rev. B**91**, 104306 (2015).
[5] R. Becker and W. Döring, Ann. d. Physik **24**, 719 (1935).
[6] H.A. Kramers, Physica A 7, 284 (1940).
[7] J.E. Moyal, Roy. Stat. Soc, London, Ser. B 11, 150 (1949).
[8] A.A. Semenov and C.H. Woo (2015), unpublished.

Calculation of the NRT dpa cross section by SRIM-2013 and comparison with DXS, B. Marcinkevicius, S. Simakov

Nuclear Data Section of IAEA,
Vienna, Austria

Introduction

The radiation induced damage in materials is one of the key issues for safe operation of the power and research nuclear facilities, such as power fission and projected fusion reactors, spallation sources and accelerators. The accurate knowledge of the nuclear quantities such as displacement cross sections and gas production are necessary for quantification of induced damages and intercomparison of nuclear facilities.

The SRIM code [1] is a "standard tool" for the calculations of the ion induced displaced atoms, sputtering, ions ranges and stopping power up to 1 GeV. The practical usage of code was already discussed in the several publications [2, 3]. On the other hand, the up-today nuclear reaction models are capable to precisely compute the neutron or ion reaction cross sections and eventually the dpa cross sections [4, 5]. In frame of such approach the specialised database of the protons and neutrons induced displacement both *NRT*- and *arc*-) and gas production cross sections (DXS) was produced for several materials [6].

The goal of this work (carried out by B. Marcinkevicius during his Internship at NDS) was a calculation of the proton induced *NRT* displacement cross sections by SRIM and comparison with the same quantity from DXS.

Review of the SRIM-2013 code options

SRIM is a Monte Carlo code, which transport the ions as a series of binary collisions and computes ions implantation, induced damage and spatial distribution within material. There are two options for calculation of the ion induced damage: “Quick calculation of damage” which uses Kinchin-Pease (K-P) model [7] for vacancy calculation and “Detailed calculation with full damage cascades” (F-C). In K-P, the Primary Knock-on Atom (PKA) energy distribution for every incident proton is calculated, while in full cascade all PKA are transported until their energy drops below the displacement threshold energy E_d, i.e. the atom binding energy in lattice.

SRIM divides the material layer into 100 equal-width bins and calculates the number of vacancies, lattice phonons, ionisation losses and the energy transferred to the recoil atoms in every bin. It is also possible to calculate the energy and spatial distributions of recoils and estimate the ions backscattering. The code output files and information they contain are listed in the Table 1.

Table 1. Short description of SRIM-2013 output files.

SRIM output file	Description
COLLISON.txt	For K-P option: stores every ion and primary knock-on collision details. For F-C: stores every ion, primary and secondary knock-on collision details.
Phonon.txt	Distribution of energy transferred to phonons within each bin.
Vacancy.txt	Distribution of K-P or F-C vacancies produced within each bin.
Ionz.txt	Distribution of ionisation losses within each bin.
E2recoil.txt	Distribution of energy ion transferred to recoils.

Ion induced displacements from SRIM

We confirm that the ion induced displacements calculated by SRIM with Kinchin Pease (K-P) and Full Cascade (F-C) options differ significantly, that may cause the misinterpretation of results.

R. Stoller et al. [2] suggested to calculate the number of displacements using damage energy T_{dam}. Following the equations of papers [2, 3] the damage energy can be calculated from ionisation losses and phonons:

$$T_{dam} = E_i^0 - E_i^I - E_T^I = E_i^P + E_T^P \quad (1)$$

$$E_i^0 = E_i^P + E_T^P + E_i^I + E_T^I \quad (2)$$

where:

$E_i^0 - incident\ ion\ energy;$
$E_i^I - incident\ ion\ Ionisation\ energy\ losses;$
$E_T^I - recoil\ atom\ Ionisation\ energy\ losses;$
$E_i^P - incident\ ion\ energy\ lost\ to\ Phonons;$
$E_T^P - recoil\ energy\ lost\ to\ Phonons.$

Then number of vacancies ϑ_{NRT} can be estimated from damage energy T_{dam} using Norgett-Robinson-Torrens (NRT) [8] equation:

$$\vartheta_{NRT} = 0.8\, T_{dam}(E_{PKA})/2E_d \quad (3)$$

where:

$E_d - displacement\ threshold\ energy;$
$E_{PKA} - energy\ of\ primary\ recoil\ atom.$

Displacements inside iron layer were calculated for different energies and ions. Results are presented in the Table 2. These results do not differ significantly from the ones obtained by Stoller et al. [1] who used the earlier version SRIM-2008. As seen in Table 2, the SRIM-2013 displacements calculated from the F-C and K-P vacancies differ by factor ~ 2, whereas the displacements calculated from the damage energy T_{dam} using both modes practically agree.

Table 2. Calculation of displacements per one incident ion in Iron by SRIM-2013.
(in all cases the lattice binding energy was set to 0 keV, displacement energy E_d = 40 eV).

Inc. Ion	E, keV	SRIM Model	No. of sampled Ions	Number of Displaced Atoms from SRIM file "vacancy.txt"			Number of Displaced Atoms calculated from damage energy		
				Summary in file	Integrat. of file	F-C/ K-P ratio	Damage Energy (1) keV	ϑ_{NRT} (3)	F-C/ K-P ratio
Fe	69	K-P	59390	469	469.1	1.99	47.17	472	**1.06**
	69	F-C	11759	935	932.1		50.08	501	
Fe	5000	K-P	7378	7874	7874.0	2.06	79.12	7912	**1.11**
	5000	F-C	7016	16329	16262.0		87.50	8750	
^{1}H	2000	K-P	30482	14	13.6	1.96	1840	18	**1.14**
	2000	F-C	59360	27	26.7		2090	21	

Because of the questionable results with the F-C option, we performed systematic calculation of the number of displacements by SRIM using the K-P option and using damage energy and equation (3).

It was noticed that the total energy deposition in the target calculated by SRIM-2013 exceeds the incident ion energy by up to 1%. This also leads to the differences of damage energy calculated from phonon energy and ionisation losses. This might be due to the precision of code and does not have significant impact on the total production of displacements.

To convert the depth profile distribution in displacements cross section the average proton energy within each bin was estimated by equation (4):

$$E_a^{Average} = E^0 - \sum_{a=1}^{a} E_a^{lost} + E_a^{lost}/2 \quad (4)$$

where:

$E_a^{Average} - Average\ proton\ energy\ within\ bin\ \boldsymbol{a}$

$E_a^0 - Initial\ proton\ energy$

$E_a^{lost} - Incident\ ion\ energy\ lost\ to\ recoils, ionisation\ and\ creation\ of\ phonons$

$E_{recoil}^I - Energy\ transfered\ to\ the\ primary\ knock - on\ atom$

The recoil energy transmitted to phonons was estimated using expression (5) because of observed issue in the SRIM calculations of phonons produced by recoils:

$$E_T^P = E_{recoil}^I - E_T^I \quad (5)$$

The average energy calculated by equation (4) was compared with the actual incident proton energy distribution within bin #50 of the iron layer.

Fig. 1 shows the proton energy distribution obtained from COLLISON.txt. The average energy calculated using (4) was 2810 keV or 80 keV lower than 2890 keV obtained from COLLISON.txt. Such difference becomes negligible at higher proton energies, however increases at lower energies. For example, for 250 keV incident protons the average energy within bin #50 is 76.9 keV following the eq. (4), but 69.2 keV - from file COLLISON.txt. The difference is a result of contribution of backscattered protons which are not accounted in eq. (4).

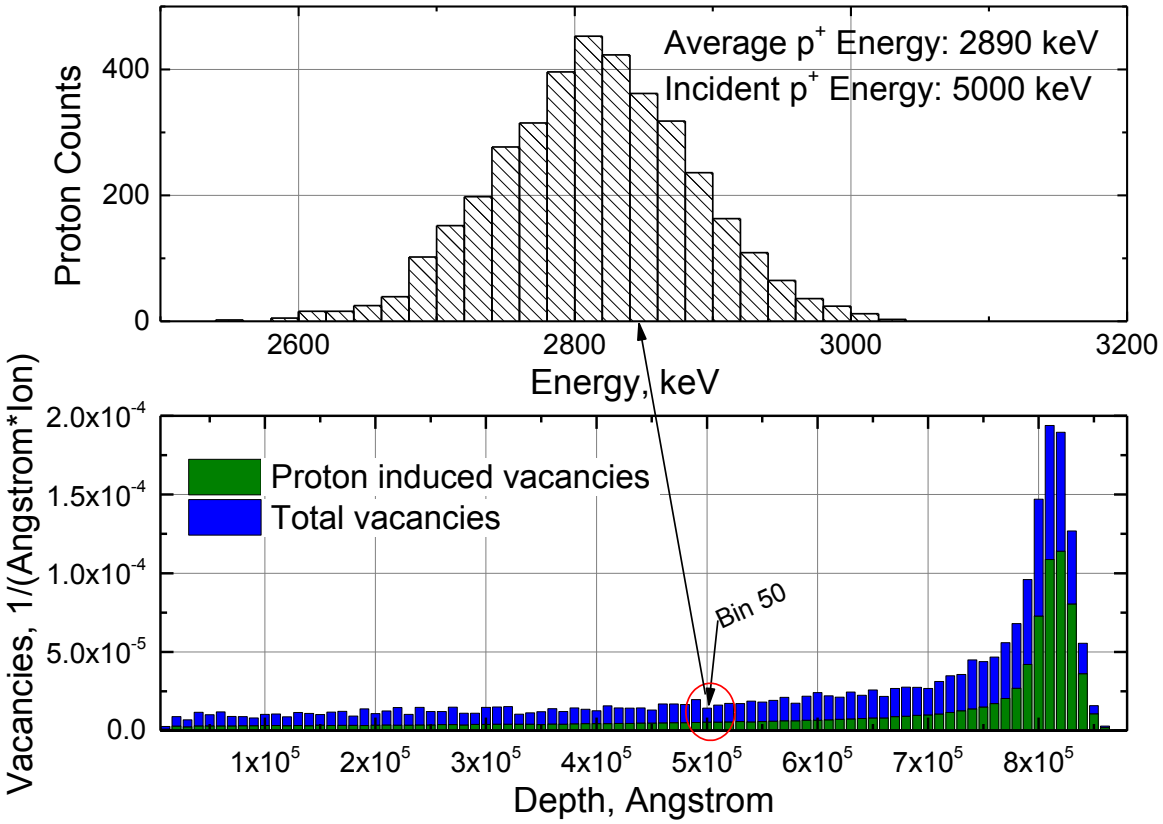

Fig. 1. Top: the proton energy distribution in the iron bin #50 for incident proton energy 5000 keV. Bottom: number of vacancies produced in the Fe bins (depth profile) by protons (green) and by protons and recoils (total - blue).

Results of the displacement cross section calculation by SRIM and comparison with DXS

The SRIM calculations were done for Zr, Fe, Cu, Ni, Cr and Al using the displacement energies E_d = 40, 40, 30, 40, 40 and 25 eV, correspondingly, as recommended by [9]. The SRIM input parameter "Lattice binding energy", which allows transfer of the recoil energy to collective motions of lattice phonons, was set to zero in all cases. The SRIM calculated atom displacement cross sections are denoted as "SRIM/K-P" (K-P option) and as "SRIM/T_{dam}/NRT" (damage energy T_{dam} and NRT model). The obtained results were compared with the NRT proton induced dpa cross sections (MT = 901) available in the DXS database [2].

Fig. 2 shows such comparison for Fe. Below 100 keV one may observe the impact of the too wide layer bins and contribution of the low energy back scattered protons. For the energy interval 100 keV to 10 MeV the SRIM/K-P agrees with DXS within 20%, whereas SRIM/T_{dam}/NRT predicts up to 60% higher values than DXS. Above 20 MeV we observed significant deviations since SRIM does not account for the opening of the other nuclear reaction channels, besides the elastic scattering, which also contribute to the displacements.

Thus we decided to perform SRIM calculations for other materials (Zr, Ni, Cr, Cu and Al) only from ~ 0.025 MeV to ~ 20 MeV, since large differences observed outside, see Figs. 2 - 4.

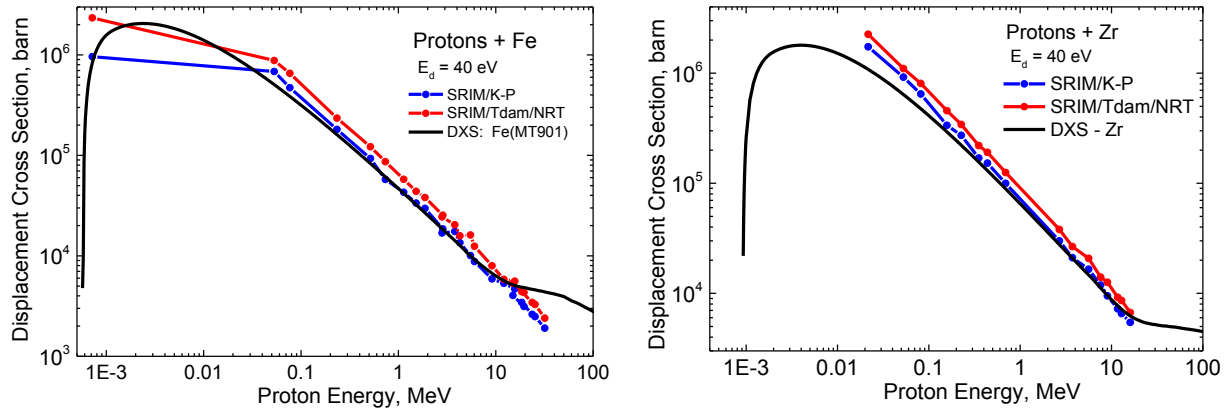

Fig. 2. Proton induced displacement cross section for Fe and Zr: comparison of SRIM/K-P and SRIM/T_{dam}/NRT with recommended values from DXS.

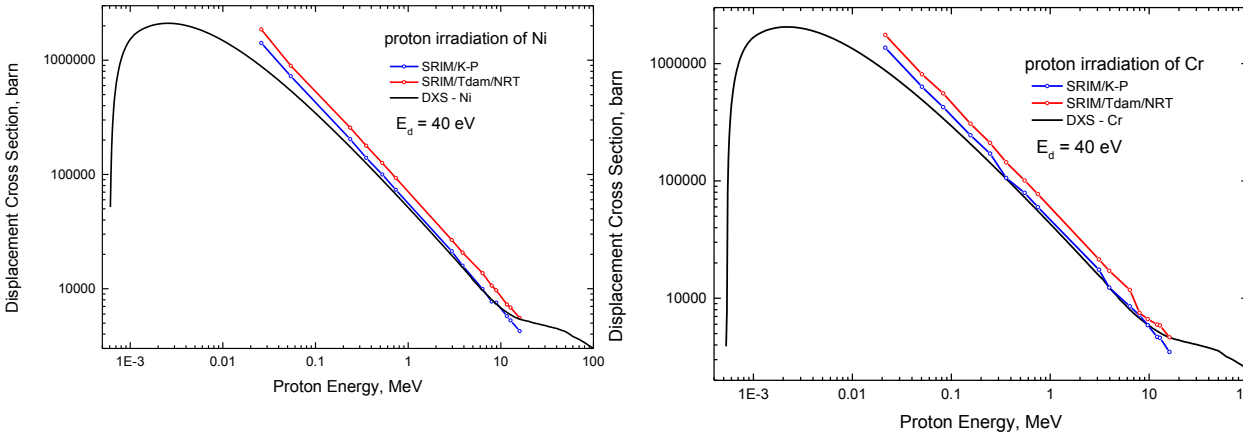

Fig. 3. Proton induced displacement cross section for Ni and Cr: comparison of SRIM K-P and SRIM/T_{dam}/NRT with recommended values from DXS.

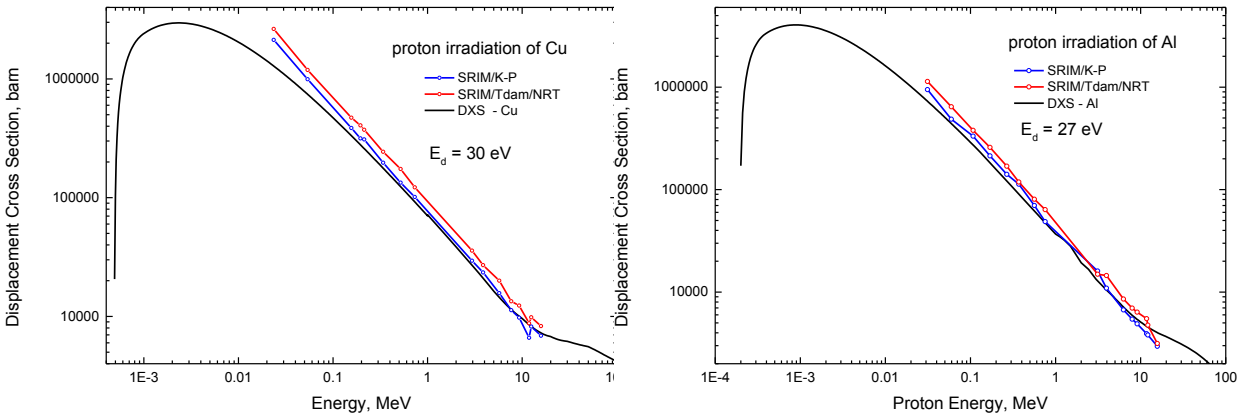

Fig. 4. Proton induced displacement cross section for Cu and Al: comparison of SRIM K-P and SRIM/T_{dam}/NRT with recommended values from DXS.

Conclusions

The proton induced displacement cross sections (vacancies) for Fe, Ni, Cr, Zr, Cu and Al were calculated by SRIM-2013 in the energy range 0.025 MeV to 19 MeV. Two options "Quick calculation of damage" (K-P) and "Detailed calculation with Full Cascades" (F-C) give results differing by factor up 2 for iron, that was already observed by R. Stoller et al. [2].

We also calculated the atom displacement cross sections employing the damage energy T_{dam} from the SRIM code and the NRT equation (SRIM/T_{dam}/NRT). The SRIM/K-P dpa cross sections are lower than SRIM/Tdam/NRT by 20 - 30% for materials investigated.

The comparison of SRIM/K-P results with the NRT dpa cross sections from the DXS database has shown an agreement for proton energies between 1 and 10 MeV. SRIM/NRT/T_{dam} cross sections are systematically larger than DXS by 20 - 30%.

SRIM does not estimate the contribution of inelastic nuclear reaction channels which becomes important at energies above 15 MeV.

References

1. J.F. Ziegler, M.D. Ziegler and J.P. Biersak, "SRIM – The stopping and range of ions in matter", Nucl. Instr. Meth. Phys. Res., Sect. B, vol. 268, pp. 1818 - 1823, 2010; http://www.srim.org/
2. R. Stoller, M.B. Toloczko, G. Was, A. Certain, S. Dwaraknath and F. Garner, "On the use of SRIM for computing radiation damage exposure", Nucl. Instr. and Meth. in Phys. Research B, vol. 310, pp. 75 - 80, 2013.
3. "Primary Radiation Damage in Materials", Report NEA/NSC/DOC(2015)9, OECD, Paris, 2015.
4. A.Yu. Konobeyev, C.H.M. Broeders and U. Fischer, "Improved displacement cross sections for structural materials irradiated with intermediate and high energy protons", Int. Meeting on Nuclear Applications and Utilization of Accelerators, Pocatello US, 2007.
5. A. Konobeyev, U. Fischer and L. Zanini, "Advanced Evaluation of Displacement and Gas Production Cross Sections for Chromium, Iron and Nickel up to 3 GeV Incident Particle Energy," in Int. Meeting on Nuclear Applications and Utilization of Accelerators, Knoxville, US, 2011.
6. A. Konobeyev et al., "DXS - Advanced Evaluations of Displacement and Gas Production Cross Sections"; available from: https://www-nds.iaea.org/public/download-endf/DXS/ .
7. G.H. Kinchin and R.S. Pease, "The Displacement of Atoms in Solids by Radiation", Reports on Progress in Physics, vol. 18, p. 1, 1955.
8. M. Norgett, M. Robinson and I. Torrens, "A Proposed Method of Calculating Displacement Dose Rates", Nucl. Eng. Des, vol. 33, pp. 50 - 54, 1975.
9. "Standard Practice for Neutron Radiation Damage Simulation by Charged-Particle Irradiation", ASTM E521, see ASTM web: http://www.astm.org/Standards/E521.htm.

Appendix 1

Second Research Coordination Meeting (RCM-2) of the IAEA CRP # F44003
"Primary Radiation Damage Cross Sections"

29 June - 2 July 2015
IAEA Headquarters, Vienna, Austria
Conference Meeting Room C-5

AGENDA
(presentations' time is approximate and includes questions and breaks)

Monday, 29 June

Opening (9:30 - 10:30)
Welcome address – R. Capote (NDS, Deputy Section Head) Administrative announcements – Alexander Öchs (NDS) Election of Chairperson and Rapporteur - All Approval of Agenda - All Evolution of CRP and objectives of RCM-2 - S. Simakov (NDS)

Session 1: Individual Presentations of Studies performed and future Plans
morning 10:30 - 12:00
R. Stoller, "Comments on dose, damage and dose-damage relationships" Y. Iwamoto, "Calculations of PKA spectra using the PHITS code and measurement of displacement cross section of copper irradiated with 125 MeV protons at cryogenic temperature" A. Konobeev, "Assessment of uncertainties of recoil spectra and displacement cross-sections associated with the use of evaluated data files and results of model calculations"
12:00 - 13:30 Lunch break + Administrative issues
evening 13:30 - 18:00
J. Kwon, "Calculation of primary radiation damage parameters using ENDF/B-VII: Recoil spectra and damage cross section" A. Koning, "TALYS, TENDL and Total Monte Carlo: Input for radiation damage analysis" P. Griffin, "Uncertainty Analysis of Metrics Used for Assessing Primary Radiation Damage" V. Khryachkov, "Improved spectrometer for (n,α) reaction study and first experimental results" P. Helgesson, H. Sjostrand, "The generation of gas-production cross-sections and their uncertainties for Ni-59 and its consequences for stainless steel in a thermal spectrum"
Coffee breaks as needed

Tuesday, 30 June

morning 9:00 - 13:00
J-Ch. Sublet, M. Gilbert, "Advanced nuclear observables processing for material sciences" M. Gilbert, J-Ch. Sublet, "Radiation damage source terms: PKA spectra" A. Kahler, "NJOY2012 – Current Status" F. Mota, C. Ortiz, "Status of work committed by CIEMAT for the IAEA CRP on Primary Radiation Damage"; "A Hybrid MD-BCA approach to simulate high-energy collision cascades in materials"
13:00 - 14:00 Lunch break
evening 14:00 - 18:00
D. Simeone, L. Luneville, "Study of the damage response to irradiation: Analysis within the BCA framework: the DART code" N. Lazarev, "Comparative Simulation of Primary Damages in Polymorphous Zirconium" J.-P. Crocombette, "Applicability of the NRT dpa and arc-dpa in ordered alloys" D. Terentyev, "Primary damage in Fe-Mn-Ni-Cu system with RPV relevant composition" L. Greenwood, "Neutron Spectral Dependence of Radiation Damage Calculations"
Coffee breaks as needed

Wednesday, 01 July

Session 2: Ind. Summaries and Joint Discussion of Progress and Future Researches
morning 9:00 - 13:00
K. Nordlund, "Data on damage production and mixing for parametrization of arc-dpa and rpa equations in several metals" C. Woo, "IAEA CRP Report: (1) Effect of Para/Ferro-magnetic transition in cascade simulation using SLD; (2) Cluster Dynamics to include correlated production in cascade damage"
13:00 - 14:00 Lunch break
evening 14:00 - 18:00
B. Marcinkevicius, S. Simakov, "Calculation of the NRT dpa cross section by SRIM-2013 and comparison with DXS"
Coffee breaks as needed
18:30 ***Hospitality event in*** *"Taverne IOS - Der Alte Grieche" on Copa Cagrana*

Thursday, 02 July

Session 3: Summarization of achieved Results and formulation Action/Recommendations for the RCM-2 Summary Report
morning 9:00 - 13:00
13:00 - 14:00 Lunch break
evening 14:00 - ≈ 16:00

Appendix 2

2nd Research Coordination Meeting of the IAEA CRP # F44003
"Primary Radiation Damage Cross-Section"
29 June to 2 July 2015
VIC Room C5, Vienna, Austria

LIST OF PARTICIPANTS

BELGIUM Mr Dmitry Terentyev Centre d' Etude de l'Energie Nucleaire Boeretang 200 2400 Mol Tel.: +32 14 33 31 97 E-mail: dterenty@sckcen.be	**CHINA** Mr Chung Ho Woo The City University of Hong Kong College of Science and Engineering The Chee Avenue Hong Kong SAR Tel.: +852 3442 7848 E-mail: chungwoo@cityu.edu.hk
FINLAND Mr Kai Nordlund Department of Physics University of Helsinki P.O. Box 43 Pietari Kalmink. 2 00014 Helsinki Tel.: +358 9 19150007 E-mail: kai.nordlund@helsinki.fi	**FRANCE** Mr Jean-Paul Crocombette CEA/Saclay DEN/DANS/DMN/SRMP Bat 520 – Pce 201 91191 Gif-sur-Yvette Cedex Tel.: +33 169 089285 E-mail: jpcrocombette@cea.fr
FRANCE Mr Laurence Luneville CEA Saclay DEN/DANS/SRMA/LA2M Bat 453 – Pce 27B 91191 Gif-sur-Yvette Cedex Tel.: E-mail: Laurence.luneville@cea.fr	**FRANCE** Mr David Simeone CEA Saclay DEN/DANS/SRMA/LA2M Bat 453 – Pce 27B 91191 Gif-sur-Yvette Tel.: +33 1 69 08 29 20 E-mail: david.simeone@cea.fr
GERMANY Mr Alexandre Konobeev Institute for Neutron Physics and Reactor Technology Karlsruhe Institute of Technology Herman von Heimholtz Platz 1 76344 Eggenstein-Leopoldshafen Tel.: +49 721 608 23768 E-mail: alexander.konobeev@kit.edu	**JAPAN** Mr Yosuke Iwamoto Japan Atomic Energy Agency 2-4 Shirakata-shirane Ibaraki-ken, Nakagun Tokaimura 319-1195 Tel.: +81 029 282 5195 E-mail: iwamoto.yosuke@jaea.go.jp

KOREA Rep. Mr Junhyun Kwon Nuclear Materials Division Korea Atomic Energy Research Institute 989-111 Daedeok-daero P.O. Box 105 - 305-350 Yuseong Daejeon Tel.: +82 42 868 8588 E-mail: jhkwon@kaeri.re.kr	**THE NETHERLANDS** Mr Arjan Koning Nuclear Research and Consultancy Group (NRG) Westerduinweg 3 P.O. Box 25 1755 ZG Petten Tel.: +31 22456-4051 E-mail: koning@nrg.eu
RUSSIA Mr Vitaly Khryachkov Institute for Physics and Power Engineering Bondarenko Sq. 1 Kaluga Region Obninsk 249 033 Tel.: +7 484 39 94827 E-mail: hva@ippe.ru	**SPAIN** Mr Dieter Leichtle ITER Department Fusion for Energy c/Josep Pla 2 Barcelona Tel.: +34 93 489 7459 E-mail: dieter.leichtle@f4e.europa.eu
SPAIN Mr Fernando Mota Laboratorio National de Fusion Avenida Complutense 40 CIEMAT 28040 Madrid Tel.: +34 91 346 6578 E-mail: Fernando.mota@ciemat.es	**SWEDEN** Mr Petter Helgesson Division of Applied Nuclear Physics Department of Physics and Astronomy Uppsala University P.O. Box 516 75120 Uppsala Tel.: E-mail: petter.helgesson@physics.uu.se
SWEDEN Mr Henrik Sjöstrand Department of Physics and Astronomy Division of Applied Nuclear Physics Uppsala University Box 516 751 20 Uppsala Tel.: +46 18 4713329 E-mail: Henrik.Sjostrand@physics.uu.se	**UKRAINE** Mr Nikolai Lazarev National Science Center Kharkov Institute of Physics and Technology 1, Akademicheskaya St. Kharkov 61108 Tel.: +38 057 3356203 E-mail: lazarev@kipt.kharkov.ua
UNITED KINGDOM Mr Mark Gilbert UK Atomic Energy Authority Culham Centre for Fusion Energy Abingdon Oxfordshire OX14 3DB Tel.: E-mail: mark.gilbert@ccfe.ac.uk	**UNITED KINGDOM** Mr Jean-Christophe Sublet UK Atomic Energy Authority Culham Centre for Fusion Energy Abingdon Oxfordshire OX14 3DB Tel.: +44 1235 466400 E-mail: jean-christophe.sublet@ccfe.ac.uk
UNITED STATES OF AMERICA Mr Lawrence R. Greenwood Pacific Northwest Laboratory MS P7-22, P.O. Box 999 Richland WA 99352 Tel.: +1 509 375 5301 E-mail: Larry.Greenwood@PNL.GOV	**UNITED STATES OF AMERICA** Mr Patrick Griffin Sandia National Laboratories P.O. Box 5800 Albuquerque NM 87185 Tel.: +1 505 845 9121 E-mail: pjgriff@sandia.gov

UNITED STATES OF AMERICA Mr Albert C. III Kahler Los Alamos National Laboratory Building 200, Room 215 P.O. Box 1663, MS B214 Los Alamos NM 87545 Tel.: +1 505 606 2042 E-mail: akahler@lanl.gov	**UNITED STATES OF AMERICA** Mr Roger Stoller Oak Ridge National Laboratory P.O. Box 2008, MS 6114 Oak Ridge TN 37831-6114 Tel.: +1 865 576 7886 E-mail: rkn@ornl.gov; stollerre@ornl.gov
IAEA Mr Stanislav SIMAKOV Head of the Nuclear Data Services Unit Nuclear Data Section Division of Physical and Chemical Sciences Tel.: +43 1 2600 21717 E-mail: s.simakov@iaea.org	**IAEA** Mr Naohiko OTSUKA Nuclear Data Services Unit Nuclear Data Section Division of Physical and Chemical Sciences Tel.: +43 1 2600 21715 E-mail: n.otsuka@iaea.org
IAEA Ms Valentina SEMKOVA Nuclear Data Services Unit Nuclear Data Section Division of Physical and Chemical Sciences Tel.: +43 1 2600 21727 E-mail: v.semkova@iaea.org	**IAEA** Mr Viktor ZERKIN Nuclear Data Services Unit Nuclear Data Section Division of Physical and Chemical Sciences Tel.: +43 1 2600 21714 E-mail: v.zerkin@iaea.org
IAEA Mr Roberto Capote Noy Head of the Nuclear Data Development Unit Nuclear Data Section Division of Physical and Chemical Sciences Tel.: +43 1 2600 21713 E-mail: Roberto.CapoteNoy@iaea.org	**IAEA** Mr Andrej Trkov Nuclear Data Development Unit Nuclear Data Section Division of Physical and Chemical Sciences Tel.: +43 1 2600 21712 E-mail: a.trkov@iaea.org

Nuclear Data Section
International Atomic Energy Agency
Vienna International Centre, P.O. Box 100
A-1400 Vienna, Austria

E-mail: nds.contact-point@iaea.org
Fax: (43-1) 26007
Telephone: (43-1) 2600 21725
Web: http://www-nds.iaea.org